Performance of the Electromagnetic Pixel Calorimeter EPICAL-2 and Soft-Photon Background Studies in ALICE 3

Dissertation

zur Erlangung des Doktorgrades
der Naturwissenschaften

vorgelegt beim Fachbereich Physik
der Johann Wolfgang Goethe-Universität
in Frankfurt am Main

von
Tim Sebastian Rogoschinski
aus Bad Nauheim

Frankfurt am Main 2023
(D 30)

Vom Fachbereich Physik
der Johann Wolfgang Goethe-Universität
als Dissertation angenommen.

Dekan:	Prof. Dr. Roger Erb
Gutachter:	Prof. Dr. Henner Büsching
	Prof. Dr. Harald Appelshäuser

Datum der Disputation:

Zusammenfassung

Das übergeordnete Thema dieser Arbeit bildet die Messung von Photonen mit Teilchendetektoren, die auf digitalen Silizium-Pixelsensoren basieren. Zwei wesentliche Schritte in Upgrade-Programmen des ALICE-Experiments am CERN-LHC werden in dieser Arbeit diskutiert.

Das ALICE-Experiment entwickelt im Rahmen von Upgrade-Programmen regelmäßig neue Detektoren für den Einsatz im Experiment, um das Messprogramm des Experiments zu verfeinern oder zu erweitern. Die Studien und Ergebnisse dieser Arbeit wurden im Rahmen dieser Upgrade-Programme durchgeführt. Ein Upgrade-Projekt in ALICE durchläuft üblicherweise die folgenden Schritte: Der Motivation, ein physikalisches Signal besser oder erstmals zu messen, folgen grundsätzliche Simulationsstudien zur Messbarkeit des Signals und zum Design eines Detektors. Anschließend werden Prototypen entwickelt und Test-Messungen durchgeführt, bis, am Ende der Konstruktion und Entwicklung, ein neuer Detektor im ALICE-Experiment integriert werden kann.

In der hier vorliegenden Arbeit werden zwei wesentliche Aspekte eines solchen Upgrade-Programms in ALICE vorgestellt, die zwei verschiedenen Programmen zuzuordnen sind: Im Zusammenhang mit dem für circa 2027 geplanten FOCAL-Detektor-Upgrade [ALI+20] werden in dieser Arbeit die Detektorantwort des elektromagnetischen Pixel-Kalorimeters EPICAL-2 und die Form elektromagnetischer Schauer untersucht. Dazu werden Messungen mit EPICAL-2 in einem Test-Strahl sowie Monte Carlo Simulationen verwendet. Im Rahmen des ALICE 3-Upgrades [ALI+22], der für das Jahr 2035 geplanten Neukonzeption des ALICE-Experiments, werden in dieser Arbeit Simulationsstudien zum Untergrund in der Messung von Photonen mit sehr kleinem Transversalimpuls präsentiert. Im Folgenden werden beide Teile dieser Arbeit zusammengefasst.

Teil 1: Performance des elektromagnetischen Pixel-Kalorimeters EPICAL-2

Das EPICAL-2-Kalorimeter wurde als ein neuartiges elektromagnetisches Pixel-Kalorimeter mit einem SiW-Sandwich-Design konzipiert, das auf digitalen Silizium-Pixelsensoren basiert. Dazu nutzt das EPICAL-2 die für das ALICE-ITS entwickelten ALPIDE Sensoren [Agl17]. Weiterhin baut das EPICAL-2-Design auf dem Vorgänger-Prototypen EPICAL-1 [Haa+18] mit MIMOSA Sensor auf; es markiert somit einen weiteren Evolutionsschritt in der Entwicklung digitaler Kalorimeter. Das

EPICAL-2 besteht aus 24 identischen Lagen. Jede Lage besteht aus einer Wolfram-Absorberplatte und zwei ALPIDE Sensoren. Insgesamt besitzt das EPICAL-2 eine Tiefe von circa 20 Strahlungslängen, eine aktive Fläche von $30 \times 30\,\text{mm}^2$ und etwa 25 Millionen Pixel, von denen jedes eine Größe von $26.88 \times 29.24\,\mu\text{m}^2$ hat.

Verschiedene Test-Messungen wurden mit dem EPICAL-2 durchgeführt und im Rahmen dieser Arbeit analysiert: Im Jahr 2020 wurden an der Universität Utrecht Test-Messungen mit kosmischen Myonen durchgeführt. Darüberhinaus wurden im Jahr 2020 Test-Messungen am DESY und als Teil dieser Arbeit im Jahr 2021 am CERN-SPS durchgeführt. Während der DESY-Teststrahl nur Elektronen enthält, handelt es sich am CERN-SPS um einen gemischten Teststrahl aus Myonen, Hadronen und Elektronen. Am DESY wurden Elektron-Ereignisse bei Energien von 1, 2, 3, 4, 5 und 5.8 GeV gemessen. Im Gegensatz dazu, wurden am CERN-SPS Myon-, Hadron- und Elektron-Ereignisse bei Energien von 20, 40, 60 und 80 GeV aufgenommen.

In der hier präsentierten Arbeit wird das EPICAL-2 im Simulationspaket ALLPIX^2 implementiert, um die Test-Messungen mit einer Monte Carlo Simulation vergleichen und validieren, und außerdem das Detektorverhalten in einer Simulation studieren zu können. Die EPICAL-2-Simulation stellt die erste Implementierung eines vollständig digitalen Kalorimeters im Simulationspaket ALLPIX^2 dar.

Jede wesentliche Eigenschaft des EPICAL-2 wird sorgfältig in der Simulation umgesetzt. Dazu wird vor allem die detaillierte EPICAL-2-Geometrie mit jedem einzelnen Detektorbauteil mit hoher Präzision implementiert. Mithilfe einer TCAD-Simulation mit einer Back-Bias-Spannung von $V_{\text{RB}} = 1.4\,\text{V}$ und den exakten Dotierungskonzentrationen jeder ALPIDE-Komponente, wird in Zusammenarbeit mit [Has21b] das elektrische Feld der Pixel im ALPIDE in der Simulation präzise realisiert. Weiterhin werden die Pixel-Schwellenwerte (82 e) und das Pixel-Rauschen (20 e) als Durchschnittswert der Chips im EPICAL-2 implementiert.

Neben der detaillierten Implementierung des EPICAL-2 werden die Eigenschaften der Test-Strahlen in der Simulation integriert. Um insbesondere die Test-Strahl-Messungen zu modellieren, wird die sogenannte Propagationszeit freier Ladungsträger in der Simulation zu 25.1 ns bestimmt. Dazu wird die Übereinstimmung der Verteilung der Pixel-Treffer für Elektron-Ereignisse bei 5 GeV zwischen gemessenen Test-Daten und der Simulation mit Hilfe eines χ^2-Tests, eines Kolmogorov-Tests und der Mittelwerte der Verteilungen getestet.

Die Stabilität der EPICAL-2-Simulation und insbesondere der Reproduzierbarkeit der Teststrahl-Daten durch die Simulation wird durch systematische Variationen der Implementierung zentraler Simulationsparameter überprüft. So lassen sich zudem, über die eigentliche Simulation hinaus, grundsätzliche Erkenntnisse zum Response-Verhalten des EPICAL-2 gewinnen. Beispielsweise beeinflusst besonders der Pixel-Schwellenwert das Simulationsverhalten: Je höher der Schwellenwert, desto niedriger die Anzahl der Pixel-Treffer und desto kleiner die Größe der Cluster. Insgesamt kann gezeigt werden, dass die Simulationsrechnungen des EPICAL-2 auch unter stärkeren Variationen der zentralen Simulationsparameter stabile Ergebnisse liefert; die Implementierung des Detektors in der Simulation wird so validiert.

Um mit Hilfe der Test-Messungen die Form elektromagnetischer Schauer und die Detektorantwort des EPICAL-2 zu bestimmen, werden in dieser Arbeit zunächst die folgenden Schritte zur Datenaufbereitung der Teststrahl-Daten durchgeführt:

- Ausschluss fehlerhafter Pixel
- Clustering der Pixel-Treffer
- Rel. Ausrichtung der Chips
- Kalibrierung der Chips
- Strahlwinkel-Korrektur
- Selektion von Elektronen

Im Speziellen werden in den Schritten der Datenaufbereitung folgende Besonderheiten beobachtet: Weniger als 1 % aller Pixel im EPICAL-2 sind fehlerhaft. Die Verteilung der Clustergröße zeigt eine hohe Wahrscheinlichkeit ($\sim 72\,\%$) für Cluster, die weniger als fünf Pixel enthalten. Es werden zudem sehr große Cluster (circa 100 Pixel) mir einer Spur-ähnlichen Form beobachtet. Die spezifische Chip-Antwort der EPICAL-2-Chips resultiert aus den unterschiedlichen Schwellenwerten der Chips. Die Kalibrierung und Ausrichtung der Chips bleiben stabil, unabhängig davon, ob kosmische Myonen oder Hadronen für die Korrekturen verwendet werden. Sowohl am DESY als auch am SPS liegt der Winkel zwischen Test-Strahl und EPICAL-2 bei etwa 0.4°. Die Kontamination von Hadronen in den SPS-Daten liegt unterhalb von 2 %.

In der vorliegenden Arbeit werden in den Test-Daten das longitudinale und das laterale Profil elektromagnetischer Schauer bestimmt. Für die DESY-Energien wird anhand des longitudinalen Profils Folgendes beobachtet: Das Schauermaximum für die Pixeltreffer-Messung liegt tiefer im EPICAL-2 (in späteren Lagen) als für die Cluster-Messung. Der entgegengesetzte Trend wird bei SPS-Energien beobachtet. Beides lässt sich auf Saturationseffekte und die Abhängigkeit der Chip-Antwort von dem Winkel, mit dem Schauerteilchen den Chip durchqueren, zurückführen.

Insgesamt beschreibt die Simulation die charakteristischen Eigenschaften der longitudinalen Profile aus den Test-Daten. Allerdings prognostiziert die Simulation ein Schauermaximum, das tiefer im EPICAL-2 liegt (circa $0.1\,X_0$ bis $0.3\,X_0$). Diese Diskrepanz könnte durch zusätzliches Material während der Test-Messung oder durch eine unvollkommene Beschreibung der Schauerentwicklung in GEANT4 entstehen.

Das laterale Profil elektromagnetischer Schauer nimmt mit steigender Energie stark zu und eine klare Abhängigkeit von den EPICAL-2-Lagen wird festgestellt, was sich auf die verschiedenen Entwicklungsstufen eines elektromagnetischen Schauers zurückführen lässt. Insbesondere wird in der Arbeit das Verhältnis zwischen lateraler Treffer- und Clusterdichte untersucht, wodurch der Einfluss von Saturationseffekten deutlich hervorgeht: Bei hohen Energien, im Bereich des Schauermaximums und nahe der Schauerachse nimmt die Saturation besonders stark zu.

In der Arbeit wird die Entfernung, bis zu der nahegelegene Schauer voneinander getrennt werden können, mit Hilfe der mittleren lateralen Breite eines elektromagnetischen Schauers evaluiert. Eine klare Abhängigkeit von den EPICAL-2-Lagen wird beobachtet: Je später die Lage, desto breiter wird der elektromagnetische Schauer. Insbesondere wird gezeigt, dass die mittlere Schauer-Breite für alle Energien in den ersten EPICAL-2-Lagen bei etwa 0.2 mm liegt. Dies zeigt die Möglichkeit auf, elektromagnetische Schauer mit einer Distanz von circa 0.2 mm zueinander zu unterscheiden.

Darüber hinaus wird die Schauertrennung anhand der Simulation von zwei Elektronen untersucht (30 und 250 GeV, 1.1 mm Abstand zueinander). Beide Schauer können eindeutig mit dem EPICAL-2 identifiziert werden. Besonders beeindruckt diese Beobachtung im Kontext des ALICE-FOCAL, wo sie bedeutetet, dass beispielsweise zwei Photonen aus einem symmetrischen π^0-Zerfall bis zu einer π^0-Energie von circa 1.6 TeV unterschieden werden können.

In der vorliegenden Arbeit wird außerdem die Energie-Antwort des EPICAL-2 bestimmt. Die Energie-Antwort wird mit einer linearen Funktion sowie mit einer Potenz-Funktion parametrisiert, um die Linearität der Energie-Antwort in den Test-Daten und der Simulation zu untersuchen. In den Test-Daten wird eine nicht-lineare Energie-Antwort beobachtet, wobei größere Abweichungen von einem linearen Zusammenhang für Cluster (bis zu $\sim 18\,\%$) als für Pixeltreffer (bis zu $\sim 5\,\%$) vorliegen. Auch in der Simulation wird eine nicht-lineare Energie-Antwort beobachtet. Allerdings liegen die Abweichungen von einem linearen Zusammenhang für Cluster bei weniger als $\sim 10\,\%$ und für Pixeltreffer bei weniger als $\sim 3\,\%$. Das beobachtete nicht-lineare Verhalten lässt sich teilweise auf Saturationseffekte, das longitudinale und laterale Austreten des Schauers aus dem begrenzten Detekorvolumen und bei DESY-Energien auf die Unsicherheit der Strahlenergie zurückführen.

Neben der Linearität wird in dieser Arbeit die Energieauflösung des EPICAL-2 untersucht. Die Energieauflösung für Cluster ist besser als für Pixeltreffer. Bereits für Pixeltreffer ist die Energieauflösung des EPICAL-2 besser als die Energieauflösung des Vorgängers EPICAL-1 [Haa+18]. Unter Verwendung von Clustern wird die Energieauflösung des EPICAL-2 in dieser Arbeit zu

$$\frac{\sigma_E}{E} = \frac{18.16\ \%}{\sqrt{E/\mathrm{GeV}}} \oplus 2.68\ \%$$

bestimmt. Diese Energieauflösung kommt sehr nahe an jene des analogen CALICE Protoypen [Adl+09] heran und macht somit digitale Pixel-Kalorimeter zu einer kompetitiven Kalorimeter-Technologie. Die Energieauflösung aus den Test-Daten wird in der Arbeit mit zwei Simulationsszenarien verglichen: Im einen Szenario fluktuiert die Energie des Teststrahls gemäß der Spezifikationen des Strahls am DESY und CERN, wohingegen im anderen Szenario die Strahlenergie konstant bleibt. Insgesamt zeigt sich in der Simulation eine bessere Energieauflösung als in den Test-Daten und die Berücksichtigung von Schwankungen in der Strahlenergie führt zu einer schlechteren Energieauflösung. Daher kann die mit den aufgenommenen Test-Daten bestimmte Energieauflösung des EPICAL-2 als obere Grenze für die intrinsische Energieauflösung des EPICAL-2 betrachtet werden. Weiterhin mindern die bereits genannten Saturationseffekte, das teilweise Austreten des Schauers aus dem begrenzten Detekorvolumen, die Unsicherheit über die Strahlenergie sowie Rest-Kontamination in den Test-Daten die Energieauflösung.

Die mit Hilfe der Simulationen und Test-Messungen bestimmten Ergebnisse dieser Arbeit wurden auszugsweise in [Alm+23] veröffentlicht. Insgesamt zeigen die Ergebnisse die gute Performance des Prototypen hinsichtlich der Energiemessung und der Bestimmung der Form elektromagnetischer Schauer basierend auf der hohen Granularität des EPICAL-2. Im Zusammenhang mit dem FOCAL-Upgrade des ALICE-Experiments unterstützen die Untersuchung zur Schauerbreite und die Simulationsszenarien in Bezug auf die Trennung von Schauern den Einbau von Pixel-Lagen im FOCAL. Zusammengefasst demonstriert die Performance des EPICAL-2 das Potential der Technologie digitaler Kalorimeter und deren zukünftigen Einsatz im Bereich der Hochenergiephysik.

Teil 2: Untergrund in der Messung von Photonen in ALICE 3

In ALICE 3 soll ein Forward Conversion Tracker (FCT) integriert werden, um weiche Photonen in Vorwärtsrapidität zu messen. Die präzise Messung weicher Photonen könnte dazu beitragen, die eindeutige Diskrepanz zwischen der theoretischen Vorhersage und experimentellen Messungen weicher Photonen zu verstehen [Rey+21]: Die verschiedenen Messungen zeigen einen Überschuss weicher Photonen in Bezug zur theoretischen Vorhersage um einen Faktor von typischerweise zwei bis acht. In der vorliegenden Arbeit wird der Untergrund in der Messung weicher Photonen mit Hilfe von Simulationen untersucht. Teile dieser Arbeit wurden in [ALI+22] veröffentlicht.

Die vorgeschlagene Detektorgeometrie von ALICE 3 wird in dieser Arbeit in einem GEANT4-Setup in das Simulationspaket G4ME implementiert [Pre22]. Insbesondere werden das Strahlrohr, die zylindrischen Silizium-Lagen, die End-Kappen und ein Detektionsvolumen für Photonen an der Position des ALICE 3-FCT implementiert. Um den Untergrund zu studieren, werden mit PYTHIA pp-Kollisionen bei $\sqrt{s} = 13\,\text{TeV}$ erzeugt und die dabei produzierten Teilchen werden durch die GEANT4-Detektorgeometrie propagiert.

Die Simulationsstudien dieser Arbeit zeigen, dass sich der Untergrund im Wesentlichen aus Zerfallsphotonen und Photonen, die im Detektormaterial via externer Bremsstrahlung produziert werden, zusammensetzt. Während die Anzahl produzierter Zerfallsphotonen für $p_{\mathrm{T}} < 10\,\text{MeV}$ stark abnimmt, steigt die Anzahl von Photonen aus externer Bremsstrahlung für $p_{\mathrm{T}} \rightarrow 0$ ähnlich zum erwarteten theoretischen Signal mit $1/p_{\mathrm{T}}$ an. Im Akzeptanzbereich des FCT liegt der gesamte Untergrund einen Faktor 5 bis 10 über der theoretischen Erwartung für das Signal weicher Photonen. Da Photonen aus externer Bremsstrahlung insgesamt den Untergrund dominieren, wird in dieser Arbeit das Material in ALICE 3 mit Hilfe von Geantinos in GEANT4 zu $8\% - 14\%\,X_0$ bestimmt. Bereits für $5\,\%\,X_0$ an Material wird der Untergrund genauso groß, wie das zu erwartende Signal. Für eine Messung weicher Photonen ist es daher essentiell, den Untergrund durch Photonen aus externer Bremsstrahlung zu reduzieren.

In dieser Arbeit werden zwei verschiedene Möglichkeiten zur Reduzierung des Untergrunds untersucht. Deutliche Verbesserungen können durch die Einführung eines Elektron-Vetos (Signal-zu-Untergrund-Verhältnis um Faktor ~ 30 besser) und durch die Reduktion des Materials mit Hilfe eines optimierten Strahlrohrs (Signal-zu-Untergrund-Verhältnis um Faktor ~ 7 besser) erzielt werden.

Content

0 Introduction

One of the most exciting endeavours in the field of high-energy physics is the study of the quark-gluon plasma (QGP), a state of strongly-interacting matter that is believed to have existed in the earliest moments of our universe right after the big bang [Bar09; SSS10]. To study the properties of the QGP, at the Large Hadron Collider (LHC) at the European Organization for Nuclear Research (CERN), heavy ions are accelerated and brought to collision. In heavy-ion collisions, similar conditions to those that existed right after the big bang are created. ALICE, one of the four big experiments at the CERN-LHC, is focussing on the study of the QGP properties [ALI+08a; ALI+21a].

The research of this work thematically belongs to the field of high-energy physics and has been performed in context and in the framework of the ALICE collaboration. Among a broad range of topics and analyses that the ALICE collaboration is constantly working on, upgrade programs are essential to expand or to refine the ALICE measurement program. A typical ALICE upgrade consists of different steps: After a motivation to measure a physics signal either for the first time or with higher precision, fundamental simulation studies are performed to evaluate the feasibility of a measurement of the physics signal and possible detector designs. Afterwards, prototypes are developed and test measurements are performed. Finally, the construction and the development leads to a new detector being integrated in the ALICE experiment.

The steps discussed above typically belong to one of the three main stages of maturity in an upgrade program of ALICE: First, the Letter of Intent (LOI), where the physics goals are defined and the feasibility of their measurement based on simulation is discussed. Second, the Technical Design Report (TDR), where a full detector concept is outlined with all the details regarding the choice of detector technologies and components. If present, prototypes and their performance are discussed as well. Third, the actual construction and commissioning of the new detector. Finally, the ALICE experiment is ready to take new data and perform analyses to measure the physics signals that initiated the upgrade.

In the present work, two main aspects of such an upgrade program in ALICE are presented, which are related to two different programs: Part one focusses on the detector performance of the Electromagnetic Pixel Calorimeter Prototype (EPICAL-2) [Alm+23] in context of the proposed Forward Calorimeter (FOCAL) upgrade for the ALICE experiment in 2027 [ALI+20]. In part two of this thesis, simulation studies of the background in a photon measurement in ALICE 3, which is the proposed next-generation heavy-ion collision experiment starting in 2035 [ALI+22], are presented. In the following, both parts of this thesis are introduced briefly.

The EPICAL-2 detector has been designed and constructed within the endeavour to develop a novel electromagnetic calorimeter based on a silicon-tungsten sampling design using silicon pixel sensors with binary readout. Although the EPICAL-2 R&D is performed in the context of the proposed FOCAL upgrade it also serves the general understanding of a fully digital calorimeter. The EPICAL-2 design is the next step in pixel calorimetry utilising the ALPIDE sensors developed for the ALICE-ITS upgrade, building on and refining the first prototype EPICAL-1 with MIMOSA sensors [ALI+14; Haa+18]. EPICAL-2 has a total thickness of about 20 radiation lengths, an area of $30 \times 30\,\mathrm{mm}^2$, and circa 25 million pixels of size $26.88 \times 29.24\,\mu\mathrm{m}^2$. Test-beam measurements with EPICAL-2 have been performed to evaluate the performance of the prototype and to study the shape of electromagnetic showers in the detector.

Part one of the thesis is organised as follows: In chapter 1, calorimetry in high-energy physics is discussed in general to provide context and to set the stage for the EPICAL-2 prototype. In chapter 2, the EPICAL-2 prototype is presented focussing on the setup, the measurement principle and the experimental test-beam measurements. In chapter 3, a simulation of the prototype is discussed. Both the implementation of the setup in a simulation framework is described and the behaviour of the prototype in simulation is studied. Chapter 4 discusses the analysis and the preparation of the test-beam data. Finally, chapter 5 presents the results: Both the shape of electromagnetic showers and the performance of the energy measurement with the EPICAL-2 prototype are discussed.

The background study presented in part two of this thesis serves as a baseline study for the proposition to include a Forward Conversion Tracker (FCT) in ALICE 3 to measure soft photons, i.e. photons of a few MeV in transverse momentum, at forward rapidities [ALI+22]. A new soft-photon measurement has the potential to resolve the long standing "soft-photon puzzle": Several experiments have observed an excess of the soft-photon yield with respect to the expected yield from Low's theorem, which is fundamentally relating soft-photon production from inner Bremsstrahlung and the spectrum of charged hadrons [Rey+21]. With the background study, the dominant background in the soft-photon measurement, decay photons and external Bremsstrahlung from detector-material interaction, is investigated in simulation.

Part two of the thesis is organised as follows: In Chapter 6, the production of soft photons is introduced, the current experimental situation is outlined and the detector requirements for a new soft-photon measurement at a future LHC collider experiment as the ALICE 3 are discussed. Chapter 7 focusses on the background study: The simulation setup is described, the different background sources are evaluated, considerations on how to reject the background are discussed and implications for ALICE 3 are drawn.

Part One:

Performance of the Electromagnetic Pixel Calorimeter EPICAL-2

1 Calorimetry in High-Energy Physics

One of the main applications of the electromagnetic pixel calorimeter prototype EPICAL-2 is to measure electrons, positrons and photons. To understand the measurement of e.g. an electron with the EPICAL-2, a basic knowledge about calorimeters is important. In addition, the evaluation of the calorimeter performance requires the knowledge of calorimeter properties in general as well as the context of current calorimeters and recent developments.

In this section, basics on calorimetry are introduced, important calorimeter properties are described and typical calorimeters in high-energy physics experiments as well as EPICAL-2 related prototypes are presented.

1.1 Basics on Calorimetry

Calorimeters are detectors deployed in most modern high-energy physics experiments to measure the position and the energy of particles with energies in the range of some MeV to TeV. The particle to be detected is referred to as the incident or primary particle. Typically, the measurement of a primary particle involves several inelastic processes in which the energy of the primary particle is distributed among a huge number of secondary particles inside of the detector material. Eventually, the secondary particles deposit all their energy in the calorimeter through various interactions and a signal proportional to the energy of the primary particle is detected.

Usually, calorimeters are classified according to their construction technique. All calorimeters need a passive material to absorb the energy of both primary and secondary particles and an active material to convert the shower particles to a detectable signal. If a calorimeter is constructed using a single material which is active and passive at once, the calorimeter is referred to as being homogeneous. In contrast, if alternating active and passive material is instrumented in a calorimeter, it is called a sampling calorimeter.

Furthermore, calorimeters are classified according to the type of particle they are designed to measure: either hadrons or primarily electromagnetic interacting particles. Therefore, hadronic calorimeters are designed to measure hadrons, whereas electromagnetic calorimeters are designed to measure photons, electrons and positrons.

Both the EPICAL-2 prototype studied in this work and the related proposed FOCAL detector are electromagnetic sampling calorimeters. To further elaborate electromagnetic sampling calorimeters, a typical measurement with such a calorimeter is discussed in more detail below.

If an incident high-energy photon, electron or positron enters a calorimeter, it interacts with the material and creates secondary particles namely again photons, electrons and positrons. If the energy of the secondary particles is high enough, they interact in a similar way producing more and more shower particles with lower and lower energy until all the energy of the primary particle is deposited in the calorimeter. This cascade of secondary particles is called a particle shower. At high energies, electrons and positrons interact via Bremsstrahlung and photons undergo pair production. At low energies, ionisation is the dominant process for electrons and positrons, whereas photons interact via Compton scattering or the photoelectric effect. By the time the energy of secondary electrons and positrons is so little that Bremsstrahlung becomes unlikely compared to ionisation, no further photons are created and thus the electromagnetic shower evolution ceases.

In the creation and propagation of secondary particles, the shower broadens in the lateral direction w.r.t. the shower axis. Electrons and positrons move away from the shower axis due to multiple scattering. Photons are produced via Bremsstrahlung in which they are emitted in a similar direction as the direction of the mother electron momentum. Furthermore, both Compton scattering and photo effect lead to an additional angle of shower particles w.r.t. to the shower axis which also contributes to a broadening of the shower.

1.2 Calorimeter Properties

The fundamental properties of a calorimeter address how and how good the energy of a primary particle is measured with the calorimeter. Several quantities like the material properties of the calorimeter affect the electromagnetic shower evolution in the calorimeter and thus influence the energy measurement.

In this section, first, the material properties of a calorimeter and the description of the electromagnetic shower evolution are discussed. After this, the energy resolution, the energy linearity and the position resolution of a calorimeter are described.

The amount of material in the longitudinal direction, i.e. the depth in a calorimeter, is typically expressed in terms of radiation length X_0 [KW16], which describes the average distance after which an high-energy electron radiated all but 1/e of its initial energy via Bremsstrahlung [GZ+20]:

$$X_0 = \frac{716.408 \frac{g}{cm^2}}{\rho} \cdot \frac{A}{Z\,(Z+1) \cdot \ln\left(\frac{287}{\sqrt{Z}}\right)} \tag{1}$$

A corresponds to the mass number, Z refers to the atomic number and ρ is the density of the material. X_0 is typically expressed in units of cm for any given material. For instance, tungsten has a radiation length X_0 of 0.3504 cm and X_0 for silicon is 9.37 cm [Gro20]. Similar to the radiation length X_0, which is a measure of the probability for an electron to start to generate a shower, for hadrons it is the nuclear interaction length

λ_i, which serves as a measure for the shower probability of a hadron. Therefore, both quantities can be interpreted as a measure of the depth of a calorimeter.

Radiative and ionising energy loss of electrons show different dependencies on the particle energy E and the mass m as well as the atomic number Z of the medium [KW16]:

$$\begin{aligned} \text{ionisation:} \quad & \propto \quad Z \cdot \ln\left(E/m\right) && (2) \\ \text{Bremsstrahlung:} \quad & \propto \quad Z^2 \cdot \left(E/m^2\right) && (3) \end{aligned}$$

The energy at which the energy loss via Bremsstrahlung is as likely as ionisation is referred to as the critical energy and thus corresponds to an energy scale where the electromagnetic shower evolution ceases. The critical energy E_c depend on the material properties and is parametrised for solid (gaseous) materials as follows [GZ+20]:

$$E_\mathrm{c} = \frac{610\,(710)\ \mathrm{MeV}}{Z + 1.24\,(0.92)} \tag{4}$$

For example, the critical energy is $E_\mathrm{c} \approx 8$ MeV for tungsten and $E_\mathrm{c} = 40$ MeV for silicon [Gro20].

The longitudinal energy loss distribution of an electromagnetic shower is empirically well describes by the following function [KW16; GZ+20]:

$$\frac{\mathrm{d}E}{\mathrm{d}t} = E_0 \cdot \frac{\beta^\alpha\, t^{\alpha-1}\, e^{-\beta t}}{\Gamma(\alpha)} \tag{5}$$

E_0 corresponds to the primary particle energy, α and β are free parameters, and t corresponds to the depth in units of radiation length. As a rule of thumb, the shower maximum position t_max, i.e. the depth of the shower maximum, can be calculated as [KW16; GZ+20]:

$$t_\mathrm{max} = \frac{\alpha - 1}{\beta} \approx \ln\left(\frac{E_0}{E_\mathrm{C}}\right) + C \quad \begin{cases} C = -0.5, & \text{for electrons} \\ C = +0.5, & \text{for photons} \end{cases} \tag{6}$$

t_max is modified for the incident particle being either electron or photon.

The transverse shower development typically scales well with the Molière radius R_M which is defined as the radius of a cylinder in which 90 % of the total energy of an electromagnetic shower is situated. Roughly 99 % of the total energy of an electromagnetic shower is contained within 3.5 R_M [GZ+20]. Given the definition, R_M quantifies the lateral size of an electromagnetic shower in a calorimeter. R_M relates to both radiation length and critical energy as follows [KW16; GZ+20]:

$$R_{\mathrm{M}} = X_0 \cdot \frac{21\ \mathrm{MeV}}{E_{\mathrm{C}}} \tag{7}$$

For example, the Molière radius is $R_{\mathrm{M}} = 0.9327$ cm for tungsten and $R_{\mathrm{M}} = 4.944$ cm for silicon [Gro20].

The energy resolution σ_E/E of a calorimeter is typically parametrised as follows [KW16]:

$$\frac{\sigma_E}{E} = \frac{a}{\sqrt{E/\mathrm{GeV}}} \oplus b \oplus \frac{c}{E/\mathrm{GeV}} \tag{8}$$

$\oplus$ refers to the calculation as a quadratic sum of the individual terms. $a/\sqrt{E}$ is often called stochastic term which describes statistical shower fluctuations as well as sampling fluctuations, which arise from the variations of the number of charged shower particles crossing active sensors. Therefore, the resolution of a sampling calorimeter improves the higher the number of layers with thinner and thinner absorber layers. The parameter b is typically called constant term as it increases the higher the energy E. Inhomogeneities, non-linear effects like losses or calibration issues can be described and are expected to scale with E. Moreover, fluctuations in the longitudinal energy containment including leakage scale with the energy E and are also described via the parameter b. The last term, c/E, is usually referred to as the noise term since electronic noise yields a constant contribution for each energy. In addition, contributions to the energy resolution that are independent of energy can be described via this term.

Besides the energy resolution, the energy linearity reflects another material property of a calorimeter. To measure the incident particle energy with a calorimeter, the calorimeter signal should be proportional to the primary particle energy. Various effects like leakage can restrict the energy linearity. Therefore, typically, the energy linearity of a calorimeter is measured in test-beams and the deviations from linearity are considered by experiments using this calorimeter for energy measurements.

In addition to the energy measurement, the position of the incident particle impinging the calorimeter surface is a desired quantity for many experiments. The position resolution is mainly limited by the granularity of the calorimeter. i.e. the segmentation into read-out cells per unit area. Therefore, all else equal, the higher the granularity the higher the position resolution.

Overall, the design of a calorimeter is optimised so that its properties meet the requirements necessary to achieve certain physics goals. The requirements can vary from high position resolution to good energy resolution or lie in between. For an energy measurement with an electromagnetic calorimeter which provides a linear energy response, the electromagnetic shower should be fully contained in the

Figure 1: Left: *Four* EMCAL *towers each with an attached bundle of fibers [ALI+08b].* ***Right:*** *Single* PHOS *cell containing a block of PBWO$_4$ which is connected to the readout unit [ALI+99].*

calorimeter volume. Therefore, when constructing a calorimeter, it is particularly important that the total depth of the calorimeter amounts to sufficient radiation lengths that the full primary particle energy can be deposited. For a good position resolution, the transverse segmentation of the calorimeter plays an important role and should be in the order of and preferably less than the Molière radius of the calorimeter.

1.3 Existing Calorimeters and Prototypes

Different calorimeter techniques are deployed in modern high-energy physics experiments to measure mainly (high-energy) photons. The ALICE experiment uses both a homogenous and sampling calorimeters for photon measurements. In this section, an overview of existing calorimeters and prototypes is presented with an emphasis on the material properties and the granularity of the calorimeters and starting with the prominent calorimeters EMCAL and PHOS of the ALICE experiment.

The Electromagnetic Calorimeter EMCAL is a large acceptance sampling electromagnetic calorimeter embedded in the ALICE detector primarily to enhance jet measurement capabilities and to augment existing photon measurement capabilities. EMCAL is made up of 12288 detection cells, so-called towers, which have a transverse area of $60 \times 60\,\text{mm}^2$. Figure 1 (left) shows a group of four towers each attached to a bundle of fibres. Each tower consists of 76 alternating layers of 1.44 mm Pb and 77 layers of 1.76 mm of scintillator (Sc). The depth of EMCAL equals 20.1 X_0 and $R_\text{M} = 3.2$ cm. More information on the ALICE-EMCAL is provided in the technical design report of EMCAL [ALI+08b].

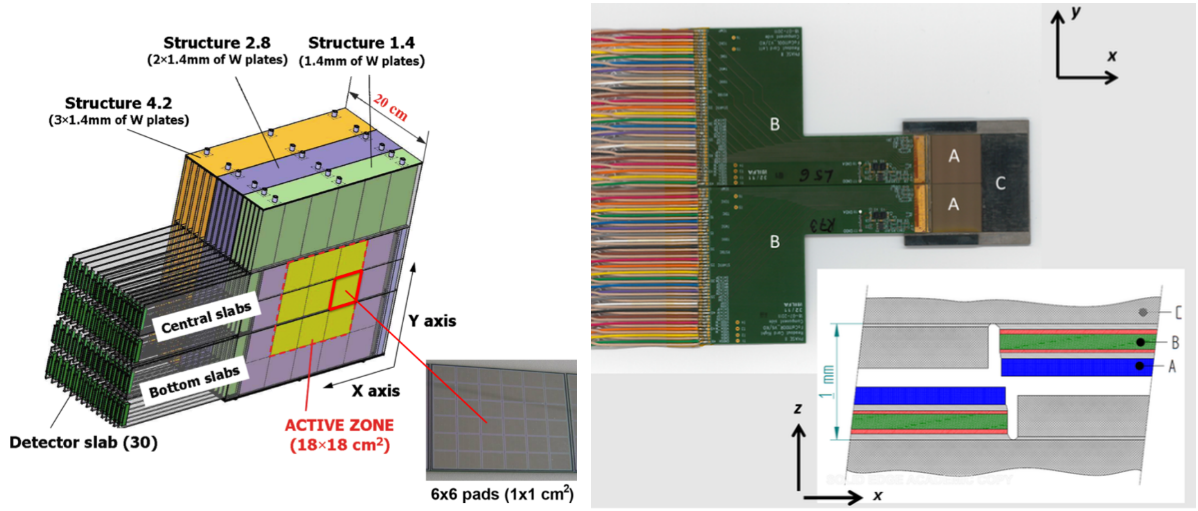

Figure 2: ***Left:*** *Design drawing of the CALICE-ECAL [Bil+15].* ***Right:*** *An EPICAL-1 module in top view with two sensors A connected to the readout B on top of the tungsten absorber C [Haa+18].*

In contrast, the EMCAL as sampling calorimeter, the Photon Spectrometer PHOS is a homogenous electromagnetic calorimeter embedded in the ALICE detector. PHOS is optimised for the measurement of neutral mesons and photons directly produced in high-energy particle collisions. PHOS consists of 17280 lead-tungstate ($PBWO_4$) detection cells, each of size $22 \times 22 \times 180\,\mathrm{mm}^3$ and coupled to a photodetector with integrated low noise preamplifier. Figure 1 (right) displays a single PHOS detection cell. The material properties of $PBWO_4$ are $R_M = 2.0$ cm and $X_0 = 0.89$ cm. Thus, the total depth of PHOS equals 20 X_0. Further details about PHOS can be found in its technical design report [ALI+99].

To broaden the view on calorimeters in experiments at the LHC other than the ALICE experiment, one can consider, for example, the CMS and LHCB experiment. The Electromagnetic Calorimeter ECAL of the CMS experiment is a homogenous $PBWO_4$ crystal calorimeter embedded in the experiment primarily to measure the two-photon decay mode of the Higgs. Despite a larger acceptance with 82000 crystals, the CMS-ECAL material properties are similar to those of the ALICE-PHOS. More details about the CMS-ECAL are reported in its technical design report [CMS97].

Contrary to the homogenous CMS-ECAL, the Electromagnetic Calorimeter ECAL of the LHCB experiment is a sampling calorimeter primarily implemented for triggering on high-energy hadron, electron and photon candidates as well as for photon reconstruction. Although the LHCB-ECAL features different cell sizes for the inner, middle and outer section, the inner section cells have the highest granularity with a size of $40.4 \times 40.4\,\mathrm{mm}^2$. Each cell is made up of a sampling structure which consists of alternating 2 mm lead sheets and 4 mm thick scintillator plates

	Material	Molière Radius (mm)	Granularity (mm^2)	depth (X_0)
ALICE-EMCAL	Pb+Sc	32	60 x 60	20.1
ALICE-PHOS	$\mathrm{PBWO_4}$	20	22 x 22	20
CMS-ECAL	$\mathrm{PBWO_4}$	21.9	22 x 22	26
LHCB-ECAL	Pb+Sc	36	40.4 x 40.4	25
CALICE physics prototype	Si-W	~ 15.25	10 x 10	24
EPICAL-1	Si-W	~ 11	0.03 × 0.03	28
proposed ALICE-FOCAL-E	Si-W	< 15	1 x 1 (pads) 0.03 × 0.03 (pixels)	> 20
EPICAL-2	Si-W	~ 10	0.03 × 0.03	21

Table 1: *Detector material, granularity, Molière radius and the total depth for selected calorimeters and prototypes as discussed in the text.*

interspersed with fibers. The LHCB-ECAL features 25 X_0 and $R_\mathrm{M} \approx 3.6$ cm. In the LHCB-ECAL technical design report more information can be found [Ama+00].

In addition to the current calorimeters in the experiments at the LHC, various calorimeter prototypes exist and are in development building on and refining existing calorimeter designs. The CALICE Collaboration, performing detector research and development on calorimetric systems for the International Linear Collider ILC [Aar+07], has designed and constructed an analog sampling silicon-tungsten (Si-W) electromagnetic calorimeter prototype ECAL [Bil+15]. Figure 2 (left) shows a design drawing of the CALICE-ECAL. Overall, the detector consists of 6480 silicon pads each of size $1 \times 1\,\mathrm{cm}^2$. The tungsten thickness is 1.4 mm per layer in the first 10 layers, 2.8 mm in the second 10 layers and the last 10 layers are 4.2 mm thick. Therefore, the CALICE-ECAL has a total of 30 layers which equal 24 X_0. The Molière radius is estimated at $R_\mathrm{M} \approx 15.25$ mm. The CALICE-ECAL has been successfully tested in electron and hadron beams [Adl+09; Bil+15].

Besides using silicon pads as in the CALICE-ECAL prototype, one can use other sensor technologies like e.g. silicon pixel sensors. The EPICAL-1 [Haa+18], a Si-W calorimeter prototype using pixel sensors with high granularity and small Molière radius, has been designed and constructed to investigate the potential of digital calorimeters and to explore the electromagnetic shower shape. EPICAL-1 consists of 24 layers. Each 4 mm thick layer is made up of a 3 mm thick tungsten absorber plate, four silicon pixel sensors with a cell size of $30 \times 30\,\mu\mathrm{m}^2$, readout boards, and tungsten spacers. Figure 2 (right) displays the construction of a single EPICAL-1 layer. The total depth equals 28 X_0 and the Molière radius is calculated to be $R_\mathrm{M} \approx 11$ mm. EPICAL-1 is considered as predecessor prototype w.r.t. to EPICAL-2 given their similar construction and measurement principle.

Table 1 summarises the properties of the calorimeters described above as well as the EPICAL-2 properties and the properties of the ALICE-FOCAL since the research

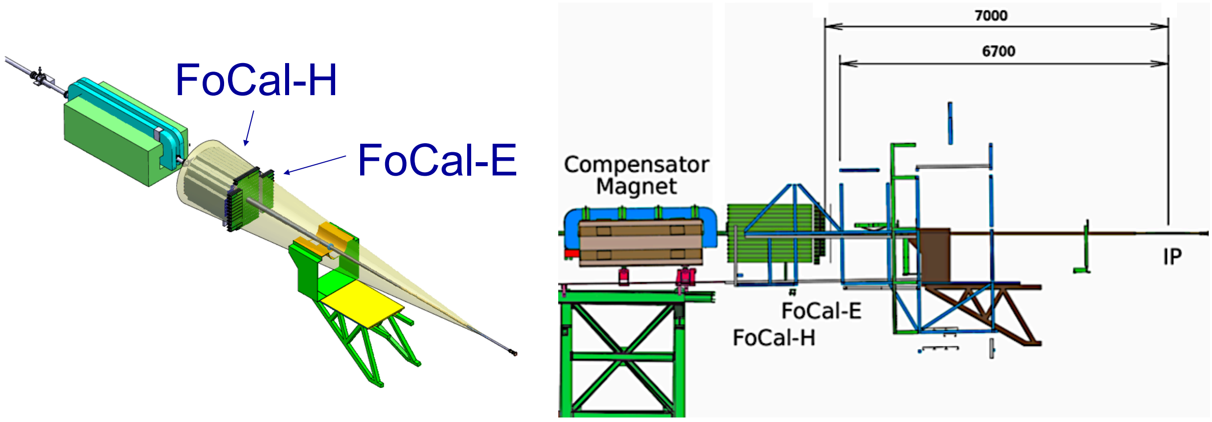

Figure 3: *FoCal design with the two components FoCal -H and FoCal -E (left) and the positing of FoCal in a distance of 7 m to the interaction point (IP) in side view (right) [ALI+20].*

subject of this thesis part, the Epical-2 prototype, has been carried out in context of the proposed Alice-FoCal upgrade. Alice-FoCal is discussed in the next section in detail and the following chapter 2 focusses on Epical-2.

1.3.1 Alice-FoCal

The Alice experiment has been upgraded several times in the recent years at the time of this work [ALI+12]. However, the general detector concept remains unchanged and is extensively discussed in various publications and references therein [ALI+08a; ALI+21a; ALI+95]. In relation to this thesis, a major upgrade proposal involves the extension of the scope of Alice by a Forward Calorimeter FoCal in 2027 to constrain small-x parton structure via forward direct-photon measurements [ALI+20].

To measure both photons and hadrons, FoCal will be equipped with a hadronic (FoCal -H) and an electromagnetic (FoCal -E) detector component. Figure 3 displays the design of FoCal in a 3D view on the left and in a side view on the right. It is foreseen to operate FoCal seven meters away from the collision interaction point at $3.4 < \eta < 5.8$. FoCal -E is designed as a sandwich structure, whereas FoCal -H will be operated as a spaghetti type calorimeter for hadron measurements. The work of this thesis with the electromagnetic calorimeter prototype Epical-2 has been carried out within the research and development (R&D) efforts of FoCal -E. Therefore, FoCal -E is discussed in more detail below. More information on FoCal -H can be found in [ALI+20].

FoCal -E is designed as a sampling calorimeter with alternating silicon sensor and absorber layers in a compact structure featuring approximately 1 X_0 per layer by utilising tungsten as absorber material with $X_0 = 3.504\,\text{mm}$ [Gro20]. To maintain good energy linearity also at high energies it is key to minimise longitudinal leakage

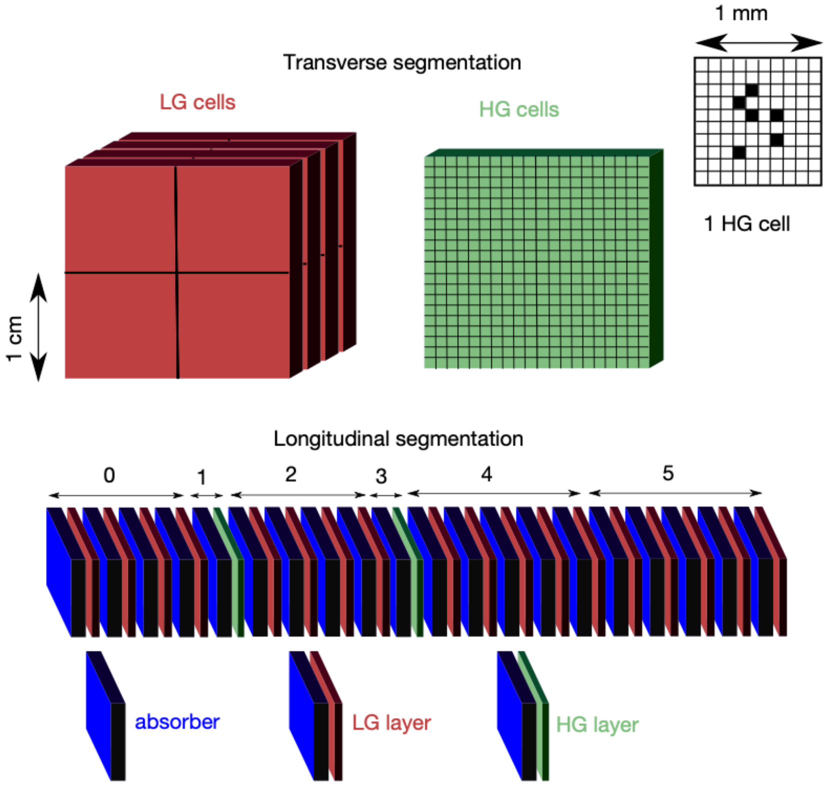

Figure 4: *Conceptual design of* FOCAL *-E. The transverse segmentation (top) is illustrated for both low-granularity (LG) layers and high-granularity (HG) layers. In the longitudinal segmentation (bottom), LG layers and HG layers are arranged between the tungsten absorber plates [ALI+20].*

which is achieved by implementing at least 20 X_0. Moreover, tungsten confines the shower in a rather compact volume given the tungsten Molièr radius of $R_\mathrm{M} = 0.9327\,\mathrm{cm}$ [Gro20].

FOCAL -E involves two different silicon sensor technologies namely silicon pads with low granularity (LG) cells and silicon pixels with high granularity (HG) cells. Figure 4 illustrates the transverse segmentation with the two different types of cells and the longitudinal segmentation with alternating silicon sensor and absorber layers. In Figure 4, the FOCAL -E structure involves 18 pad layers and two pixel layers positioned in layer 5 and in layer 10. The Pad layers with a cell size of $1 \times 1\,\mathrm{cm}^2$ deliver a precise time information $\mathcal{O}(25\,\mathrm{ns})$ and are used for the energy measurement given their larger sampling fraction compared to the pixel layers. In contrast, the pixel layers are rather slow $\mathcal{O}(5\,\mu\mathrm{s})$ but much more granular as they consist of $30 \times 30\,\mu\mathrm{m}^2$ pixel cells with digital readout. The high granular pixel layers meet the FOCAL -E requirement to separate near-by showers, which allows to distinguish direct photons and photons from neutral pion decays. For instance, for a neutral pion with $p_\mathrm{T} = 25$ GeV at a pseudorapiditiy of $\eta = 4.5$ and an energy asymmetry of the decay photons of $\alpha = 0.5$, the spatial distance between the two decay photons amounts to 1 mm at the distance of 7 m [ALI+20].

In this thesis, one of the most important features of FOCAL -E, the high-granularity, is investigated in a calorimeter application by analysing data from test-beam measurements with the EPICAL-2 prototype, which only employs pixel layers in contrast to FOCAL -E with both pad and pixel layers. Relying solely on pixel layers in a calorimeter, the EPICAL-2 energy measurement in terms of energy resolution and energy linearity is studied. Furthermore, the details of the electromagnetic shower evolution is investigated by exploiting the high granularity. The next section presents the EPICAL-2 prototype, its construction and the test-beam measurement campaigns in which the data analysed in this work were acquired.

2 The EPICAL-2 Prototype

The electromagnetic pixel calorimeter EPICAL-2 is a new digital calorimeter prototype. It uses a sandwich structure of silicon and tungsten layers, with Monolithic Active Pixel Sensors (MAPS) that provide a high granularity. In this chapter, first, the EPICAL-2 prototype is presented and the energy measurement principle of EPICAL-2 is discussed. After this, the test-beam measurements with EPICAL-2 in which the data analysed in this work were obtained are described focussing on the test setups and the details of the acquired data. Finally, the coordinate system used for the data analysis and for the presentation of results is described.

2.1 Design and Setup

Figure 5 gives an overview of EPICAL-2, basically a sandwich calorimeter consisting of alternating tungsten (W) absorber and silicon (Si) sensor layers employing the binary readout ALICE Pixel Detector (ALPIDE) chip [Agl17], which is described in the following section 2.1.1. In Figure 5, the full setup is visible in front view where the active volume of $\approx 3 \times 3 \times 8.5\,\mathrm{cm}^3$ is housed in a metal frame that provides both the mechanical stability and cooling for the setup. EPICAL-2 is equipped with a water cooling system to ensure stable measurement conditions regarding temperature. As shown in Figure 5, each sensor layer in the EPICAL-2 stack of Si/W layers is connected via layer cables to a readout unit alternately on the right and left.

The EPICAL-2 stack consists of 24 identical layers. Figure 6 (left) displays a design drawing in explosion view of a single instrumented EPICAL-2 layer and Figure 6 (right) shows a photo of one final-constructed layer. Each layer is 3.5 mm thick and consists of a tungsten absorber plate, two tungsten spacers and two ALPIDE chips which are connected to a module chip and layer cable. On top of each 3.0 mm thick absorber plate with a surface of $40 \times 40\,\mathrm{mm}^2$ are two 0.5 mm thick tungsten spacers of 4 mm width which are placed at two opposite edges of the absorber plate as shown in Figure 6. The spacers are used to protect the 50 µm thick ALPIDE chips and the cabling which are both positioned between the spacers. Given the total thickness of ALPIDE and cabling of less than 0.5 mm, only minor space between layer cables and the following absorber plate is left ensuring a compact design. Per layer, one ALPIDE chip is rotated by 180° w.r.t. to the other as visible in Figure 6 (left). Facing each other with their long edges, the two chips are glued onto the absorber with as minimal separation as possible. However, a residual $\approx 100\,\mu\mathrm{m}$ gap is left leading to a pixel-free region between the two chips, i.e. in the centre of each EPICAL-2 layer.

The total active area of $\approx 30 \times 30\,\mathrm{mm}^2$ is sufficient to laterally contain full electromagnetic showers given the tungsten Molière radius of $R_\mathrm{M} = 9.327$ mm [Gro20]. The amount of material in longitudinal direction is dominated by the

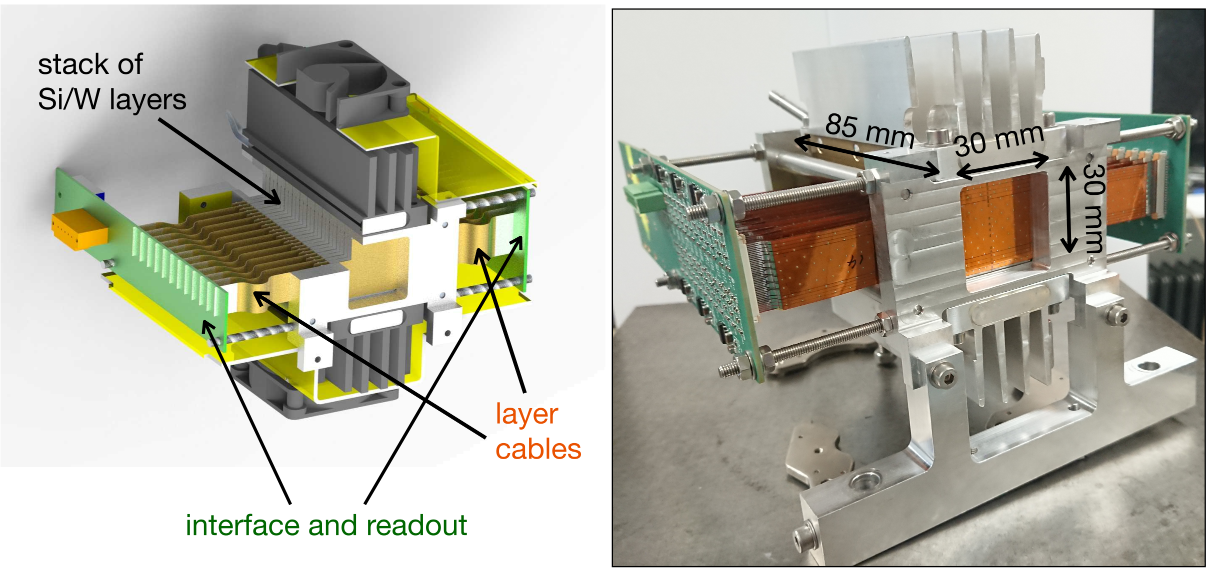

Figure 5: ***Left:*** *Design drawing of the* EPICAL-2 *prototype.* ***Right:*** *Front view of the final construction of the* EPICAL-2 *prototype.*

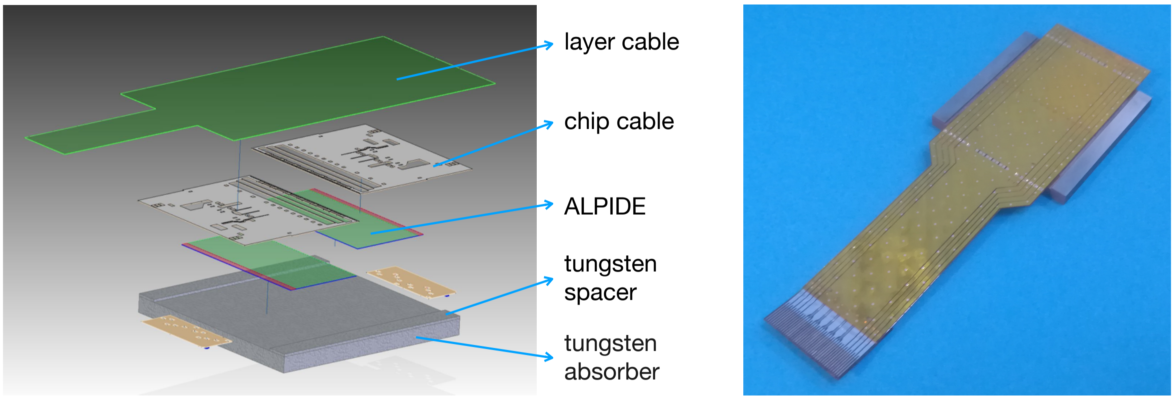

Figure 6: ***Left:*** *Explosion view of a single instrumented* EPICAL-2 *layer visualising the main components.* ***Right:*** *Photo of a single assembled layer of* EPICAL-2.

tungsten absorber plates of 72 mm in total. Given the tungsten radiation length of 3.504 mm and the nuclear interaction length of 99.46 mm [Gro20], the total depth of EPICAL-2 corresponds to $\approx 21\ X_0$ and $\approx 0.72\,\lambda_i$. $21\ X_0$ are sufficient to longitudinally contain electromagnetic showers, whereas with $0.72\,\lambda_i$ it is very unlikely for hadrons to shower at all.

2.1.1 The ALPIDE Chip

The ALICE Pixel Detector (ALPIDE) chip [Agl17] is a $1.5 \times 3\,\text{cm}^2$ large Monolithic Active Pixel Sensor (MAPS) [Sno14] produced in a 180 nm CMOS technology process for imaging sensors by Tower Semiconductor [Sem+23]. Figure 7 shows a picture of a single ALPIDE chip. Originally, the ALPIDE chip was designed for the upgrade of the

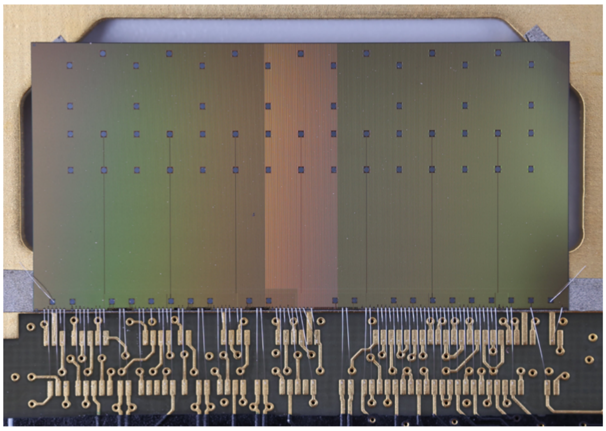

Figure 7: *Photo of a single* ALPIDE *chip positioned on a testing device [ALI+23].*

ALICE Inner Tracking System (ITS) [ALI+14], which has been realised in 2020 by the integration of the ITS fully composed of bent MAPS into the ALICE detector system [ALI+23].

In context of this thesis, 48 ALPIDE chips are equipped in EPICAL-2. A single ALPIDE chip consists of 512 × 1024 pixels each of size $26.88 \times 29.24\,\mu\mathrm{m}^2$. This leads to a total number of ≈ 25 Million pixels in EPICAL-2 and an active area of $13.762\,56 \times 29.941\,76\,\mathrm{mm}^2$. In the following, the operating principle of the ALPIDE chip is described first. After this, the temperature dependence of the chip response is discussed. Finally, the fundamental building block of the ALPIDE, a p-n junction, and the influence of voltage settings on the ALPIDE is described.

Figure 8 illustrates a schematic cross-section of the ALPIDE chip. When an electrically charged particle, shown as a black arrow in Figure 8, propagates through the epitaxial layer, it creates electron (e)-hole (h) pairs along its trajectory. The charge carriers will diffuse through the epitaxial layer until they reach a drift region shown as white bulbs below the n-well collection diode in the figure. In the drift region, the presence of an electric field leads to charge carriers drifting towards the collection diode. If charge above a certain threshold is collected by the electrode, a signal is generated. The signal is referred to as a pixel hit revealing the presence of a charged particle and its impinging point on the sensor surface. Typically, the deposited charge is shared among neighbouring pixels due to diffusion and geometrical effects. Therefore, the typical pixel hit response to a charged particle includes several adjacent pixels, called a cluster.

The pixel hit response to a charged particle changes with temperature. For instance, in [Sol20], it is found that the average number of pixel hits per charged particle increases from 3.690 ± 0.006 at 20 °C to 3.850 ± 0.004 at 30 °C. Furthermore, the fake-hit rate of ALPIDE increases about a factor of ten when the temperature increases from 12 °C to 36 °C as reported in [Hoo15]. Therefore, a constant

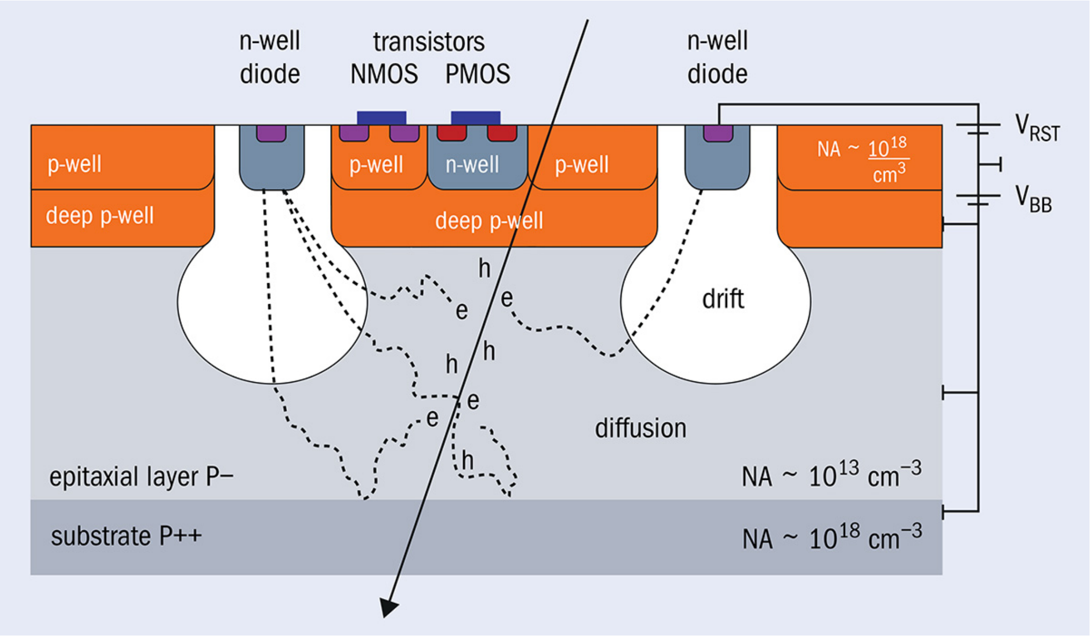

Figure 8: *Schematic cross-section of the ALPIDE chip showing a charged particle crossing which liberates charge carriers in terms of electron-hole pairs. The charge carriers propagate trough the epitaxial layer in terms of diffusion and drift until they reach one of the two n-well pixel diodes [ALI+21b].*

temperature has to be assured to operate the ALPIDE chips and thus EPICAL-2 under stable measurement conditions. This is achieved by the usage of a water cooling system in the EPICAL-2 prototype as discussed before.

The main building block of a single ALPIDE pixel is a reversely biased p-n junction. In terms of the so-called band model [KW16], in p-type silicon more holes than electrons exist while in n-type silicon more electrons than holes exist. At the junction of p- and n-type silicon, a diffusion current leads to electrons filling up the holes in the p-type silicon. Therefore, the p-type material is often referred to as the acceptor while the n-type material is called the donor. As a result, an electric field is build up at the junction creating a drift current working against the diffusion current. In equilibrium, a so-called depletion zone without free charge carriers is created and a constant electric field emerges. The strength of the electric field at the ALPIDE p-n junction is determined by the different doping concentrations of the n-well diode and the p-type epitaxial layer. For an abrupt, planar p-n junction with constant doping concentrations at both sides, the electric field is characterised by the so-called built-in voltage U_{BI} [KW16]:

$$U_{\mathrm{BI}} = \frac{k_{\mathrm{B}}\, T}{e} \cdot \ln\left(\frac{N_{\mathrm{A}} \cdot N_{\mathrm{D}}}{n_i^2}\right) \approx 0.6\ \mathrm{V} \tag{9}$$

The p^--type epitaxial layer (acceptor) has a doping concentration of $N_\text{A} \approx 10^{13}\ \text{cm}^{-3}$, i.e. 10^{13} impurity atoms per cubic centimetres, and the n^+-well (donor) on top of the epitaxial layer has a doping concentration of $N_\text{D} \approx 10^{18}\ \text{cm}^{-3}$ [ALI+21b]. The factor $k_\text{B}T/e$ corresponds to the so-called thermal potential and is $\approx 25\,\text{mV}$ at $T = 20°\text{C} = 293.15\ \text{K}$ [Hoo15]. Furthermore, n_i corresponds to the so-called intrinsic charge carrier concentration of silicon which is $n_\text{i} \approx 1.03 \cdot 10^{10}\ \text{cm}^{-3}$ [KW16]. Using the given values, the ALPIDE built-in voltage yields $U_\text{BI} \approx 0.6\,\text{V}$.

In contrast to the built-in voltage which is intrinsically predefining the depletion zone and the electric field strength via the different doping concentrations, ALPIDE can be operated using the so-called back-bias voltage which enables to change both the depletion region and the electric field strength externally. In particular, an increase of the depletion region and the ALPIDE electric field strength is achieved by increasing the total reverse bias voltage V_RB:

$$V_\text{RB} \approx V_\text{RST} + V_\text{BB} \tag{10}$$

V_RB is formed by the pixel reset voltage V_RST and the reverse substrate bias voltage V_BB as depicted in Figure 8. During the EPICAL-2 test-beam data takings at Utrecht, DESY and CERN-SPS, which will be discussed in detail in the subsequent section 2.3, the reverse substrate bias voltage was set to $V_\text{BB} = 0.0\,\text{V}$ while the pixel reset voltage was set to $V_\text{RST} = 1.4\,\text{V}$.

Together, U_BI and V_RB define the depletion zone. In [KW16] it is demonstrated, that the spatial contribution to the depletion zone is negligible for the material having the higher doping concentration. Since $N_\text{A}(\text{n-well diode}) \gg N_\text{D}(\text{epitaxial layer})$ for the ALPIDE chip, the width w_d of the depletion zone extends completely into the epitaxial layer. For an abrupt, planar p-n junction, w_d can be expressed as following [KW16]:

$$w_\text{d} \ = \ \sqrt{\frac{2\,\epsilon_0\,\epsilon_\text{r}}{e} \cdot \frac{1}{N_\text{D}} \cdot (U_\text{BI} + V_\text{RB})} \tag{11}$$

ϵ_0 (unit A s / V m) describes the vacuum permittivity and ϵ_r the material dependent permittivity number, which is $\epsilon_\text{r} \approx 11.9$ for silicon [KW16]. Using the values given above, this leads to $w_\text{d} \approx 9\,\mu\text{m}$ for $V_\text{RB} = 0.0\,\text{V}$ and $w_\text{d} \approx 17\,\mu\text{m}$ for $V_\text{RB} = 1.4\,\text{V}$.

Although the calculations are performed under the assumption of an abrupt, planar junction, one can conclude that the drift region extends into the ALPIDE epitaxial layer as shown via the bulb in Figure 7. In addition, one can conclude that the total charge carrier motion in the ALPIDE sensors equipped in EPICAL-2 is not dominated by diffusion but rather consists of both diffusion and drift.

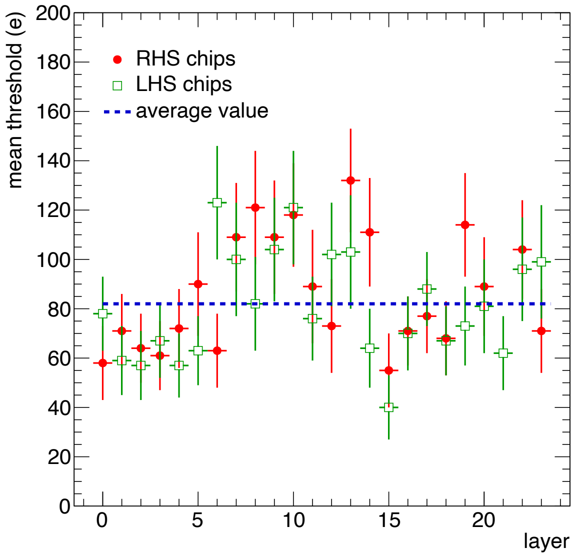

Figure 9: *Pixel threshold of the* ALPIDE *chips instrumented in* EPICAL-2*. The mean value is derived from the threshold distribution of each* ALPIDE *chip (see text). The error bars correspond to the standard deviation of each threshold distribution.*

2.1.2 Sensor Thresholds

As described in the previous section, a pixel hit occurs if the charge collected at the pixel diode is above a certain chip threshold. Therefore, the charge threshold of the ALPIDE chips governs their overall performance. For example, a particle crosses two identical chips, except for one having a high and the other a low chip threshold, and generates the same number of electron-hole pairs in the epitaxial layers. Then, the low-threshold chip would have e.g. five pixel hits, while the high-threshold chip would have e.g. only two hits. From this it follows that the higher the chip threshold, the less pixel hits are created for a charge particle crossing a chip.

Typically, the chip threshold is determined via a so-called pixel threshold scan [Sul18]: In each pixel, a test charge is injected N_{inj} times and the number N_{hit} of times the charge injection yields a pixel hit is counted. This procedure is performed within a specific test charge range yielding a typical so-called $s-curve$ [Sul18], i.e. N_{hit}/N_{inj} as a function of injected test charge. For each pixel, the pixel threshold is defined as the test charge for which the test charge injection leads to a pixel hit in 50 % of the times, i.e. when $N_{hit}/N_{inj} = 50$ %. This procedure leads to a distribution of pixel thresholds, i.e. all pixel thresholds in a chip contribute to this distribution. The mean value of this threshold distribution is referred to as chip threshold although it is actually a distributions mean.

Figure 9 displays the mean thresholds of the 48 ALPIDE chips equipped in EPICAL-2. Chips positioned on the right hand side (RHS) of the EPICAL-2 stack are shown in red and those in the left hand side (LHS) in green. The error bars in Figure 9

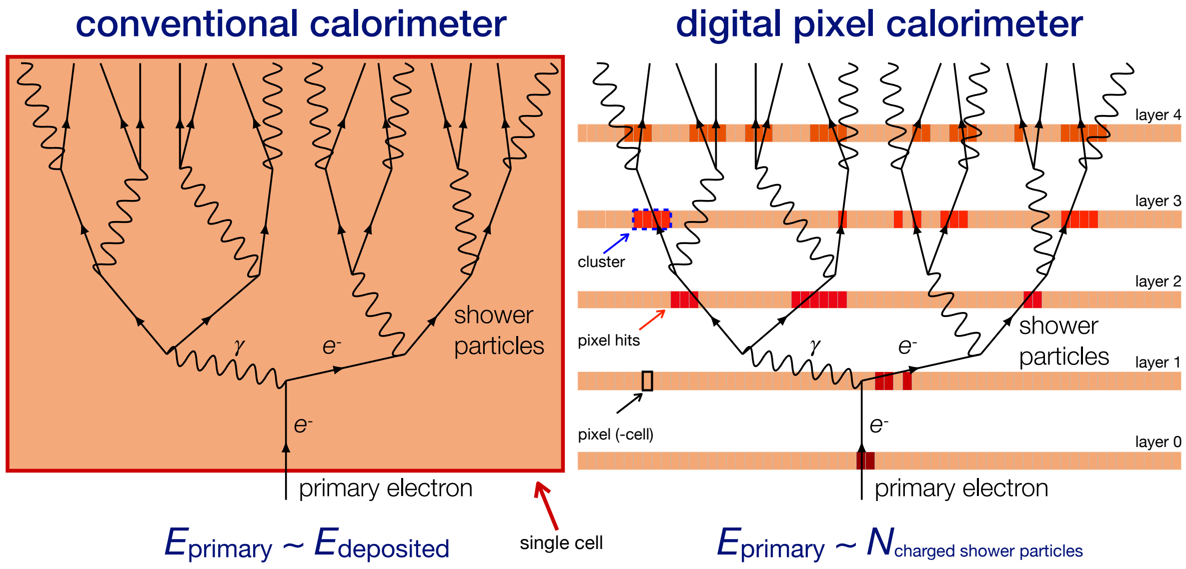

Figure 10: *Illustration of the electromagnetic shower evolution in a conventional calorimeter (left) and in a digital pixel calorimeter (right).*

correspond to the standard deviation of the chip threshold distributions. The EPICAL-2 chip thresholds are taken from [ALI20]. As visible in Figure 9, the mean chip thresholds fluctuate between ∼ 40 e in the LHS chip in layer 15 and ∼ 130 e in the RHS chip in layer 13. The average mean threshold value is ∼ 82 e as displayed via the blue dashed line in Figure 9. The average standard deviation of all chips is ∼ 20 e.

2.2 Measurement Principle

The basic principle of EPICAL-2 and in general of a digital pixel electromagnetic calorimeter is that energy is measured by counting the number of charged particles in an electromagnetic shower. Just as the hit response of a charged particle crossing the ALPIDE chip as discussed in the previous section 2.1.1, a charged shower particle induces a group of adjacent pixel hits, a cluster. Therefore, counting the number of pixel hits or clusters serves as an effective count of the charged shower particles. An energy measurement via the total number of hits or clusters assumes, that the energy is proportional to the charged particle shower multiplicity which in turn is proportional to the number of pixel hits or clusters. To ensure this proportionality, the pixel size has to be small enough to guarantee that charged shower particles do not merge into the same hit or cluster, even in the core of electromagnetic showers with high particle densities. This is possible due to the high granularity of the ALPIDE sensor, given the pixel size of $26.88 \times 29.24\,\mu\text{m}^2$.

To highlight the fundamental difference between a conventional calorimeter like the ALICE-PHOS or the ALICE-EMCAL, both discussed in section 1.3, Figure 10

Particles	Energies (GeV)	Location	Date
cosmic muons	-	Utrecht lab	2020
$e^{\pm}$	1, 2, 3, 4, 5, 5.8	DESY TB22	Feb. 2020
e^{+}, h^{+}, μ^{+}	20, 40, 60, 80	CERN-SPS H6	Sept./Oct. 2021

Table 2: *Overview of the measurement campaigns with* EPICAL-2 .

illustrates the measurement principle of a conventional calorimeter (left) and of EPICAL-2, a digital pixel calorimeter (right). In Figure 10, a primary electron enters both calorimeters from the bottom. This primary electron starts the development of an electromagnetic shower, where electrons and positrons radiate photons and photons produce electron-positron pairs.

In the conventional calorimeter case (left), the shower develops within one or a few cells basically in a (coarse segmented) block of material, where the energy E_{primary} of the primary particle is proportional to the deposited energy $E_{\text{deposited}}$, which in detail depends on the type of the calorimeter. The full shower and thus energy deposition is contained within one or a few cells.

In the digital calorimeter case (right), each charged shower particle produced in the electromagnetic shower generates a few number of pixel hits. The energy measurement of a primary particle with E_{primary} is based on the detection of individual shower particles with the pixel cells of the ALPIDE sensor. Therefore, E_{primary} is proportional to the total number N_{hits} of pixel hits or the total number N_{clus} of clusters, both considered as energy measurement observable here.

2.3 Experimental Measurements

The data analysed in this thesis were gathered in three measurement campaigns with the EPICAL-2 prototype. A measurement of cosmic muons was performed at the University of Utrecht in the Netherlands. At the DESY facility in Hamburg, measurements of electromagnetic showers have been carried out using a beam of electrons. Furthermore, at CERN-SPS, electrons, hadrons and muons were measured using a mixed beam containing the three types of particles. Table 2 gives an overview of the different test measurements performed with EPICAL-2.

In this thesis, electron events are used to determine the energy measurement performance of EPICAL-2 and to investigate the electromagnetic shower shape, both discussed in section 5. Muons and non-showering hadrons are used in this work for various corrections of the acquired test data, which are discussed in section 4. The test measurements at Utrecht, DESY and CERN-SPS are discussed in the following sections 2.3.1 to 2.3.3 focusing on the details of each setup and the measurement conditions.

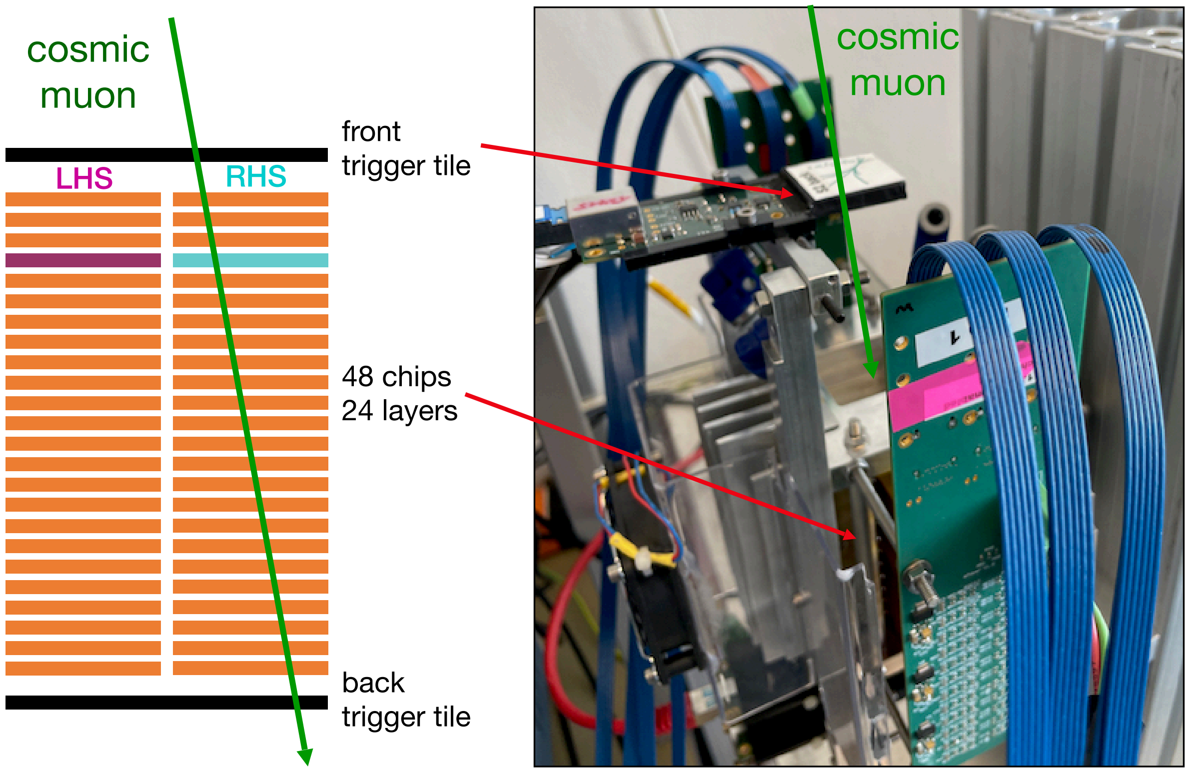

Figure 11: ***Left:*** *Sketch of the upward facing* EPICAL-2 *setup for cosmic muon measurements. A cosmic muon track is illustrated as dark green line traversing only the RHS chips but both trigger tiles.* ***Right:*** *Picture of* EPICAL-2 *at the University of Utrecht in the Netherlands. The linking between sketch and picture is shown. However, the chips are not directly visible in the picture since they are embedded in the metal housing of* EPICAL-2.

2.3.1 Cosmic-Muon Setup

At Utrecht University in the Netherlands, cosmic muon events were recorded for a period of approximately 6 months in 2020 gathering a total of approximately 8000 events including both muon events and noise.

Figure 11 (left) illustrates the setup for the measurement of cosmic muons and Figure 11 (right) shows a photo of the EPICAL-2 detector positioned facing upwards in the laboratory. Two trigger tiles with the same active area as EPICAL-2, one on top of EPICAL-2 and one below, are utilised for triggering on coincidence events between signals from both tiles. This ensures that recorded cosmic muon tracks cross both trigger tiles and thus have traversed all 24 layers. As a consequence of this restriction of triggering on coincidence events, only cosmic muons tracks with specific angles w.r.t. to the setup are recorded. For example, a maximum entrance angle θ_{acc} is defined by a cosmic muon, which enters EPICAL-2 in one corner and leaves EPICAL-2 in the diagonally opposite corner. With the diagonal $d \approx 4.2$ mm of the active area and the distance between the two trigger tiles of approximately 90 cm, this leads to

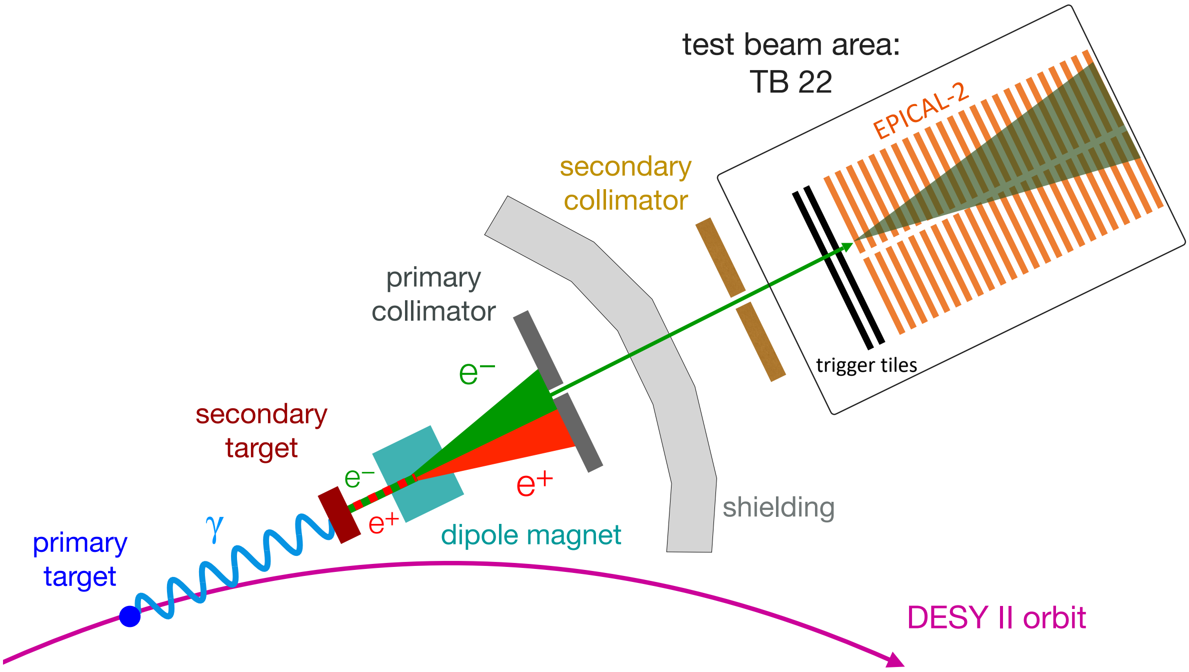

Figure 12: *Schematic overview of the test-beam generation at* DESY *and the installation of* EPICAL-2 *in the beam of TB22. Based on [Die+19].*

$\theta_{\mathrm{acc}} \approx 2.7°$. To understand what the trigger means in terms of the number of cosmic-muon events one can expect to record e.g. per day, one can estimate this number by using the integrated number N_{cosmics} of cosmic muons above 1 GeV energy and above sea level given by [GZ+20]:

$$N_{\mathrm{cosmics}} \approx 70\ \frac{1}{m^2\,s\,sr}$$

Given the solid angle coverage of EPICAL-2 of $\Omega \approx 0.004$ sr and its active area of $A \approx 9$ cm^2, the number of cosmic muons traversing both trigger tiles is $\approx 2.5 \cdot 10^{-4}$ cosmic muons per second, i.e. approximately 22 cosmic muon events per day.

2.3.2 DESY Test Beam Setup

The analysis and results of electron events with energies up to 5.8 GeV presented in this thesis are based on the data acquired during a test-beam measurement campaign with EPICAL-2 at the electron-positron synchrotron DESY II Test Beam Facility [Die+19] in Hamburg (Germany) in February 2020.

At DESY, three areas corresponding to the three test beam lines TB21, TB22 and TB24 provide usage of an electron or positron test beam. EPICAL-2 was installed in TB22. Figure 12 illustrates the test-beam generation at DESY II. The test-beam generation involves the following steps [Die+19]: Inside of the DESY II beam orbit, the primary electron or positron beam of DESY II hits the primary target station, which

E (GeV/c)	E_{eff} (GeV/c)	ΔE (GeV/c)	N_{events}
1.0	1.119	0.158 ± 0.006	$2.4 \cdot 10^6$
2.0	2.045	0.158 ± 0.006	$2.0 \cdot 10^6$
3.0	3.026	0.158 ± 0.006	$1.8 \cdot 10^6$
4.0	4.016	0.158 ± 0.006	$2.2 \cdot 10^6$
5.0	4.989	0.158 ± 0.006	$3.5 \cdot 10^6$
5.6	5.560	0.158 ± 0.006	–
5.8	–	0.158 ± 0.006	$1.5 \cdot 10^6$

Table 3: *Nominal beam energy E defined by the magnet settings during the* EPICAL-2 *test-beam measurement in the test-beam area TB22, the effective beam energy E_{eff} as measured in TB21 for a given nominal energy and the constant beam energy spread [Die+19]. The number of events recorded at each energy is given as the sum of both electron and positron events.*

consists of up to six 7 µm thick and 30 mm long carbon fibres. At the primary target, photons are generated via Bremsstrahlung in the energy range from 0.45 GeV up to the maximum energy of 6.3 GeV. These photons from Bremsstrahlung propagate tangentially to the DESY II orbit in an extraction tunnel before they leave the DESY II vacuum by passing a 500 µm thick aluminum foil. The photons travel 22 m through air before they hit the secondary target, where electron-positron pairs are generated via pair production. The pair-production rate is defined by one of the eight secondary targets provided by DESY II. Behind the secondary target, a dipole magnet is installed in 60 cm distance to select either electrons or positrons and also the desired momentum by choosing the strength and polarity of the magnetic field. The electrons travel through an evacuated beam pipe, before they reach controllable collimators, a primary collimator and a secondary collimator to narrow the test beam. Finally, the electrons or positrons enter EPICAL-2 in the test-beam area.

The electron events which are used for the analysis presented in this thesis were recorded at DESY under the following data taking conditions: Water cooling was set to 20°C to keep the temperature of EPICAL-2 at a constant level, which is important as the response of the ALPIDE chips to charged particles changes as a function of temperature as discussed in section 2.1.1. The active surface of EPICAL-2 is positioned perpendicular to the direction of the test beam, i.e. with 0°. The DESY collimators are set to $14 \times 14\,\mathrm{mm}^2$ for the primary collimator and $12 \times 12\,\mathrm{mm}^2$ for the secondary collimator.

Under these default conditions, a beam energy scan at DESY TB22 with electron energies ranging from 1 GeV up to 5.8 GeV was performed from the 17th to 24th February 2020. In Table 3, the number of events recorded at each energy E as defined by the magnet settings in TB22 are summarised. In [Die+19], an effective beam energy E_{eff} is reported which is derived from a measurement in TB21 at a set energy E. In addition to the deviation between set and effective electron energy, the energy of

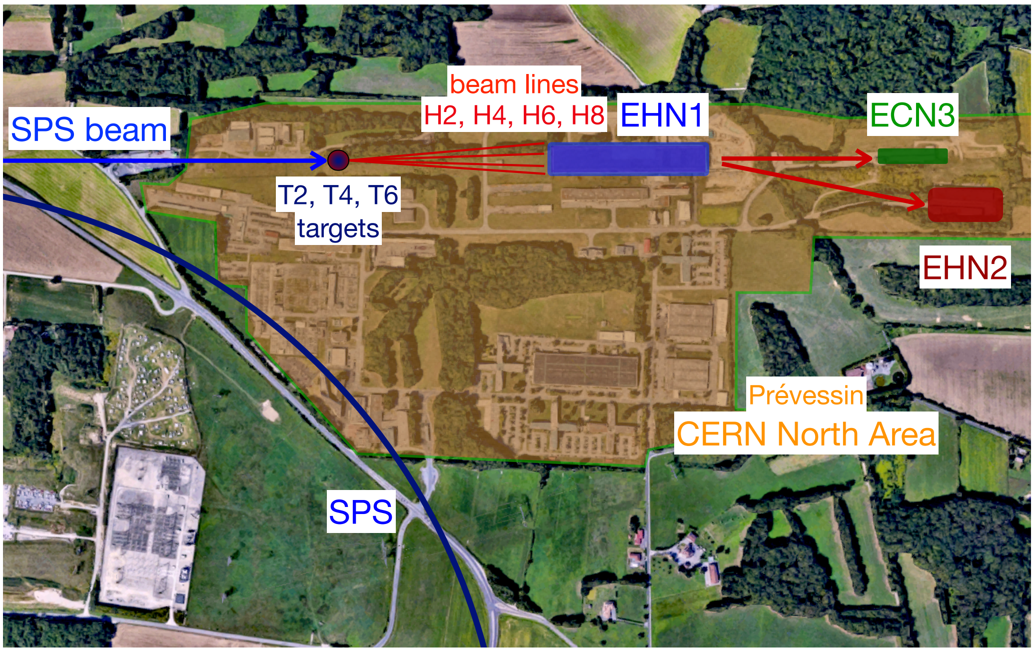

Figure 13: *Geographical map of the North Area at CERN including the experimental areas EHN1, EHN2 and ECN3, as well as the SPS and the beam lines H2 to H8 which are delivered by the SPS beam after hitting the targets T2 to T6 [Goo21].*

electrons in the DESY beam are spread around the nominal energy. The beam energy spread is given by DESY as a constant spread of 158 MeV independent of the beam energy [Die+19]. Both the effective energies and the energy spread of the beam are summarised in Table 3. Electron events are recorded when both trigger tiles in front of EPICAL-2, as shown in Figure 12, deliver a signal in coincidence. Approximately two million events per energy were recorded during the test-beam campaign with EPICAL-2 at DESY. The total number of recorded events are summarised in Table 3 for each energy.

2.3.3 SPS Test Beam Setup

The analyses and results at beam energies between 20 GeV to 80 GeV presented in this thesis are based on the test-beam measurements with EPICAL-2 at the Super Proton Synchrotron SPS at CERN in September and October 2021.

Figure 13 shows the North Area at the CERN Prevéssin side, which is connected to the CERN-SPS that provides the area with a beam of protons with energies up to a maximum of 400 GeV. The North Area includes the two experimental halls, EHN1 and EHN2, and one experimental cavern ECN3. To provide particle beams to as many experiments as possible at once, several primary targets (T2, T4 and T6) and different coupled beam lines (H2 to H8) are available and can be used simultaneously with only

E (GeV)	ΔE (GeV)	N_{events}
20.0	0.3	$2.35 \cdot 10^4$
40.0	0.6	$2.37 \cdot 10^5$
60.0	0.9	$1.54 \cdot 10^5$
80.0	1.2	$5.56 \cdot 10^5$

Table 4: *Number of recorded events at the different beam energies E with* EPICAL-2 *at the* SPS *and the corresponding beam energy uncertainty ΔE [GF22].*

one primary beam from the SPS. Details on the different beam line infrastructures can be found in [Nuc21].

EPICAL-2 was positioned along the SPS beam line H6 in the experimental hall EHN1 in the North Area of CERN. The test beam used for the measurements with EPICAL-2 is generated in a three step process, which is described in the following: First, a primary 120 GeV proton beam encounters the primary beryllium target T4 as illustrated in Figure 13. The primary target is embedded in a so-called wobbling station which on the one hand allows for the production of several secondary particle beams and on the other hand for a selection in terms of angle, particle type and momentum as requested from (test-beam) experiments [Eft03]. In the proton-beryllium reaction, a secondary beam is generated which consists of electrons, hadrons and muons. This secondary beam traverses a secondary target, which is either some millimetres of lead or some centimetres of copper thick. In the copper case ($\approx 30\ X_0$), a pure hadron tertiary beam is generated. In contrast, in the lead case ($\approx 1\ X_0$), electrons will loose a portion of their energy while hadrons mostly won't. Therefore, electrons can be selected by momentum using a bending magnet. Ideally, only the lower-energy electrons are selected and the hadrons continue straight. The selection of electrons works the better the lower the desired electron energy. Finally, the tertiary beam reaches the EPICAL-2 prototype which is however not a pure particle beam but rather consists of hadrons, muons and electrons.

The EPICAL-2 data taking conditions at SPS are similar to those at DESY discussed in the previous section 2.3.2: Water cooling was set to 20°C and the angle of beam incidence was aligned with 0° to EPICAL-2. A beam energy scan was performed with EPICAL-2 at the SPS from September 22nd to October 6th in 2021. In total, about one million events were recorded during the test-beam campaign at SPS. About 0.5 million events at 80 GeV, 0.2 million events at both 40 GeV and 60 GeV and 20 thousand events at 20 GeV were recorded. Table 4 summarises the measured number of events at each energy. In addition, the beam energy uncertainty of the SPS beam is given in Table 4 for each energy, which corresponds to the relative energy uncertainty of $\Delta E / E = 1.5\%$ [GF22].

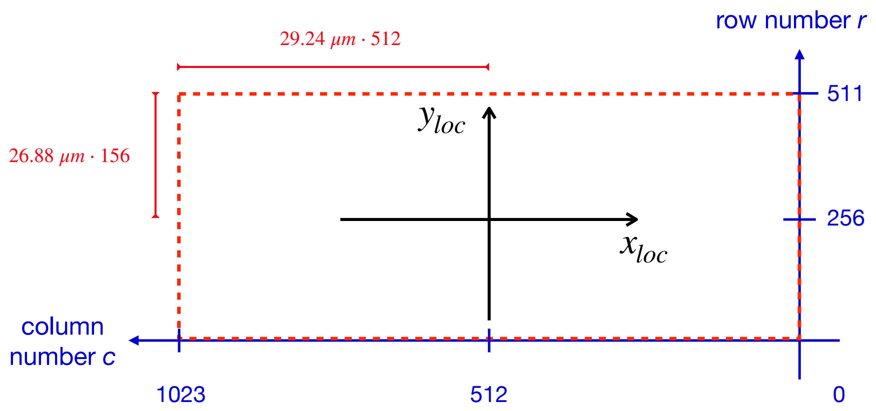

Figure 14: *Visualisation of the relation between local pixel hit coordinates x_{loc} and y_{loc} and the column number c and the row number r. The ALPIDE chip borders are illustrated by the red dotted rectangle and the center of the chip defines the center of the local coordinate system.*

2.4 Coordinate System

During the test measurements, which were discussed in the previous section, the acquired raw data is stored on an event basis, i.e. data is read-out when both trigger tiles deliver a signal in coincidence. Per event and for each pixel hit, the position of the pixel hit is stored. The pixel hit position is uniquely defined via its column number, its row number and its lane number. The column number and the row number correspond to the pixel hit position in the ALPIDE chip pixel matrix of 512 rows times 1024 columns. The lane number refers to a unique chip identifier number defining the position in the EPICAL-2 stack, i.e. the layer number and the left hand side (LHS) chip or the right hand side (RHS) chip in the EPICAL-2 stack. For the analysis of the EPICAL-2 data and the presentation of the results, two coordinate systems are used in this work, which are described below.

An in-chip coordinate system, referred to as local coordinates $\vec{v}_{\mathrm{local}}$, is introduced by converting the column number c and the row number r into the local coordinates x_{loc} and y_{loc} [Yok21]:

$$\vec{v}_{\mathrm{local}} = \begin{pmatrix} x_{\mathrm{loc}}(c) \\ y_{\mathrm{loc}}(r) \end{pmatrix} = \begin{pmatrix} 29.24\ \mu\mathrm{m} \cdot [512 - (c + 0.5)] \\ 26.88\ \mu\mathrm{m} \cdot [(r + 0.5) - 256] \end{pmatrix} \tag{12}$$

In the coordinate system conversion, 0.5 is added to c and r, so that the pixel centre is referenced when specifying local pixel coordinates. Figure 14 shows the relation between the column number c and x_{loc} as well as between the row number r and y_{loc}. The origin of the local coordinate system is defined in the middle of each chip.

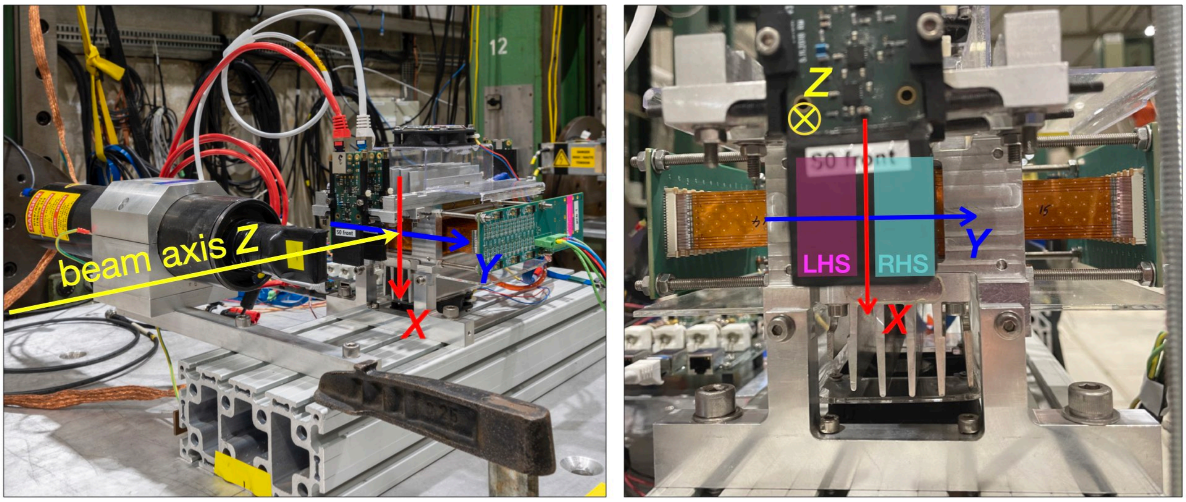

Figure 15: *Overlay of the* EPICAL-2 *setup during the* SPS *test-beam measurement and the global coordinate system as front view (right) and partial side view (left). x means vertically, y translates to the horizontal direction and z corresponds to the depth in* EPICAL-2 .

Column number and row number as well as x_{loc} and y_{loc} are related to individual chips and are convenient when referring to in-chip observations and calculations. However, observables w.r.t. the full EPICAL-2 setup are better described using a global coordinate system. Global coordinates allow for specifying the exact 3D position of a pixel hit or any observations w.r.t. the full EPICAL-2 setup. Figure 15 gives an overview of the global coordinate system used throughout this thesis. The global coordinate system is visualised on top of a picture of the EPICAL-2 setup at the SPS test-beam measurement, which was discussed in the previous section. The z axis refers to the depth in EPICAL-2. The horizontal y and vertical x coordinate axis have their origin in the EPICAL-2 centre, i.e. between the two chips in a layer.

Global pixel coordinates $\vec{v}_{\text{global}}$ are derived from local coordinates with the following transformation matrix $M_{\text{RHS/LHS}}$ [Yok21]:

$$\vec{v}_{\text{global}} = M_{\text{RHS/LHS}} \times \vec{v}_{\text{local}} = \begin{pmatrix} \cos\Delta\theta & -\sin\Delta\theta & \Delta X \\ \sin\Delta\theta & \cos\Delta\theta & \Delta Y \\ 0 & 0 & 1 \end{pmatrix} \times \vec{v}_{\text{local}} \tag{13}$$

ΔX , ΔY and $\Delta\theta$ are referred to as alignment parameters. For the global coordinates, it is assumed that the longitudinal stack position (z) and layer orientation (rotation around x and y) are well constrained by the mechanical construction given the tungsten absorber plates and spacers. This leads to the three alignment parameters in $M_{\text{RHS/LHS}}$. $M_{\text{RHS/LHS}}$ consists of a rotation around the z axis and a position displacement in x and y, both defined by the alignment parameters. Figure 16 (left) illustrates the coordinate transformation with $M_{\text{RHS/LHS}}$ and the interpretation of the

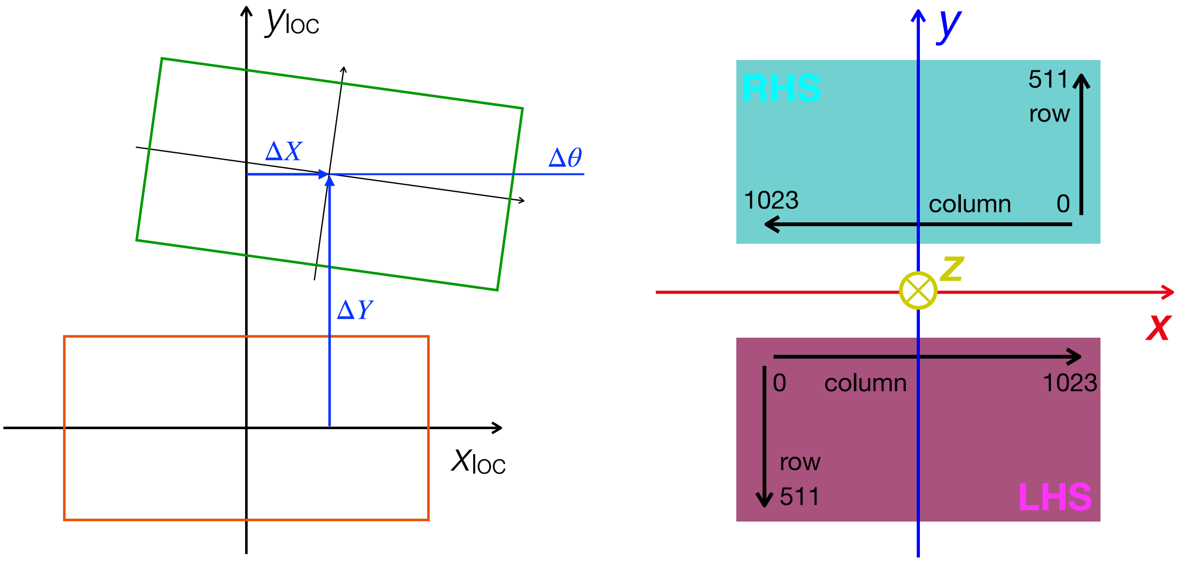

Figure 16: Left: *Visualisation of the coordinate transformation from local to global coordinates via the alignment parameters ΔX , ΔY and $\Delta\theta$.* ***Right:*** *Global coordinate system with the position of RHS and LHS chips. For the sake of clarity, the original coordinates column and row of the transformation are depicted again. Based on [Yok21].*

alignment parameters ΔX , ΔY and $\Delta\theta$. For ideal-aligned chip positions in the EPICAL-2 stack, the alignment parameters read as following [Yok21]:

$$(\Delta X , \Delta Y , \Delta\theta) = \begin{cases} (0, \quad 26.88\ \mu\mathrm{m} \cdot 256 \quad , \ 0\ ) & ;\ \text{for RHS chips} \\ (0, \ -26.88\ \mu\mathrm{m} \cdot 256 - \delta Y_{\mathrm{gap}} \ , \ \pi) & ;\ \text{for LHS chips} \end{cases} \tag{14}$$

δY_{gap} refers to the gap between the two chips in a layer of approximately $\delta Y_{\mathrm{gap}} \approx 100\ \mu\mathrm{m}$ as discussed in section 2.1. The coordinate transformation matrix $M^{\mathrm{ideal}}_{\mathrm{RHS/LHS}}$ for ideal-aligned chips are defined for the RHS and LHS chips as following:

$$M^{\mathrm{ideal}}_{\mathrm{RHS}} = \begin{pmatrix} 1 & 0 & 0 \\ 0 & 1 & 6.88128\mathrm{mm} \\ 0 & 0 & 1 \end{pmatrix} \qquad M^{\mathrm{ideal}}_{\mathrm{LHS}} = \begin{pmatrix} -1 & 0 & 0 \\ 0 & -1 & -6.98128\mathrm{mm} \\ 0 & 0 & 1 \end{pmatrix} \tag{15}$$

The coordinate transformation from local to global coordinates with $M^{\mathrm{ideal}}_{\mathrm{RHS/LHS}}$ shifts the RHS chips upwards while the LHS chips are both shifted down and rotated by 180 degrees. Finally, Figure 16 (right) shows the global coordinate system together with the original column and row information for both the RHS chips and the LHS chips.

3 EPICAL-2 Simulation

In the previous chapter, the EPICAL-2 prototype and the test-beam measurement setups with EPICAL-2 at DESY, SPS and the University of Utrecht have been discussed. To compare the test-beam measurements with a Monte Carlo simulation as well as to understand and assess the detector response in the test beam in detail, a realistic implementation of the prototype in a simulation framework is necessary. In addition, in a simulation framework it becomes possible to study the behaviour of the prototype under different conditions by changing various simulation parameters.

In this work, the EPICAL-2 prototype is implemented in ALLPIX^2 [Spa+18], a simulation framework specialised for silicon pixel detectors, to perform Monte Carlo simulations of the EPICAL-2 prototype. In this chapter, first, the ALLPIX^2 framework is introduced briefly. After this, the implementation of the EPICAL-2 prototype in ALLPIX^2 is discussed. The EPICAL-2 simulation setup is described focussing on the simulation parameters of the framework used to model the prototype. After describing the setup, a study of the EPICAL-2 simulation behaviour under variation of its simulation parameters is presented.

3.1 ALLPIX^2 Pixel Detector Simulation Framework

The ALLPIX^2 framework is based on GEANT4 [Ago+03] and on ROOT [BR97] and is designed as a generic simulation framework on the basis of the so-called building-block principle. Each building block is referred to as a module in ALLPIX^2 and each module performs a specific task. While some modules can be used for the detector description, others fulfil a special task in a physical detection process. Via a combination of several ALLPIX^2 modules a simulation chain can be constructed.

A typical simulation chain involves the following steps as depicted in Figure 17: First, the geometry setup of the detector is defined and constructed via GEANT4. Second, the pixel electric field is initialised for each sensor and then added to the detector description. Third, generated particles are transported through the setup, where the particles deposit energy in sensors in form of free charge carriers. Fourth, the deposited charge carriers are propagated inside the sensors according to the electric field. Fifth, the charges are transferred to the nearest pixel diode. Sixth, the readout-electronic digitisation process of the transferred charges at the pixel diode is emulated. Finally, monitoring histograms are created and the simulation output is generated and stored.

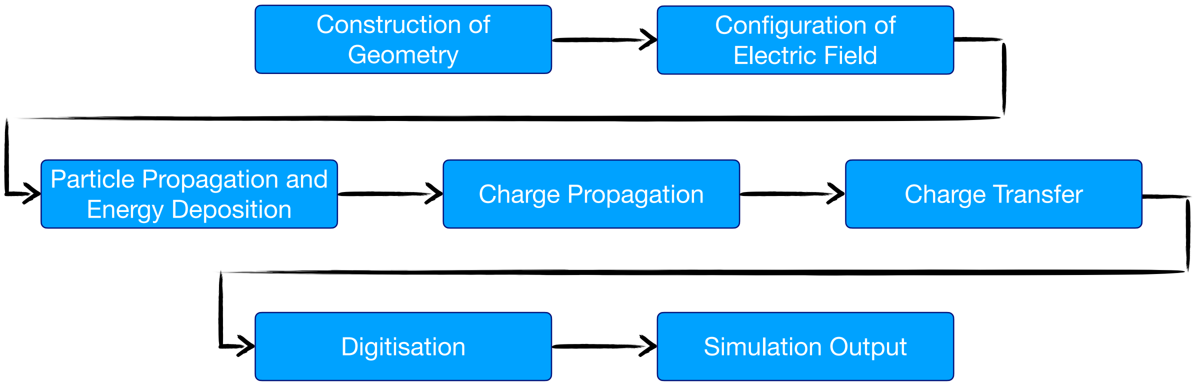

Figure 17: *A typical simulation workflow chain of a single detector in* ALLPIX^2*. Each box corresponds to a single module which performs the task written in the box. Based on [Spa+18].*

3.2 EPICAL-2 Simulation Setup

The implementation of the EPICAL-2 prototype in the ALLPIX^2 framework is based on the ALLPIX^2 simulation chain shown in Figure 17. Each of the depicted modules is described in the following with a focus on the parameters of each module that are used to implement EPICAL-2 in the ALLPIX^2 framework[1].

3.2.1 Construction of Geometry

As discussed in section 2.1, the EPICAL-2 setup is made up of a stack of 24 identical 3.5 mm thick layers. Each layer consists of a tungsten absorber plate, two tungsten spacers, two ALPIDE sensors and layer cables.

In this thesis, the detailed EPICAL-2 geometry is implemented in ALLPIX^2 with the so-called *GeometryBuilderGeant4* module. In this module, all detector components are specified by their type, material, size and position in the so-called ALLPIX^2 world frame. Since the EPICAL-2 test-beam measurements are performed in air, the simulation world material is defined as air for similar conditions.

Figure 18 visualises a single instrumented EPICAL-2 layer as implemented in the ALLPIX^2 framework. One ALPIDE sensor referred to as sensor A in Figure 18 is positioned centred to the ALLPIX^2 world frame. The two sensors per layer are placed on top of the tungsten absorber and in between the two tungsten spacers A and B. The sensors are implemented using the ALPIDE characteristics described in section 2.1.1: A grid of 512 x 1024 pixels with each pixel being of size $29.24 \times 26.88\,\mu\text{m}^2$. In addition, the two sensors are separated by a 100 µm wide gap. In the simulation, the gap is filled with silicon to account for the guard ring of ALPIDE. To account for the peripheral circuitry of ALPIDE, in the simulation, silicon material is positioned on the

---

[1] ALLPIX^2 v1.6.0 with GEANT4 v4.10.07 and ROOT v6.23/01

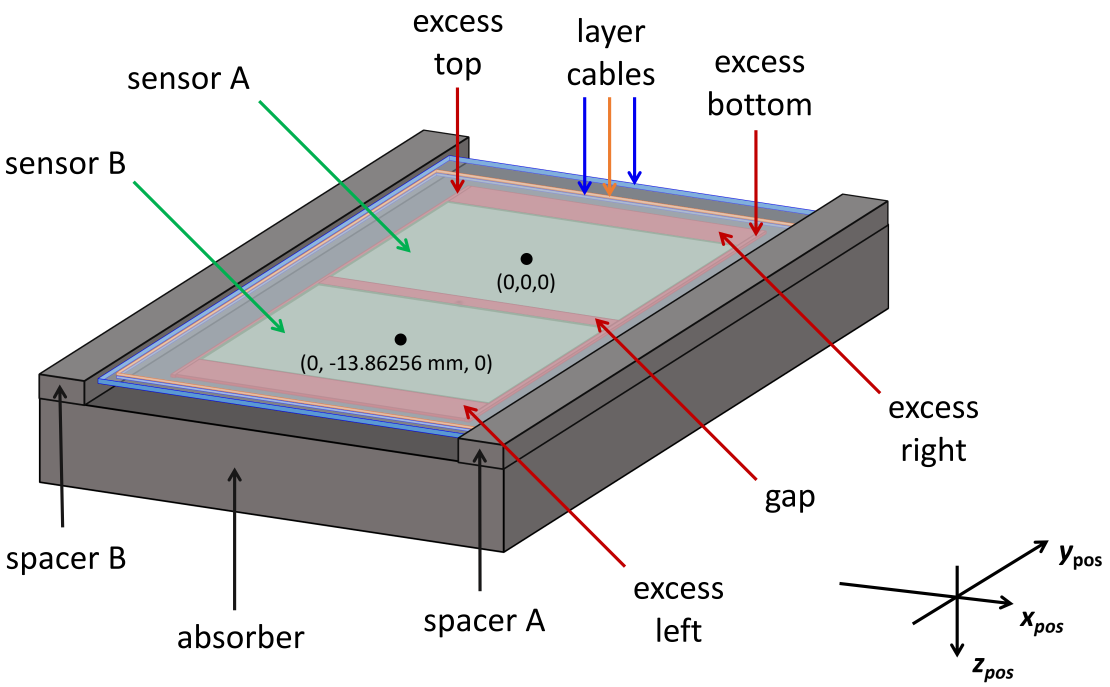

Figure 18: *Illustration of the composition of one EPICAL-2 layer as implemented in the* ALLPIX^2 *framework.*

opposite side of the gap next to the sensors referred to as excess left and excess right in Figure 18. In addition, silicon material is placed beside the sensors to account also there for the guard ring in simulation which is named excess top and excess bottom in Figure 18. The two sensors A and B both include 5 µm of silicon material, each representing the in-pixel circuitry. On top of the two sensors A and B, the layer cables are positioned. In addition, Figure 18 displays the orientation of the coordinate system.

Table 5 lists the implementation of the first EPICAL-2 layer, i.e. layer 0, in ALLPIX^2 : The material, the position (x_{pos}, y_{pos}, z_{pos}) and the size (x_{size}, y_{size}, z_{size}) of every component are shown. For layers other than layer 0 the z_{pos}-position of each component as given in the table needs to be increased by a factor (3.5 mm x layer number), as a single layer is 3.5 mm thick. The component names given in Table 5 correspond to the labels of the components shown in Figure 18. For the calculation of the component positions, sensor A has been placed centred to the world frame and the relative positions of all other components relative to sensor A are computed. It is particularly important to notice, that the specified position of each component is the centre of gravity of the corresponding component dimensions specified via the component size. For instance, the tungsten spacer B is positioned at $x_{\text{pos}} = -18\,\text{mm}$ with a size of $x_{\text{size}} = 4\,\text{mm}$. Therefore, the tungsten spacer expands in the $x-$direction from $-16\,\text{mm}$ to $-20\,\text{mm}$ with the centre of the tungsten spacer at $x_{\text{pos}} = -18\,\text{mm}$. Moreover, the layer design is compact and there is no spare volume between the layer

component	**material**	x_{pos} **(mm)**	y_{pos} **(mm)**	z_{pos} **(mm)**
	type	x_{size}	y_{size}	z_{size}
sensor A	silicon	0	0	0
	active	1024 x 29.24 μm	512 x 26.88 μm	50 μm + 5 μm
sensor B	silicon	0	-13.86256	0
	active	1024 x 29.24 μm	512 x 26.88 μm	50 μm + 5 μm
gap	silicon	0	-6.93128	0
	passive	1024 x 29.24 μm	100 μm	55 μm
excess left	silicon	0	-21.34784	0
	passive	1024 x 29.24 μm	1208 μm	55 μm
excess right	silicon	0	7.48528	0
	passive	1024 x 29.24 μm	1208 μm	55 μm
excess top	silicon	14.98588	-6.93128	0
	passive	30 μm	30.04112 mm	55 μm
excess bottom	silicon	-14.98588	-6.93128	0
	passive	30 μm	30.04112 mm	55 μm
layer cables	kapton	0	-6.93128	-0.0425
	passive	31 mm	32 mm	30 μm
	aluminum	0	-6.93128	-0.0725
	passive	31 mm	32 mm	30 μm
	kapton	0	-6.93128	-0.2175
	passive	31 mm	40 mm	145 μm
absorber	tungsten	0	-6.93128	1.53
	passive	40 mm	35 mm	3 mm
spacer A	tungsten	18	-6.93128	-0.22
	passive	4 mm	35 mm	0.5 mm
spacer B	tungsten	-18	-6.93128	-0.22
	passive	4 mm	35 mm	0.5 mm

Table 5: *Implementation of layer 0 in* ALLPIX^2*. The position, the size and the material of each component is given.*

components which would allow for a coarse implementation of the components in terms of position and size. If any volume is not implemented accurately with respect to the EPICAL-2 implementation, it is likely to create overlapping volumes. At a space coordinate with more than one volume specified, the simulation randomly determines which volume a particle traverses and this leads to unexpected simulation behaviour.

3.2.2 Configuration of Electric Field

The electric field is implemented for each pixel in every sensor and added to the EPICAL-2 detector description using the *ElectricFieldReader* module. The strength of the electric field strongly influences the motion of deposited charge carriers. Since the EPICAL-2 response is based on the measurement of deposited charge carriers, the

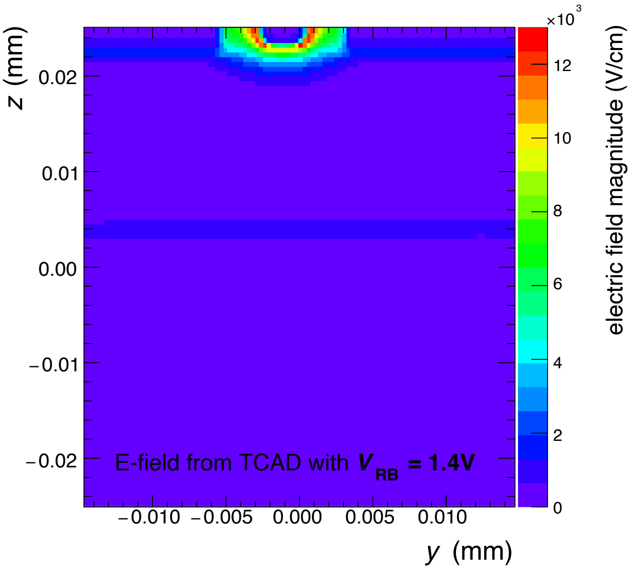

Figure 19: *Electric field magnitude of the pixel electric field as a function of the pixel* x*- and* y*-position at* $x = 0$ *(local pixel coordinate system) for* $V_{RB} = 1.4$ *V as implemented in* ALLPIX^2 *to model the electric field of the* ALPIDE *chips equipped in* EPICAL-2 *.*

electric field is of particular importance for the simulation to model the performance of the EPICAL-2 prototype.

As discussed in context of Figure 8 in section 2.1.1, the electric field strength is defined by the total reverse bias voltage V_{RB} which was set to $V_{\mathrm{RB}} = 1.4\,\mathrm{V}$ during the EPICAL-2 data taking periods. For this thesis, the ALPIDE electric field with $V_{\mathrm{RB}} = 1.4\,\mathrm{V}$ is taken from [Has21b], where the field is calculated using Technology Computer-Aided Design (TCAD) simulations [Has21a]. In this TCAD simulation, each pixel component of ALPIDE with its corresponding doping concentration is placed in a fixed pixel region, which is defined as:

$$-13.5\,\mu\mathrm{m} < x_{\mathrm{TCAD}} < 13.5\,\mu\mathrm{m} \tag{16}$$

$$-25.0\,\mu\mathrm{m} < y_{\mathrm{TCAD}} < 25.0\,\mu\mathrm{m} \tag{17}$$

$$-13.5\,\mu\mathrm{m} < z_{\mathrm{TCAD}} < 13.5\,\mu\mathrm{m} \tag{18}$$

The space coordinates $(x_{\mathrm{TCAD}}, y_{\mathrm{TCAD}}, z_{\mathrm{TCAD}})$ and the pixel size differ from the EPICAL-2 implementation of the ALPIDE sensor in the ALLPIX^2 framework. In the TCAD simulation, the pixel diode is positioned at the centre of the pixel region at $x_{\mathrm{TCAD}} = 0$, $z_{\mathrm{TCAD}} = 0$ and $y_{\mathrm{TCAD}} = -25\,\mu\mathrm{m}$. Half of the pixel region $(-25\,\mu\mathrm{m} < y_{\mathrm{TCAD}} < 0\,\mu\mathrm{m})$ emulates the epitaxial layer of ALPIDE and the other half $(0\,\mu\mathrm{m} < y_{\mathrm{TCAD}} < 25\,\mu\mathrm{m})$ represents the substrate of ALPIDE. The output of the TCAD simulation from [Has21b] used in this thesis contains a direct mapping of each space point in a pre-defined grid and the corresponding electric field at this space point.

The ALLPIX^2 *MeshConverter* module is used to convert the ALPIDE electric field from TCAD into the so-called Allpix Squared Field (APF) format, a data format loadable by the *ElectricFieldReader* module. During the conversion from TCAD to APF, the space coordinates are re-arranged to match the EPICAL-2 geometry implementation discussed in section 3.2.1. The space-coordinate conversion is performed as following:

$$(z_{\mathrm{TCAD}},\ x_{\mathrm{TCAD}},\ -y_{\mathrm{TCAD}}) \quad \rightarrow \quad (x,\ y,\ z) \tag{19}$$

In addition, the electric field is scaled to the ALPIDE pixel size implementation in the *GeometryBuilderGeant4* module.

Figure 19 shows the electric field magnitude for a single pixel as function of the pixel y- and z-position at $x = 0$ for $V_{\mathrm{RB}} = 1.4\,\mathrm{V}$ as used in the EPICAL-2 simulation. The magnitude of the electric field is strongest at the pixel diode ($y = 0$, $z = 25\,\mu\mathrm{m}$). In general, the electric field magnitude increases towards the diode.

3.2.3 Particle Propagation and Energy Deposition

Both the transport of particles through the EPICAL-2 detector geometry and the interactions of the particles with the detector material, especially the energy deposition in the sensors, is performed with the *DepositionGeant4* module of ALLPIX^2. The *DepositionGeant4* module acts as an interface to GEANT4. To model the physical processes of particles in the detector material, GEANT4 provides a variety of available physics processes which are defined in so-called physics lists. For the simulation, the physics list *FTFP_BERT_EMZ* is used describing all particle interactions. *FTFP_BERT* is the current default of GEANT4 [All+16] and is used by LHC experiments and also recommended by [Gea22] for high energy physics calorimetry application. The addition *EMZ* ensures that for each energy the most accurate available physics process modelling is used.

The physics process modelling with *FTFP_BERT_EMZ* in GEANT4 includes the electromagnetic shower development. All shower particles can be studied within ALLPIX^2 by accessing the true Monte Carlo particle information provided by GEANT4. Figure 20 (left) shows the distribution of produced shower particles traversing any of the 48 ALPIDE sensors in the EPICAL-2 simulation at a primary electron energy of 1 GeV. Positrons are shown in red, electrons in blue and photons in green. All distributions show a Gaussian peak structure: on average circa 728 photons, 46 electrons and 20 positrons are produced and traversing the ALPIDE sensors per event. Approximately 90 % of all shower particles are photons. Only photons, electrons and positrons are shown in Figure 20 as they make up more than

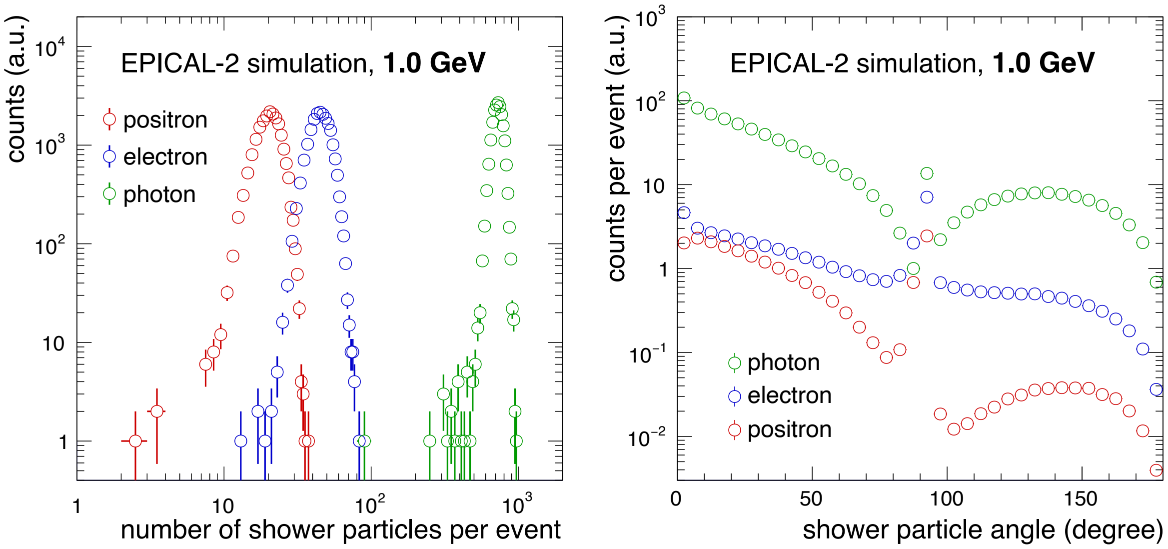

Figure 20: *Distribution of the number of produced shower particles traversing any* ALPIDE *sensor (left) and the distribution of their angle w.r.t. to the z-axis of* EPICAL-2 *(right).*

99.9 % of all produced particles in the electromagnetic shower induced by the primary electron with an energy of 1 GeV.

Figure 20 (right) displays the distribution of the shower particle angle w.r.t. the EPICAL-2 z-axis for electrons in blue, positrons in red and photons in green. The angles 0° and 180° correspond to shower particles traversing perpendicular to the sensor surface and thus 0° corresponds to forward moving particles and 180° to backward moving particles. Therefore, all particles between 0° and 90° are forward moving and all particles between 90° and 180° are back-scattered particles. Approximately 85 % of all shower particles are forward moving and 15 % are backward moving, calculated from Figure 20 (right) by integrating the sum of all distributions in the corresponding regions. Since photons dominate sum of the distributions, considering only electrons, approximately 70 % of the electrons are forward moving and 30 % are backward moving. Considering only photons or positrons, both are in line with the sum of all shower particles. The peak structure at 90° corresponds to particles, which enter a sensor from one side and leave the sensor at the same side. These particles are not crossing the sensors and therefore, the vector between the sensor entrance position and the sensor exit position is always perpendicular to the beam axis. The calculation of the angle yields 90°.

In the EPICAL-2 simulation, each charged particle in the electromagnetic shower deposits energy in the ALPIDE sensors they traverse. The energy deposition E_d of charged particles crossing the sensors is converted into electron-hole pairs using the mean pair creation energy $E_\text{e-h}$ in silicon of $E_\text{e-h} \approx 3.6$ eV [Spa+18]. In addition, the so-called Fano factor $F = 0.115$ is used to simulate fluctuations of the energy deposition due to electronic and lattice excitations [Spa+18; GZ+20]. The final number of electron hole pairs is drawn from a Gaussian distribution with a mean of $E_\mathrm{d}/E_\text{e-h}$ and a width of $\sqrt{F \cdot E_\mathrm{d}/E_\text{e-h}}$.

In the following, an estimate of the average energy deposited in the ALPIDE sensor by an electron traversing the sensor is discussed: To estimate the energy deposition of electric-charged shower particles in the sensor, one can use the mean energy loss $\langle \mathrm{d}E/\mathrm{d}x \rangle$ of an electric charged particle in material. $\langle \mathrm{d}E/\mathrm{d}x \rangle$ is typically described by the Bethe-Bloch equation [GZ+20]:

$$-\frac{1}{\rho} \cdot \left\langle \frac{\mathrm{d}E}{\mathrm{d}x} \right\rangle = \frac{\mathrm{K}}{\mathrm{A}} \frac{\mathrm{Z}\,\mathrm{z}^2}{\beta^2} \left[\frac{1}{2} \ln \left(\frac{2\,\mathrm{m_e}\, c^2\, \beta^2\, \gamma^2\, \mathrm{W_{max}}}{\mathrm{I}^2} \right) - \beta^2 \right] \tag{20}$$

$$\text{with:} \qquad \mathrm{K} = 4\,\pi\,\mathrm{N_A}\,\mathrm{r}_e^2\,\mathrm{m_e}\,c^2 \quad \text{and} \quad \mathrm{W_{max}} = \frac{2\,\mathrm{m_e}\,c^2\,\beta^2\,\gamma^2}{1 + 2\gamma\,\mathrm{m_e}/\mathrm{M} + (\mathrm{m_e}/\mathrm{M})^2}$$

The variables in the Bethe-Bloch equation above correspond to the following:

$\mathrm{m_e}$	electron mass
$\mathrm{r_e}$	classical electron radius
z	electric charge of incident particle
M	mass of incident particle
A	atomic mass of absorber material traversed by incident particle
Z	number of protons in nuclei of absorber material
I	mean excitation energy of absorber material
$\mathrm{W_{max}}$	maximum energy transfer to an electron in one collision

So-called density-effect corrections restricting the logarithmic increase at high energies and the special characteristics of the radiative and collision energy loss by electrons in medium, both described in [GZ+20], are omitted in Equation 20 to simplify the calculation for the energy loss. The energy loss is used here to estimate the average total energy deposition of an electron traversing an ALPIDE sensor in EPICAL-2.

Neglecting the corrections, Figure 21 shows the estimate of the average electron energy deposition in silicon over a depth of 25 µm as a function of the electron momentum. For example, the energy deposition increases from circa 10 keV at an electron momentum of 10 MeV to circa 15 keV at 1 GeV.

Neglecting any modifications of generated electron-hole pairs due to fluctuations, the average number $N_\text{e-h}$ of electron-hole pairs generated by the deposited energy can be estimated as:

$$N_\text{e-h} = \frac{25\,\mu\mathrm{m} \cdot \langle \mathrm{d}E/\mathrm{d}x \rangle}{E_\text{e-h}}$$

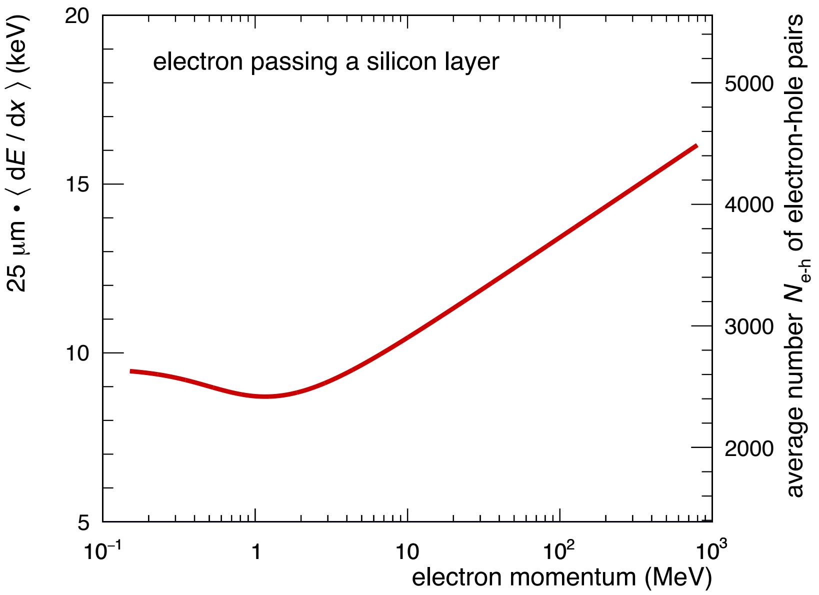

Figure 21: *Estimate of the average electron-energy deposition and the corresponding number of electron-hole pairs $N_{e\text{-}h}$ in* 25 µm *thick silicon as a function of the electron momentum.*

Figure 21 displays $N_{\text{e-h}}$ as a function of the electron momentum. As can be seen in Figure 21, the energy deposition of an electron in 25 µm silicon converts into several thousands of electron-hole pairs. This corresponds to a creation of approximately 100 electron-hole pairs per µm in silicon traversed by a charged particle. In ALLPIX^2 the electrons are considered as free charge carriers.

3.2.4 Charge Propagation and Charge Transfer

All free charge carriers deposited in a sensor are propagated through the sensor volume via the *GenericPropagation* module. In this module, the transport of charge carriers is implemented as an iterative motion consisting of diffusion in terms of random walk and drift according to the pixel electric field (see section 3.2.2).

For instance, a 5 GeV electron traversing the sensor in layer 0 deposits $\sim$ 3000 charges in this layer 0 via the *DepositionGeant4* module. As all charge carriers would be propagated independent in the *GenericPropagation* module, to speed up the EPICAL-2 simulation, groups of 50 charges each are created and the groups are propagated. The number of charges in a group is here referred to as the number N_{ch} of charge carriers propagated together.

In addition, the time span in which charge carriers are propagated is defined in the *GenericPropagation* module. This propagation time is referred to as the integration time t_{int} in the module. The charge carrier transport of a set either stops by exceeding t_{int} or by the set of charge carriers reaching any surface of the sensor under consideration.

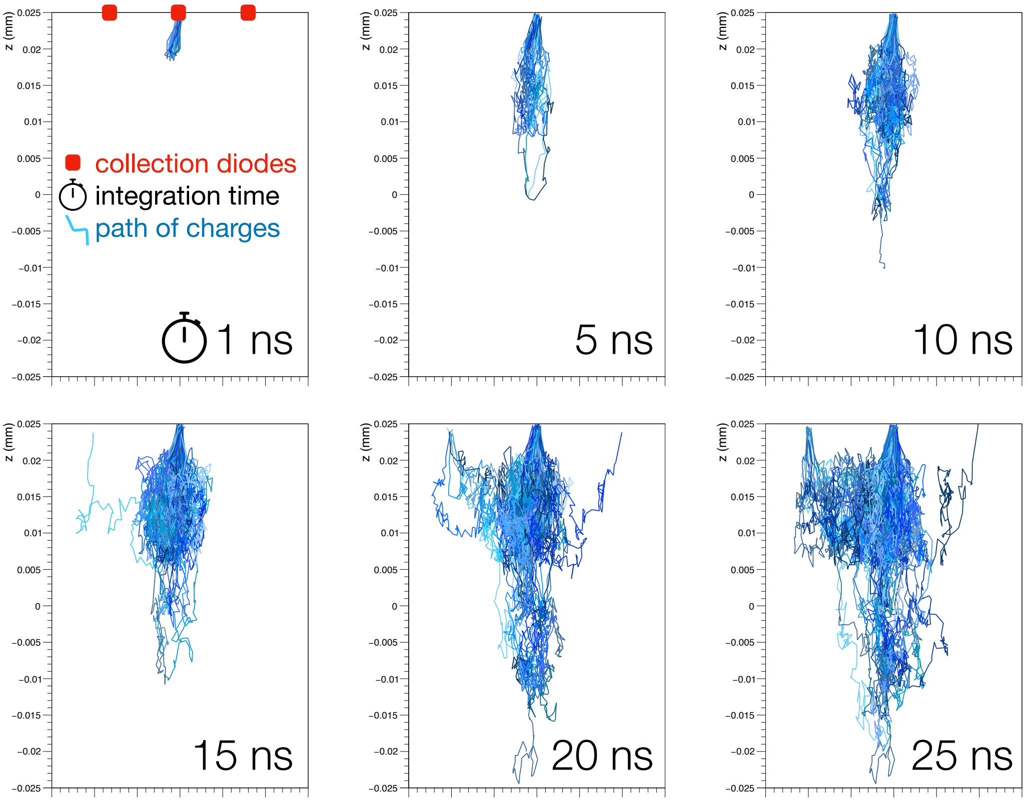

Figure 22: *Visualisation of the charge carrier propagation in Allpix^2 via the GenericPropagation module for different integration times.*

The charge propagation time in the ALPIDE sensors deployed in EPICAL-2 is not directly known. Therefore, t_{int} is a simulation parameter that is unconstrained by the ALPIDE sensor characteristics. However in [Sul18], the charge propagation time has been studied, showing that for a reverse substrate bias voltage of $V_{\text{BB}} = -1V$ the mean charge propagation time is $\sim$ 20 ns. For $V_{\text{BB}} < -1$ V the mean charge propagation time decreases to $\sim$ 13 ns at $V_{\text{BB}} < -6$ V. Considering the usage of $V_{\text{BB}} = 0$ V for the EPICAL-2 chips, a reasonable value for t_{int} that could be used for the EPICAL-2 simulation is $\sim$ 20 ns; probably slightly higher. Besides t_{int} being a free parameter, t_{int} strongly influences the EPICAL-2 response, especially the number of pixel hits which is discussed later in section 3.4.6. Therefore and because the value is a priori not known, t_{int} has been used to tune the EPICAL-2 simulation so that the simulation describes the EPICAL-2 test-beam data. The tuning and the modelling of the test-beam measurements with the simulation are discussed later in section 3.3. Especially the determination of the integration time to $t_{\text{int}} = 25.1$ ns, which is used to model the test-beam data with the simulation, is discussed in this section.

To visualise the propagation of charge carriers, the path of charges deposited in a single pixel cell embedded in the ALPIDE pixel matrix can be studied in ALLPIX^2. Figure 22 visualises the propagation of charges deposited in a single pixel cell in the transverse plane of ALPIDE for different t_{int} using the *GenericPropagation* module of ALLPIX^2. In Figure 22, each blue line corresponds to a set of 10 electrons which is propagated through the active area of the sensor in terms of diffusion and drift. The path of charge carrier sets is drawn if a set reaches a collection diode within the given integration time. As visible in Figure 22, after $\sim 10\,\text{ns}$ charges from the substrate start contributing to the total collected charge and already after $\sim 15\,\text{ns}$ deposited charge carriers are shared among neighbouring pixel diodes.

When the integration time is exceeded, first, all charge carriers are linked to their nearest pixel via the *SimpleTransfer* module. Second, for each pixel, all linked charges are summed up ignoring those exceeding the maximum distance in depth of $5\,\mu\text{m}$ to the sensor surface at the pixel diode side. $5\,\mu\text{m}$ is the default in ALLPIX^2 and variations of this default value do not lead to a change of the simulation behaviour (see section 3.4.2). In addition, only charge carriers within the pixel diode region of a pixel are considered, instead of considering all charges within the maximum depth over the whole pixel surface. Finally, the total collected charge is processed by the frond-end electronics. This digitisation step is discussed in the next section.

3.2.5 Digitisation

The frond-end electronics is simulated using the *DefaultDigitizer* module, where all input charge carriers assigned to a pixel via the *SimpleTransfer* module are processed and translated into a digital signal.

To simulate electronic noise contributions and their fluctuation from the readout electronics, for each pixel, the noise level is drawn from a Gaussian noise distribution and then added to the input charge value. A noise level between 7 e and 20 e is reported for a predecessor of ALPIDE in [Agl+21]. In contrast, in [Sul18], an average noise of $\sim$ 5 e has been measured for an exemplary ALPIDE sensor. More general, a strong dependence of the noise value on the threshold, which is discussed below, is observed in [Hoo15]. Later in section 3.4.5, it is shown that the bulk properties in the EPICAL-2 simulation are stable for noise values between zero and 25 e. To not underestimate the noise, for the EPICAL-2 simulation the Gaussian noise distribution is defined with a mean of zero and a width of 20 e.

In addition to noise, a pixel threshold is defined in the module. With this pixel threshold, a pixel hit is only registered when the sum of noise and input charge surpasses the threshold. As discussed in section 2.1.2, the different EPICAL-2 sensor thresholds bias the overall EPICAL-2 response for observables where the pixel hit information of all sensors is combined. To equalise the different sensor responses in EPICAL-2, for real data, all sensors are calibrated to the average sensor response (see section 4.2.5). In contrast to the real thresholds of the sensors deployed in EPICAL-2, in the simulation, the average sensor threshold is used directly. 82 e is the average

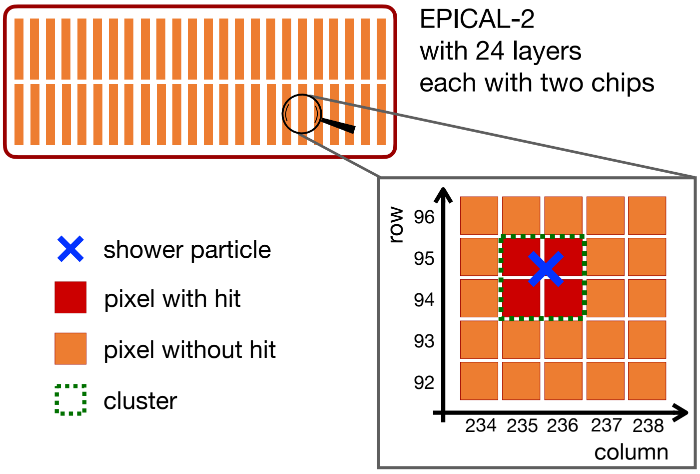

***Figure 23:** Illustration of the* EPICAL-2 *simulation output.*

sensor threshold of the ALPIDE sensors equipped in EPICAL-2 and 20 e is the average standard deviation (see section 2.1.2). In the simulation, the threshold is derived from a Gaussian distribution with a mean of 82 e and width of 20 e to simulate fluctuations of the threshold level in each pixel.

3.2.6 Simulation Output

To store the output of the simulation in the same format as the data acquired during the various EPICAL-2 test-beam measurements discussed in section 2.3, in context of this thesis, an ALLPIX^2 module named *CaloOutputWriter* has been developed and embedded into the ALLPIX^2 framework.

As discussed in section 2.1, one ALPIDE chip per layer is rotated by 180 ° w.r.t. the other chip in the EPICAL-2 setup. It is of particular importance to account for this special chip orientation in the *CaloOutputWriter* module, to match the data formats.

The same format of the simulation output as the test-beam data is achieved by storing the simulation output in terms of the pixel hit information column, row and lane (see section 2.4 for the definitions). The stored output of the EPICAL-2 simulation is visualised in Figure 23 exemplary for four pixel hits in one chip in layer 18.

Adjacent hits are grouped to a cluster via the clustering algorithm as applied to data (see section 4.2.2). Clusters are also stored together with a linking to their constituent pixel(s). A free-standing hit is a cluster and the number of pixel hits contributing to a cluster is referred to as cluster size.

In addition to the pixel hit information, the type, the energy, the entering and the exit point of all shower particles crossing the ALPIDE sensors are stored in the simulation output via the *CaloOutputWriter* module for detailed shower particle analyses beyond the scope of this work.

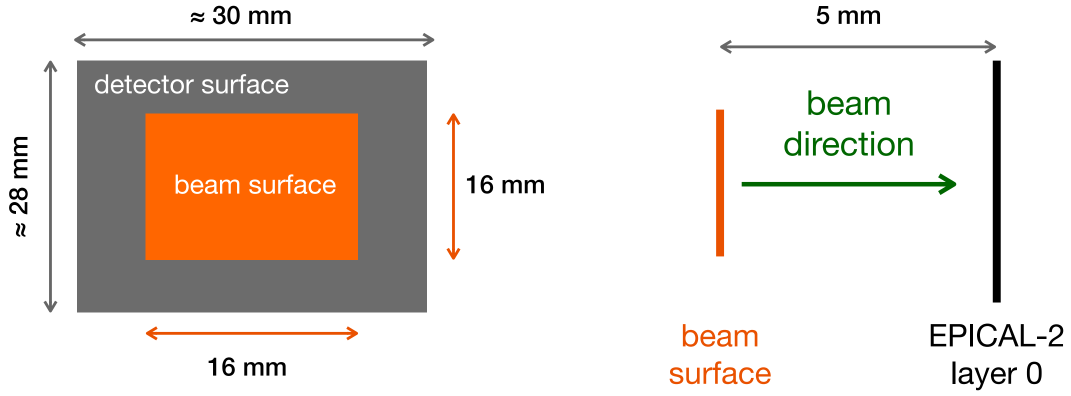

Figure 24: *Illustration of the geometry of the primary particle source. The primary particles are generated uniformly from and perpendicular to the square beam surface in a distance of 5 mm to the* EPICAL-2 *layer 0.*

3.3 Modelling the Test-Beam Measurements

To model the test-beam measurements, the test-beam properties need to be implemented in the simulation and the simulation must be tuned to describe the actual response of EPICAL-2 in the test-beam measurements.

To model the test-beam, the primary particle source in the simulation is defined according to the characteristics of the beam at DESY and SPS. The primary particle source is implemented via the *DepositionGeant4* module using the so-called general particle source of GEANT4. The type, the energy and the emission pattern of the primary particle are defined.

As discussed in section 2.3, electron events are recorded at the DESY and electron, kaon, pion, proton and muon events are recorded at the SPS. The beam energy at DESY ranges from 1 GeV up to 5.8 GeV with an absolute energy uncertainty of 158 MeV for each energy and the beam energy at SPS ranges from 20 GeV up to 80 GeV with a relative uncertainty of 1.5 % of each energy. In the simulation, the beam energy, the beam energy uncertainty and the particle type are defined according to the recorded test-data as described above.

Regardless of the particle type and the energy, the emission pattern in the simulation is defined as a $16 \times 16\,\mathrm{mm}^2$ square surface which is centred at the EPICAL-2 surface as depicted in Figure 24. The beam surface is positioned 5 mm in front of the EPICAL-2 layer 0 and one particle per event is uniformly generated from the square surface in the simulation. Furthermore, the beam direction is perpendicular to both the beam surface and the EPICAL-2 surface. The $16 \times 16\,\mathrm{mm}^2$ square surface is chosen in the simulation because in the test-beam data only events with a beam impact position in this square are selected. This selection avoids lateral leakage and will be discussed later in section 4.2.7 and section 4.2.8.

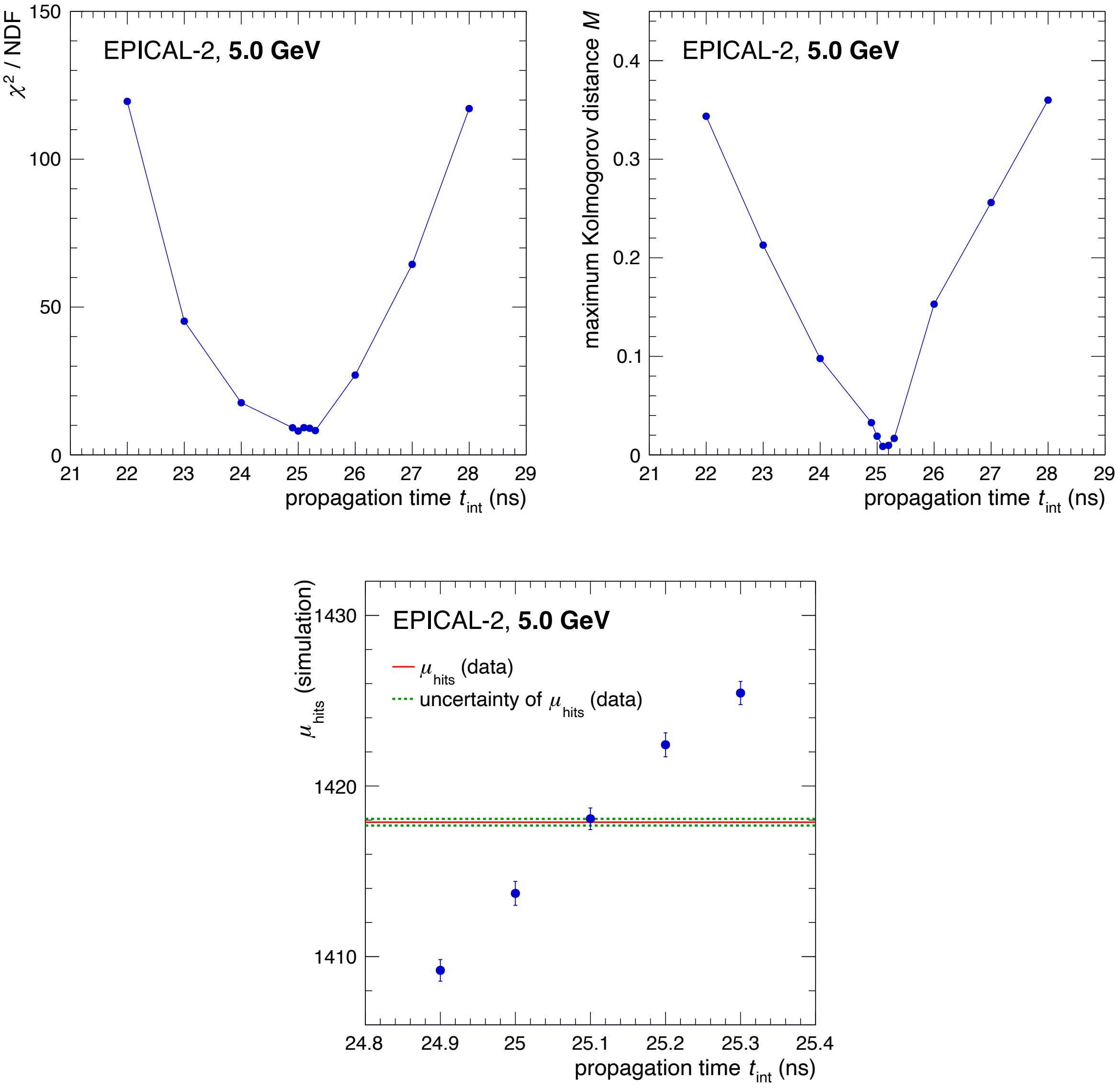

Figure 25: *Comparison between the distribution of the total number of hits at* 5 GeV *in data and in simulation for different propagation times using three comparison methods: The* χ^2 *test (left), the Kolmogorov test (right) and the mean number* μ_{hits} *of pixel hits.*

For the tuning of the simulation to describe the detector response of EPICAL-2 in the test-beam measurements, the propagation time of charge carriers is used. As discussed in section 3.2.4 about the charge propagation, the propagation time is unconstrained by the ALPIDE sensor characteristics and strongly influences the detector response of EPICAL-2 in the simulation. To obtain the propagation time where the measured test-beam data and the simulation agree, the distribution of the total number N_{hits} of pixel hits is compared between electron events in the test-beam data and electron events in the simulation at 5 GeV for different propagation times. Only one energy has been chosen to determine the propagation time. It is assumed that this integration time can also be used to simulate the other primary-particle energies. The energy of 5 GeV is chosen because at 5 GeV the DESY beam energy uncertainty is lowest and the highest number of test-beam events is available (see section 2.3.2).

Here, the agreement between the data and the simulation for different propagation times is tested using three complementary methods which are described below: the χ^2 test, the Kolmogorov test and the mean of the N_{hits} -distribution.

In the χ^2 test, the squared sum of the uncertainty weighted difference between all bin contents of two histogram distributions is calculated: the χ^2. The calculated χ^2 is normalised with the number of the degrees of freedom (NDF). In case of histograms as the N_{hits} -distribution, NDF equals the total number of histogram bins evaluated. Figure 25 (left) shows χ^2/NDF between data and simulation for different propagation times ranging from 22 ns to 28 ns. The χ^2 test rules out propagation times ≤ 24 ns and ≥ 26 ns and favours a propagation time close to 25 ns. However, the χ^2-test seems insensitive to the propagation times closely around 25 ns, namely 24.9 ns, 25.0 ns, 25.1 ns, 25.2 ns and 25.3 ns as visible in Figure 25 (left).

The Kolmogorov test aims at quantifying the compatibility in shape between two distributions. For the comparison of two distributions with the Kolmogorov test, first, the cumulative distributions are calculated for both distributions. For each bin, the difference between the two cumulative distributions is determined. The maximum value of the difference between the two cumulative distributions, the so-called Kolmogorov distance M, is considered as a measure for the compatibility in shape of the two distributions under study. Figure 25 (right) displays the maximum Kolmogorov distance M between data and simulation as a function of the propagation time. Similar to the χ^2-test, the Kolmogorov test rules out the propagation times ≤ 24 ns and ≥ 26 ns. However, in contrast to the χ^2-test, the Kolmogorov test is sensitive to the propagation times closely around 25 ns and particularly favours 25.1 ns.

In addition to the χ^2- and Kolmogorov test, Figure 25 (bottom) shows the mean number μ_{hits} of pixel hits derived from the N_{hits} -distribution in the simulation for the propagation times closely around 25 ns from 24.9 ns to 25.3 ns. The simulation for different propagation times is compared to the mean in data, which is shown as a red solid line in Figure 25 (bottom). For 25.1 ns, the mean value in the simulation agrees best with the mean value in the data.

Combining the results of the three comparison methods, the EPICAL-2 simulation is performed utilising a propagation time of 25.1 ns, which results in an agreement between the N_{hits} -distribution in the data and the N_{hits} -distribution in the simulation.

The settings for the EPICAL-2 simulation as implemented in ALLPIX^2 to model the test-beam measurements are summarised in Table 6. The seven modules which are used for the simulation are shown together with the implemented parameter values. ALLPIX^2 parameters not listed in Table 6 remain at their default values of the ALLPIX^2 framework. Information about further ALLPIX^2 modules as well as the documentation of all user-configurable parameters for each module can be found in [All21; Spa+18].

modules and parameters	**default values**
GeometryBuilderGeant4:	
world material	air
position, size and type of detector volumes	see Table 5
ALPIDE sensor geometry	pixel matrix: 512 × 1024 pixel size: $26.88 \times 29.24\,\mu m^2$
ElectricFieldReader:	
electric field configuration	derived from TCAD simulation with $V_{RB} = 1.4\,V$ (see section 3.2.2)
DepositionGeant4:	
GEANT4 physics list	*FTFP_BERT_EMZ*
particle beam: position, size, type and energy	$(e^{\pm}, \mu^{\pm}, h^{\pm})$: 1 GeV to 80 GeV uniformly from a $16 \times 16\,mm^2$ square surface, 5 mm in front and centred to the EPICAL-2 layer 0 surface
GenericPropagation:	
number N_{ch} of charges propagated together	50
integration time t_{int} within charge is propagated	25.1 ns
SimpleTransfer:	
charge collection depth d_{count} below the pixel diode	5 µm
DefaultDigitizer:	
noise mean	0 e
noise standard deviation	20 e
pixel threshold mean	82 e
pixel threshold standard deviation	20 e
CaloOutputWriter:	
pixel hit information column, row and chip ID in each layer	

Table 6: *Summary of the* ALLPIX^2 *modules including the parameters used to implement the* EPICAL-2 *prototype in the* ALLPIX^2 *framework and to model the test-beam measurements.*

3.4 Behaviour Study of the Simulation

As discussed in the previous section, the EPICAL-2 prototype is implemented in the ALLPIX^2 framework on the basis of the actual EPICAL-2 properties. The simulation parameters that are unconstrained by the prototype characteristics have been used to tune the simulation to describe the test-beam measurement of electrons with an energy of 5 GeV.

To assess the stability of the detector response in simulation at a fixed energy, one can change the parameters of the simulation in a reasonable range and then study the influence on the response. By doing this, one can understand how the simulation behaves when simulation parameters are changed and gain insight into the mechanism that change the behaviour. Furthermore, one can identify the simulation parameters that influence the behaviour and the parameters that do not influence the behaviour.

In this section, the qualitative behaviour of the EPICAL-2 simulation under variation of the simulation parameters described in the previous section is presented. For each simulation parameter variation, the behaviour is characterised on the basis of global observables representing the bulk properties of an electron measurement with the EPICAL-2 prototype. The study of the behaviour is discussed exemplary for 5 GeV electron events. Before each simulation parameter variation is discussed, the observables are introduced first.

3.4.1 Behaviour Observables

The EPICAL-2 simulation output contains all pixel hits and clusters as energy response to the electromagnetic shower development in EPICAL-2. The most basic global energy response observables can be derived by summing up all pixel hits and clusters in all layers to derive the total number of pixel hits and the total number of clusters.

Figure 26 (left) shows the distribution of the total number of pixel hits in blue and the distribution of the total number of clusters in green exemplary for electron events at a primary electron energy of 5 GeV. Both distributions show a Gaussian peak structure. The mean μ and the standard deviation σ of both distributions are determined arithmetically and are included in Figure 26 (left) by vertical lines and shaded areas: μ_{hits} (μ_{clus}) refers to the mean number of pixel hits (clusters) shown as blue (green) horizontal line and the shaded blue (green) area refers to the region $\mu_{\text{hits}} \pm \sigma_{\text{hits}}$ ($\mu_{\text{clus}} \pm \sigma_{\text{clus}}$). The mean values reflect the mean energy response, the standard deviation the spread around the mean and the ratio of standard deviation and mean reflects the energy resolution.

While the total number of hits and clusters correspond to the energy response of 5 GeV electrons, the average cluster size is linked to the average shower particle response. Figure 26 (right) shows the distribution of the cluster size for electron

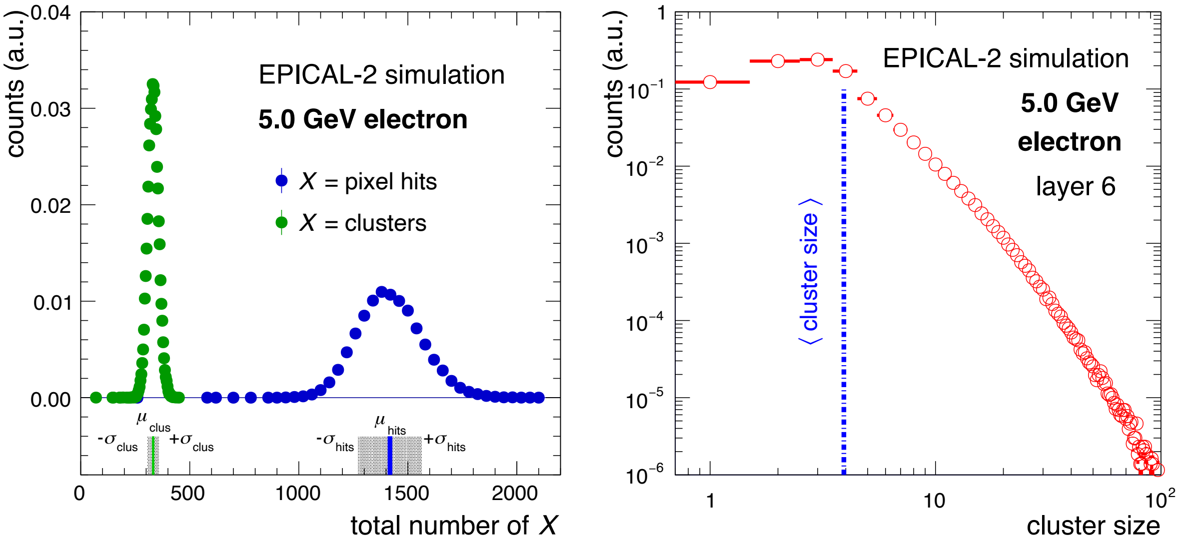

Figure 26: *The distribution of the total number of pixel hits and clusters (left) and as the cluster size distribution in layer 6 (right) for 5 GeV electron events.*

events at a primary electron energy of 5 GeV and exemplary for layer 6. Cluster sizes smaller than four dominate the total distribution, while cluster sizes larger than four become less likely the larger they are. In addition to the cluster size distribution, Figure 26 (right) shows the average cluster size ⟨cluster size⟩ as a vertical blue dashed line around ⟨cluster size⟩ ≈ 4.

In the next sections 3.4.2 to 3.4.7, the observables mean number of hits (μ_{hits}) and clusters (μ_{clus}), standard deviation of hits (σ_{hits}) and clusters (σ_{clus}) and the average cluster size (⟨cluster size⟩) are used to discuss the behaviour of the EPICAL-2 simulation under variation of its simulation parameters. The parameters are discussed in the following order:

(1) Pixel depth of charge registration

(2) Electric field strength

(3) Pixel threshold

(4) Electronic noise

(5) Charge carrier propagation time

(6) Number of charges propagated together

3.4.2 Pixel Depth of Charge Registration

As discussed in section 3.2.4, deposited charge carriers within a sensor exceeding a maximum distance in depth to the sensor surface at the pixel implant side are ignored in simulation. In a real detector, charge carriers either reach the pixel diode or not. Therefore, the depth is a pure simulation parameter. As an educated guess, taking the whole sensor thickness into account and no depth seam senseless. Since the pixel

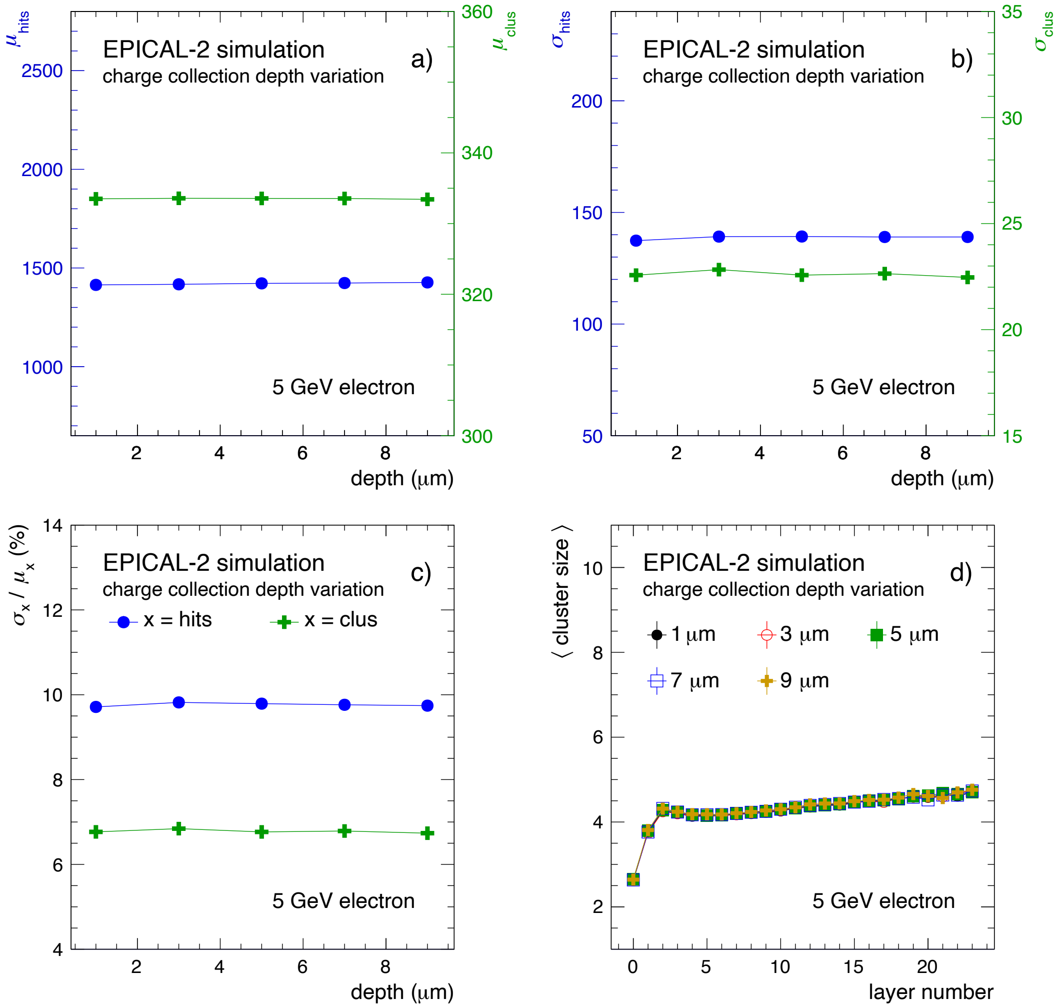

Figure 27: *EPICAL-2 simulation behaviour under variation of the depth where charge carriers are assigned to the pixel diode. The data-point-connecting lines are drawn to guide the eye.*

diode itself has a certain depth, a reasonable value range in depth to study is between greater zero and the so-called CMOS stack thickness of 10 μm which is situated on top of the epitaxial layer and contains the pixel diode [ALI+14]. Here, the depth is varied between 1 μm and 9 μm; 4 % and 36 % of the epitaxial layers thickness of 25 μm.

Figure 27 shows the simulation behaviour under variation of the charge collection depth. The average number of pixel hits μ_{hits} and clusters μ_{clus} is shown in Figure 27 a) and the corresponding standard deviations σ_{hits} and σ_{hits} in Figure 27 b). Their ratio σ/μ is shown in Figure 27 c) for both hits and clusters. In addition, the average cluster size ⟨cluster size⟩ as a function of layer is displayed in Figure 27 d).

The mean energy response, the resolution and the average cluster size are stable for a charge collection depth between 1 μm and 9 μm. Therefore, no dependence of the simulation behaviour on the charge collection depth is observed validating the choice of 5 μm as default simulation parameter value for the pixel depth.

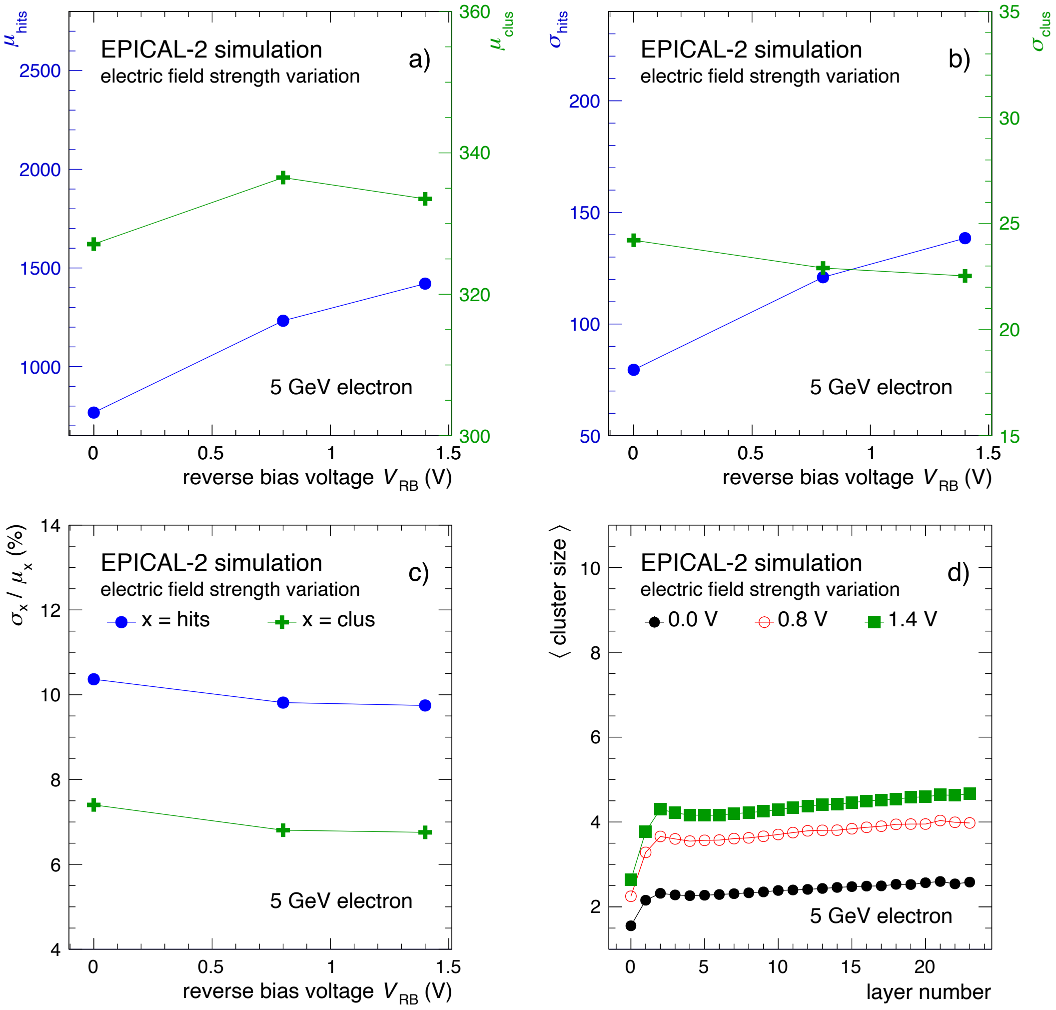

Figure 28: EPICAL-2 *simulation behaviour under variation of the pixel electric field which influences the (drift) motion of charge carriers. The data-point-connecting lines are drawn to guide the eye.*

3.4.3 Electric Field Strength

In general, one would expect a strong change in the behaviour of the simulation when using a different electric field as it strongly influences the motion of deposited charge carriers in the ALPIDE sensors. As discussed in context of Figure 8 in section 2.1.1, the electric field strength is defined by the total reverse bias voltage V_{RB}:

$$V_{RB} \approx V_{RST} + V_{BB} \tag{21}$$

V_{RST} is the pixel reset voltage and V_{BB} the reverse substrate bias voltage. For example, if $V_{RB} = 0$, the electric field emerges only from the different doping concentrations of the pixel components. To enhance the electric field strength inside a pixel either V_{RST} or V_{BB} can be increased. During the EPICAL-2 data taking periods the voltage settings were $V_{RST} = 1.4\,V$ and $V_{BB} = 0$ yielding the total reverse bias voltage of $V_{RB} = 1.4\,V$. Here,

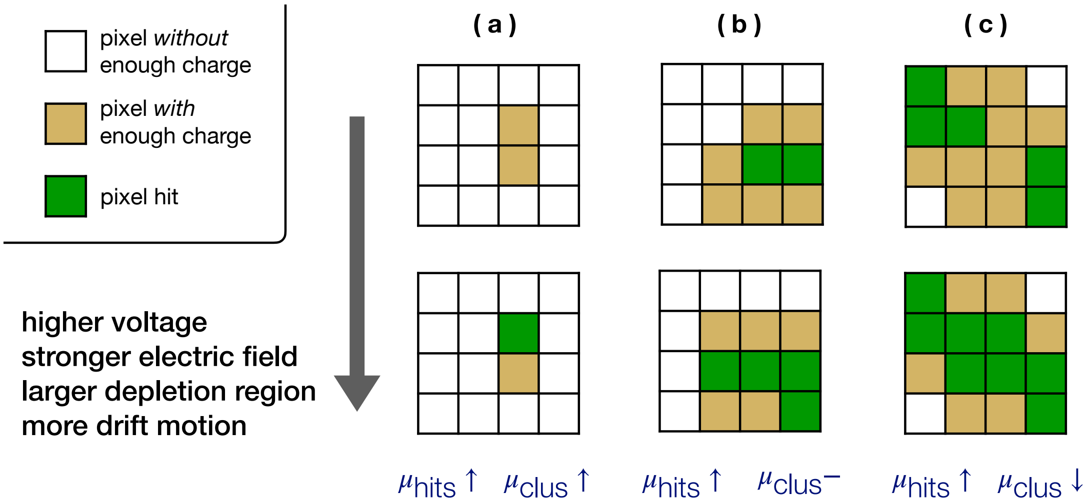

Figure 29: *Visualisation of the influence of a higher reverse bias voltage V_{RB} on the number of pixel hits and clusters.*

the influence of the electric field strength on the simulation behaviour is presented by changing the total reverse bias voltage to $V_{\mathrm{RB}} = 0$ and $V_{\mathrm{RB}} = 0.8\,V$.

Figure 28 shows the simulation behaviour for different electric field configurations derived from TCAD simulations using different reverse bias voltages V_{RB}, which leads to different pixel electric fields. Similar to the presentation of Figure 27 in the previous section 3.4.2, μ_{hits} and μ_{clus} are shown in Figure 28 a), the corresponding σ_{hits} and σ_{hits} in Figure 28 b), their ratio σ/μ in Figure 28 c) and finally $\langle$cluster size$\rangle$ as a function of layer is shown in Figure 28 d).

As visible in Figure 28 a), the mean number of hits and clusters changes as follows:

V_{RB} (V)	0	0.8	1.4
μ_{hits}	~ 767	~ 1232	~ 1420
μ_{clus}	~ 327	~ 337	~ 333

Compared to the increase in the mean number of hits, the change in the mean number of clusters is negligible small.

In the following, the behaviour of the detector response under the variation of the electric field strength is discussed: For $V_{\mathrm{RB}} = 0$, the motion of charge carriers is dominated by diffusion and barely influenced by drift in the electric field emerging only from the different doping concentrations of the pixel components. Therefore, there might be pixels where in principle enough charge carriers are deposited or have entered the pixel by diffusion, but not enough of those charge carriers reach the pixel diode within the charge propagation time. The higher the V_{RB} the stronger the electric field strength. This leads to an increase of charge carrier motion via drift. With this in mind, one can think of three scenarios influencing μ_{clus} and μ_{hits} when increasing V_{RB} which are illustrated in Figure 29: In scenario (a), a free-standing charge will be collected with an increased field. This leads to higher μ_{hits} and μ_{clus}. In scenario (b), a cluster of two hits is still surrounded by uncollected charge. An increase of the field will soak in those charges, which leads to higher μ_{hits} but leaves μ_{clus} unaffected as those hits will be assigned to the existing cluster. In scenario (c), two nearby clusters of three and two hits are both still surrounded by uncollected charge. An increase of the field will soak in those charges connecting both clusters. This yields a higher μ_{hits} but decreases μ_{clus}. An interplay of the scenarios (a) to (c) leads to the behaviour of μ_{clus} and μ_{hits} when increasing V_{RB} as shown in Figure 28.

In relation to the three scenarios, the variable $\langle\text{cluster size}\rangle$ shown in Figure 28 d) increases from $\langle\text{cluster size}\rangle \sim 2.5$ at $V_{\text{RB}} = 0$ to $\langle\text{cluster size}\rangle \sim 4.5$ at $V_{\text{RB}} = 1.4\,\text{V}$, which supports the scenario (b) dominating the overall interplay.

While σ_{hits} increases for higher V_{RB}, σ_{clus} decreases. If more pixels collect enough charge for a hit, also the fluctuations in N_{hits} increase. In contrast, clusters absorb part of these fluctuations if newly fired pixels are linked to a cluster resulting only in a change of the cluster size and therefore, σ_{clus} is rather flat w.r.t. σ_{hits}.

Both $\sigma_{\text{hits}}/\mu_{\text{hits}}$ and $\sigma_{\text{clus}}/\mu_{\text{clus}}$ decrease from $V_{\text{RB}} = 0$ to $V_{\text{RB}} = 0.8\,\text{V}$ and are constant from $V_{\text{RB}} = 0.8\,\text{V}$ to $V_{\text{RB}} = 1.4\,\text{V}$. The energy measurement is based on counting the number of shower particles by counting the number of pixel hits they traversed. The performance increases when going from a diffusion dominated scenario ($V_{\text{RB}} = 0$) to higher pixel electric fields ($V_{\text{RB}} > 0$) because more shower particles depositing energy in a pixel are counted due to a better charge collection.

The change in the number of hits, the resolution and the cluster size show, that the electric field strength influences the detector response. Both the number of hits and the average cluster size increase with higher electric fields. Furthermore, a better energy resolution is achieved using a higher electric field. The dependence of the simulation behaviour on the electric field confirms the usage of $V_{\text{RB}} = 1.4\,\text{V}$ in EPICAL-2 and suggests the usage of even higher electric fields.

3.4.4 Pixel Threshold

As discussed in section 3.2.5, the default average pixel threshold of 82 e is implemented in the EPICAL-2 simulation according to the EPICAL-2 settings during the data-taking campaigns at SPS and DESY. It is expected that the simulation is particularly sensitive to the pixel threshold because only collected charge by a pixel surpassing this threshold is registered as a pixel hit. Therefore, the behaviour of the simulation for different threshold levels in the range from 0 to 150 e is investigated here.

In Figure 30, the behaviour of the EPICAL-2 simulation for different pixel thresholds is presented. First, Figure 30 a) shows the average number of pixel hits μ_{hits} and clusters μ_{clus}. The corresponding standard deviations σ_{hits} and σ_{hits} are

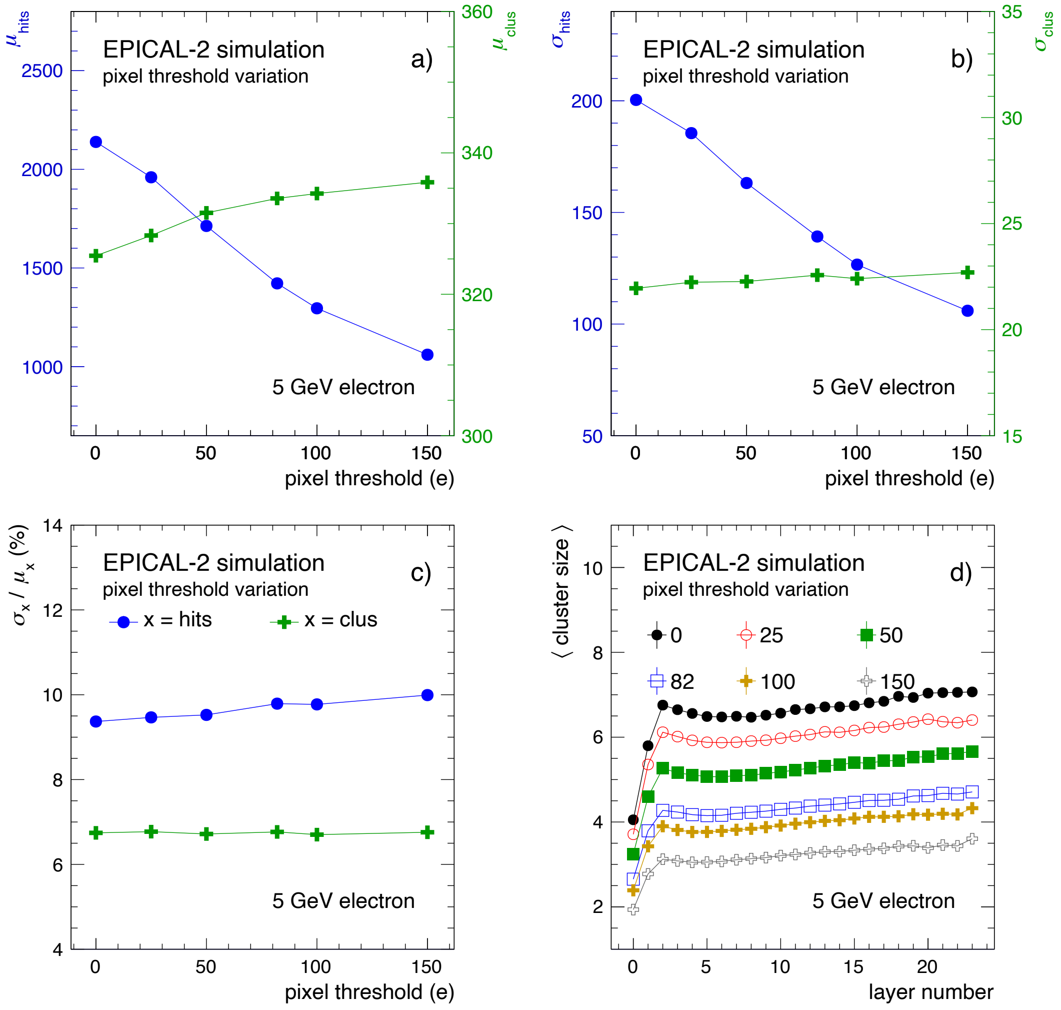

Figure 30: EPICAL-2 *simulation behaviour under variation of the pixel threshold. A pixel fires when its collected charge surpasses this threshold. The data-point-connecting lines are drawn to guide the eye.*

displayed in Figure 30 b). Third, the ratio σ/μ is shown in Figure 30 c) for both hits and clusters. Finally, Figure 30 d) displays the variable ⟨cluster size⟩ as a function of the layer number for different pixel thresholds. The strongest change is observed in the following observables and amounts:

threshold (e)	μ_{hits}	σ_{hits}	⟨cluster size⟩
0	~ 2140	~ 200	~ 6.5
150	~ 1060	~ 105	~ 3

The higher the threshold the lower the ⟨cluster size⟩. From 0 to 150 e, ⟨cluster size⟩ decreases by a factor of ~ 2.2. The decrease of μ_{hits} and σ_{hits} the higher the threshold results from less pixels that produce a hit given an underlying constant collected-charge distribution. For example, the total reduction in μ_{hits} is a factor of ~ 2 from 0 to 150 e. In contrast, μ_{clus} and σ_{clus} increase the higher the pixel threshold, although this increase is only ~ 3 % from a threshold of 0 to a threshold of 150 e. The resolution increases by ~ 10 % for hits and stays rather constant for clusters at $\sigma_{\text{clus}}/\mu_{\text{clus}} \sim 6.7$ %.

In general, the higher the threshold the fewer the pixels with a deposited charge that surpasses the threshold. This leads to a lower number of hits and smaller clusters. The resolution decreases slightly for hits because a higher threshold reduces the probability that a shower particle that deposits charge is registered as pixel hit. Especially the strong change in the number of hits and in the average cluster size for different pixel thresholds demonstrate the strong dependence of the chip response on the pixel threshold. This confirms the usage of a uniform pixel threshold of 82 e as default in the EPICAL-2 simulation.

3.4.5 Electronic Noise

Electronic noise contributions should emulate the read-out electronics noise. As discussed in section 3.2.5, different noise values between 5 e and 20 e are reported for the ALPIDE chip which in fact depend especially on the threshold settings. Therefore, below, the simulation behaviour is studied for noise contributions in the range of 0 to 25 e.

Figure 31 shows the EPICAL-2 simulation behaviour for different noise contributions which are added to the pixel collected charge. Similar to the discussions in the previous sections, the average number of pixel hits μ_{hits} and clusters μ_{clus} are shown in Figure 27 a) and the corresponding standard deviations σ_{hits} and σ_{hits} in Figure 27 b). Figure 27 c) shows the ratio σ/μ for both hits and clusters and finally, the average cluster size $\langle\text{cluster size}\rangle$ as a function of layer is presented in Figure 27 d). Overall, no dependence of the simulation behaviour on the noise is observed.

As discussed in section 3.2.3, approximately 3000 electrons are deposited on average in the ALPIDE sensor layer by a single charge particle crossing. Therefore, noise contributions in the range of 0 to 25 e correspond to less than 1 % of the average number of collected electrons and do not influence the overall simulation behaviour. Even only 500 deposited electrons would correspond to less than 5 % noise contributions for noise below 25 e. Therefore, and as seen in Figure 31, the simulation is insensitive to contributions from noise in the range from 0 to 25 e. This validates the usage of a Gaussian noise contribution with a standard deviation of 20 e in the EPICAL-2 simulation.

3.4.6 Charge Carrier Propagation Time

The motion of charge carriers in the EPICAL-2 simulation is calculated as a superposition of diffusion and drift according to the pixel electric field. Therefore, the

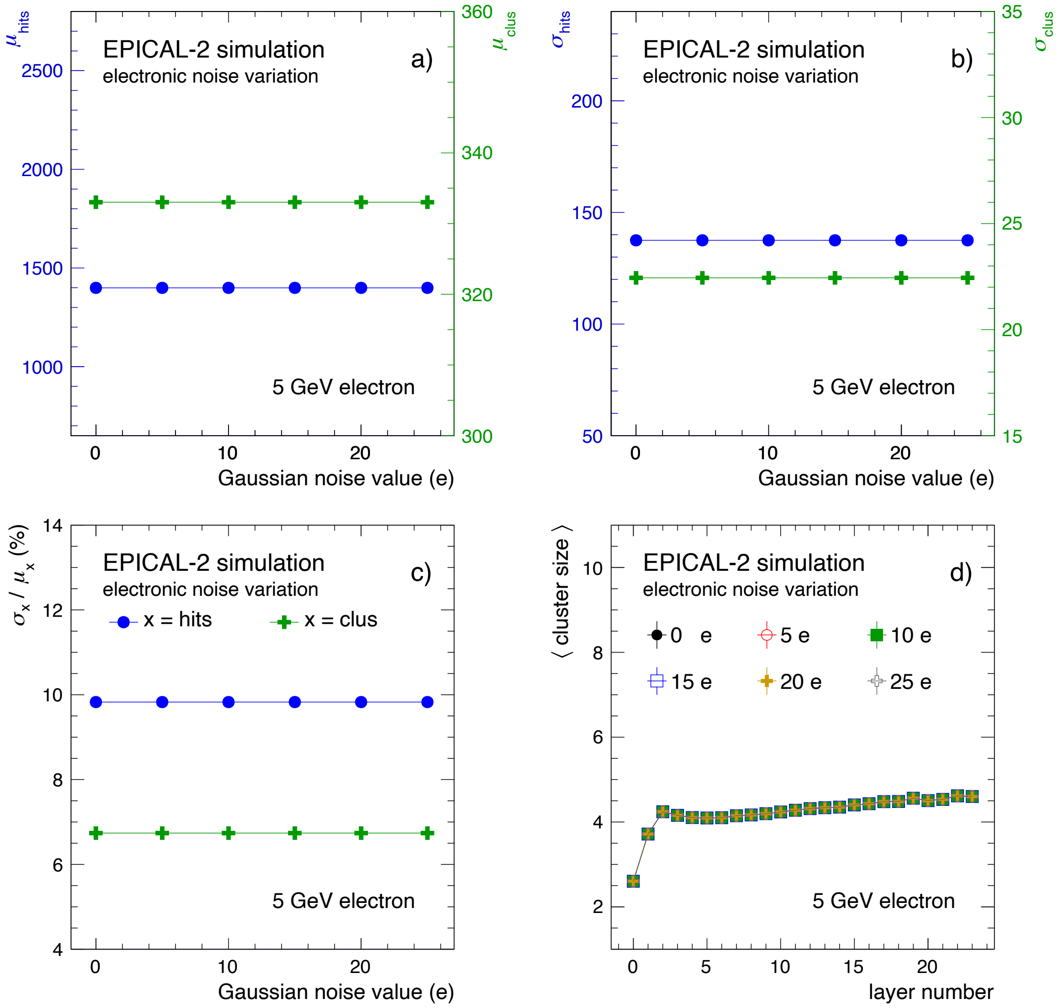

Figure 31: EPICAL-2 *simulation behaviour under variation of the mean noise per pixel. The data-point-connecting lines are drawn to guide the eye.*

integration time t_{int}, as the time in which deposited charge carriers are propagated, strongly influences the amount of collected charge at the pixel diode. As discussed in section 3.2.4, t_{int} is not directly known from the EPICAL-2 properties. Therefore, the influence of t_{int} on the EPICAL-2 simulation behaviour is studied here by varying t_{int} between 20 ns and 30 ns, which are values in the range of various ALPIDE studies with different bias voltage settings as discussed in section 3.2.4.

Figure 32 shows the behaviour of the EPICAL-2 simulation for different t_{int}. μ_{hits} and μ_{clus} are shown in Figure 32 a) while σ_{hits} and σ_{clus} are presented in Figure 32 b). The ratio σ/μ for both hits and clusters is displayed in Figure 32 c) and $\langle$cluster size$\rangle$ as a function of layer is shown in Figure 32 d).

The majority of pixel hits emerges from charge sharing which sets in after $t_{int} \sim$ 15 ns (see section 3.2.4). Therefore, the longer the t_{int}, the more charge carriers are shared among neighbouring pixels and the higher the probability that a charge reaches

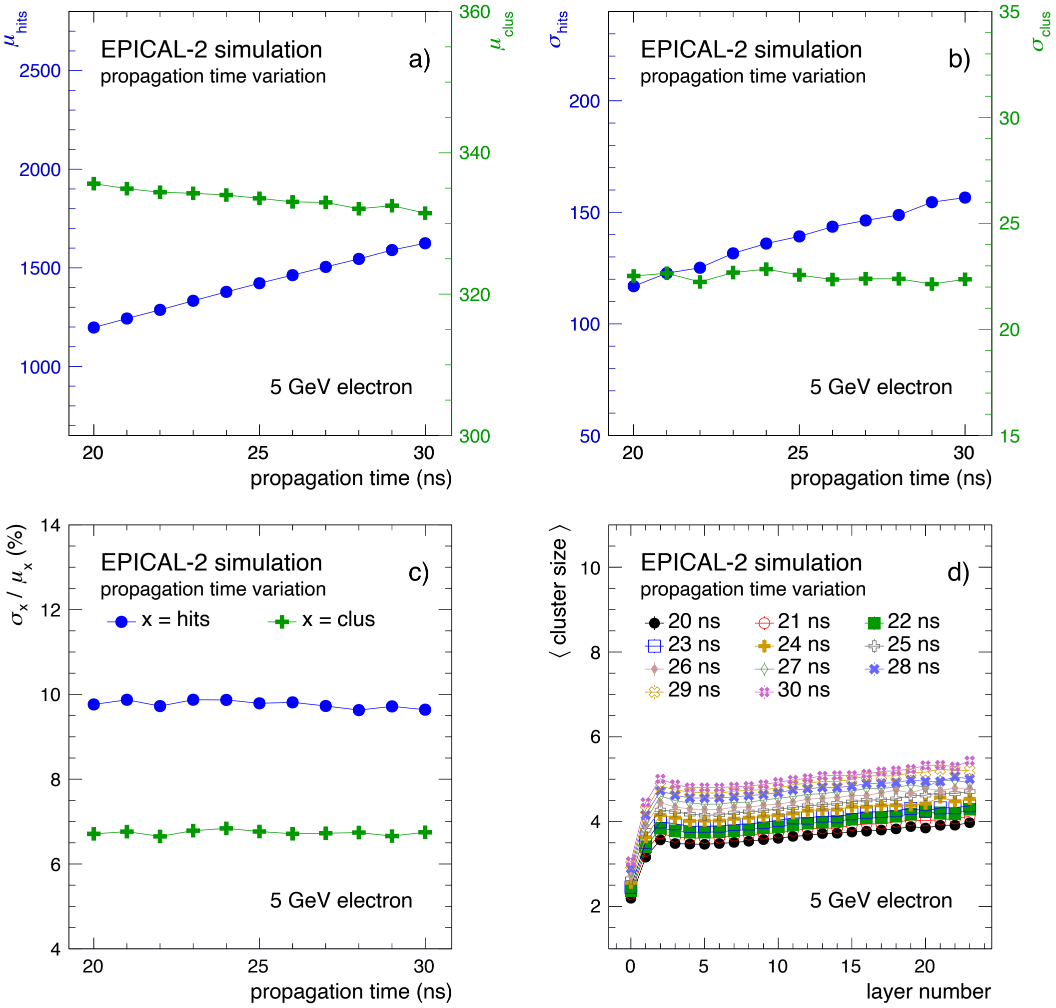

Figure 32: EPICAL-2 *simulation behaviour under variation of the time frame in which deposited charge carriers are propagated. The data-point-connecting lines are drawn to guide the eye.*

a collection diode. This leads to an increase in the number μ_{hits} of pixel hits as indicated in Figure 32 a):

t_{int} (ns)	20	30
μ_{hits}	~ 1200	~ 1625

This N_{hits}-increase leads to a factor of $\sim$ 1.5 larger clusters which is visible in Figure 32 d):

t_{int} (ns)	20	30
⟨cluster size⟩	~ 3.5	~ 5

The larger the clusters, the higher the probability that clusters merge. This leads to a ~ 1 % decrease of μ_{clus} as visible in Figure 32 a). However, the EPICAL-2 energy resolution for both hits and clusters seems unaffected by an increase of the propagation time since $\sigma_{\text{hits}}/\mu_{\text{hits}}$ and $\sigma_{\text{clus}}/\mu_{\text{clus}}$ as shown in Figure 32 c) are constant at ~ 10 % for hits and $\sim 6.5\,\%$ for clusters. t_{int} does not influence the energy resolution and barely μ_{clus}, but significantly changes μ_{hits} and $\langle$cluster size$\rangle$. This validates the usage of t_{int} as the parameter to tune the EPICAL-2 simulation to agree with the measured data (see section 3.2.4).

3.4.7 Number of Charges Propagated Together

In the EPICAL-2 simulation, the deposited charge carriers in a sensor are grouped to sets of 50 charges each and these sets are propagated independently through the sensor volume. A priori the set size is a pure simulation parameter to speed up the computing. If not set, thousands of deposited electrons per pixel are propagated independently in terms of diffusion and drift. Propagating each electron independently provides the most accurate sensor-level modelling of the charge propagation, while a higher number N_{ch} of charges propagated together reduces the computing time.

Figure 33 shows the EPICAL-2 simulation behaviour for different N_{ch}. μ_{hits} and μ_{clus} are shown in Figure 33 a) and the corresponding σ_{hits} and σ_{clus} in Figure 33 b). The energy resolution ratio σ/μ for hits and clusters is presented in Figure 33 c). Furthermore, $\langle$cluster size$\rangle$ as a function of layer is displayed in Figure 33 d).

Regarding the N_{hits} observable, the energy response is stable for $N_{\text{ch}} < 100$. In particular, μ_{hits} and σ_{hits} are constant for $N_{\text{ch}} < 100$ at:

$$\begin{array}{ll} \mu_{\text{hits}} & \sim 1420 \\ \sigma_{\text{hits}} & \sim 140 \end{array}$$

Above a number of charges of $N_{\text{ch}} = 100$, both μ_{hits} and σ_{hits} decrease by ~ 7 %. In contrast, μ_{clus} and σ_{clus} slightly increase the higher the N_{ch} but by less than 2 %:

N_{ch}	10	200
μ_{clus}	~ 332	~ 338

Although μ and σ for both hits and clusters do change with N_{ch}, the energy resolution σ/μ for both hits and clusters seems constant under variation of N_{ch}.

The average cluster size $\langle$cluster size$\rangle$ decreases for $N_{\text{ch}} > 100$. If N_{ch} increases, at some point it is likely to produce a single hit cluster not linked to the original cluster anymore. This leads to an increase of μ_{clus}, while $\langle$cluster size$\rangle$ decreases. Although the influence of N_{ch} on the EPICAL-2 simulation behaviour is in general small, above $N_{\text{ch}} = 100$ the average number of pixel hits decreases as well as the average cluster size $\langle$cluster size$\rangle$ as visible in Figure 33 d) and Figure 33 a). Therefore $N_{\text{ch}} > 100$ should not be used for a detailed modelling.

Since the influence of N_{ch} on μ_{clus} and σ_{clus} is negligible small for $N_{\text{ch}} < 100$ as discussed above, $N_{\text{ch}} = 50$ is chosen as default in the EPICAL-2 simulation. This is

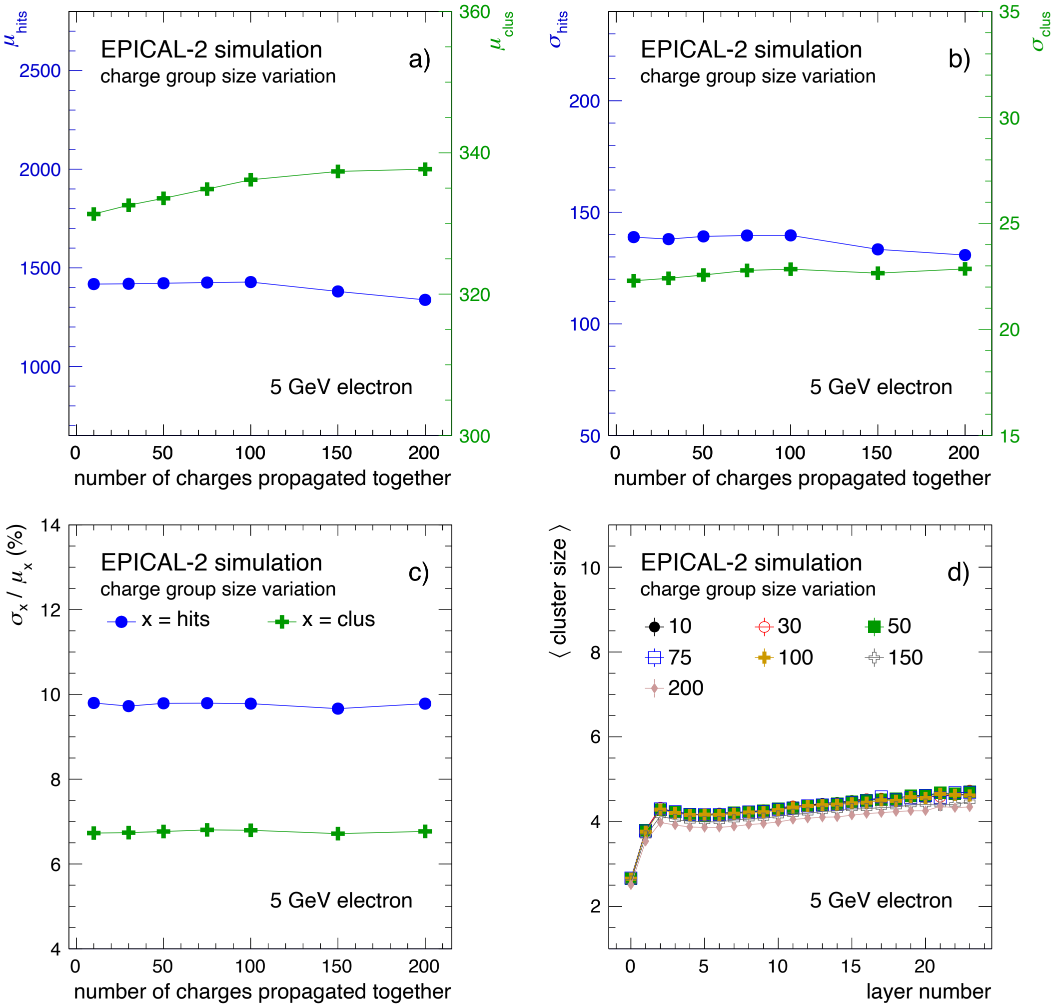

Figure 33: *The behaviour of the* EPICAL-2 *simulation under variation of the number* N_{ch} *of charge carriers propagated together. The data-point-connecting lines are drawn to guide the eye.*

a compromise between keeping an accurate level of detail in the charge propagation modelling and reducing the computing time as much as possible. For instance, a factor of 2.5 from ~ 50 s/event with $N_{\mathrm{ch}} = 10$ to ~ 20 s/event with $N_{\mathrm{ch}} = 50$ is gained in terms of computing time for EPICAL-2 simulations of primary electrons with an energy of 5 GeV.

4 Test-Beam Analysis

4.1 Raw Data

A first look at the "raw" test-beam data acquired with EPICAL-2 at DESY and at SPS is presented in this section. Here, the terminology "raw" is used since the test-beam data is presented as acquired, i.e. without any modifications or corrections which are discussed in the next section. Later, in section 5, the results for the energy measurement performance of EPICAL-2 and the shape of electromagnetic showers with EPICAL-2 are presented. Both results rely on the analysis of many events combined for which the characteristics of raw events are particularly important because they define what corrections and selections are necessary to apply to the raw data in advance.

Both the beam energy and the test-beam composition are different at DESY and at SPS. This leads to different types of events that are contained in the raw data.

At DESY, the beam contains only electrons in the energy range of 1 GeV to 5 GeV. However, the beam intensity at DESY was sufficiently high so that multiple electrons could enter EPICAL-2 at once. Multiple-particle events are here referred to as pile-up events and need to be rejected for analyses of single electron events.

In contrast to the pure electron beam at DESY, the SPS beam contains three sorts of particles: electrons, hadrons and muons in the energy range of 20 GeV to 80 GeV. Electrons will always produce a particle shower in the detector, whereas hadrons can either produce a shower or traverse the detector without showering. Non-showering hadrons and muons will be recognised as a straight line in EPICAL-2. Therefore, both non-showering hadrons and muons are here referred to as track events.

The beam profiles at DESY and SPS extend beyond the EPICAL-2 surface, so that particles can enter close to the edge of the detector surface. Particle showers will likely not be fully contained in the detector volume and are here referred to as leakage events.

In this section, first, the following event types are visualised via event displays and discussed separately, to highlight the different characteristics of the event types:

(1) 40 GeV electron event
(2) 5.8 GeV electron event
(3) leakage event
(4) pile-up event
(5) showering hadron event
(6) track event

Second, exemplary hit maps of individual EPICAL-2 layers are shown. Both single event hit maps and hit maps integrated over many events are presented. Third, the distribution of the raw number of pixel hits is discussed with an emphasis on the difference between DESY and SPS. Finally, conclusions are drawn in terms of corrections and selections necessary to apply to the raw data.

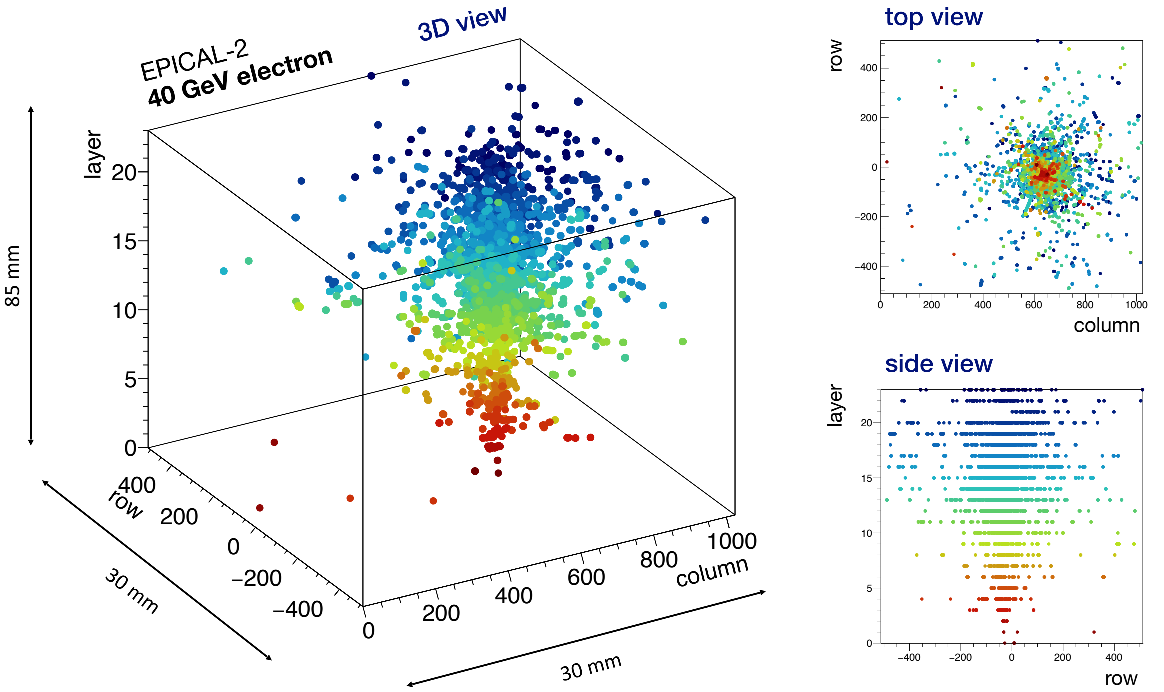

Figure 34: Left: *3D event display for an electron event at 40 GeV. Each coloured dot corresponds to a single pixel hit, while the color code represents the corresponding layer.* ***Right:*** *The projection of the 3D event display onto the row-layer axis as side view and the projection onto the column-row axis as top view.*

4.1.1 Event Displays

(1) **40 GeV electron event:**

Figure 34 shows an event display of a 40 GeV electron event from the SPS. The event display contains a 3D view (left) and both a view from the top and a view from the side (right). The event display visualises an electromagnetic shower evolution in EPICAL-2, starting with a single pixel hit as a dark red dot in layer 0. As the shower evolves, more and more secondary shower particles are produced leading to a higher number of pixel hits in the later layers of EPICAL-2. Here, the colour code corresponds to the EPICAL-2 layers. The shower broadens towards later layers as visible in the 3D view. However, at some point, the shower evolution ceases, the broadening stops and the number of pixel hits starts thinning out.

Although the shower is expanding in the transverse direction, most of the pixel hits are close to the actual shower axis which is especially visible in the top view. By eye, the majority of pixel hits is contained within the tungsten Molièr radius $R_{\mathrm{M}} = 9.327$ mm [Gro20], which corresponds to roughly 350 pixels (pixel size is $29.24 \times 26.88\,\mu\mathrm{m}^2$). The shower core is situated in an even smaller area of approximately 100×100 pixels.

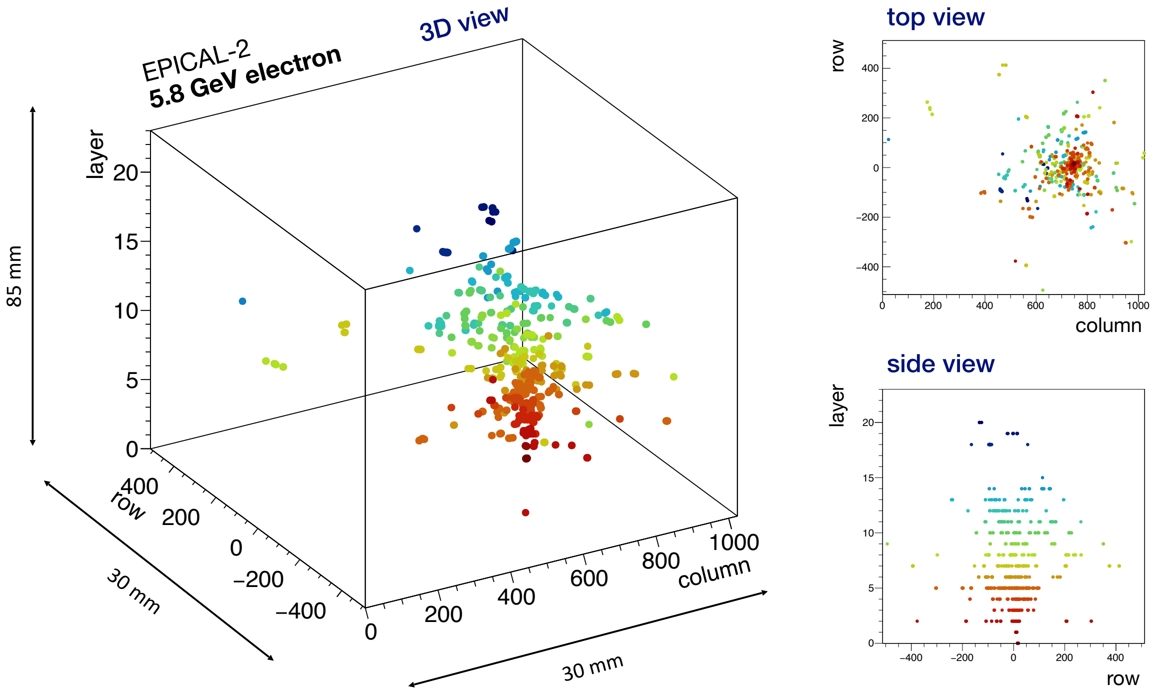

Figure 35: Left: *3D event display for an electron event at 5.8 GeV. Each coloured dot corresponds to a single pixel hit, while the colour code represents the corresponding layer.* ***Right:*** *The projection of the 3D event display onto the row-layer axis as side view and the projection onto the column-row axis as top view.*

Taking a close look at the event display, there are pixel hits which look like they are not really belonging to the electromagnetic shower: the pixel hit at (row, column, layer) $\approx$ (50, 50, 0) for example. These hits might be caused by a malfunctioning of the corresponding pixel producing a hit in the absence of a shower particle.

(2) 5.8 GeV electron event:

Figure 35 shows an event display of a 5.8 GeV electron event from DESY. The 5.8 GeV electron leads to a much lower number of pixel hits compared to the 40 GeV electron discussed before, basically as a consequence of the difference in energy. Despite the lower number of pixel hits, the main features are similar: A clear electromagnetic shower evolution can be observed with the majority of pixel hits being close to the actual shower axis. Some isolated pixel hits can be seen here as well. However, compared to the 40 GeV electromagnetic shower discussed before, the electromagnetic shower of the 5 GeV electron ceases in an earlier layer and thus extends less far into the depth of EPICAL-2.

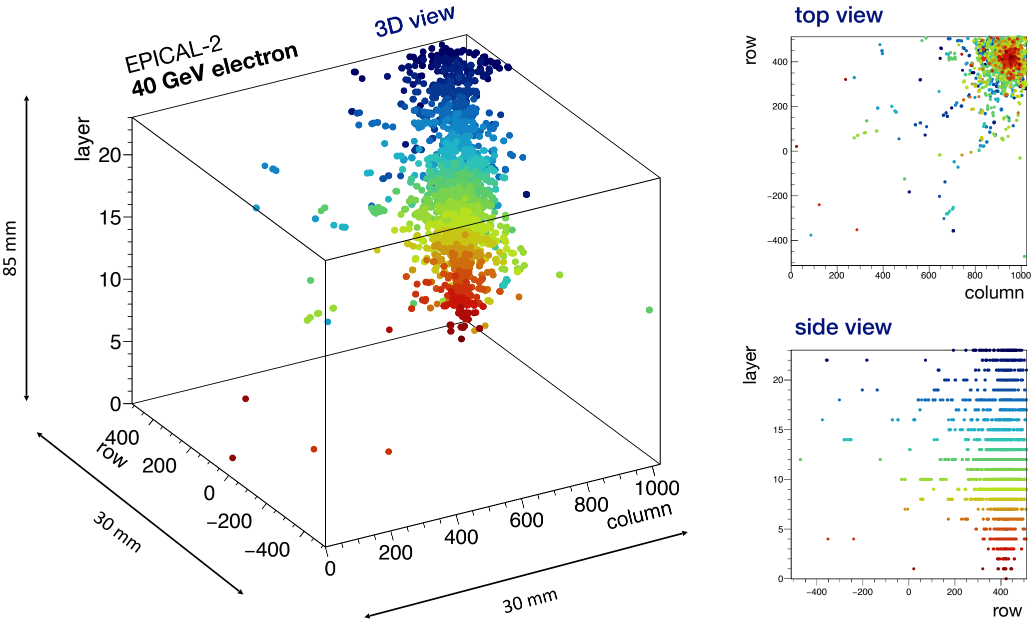

Figure 36: ***Left:*** *3D event display for an electron event at 40 GeV where the shower leaks out of the active volume. Each coloured dot corresponds to a single pixel hit, while the colour code represents the corresponding layer.* ***Right:*** *The projection of the 3D event display onto the row-layer axis as side view and the projection onto the column-row axis as top view.*

(3) Leakage event:

The event display in Figure 36 visualises a leakage event where a 40 GeV electron from the SPS enters EPICAL-2 near the back corner. In the side and top view in Figure 36 (right) one can clearly identify that the electromagnetic shower leaks out of the EPICAL-2 volume. In contrast to the electron events discussed before, here, the electron energy in not fully deposited in the EPICAL-2 volume as the particle shower is not fully contained in the volume. Therefore, the total number of hits is lower compared to a particle shower that is fully contained in the volume of EPICAL-2.

As in the event display of the 40 GeV electron event shown before (Figure 36), here, the same isolated pixel hits can be observed.

(4) Pile-up event:

In Figure 37 an event display of a pile-up event at 5.8 GeV from DESY is shown. In this event, two electrons enter EPICAL-2 at once and therefore two electromagnetic showers are produced. The high granularity of EPICAL-2 allows to discriminate the two particle showers by eye: In all the different views, 3D view on the left, and top and side view on the right, two particles entering EPICAL-2 can be distinguished. The two showers are well separated by approximately 350 pixel hits, i.e. roughly 10 mm.

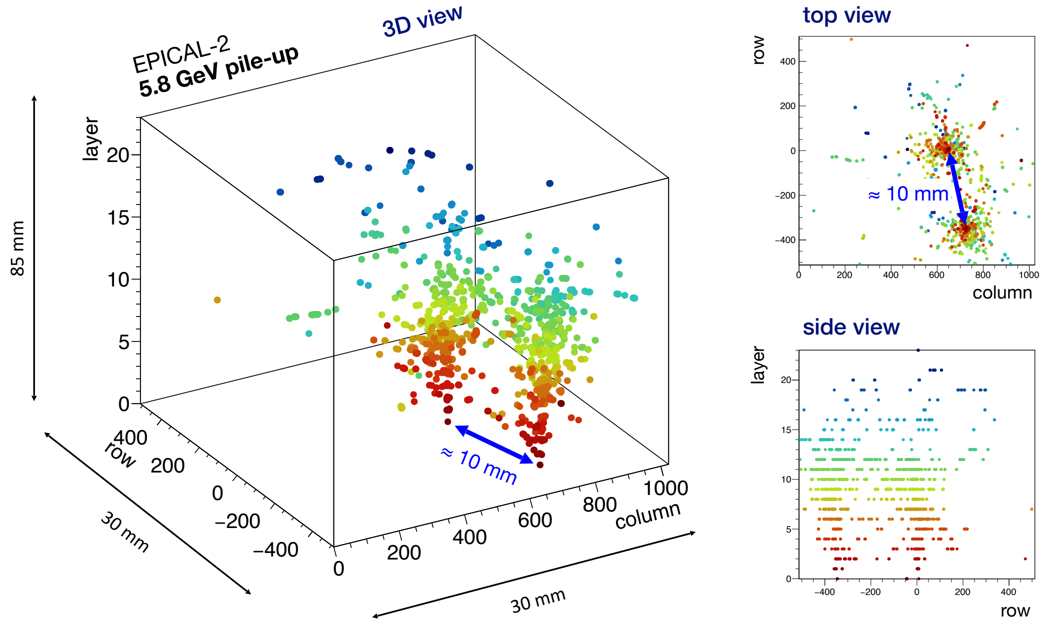

Figure 37:* *Left: *3D event display for a pile-up event at 5.8 GeV; here, two electrons are entering* EPICAL-2*. Each coloured dot corresponds to a single pixel hit, while the colour code represents the corresponding layer.* ***Right:*** *The projection of the 3D event display onto the row-layer axis as side view and the projection onto the column-row axis as top view.*

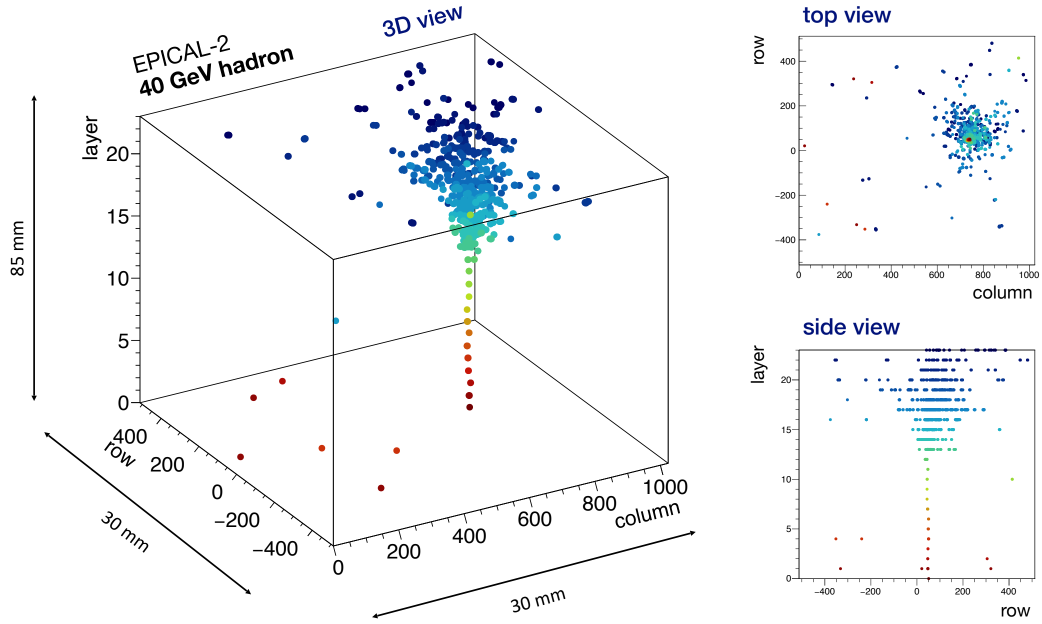

Figure 38:* *Left: *3D event display for a hadron event at 40 GeV. Each coloured dot corresponds to a single pixel hit, while the colour code represents the corresponding layer.* ***Right:*** *The projection of the 3D event display onto the row-layer axis as side view and the projection onto the column-row axis as top view, showing, that the hadron appears first as track and later as shower.*

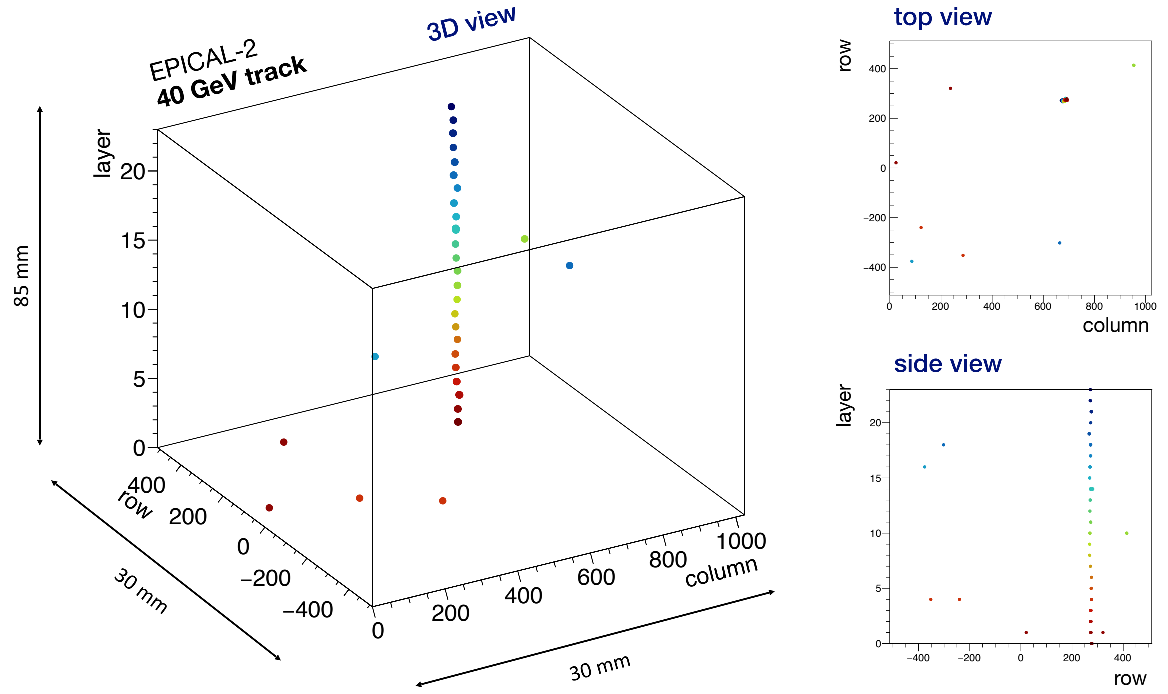

*Figure 39: **Left:** 3D event display of a track event at 40 GeV. **Right:** The projection of the 3D event display onto the row-layer axis as side view and the projection onto the column-row axis as top view. Each coloured dot corresponds to a single pixel hit, while the colour code represents the corresponding layer.*

(5) Showering hadron event:

Figure 38 shows an event display of a showering hadron event at 40 GeV from SPS. After traversing as a clear track, in the middle of EPICAL-2, in approximately layer 12, the hadronic shower evolves. As the shower evolves, more and more secondary shower particles are produced which leads to an increase in the number of pixel hits in the later layers of EPICAL-2 similar to the electromagnetic shower evolution discussed before. However, in contrast to the electromagnetic showers, which nearly all start in the first layer of EPICAL-2, hadrons entering EPICAL-2 are likely to produce an hadronic shower deep in the EPICAL-2 detector as shown here as an example. Given the fact that the depth of EPICAL-2 is less than one nuclear interaction length, hadron showers most likely start in the later layers if they occur at all.

The isolated pixel hits discussed in context of the previous event displays of the 40 GeV electron can be seen here again.

(6) Track event:

The event display in Figure 39 shows a track event at 40 GeV from SPS. One cannot identify the track as a non-showering hadron or a muon because both, non-showering

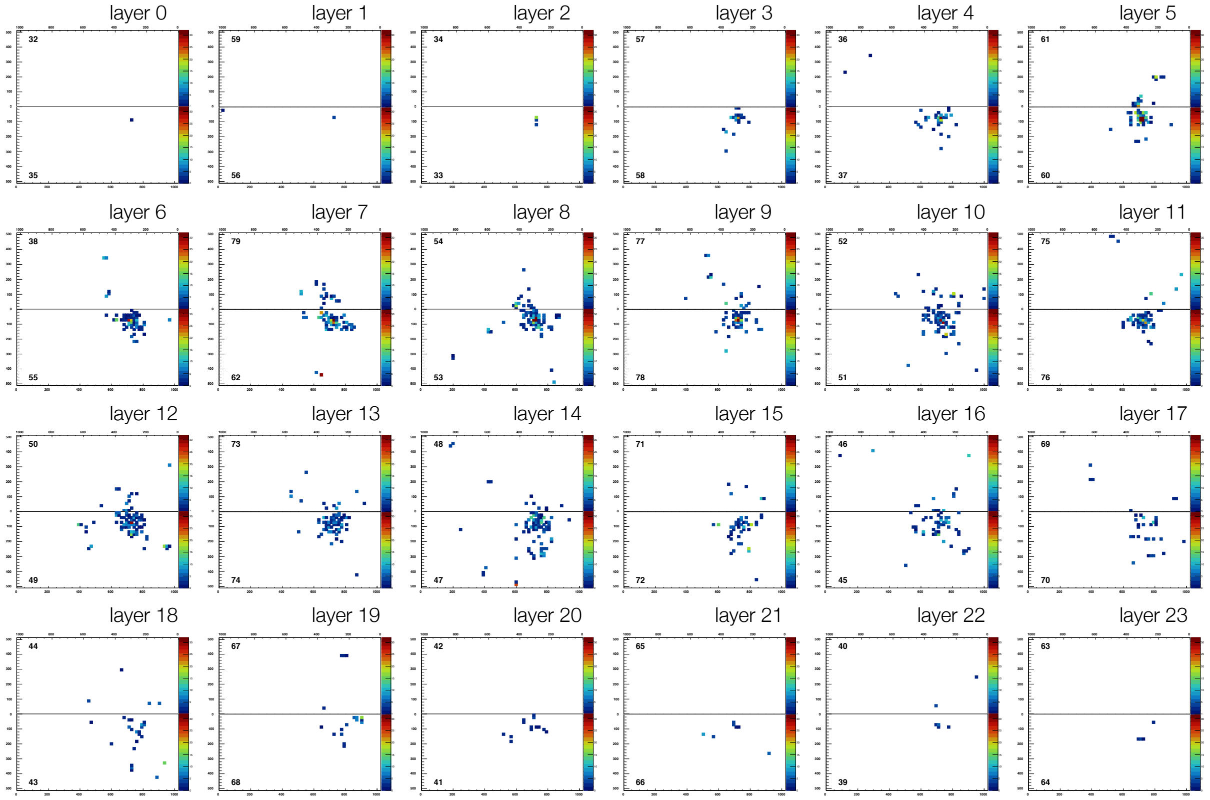

Figure 40: *Hit maps for every* EPICAL-2 *layer for an electron event at 20 GeV from the* SPS*. Each hit map is divided into two halves which correspond to the two chips per layer.*

hadrons and muons, interact via scattering and ionisation. The particle in the event displays clearly appears as a well defined track. However, in top view, the dots are not perfectly aligned on top of each other. Similar in the 3D and side view, the dots seem to fluctuate a little around a straight line because the sensors equipped in EPICAL-2 are not perfect aligned.

Like in the event displays presented before, here, the isolated pixel hits appear again which are clearly not associated with the straight track.

4.1.2 Hit Maps

After the discussion of several event displays, this section focusses on the discussion of hit maps, i.e. the number of pixel hits as a function of their spatial position for individual EPICAL-2 layers.

Figure 40 shows the hit maps for every layer of the EPICAL-2 for a single 20 GeV electron event at SPS. The hit map per layer is divided into two halves representing the two chips per layer. In each layer, the top half such as chip 32 in layer 0 corresponds to the right hand side (RHS), while the bottom half like chip 35 in layer 0 reflects the left hand side (LHS) of the EPICAL-2 stack, as discussed in section 2.4.

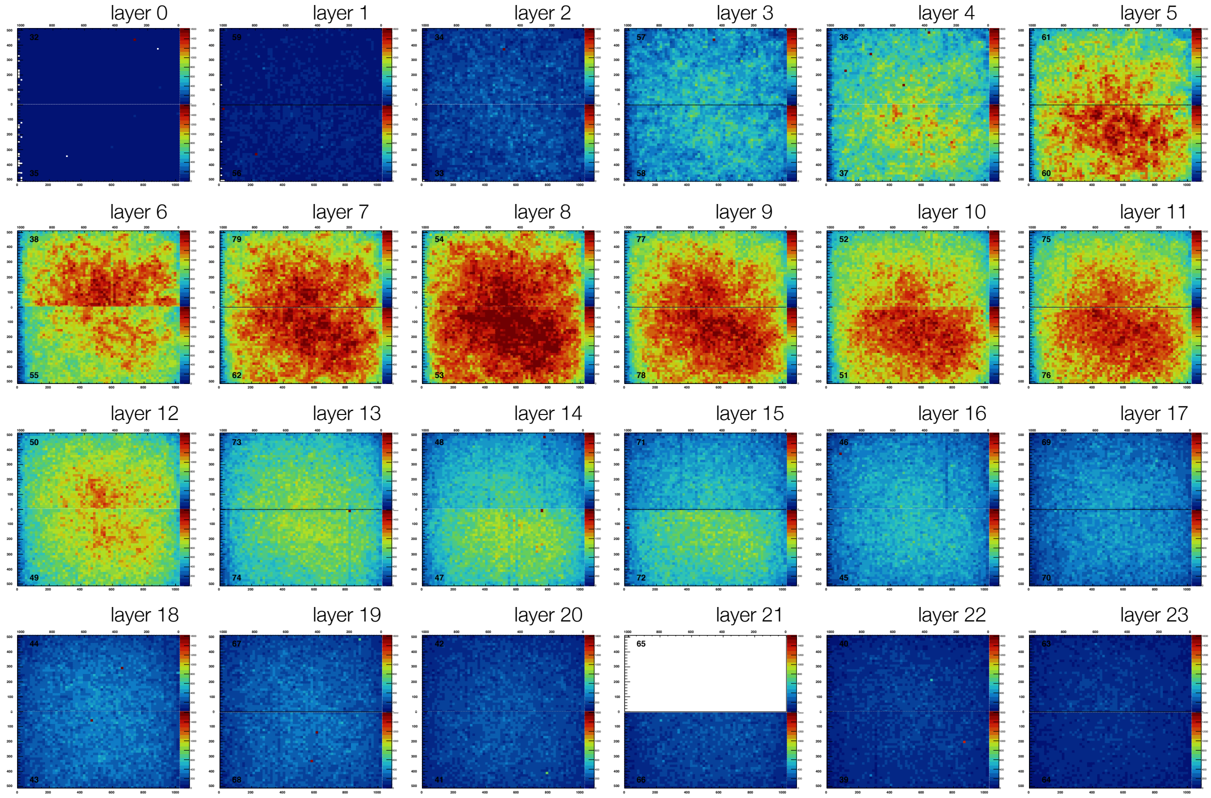

Figure 41: *Hit maps for every* EPICAL-2 *layer integrated over all 20 GeV events.*

Similar to the single event displays discussed in the previous section 4.1.1, Figure 40 visualises the shower evolution of a 20 GeV electron event in EPICAL-2. In Figure 40, an electron enters EPICAL-2 in layer 0 and the shower evolution starts. The shower evolution leads to a higher number of pixel hits in the later layers, which is visible by the rising number of counts in the hit maps of later layers in Figure 40. In between layer 7 to layer 10, the shower maximum is reached and after that, the number of shower particles and thus pixel hits decreases more and more the later the layer.

In contrast to the single event hit maps in Figure 40, Figure 41 shows the hit map for every layer of EPICAL-2 integrated over all 20 GeV events recorded at SPS. Figure 41 contains several striking features which are discussed below. First, the layer 0 hit map shows a uniform distribution. This means, that the entering point of beam particles is uniformly distributed across the 30 x 30 mm^2 EPICAL-2 surface. Second, the hit map of the chip 65 in layer 21 in Figure 41 is empty because this chip was malfunctioning during the data taking at SPS and DESY and therefore not used. Third, in all the layers besides the ones around the shower maximum, some high pixel hit density areas w.r.t. the average density can be observed. These are most likely malfunctioning pixels which produce hits in the absence of shower particles. Therefore, hits are recorded in every event which leads to an accumulation of those pixel hits in the integrated hit map. In addition, comparing different layers, e.g. layer

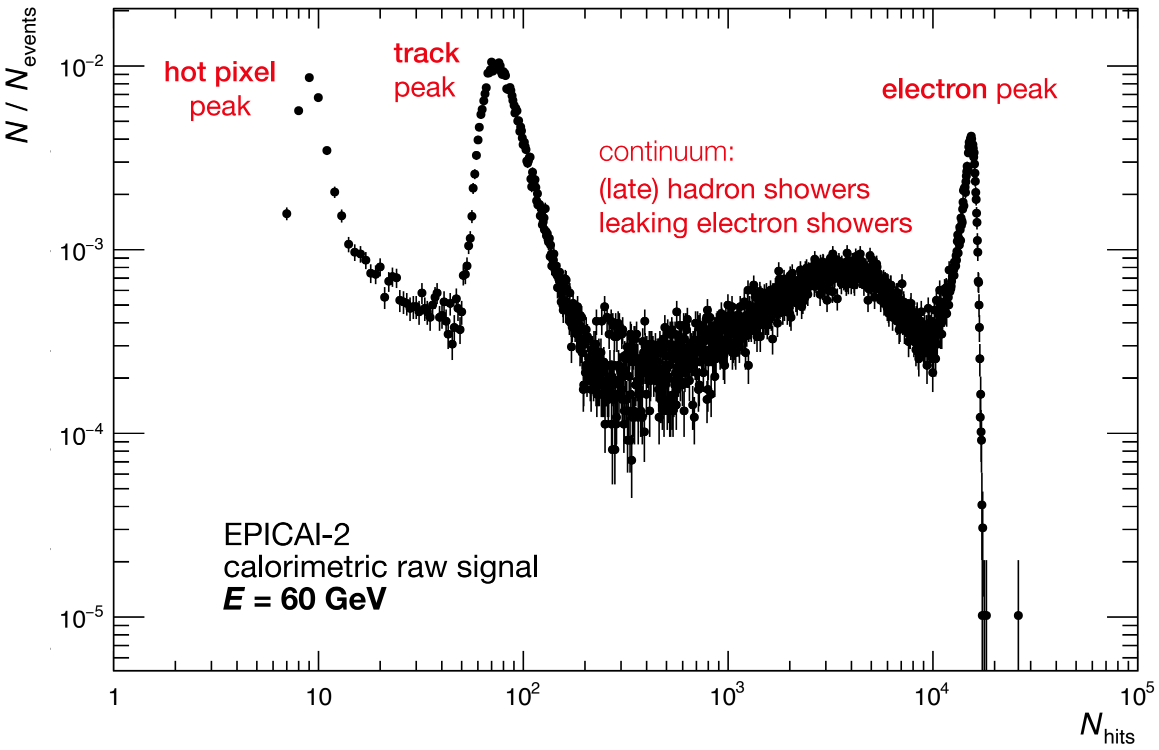

Figure 42: *A typical distribution of the total number N_{hits} of pixel hits at* SPS *exemplary for* 60 *GeV.*

5 with layer 6, the hit density is higher in the bottom half of the hit map in layer 5 (lane 60, chip ID 11), while the opposite holds true for layer 6 (lane 55, chip ID 13). Since the beam profile is uniform as discussed above, this illustrates the different sensitivity of the chips.

4.1.3 Raw Number of Pixel Hits

One of the key and most basic EPICAL-2 observables, the total number N_{hits} of pixel hits, represents the energy of the primary particle entering EPICAL-2 as discussed in context of Figure 10 in section 2.2. For an electromagnetic shower, N_{hits} provides a measure of the number of charged particles produced in the electromagnetic shower.

Figure 42 shows the raw N_{hits}-distribution for all events at 60 GeV from the SPS. All the event types discussed in section 4.1.1 contribute to the raw N_{hits}-distribution and the different event types have a different response in EPICAL-2 in terms of N_{hits}.

The peak at $N_{\mathrm{hits}} \approx 10$ emerges from malfunctioning pixels. This pixel peak reveals the low noise level of the ALPIDE chips equipped in EPICAL-2 and shows that malfunctioning pixels can be identified.

Next to the pixel peak from malfunctioning pixels, the peak at $N_{\mathrm{hits}} \approx 80$ evolves from track events like single hadrons or muons traversing EPICAL-2. Assuming 100 % efficient and identical chips so that a track induces the same response in all layers, the

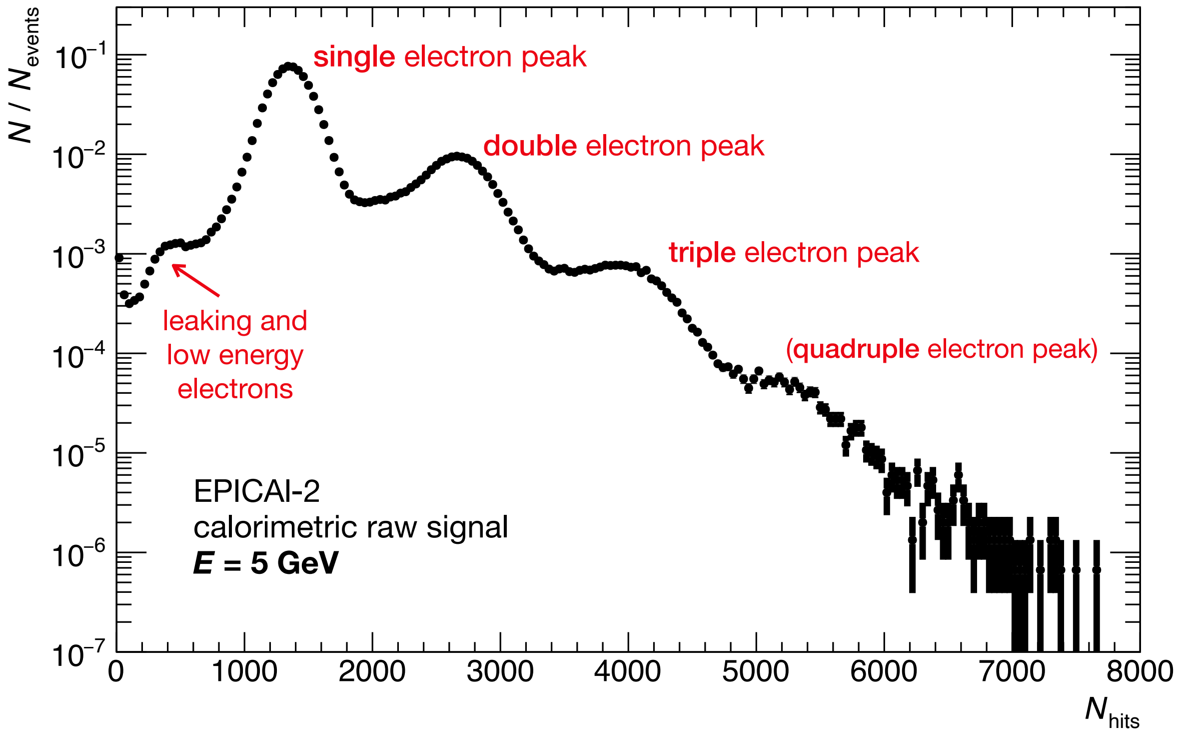

Figure 43: *A typical distribution of the total number N_{hits} of pixel hits at* DESY *exemplary for* 5 *GeV.*

value of $N_{\text{hits}} \approx 80$ corresponds to a mean number of pixel hits per layer between 3 and 4.

In the distribution at $N_{\text{hits}} \approx 16\,\text{k}$, the electron peak of electromagnetic showers fully contained in EPICAL-2 is visible. An 60 GeV electromagnetic shower produces thousands of charged particles yielding to this high number of pixel hits. Here, basically no events are recorded with a higher number of hits than those of single electromagnetic showers, i.e. multiple-electron events are not observed.

Both leaking electromagnetic showers and (late) hadron showers produce a lower number of N_{hits} which leads to entries in the N_{hits}-distribution between the electron peak and the track peak, referred to as the continuum in Figure 42.

Figure 43 shows the raw N_{hits}-distribution for events at 5 GeV from DESY. The peak at $N_{\text{hits}} \approx 1400$ emerges from single electrons entering EPICAL-2, which is referred to as the single electron peak in Figure 43. The multiple peak structure occurs due to pile-up, when multiple electrons enter EPICAL-2 at once. For instance, three electrons triple the number of pixel hits from a single electron entering EPICAL-2 to $N_{\text{hits}} \approx 4200$. In Figure 43, the peaks are referred to as the single, double, triple and quadruple peak depending one how many electrons enter EPICAL-2 at once. Similar to the continuum discussed in context of Figure 42, the left flank of the single electron peak in Figure 43 emerges from leaking electron showers and lower energy electrons.

4.1.4 Implications for Analyses

The raw data acquired with the EPICAL-2 prototype during the test-beam measurements at DESY and at SPS were presented in terms of event displays, hit maps and the distribution of the total number of hits. For this work, to determine both the shape and the energy measurement performance of electromagnetic showers with EPICAL-2, several corrections and selections need to be applied to the raw data. Below, the corrections and selections are introduced which are discussed in detail in the next section.

(1) **Pixel masking:**
In the event displays, several isolated pixel hits appear which might be caused by a malfunctioning of the corresponding pixel so that a hit is generated in the absence of a shower particle. Since the same isolated pixel hits appear in different event displays, it is likely that the pixels are malfunctioning. In addition, the integrated hit map shows some high and low pixel hit density areas w.r.t. the average density which is also likely a result of malfunctioning pixels. In the analysis, malfunctioning pixels are removed via a pixel mask.

(2) **Clustering:**
As discussed in section 2.1.1, a charged shower particle in an electromagnetic shower likely produces a group of adjacent pixel hits which is referred to as a cluster. In the analysis, a clustering algorithm is used to construct clusters of the pixel hits.

(3) **Track selection:**
Muons and non-showering hadrons traverse EPICAL-2 as straight line and they interact similarly in every chip (see the track event in Figure 39). A selection of track events is performed in the analysis because track events are ideal candidates for the corrections (4), (5) and (6).

(4) **Chip alignment:**
Although the chips are carefully assembled in the EPICAL-2 prototype, from the track event display it appears that the hits fluctuate around a straight line (see Figure 39). Therefore, a chip alignment is performed to align the 48 chips in the EPICAL-2 stack.

(5) **Chip calibration:**
Several integrated hit maps of individual layers show a different average hit density for the two chips in the layer (see Figure 41). Since the beam profile is uniform, this illustrates a different sensitivity of the chips as a result of the different chip thresholds. Therefore, a chip calibration is applied to equalise this difference in chip sensitivities. The chip calibration is especially necessary for the determination of observables which evolve from the pixel hit information of all chips such as the total number of pixel hits or clusters.

(6) **Inclination correction:**
EPICAL-2 was carefully aligned along the axis of the test-beams. However, a residual inclination angle between the test-beam and EPICAL-2 is left. In the analysis, this is taken into account via an inclination correction.

(7) **DESY event selection and (8) SPS event selection:**
After applying all the corrections mentioned before, to determine both the shape and the energy measurement performance of electromagnetic showers with EPICAL-2, only single electron events, where the shower is fully contained in the EPICAL-2 volume, should be considered. If the shower is not fully contained, only part of the total energy is measured and the performance is distorted. If multiple electrons enter the EPICAL-2, too much energy is measured compared to a single electron. For example, the total number of pixel hits approximately doubles when two electrons with the same energy are measured at once compared to a single electron. Similarly, hadrons showers distort the performance. The distributions of the total number of hits at DESY and at SPS show that the event selection needs to satisfy different requirements: In the DESY data especially pile-up events need to be excluded. In the SPS data, it is particularly important to remove hadron and muon events. Overall, the event selection for the DESY and the SPS data is designed to select single electron events, where the electromagnetic shower is fully contained in EPICAL-2.

In summary, the raw event displays show the characteristics of the different event types in EPICAL-2 and especially the need to remove malfunctioning pixels from analyses, to align the 48 chips in EPICAL-2 and to apply an inclination correction. The integrated hit maps illustrate the different chip sensitivities which must be equalised via a chip calibration. Furthermore, the different event types can be identified in the raw N_{hits}-distributions at DESY and at SPS. For the estimate of the energy measurement performance with EPICAL-2 and the description of electromagnetic showers, only fully contained single electromagnetic showers are of interest and all the other event types distort the performance and shape description. Therefore, single electron showers must be selected in the raw data. Both the corrections and the event selections are elaborated in the next section.

4.2 Data Preparation

As introduced in the previous section, the preparation of the data is described and discussed in the following order in this section:

(1) Pixel masking
(2) Clustering
(3) Track selection
(4) Chip alignment
(5) Chip calibration
(6) Inclination correction
(7) DESY event selection
(8) SPS event selection

4.2.1 Pixel Masking

The majority of the $\sim$ 25 million pixels in EPICAL-2 operate without any symptoms of failure. However, a small fraction of pixels appear to behave differently compared to the bulk of pixels. These pixels are regarded as malfunctioning pixels, which are classified either as "dead" or as "noisy". Dead pixels show no response at all to both injected test signals and particles traversing the pixel. Noisy pixels on the other hand do respond, but much more frequently than the majority of pixels.

In this thesis, a pixel mask for every EPICAL-2 chip containing dead and noisy pixels is used to exclude malfunctioning pixels from any further analysis. A diligent EPICAL-2 pixel mask has been obtained in [Pli22] and is adopted here. Therefore, the analysis methodology used in [Pli22] to identify malfunctioning pixels is described below which can be subdivided into four complementary procedures: chip classification, out-of beam measurements, beam measurements and fiducial selection.

The ALICE-ITS Collaboration has developed a series of functionality tests to classify ALPIDE chips in context of the so-called ALPIDE mass testing for the ALICE-ITS upgrade [ALI+14]. In each test, chips are classified either gold, silver or bronze. The classification corresponds to the goodness of a chip depending on the amount of dead and noisy pixels.

Speaking of noisy and dead pixels, the functionality test procedure is based on the so-called analogue scan, an internal testing function of the ALPIDE, where test signals are injected into the front-end circuits. This chip procedure involves the following three parts: First, the unmasking of all pixels. Second, a test signal injection way above the threshold in each pixel of a single row. Third, accessing the pixel hit information of all pixels in the chip, i.e. both pixels in the single row with the injected test signal and all others without a test signal, which should not have registered a hit in the absence of a test signal. These three steps are repeated for all rows in a chip. Dead pixels do not register a hit in the presence of an injected test signal. On the other hand, noisy pixels register a hit in the absence of an injected test signal. The three chip categories, gold,

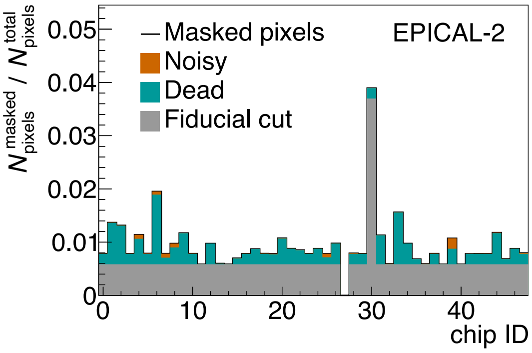

Figure 44: *Fraction of masked pixels of different origin [Alm+23].*

silver and bronze are defined according to the number $N^{\mathrm{mal}}_{\mathrm{pixels}}$ of malfunctioning pixels which are either noisy or dead:

category	$N^{\mathrm{mal}}_{\mathrm{pixels}}$
gold	< 50
silver	< 2100
bronze	< 5243

Taking only noisy pixels into account, 39 EPICAL-2 chips are categorised as gold, 8 as silver and none as bronze. In contrast, 13 EPICAL-2 chips are categorised as gold, 26 as silver and 8 as bronze when taking only dead pixels into account. Therefore, there are less noisy than dead pixels in EPICAL-2. The ALICE-ITS analogue scan applied to the ALPIDE chips deployed in the EPICAL-2 prototype results in the following number of dead and noisy pixels:

$$\begin{aligned} 45622 \text{ dead pixels} &\approx 0.19\,\% \text{ of all pixels} \\ 3448 \text{ noisy pixels} &\approx 0.014\,\% \text{ of all pixels} \end{aligned}$$

Out-of beam measurements have been performed in the absence of any beam particles in between the test-beam measurements. When no beam particle enters EPICAL-2, every pixel hit recorded originates from noise. If a pixel registers a hit significantly more often than the bulk of pixels, i.e. a hit in more than every thousandth event, this pixel is masked as noisy. This out-of beam measurement procedure leads to 128 noisy pixels, which corresponds to $\sim 0.0005\,\%$ of all pixels. To verify the procedure, the time dependence has been studied in context of [Alm+23] showing a constant number of identified noisy pixels over time. In addition, the same pixels are identified as noisy in various out-of beam measurements showing that those are really noisy pixels and not just random pixels.

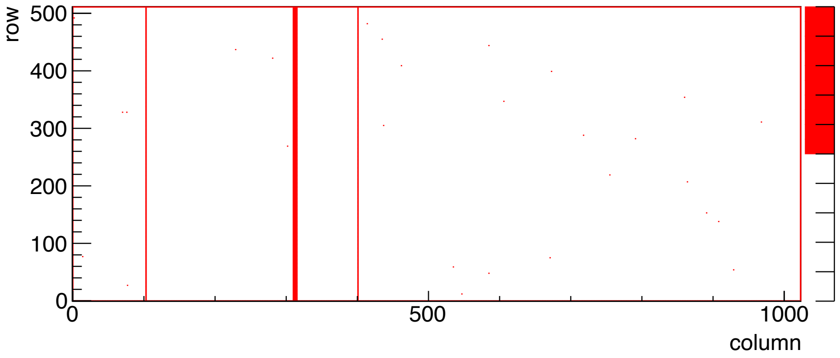

Figure 45: *Pixel mask of the LHS chip in layer 22.*

In addition to the out-of beam measurement, malfunctioning pixels are identified by in-beam measurements. If the pixel hit rate is significantly higher or lower compared to its neighbours in a 32 x 32 pixel matrix averaged over many events, a pixel is considered malfunctioning. Furthermore, whole columns and double-columns with a significantly lower number of pixel hits compared to neighbouring columns are considered malfunctioning.

On top of the chip classification, out-of beam and in-beam measurements, a fiducial edge cut masks pixels in the outermost columns and rows at the chip edge, because these pixels register systematically less hits w.r.t. to rest of all pixels as the ALPIDE pixel matrix is surrounded by the guard ring reducing the number of hits (see section 2.1.1). In chip 30, a faulty region not working properly is also masked by a fiducial cut.

In summary, Figure 44 shows the ratio of pixel hits which are masked as either noisy or dead or have been excluded via the fiducial cut to the total number of pixels. The pixel masking analysis leads to a total of only $\sim$0.95 % of all pixels being masked. Included in the $\sim$0.95 % of all pixels, 0.65 % are masked by the fiducial cut. Figure 44 also demonstrates the overall low number of masked noisy pixels and the nearly uniform performance of the chips. Overall, the noise per pixel and per event is $\sim 4 \cdot 10^{-7}$ without any pixel masking and of the order of 10^{-10} with pixel masking.

To visualise a pixel mask, Figure 45 shows the pixel mask of the LHS chip in layer 22 as an example. Figure 45 shows the masked pixels derived from the complementary analysis methods described before. Single masked pixels can be identified across the whole chip as single red dots. Masked single and double-columns are visible as red vertical lines. In addition, the fiducial edge cut can be seen as a red rectangle at the edges of the pixel matrix. The pixel masks for all 48 EPICAL-2 chips can be found in subsection A.1. Chip 27 in layer 20 is completely masked because this chip suffered from continuous read-out errors during test-beam data taking and was disabled during the DESY and the SPS test-beam measurements as already discussed in context of the hit maps in section 4.1.2.

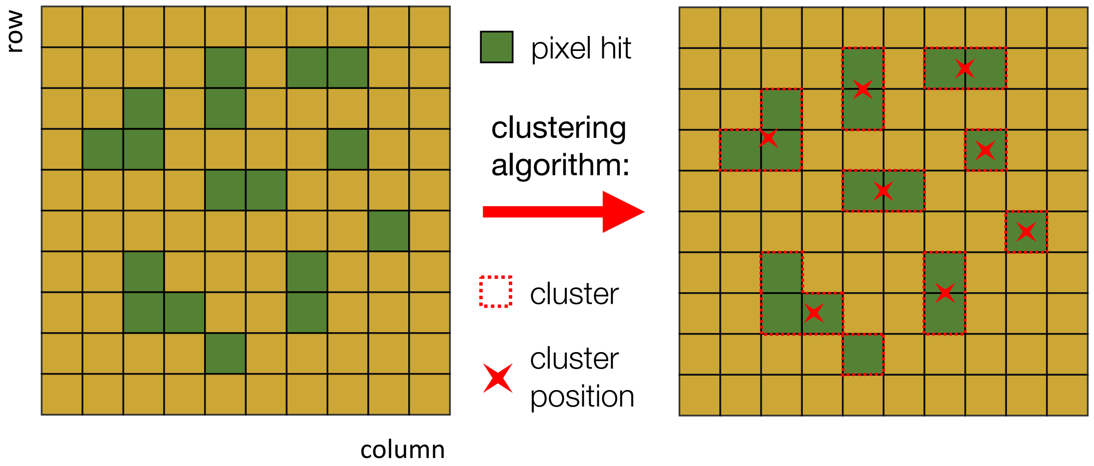

Figure 46: Clustering algorithm used to group adjacent pixel hits to a cluster.

4.2.2 Clustering

As discussed in section 2.2 and 3.2.4, a charged particle in an electromagnetic shower likely produces a cluster, a group of adjacent pixel hits as a result of geometrical effects and charge sharing. The number of adjacent pixel hits produced by a shower particle fluctuates and is strongly dependent on the chip characteristics as discussed in section 2.1.2. Therefore, besides using pixel hits as an EPICAL-2 observable, also clusters are investigated as an observable since they are considered to provide a more robust and uniform measure of the number of charged shower particles than just counting the pixel hits. In the analysis, a clustering algorithm based on geometrical patterns derived from the so-called DBSCAN algorithm [Est+96] is used to group adjacent pixel hits to a cluster. Figure 46 illustrates the working principle of the clustering algorithm as used for EPICAL-2. Figure 46 (left) shows an exemplary pixel matrix with adjacent pixel hits showing different geometrical patterns. The clustering algorithm combines adjacent pixel hits to one cluster. Adjacent pixels of a single pixel cell are all 8 pixels around this single pixel. A free-standing hit is a cluster. Figure 46 (right) shows the clusters derived from applying the clustering algorithm to the pixel hits shown in Figure 46 (left). On top of the clustering, for each cluster, the cluster position is calculated as the centre of gravity of contributing pixel hits.

In the following, the outcome of the clustering is presented in terms of (1) the distribution of the cluster size and (2) the average cluster size per layer.

(1) Cluster Size Distribution

Figure 47 shows the cluster size distribution integrated over all EPICAL-2 layers for electron events at 5 GeV (left) and at 60 GeV (right). The measured data is shown as

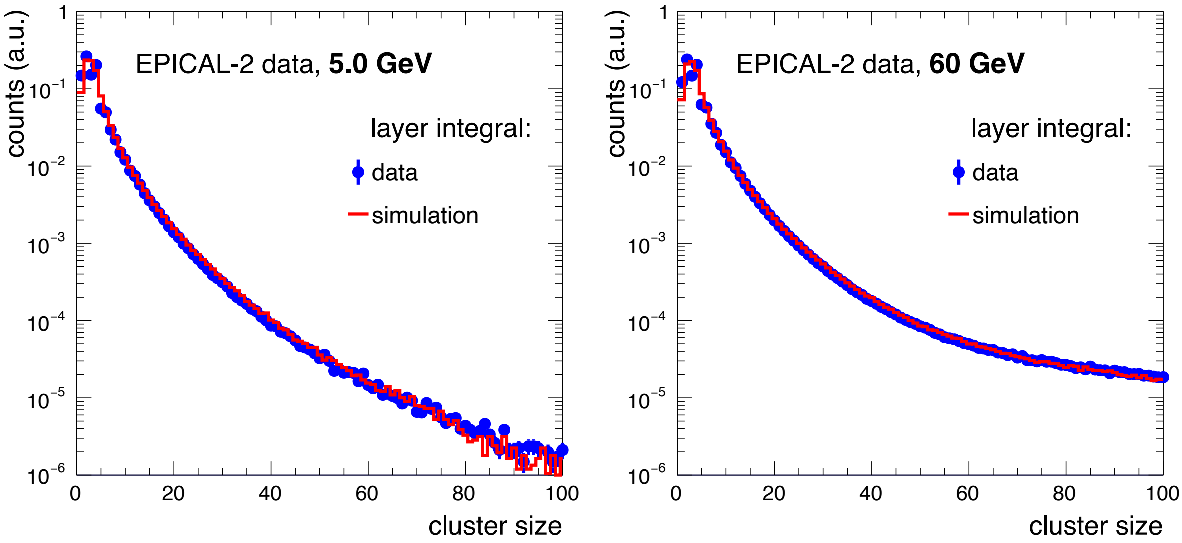

Figure 47: *Cluster size distribution integrated over all* EPICAL-2 *layers for electron events at 5 GeV (left) and at 60 GeV (right) for measured data and simulation.*

blue dots. In general, the shape of the distributions at 5 GeV and 60 GeV are similar. However at 60 GeV, the probability for large clusters is greater than at 5 GeV. The cluster size distributions are shown up to very large clusters with a size of 100 pixels. For instance at 5 GeV, approximately 72 % of all clusters have a size smaller than 4 pixels. In addition to the measured data, Figure 47 shows the simulation prediction for the cluster size distribution as a red line. The simulation can model both the cluster size distribution at 5 GeV and at 60 GeV over several orders of magnitude including the very large clusters.

It is particular noteworthy, that the simulation not only predicts these very large clusters but also their shape. This can be seen in Figure 48 which shows an event display of a single electron event at 5 GeV in the measured data (left) and in the simulation (right) for an exemplary chip as a function of the pixel x and y position. The positions are given in both pixel units and millimetres. The cluster shape is not "round" as one might expect but the clusters rather appear as track-like. As can be seen in Figure 48, very large clusters appear as track-like which expand over several hundred pixels and thus millimetres inside the chip. Further illustration of these large clusters can be found in [Sol20] and the details of the shape of clusters is discussed in [Sch23]. As discussed in section 3.2.3, in the electromagnetic shower, a large fraction of electrons traversing perpendicular to the chip surface exist. The shallower the electron angle w.r.t. the epitaxial layer surface, the larger the distance a charged shower particle traverses inside the epitaxial layer. Therefore, electrons propagating within the epitaxial layers lead to the large, track-like clusters as exemplary shown in Figure 48.

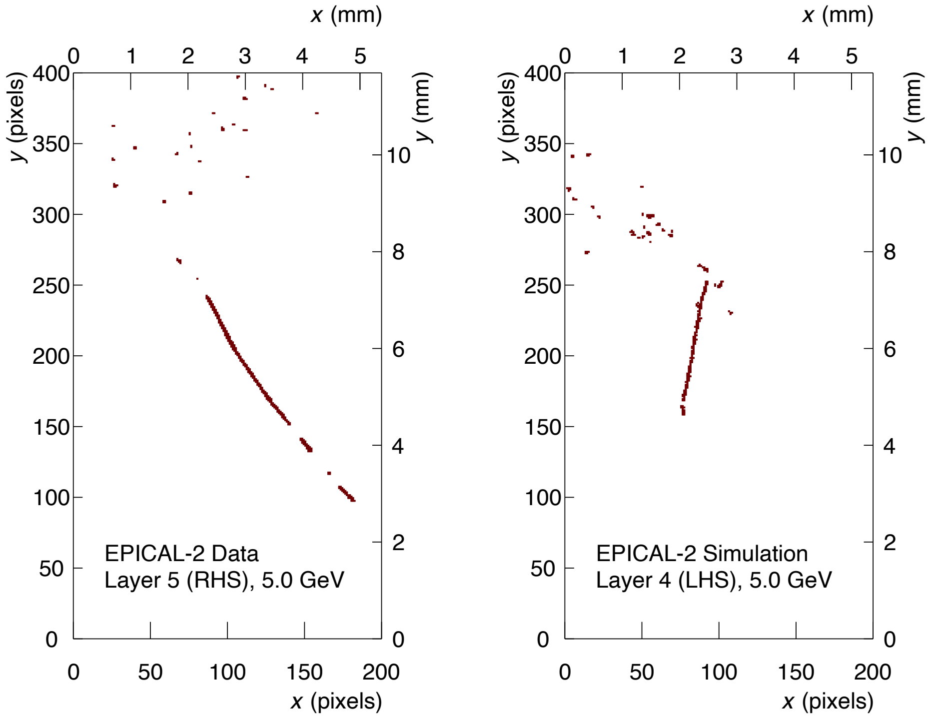

Figure 48: *Event display of an exemplary chip as function of chip x and y position in pixels and millimetres visualising a very long, track-like cluster for both data (left) and simulation (right) [Alm+23].*

(2) Mean Cluster Size

As discussed in context of Figure 47, at higher energies the probability for larger clusters is greater than at lower energies. Figure 49 (left) displays the average cluster size $\langle$cluster size$\rangle$ as a function of the layer number for LHS chips for electron events at 5 GeV and 60 GeV in the measured data. For each chip, $\langle$cluster size$\rangle$ is derived from the cluster size distribution similar to Figure 47. The average cluster size fluctuates around $\langle$cluster size$\rangle \approx 4$ for 5 GeV. In contrast to 5 GeV, at 60 GeV, $\langle$cluster size$\rangle$ is significantly higher between layer 2 and layer 14. The higher the energy the higher the density of shower particles, i.e. more shower particles per unit area traverse a chip. When the shower particle density is higher, the cluster size increases. As the particle density is highest before the shower maximum is reached, for 60 GeV, $\langle$cluster size$\rangle$ peaks around layer 5, right before the shower maximum in approximately layer 7.

To investigate the fluctuations of $\langle$cluster size$\rangle$ as a function of the layer number in the measured data as shown in Figure 49 (left), two simulation scenarios are considered: Scenario one is the default simulation setup as discussed in section 3.2.5, where for each chip the same chip threshold of 82 e is applied. In contrast to that, individual chip thresholds according to Figure 9, i.e. the EPICAL-2 chip thresholds in reality, are applied in the simulation scenario two. Figure 49 (right) shows $\langle$cluster size$\rangle$ as a function of the layer number for electron events at 5 GeV for the

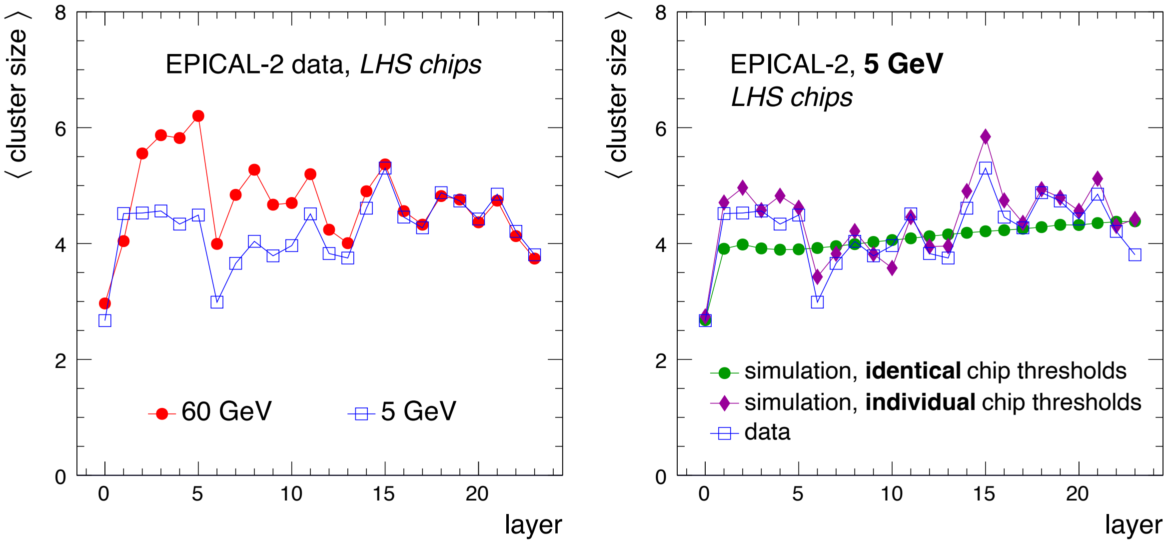

Figure 49: *Average cluster size as a function of layer for LHS chips. High (60 GeV) and low energy (5 GeV) are compared in data (left) and at 5 GeV, data is compared to two simulation scenarios (right), one with the same threshold for all* EPICAL-2 *chips and one with individual chip thresholds according to Figure 9.*

two simulation scenarios in addition to the measured data. The identical chip threshold scenario is shown as full green circles and the individual chip threshold scenario as full purple diamonds. While $\langle\text{cluster size}\rangle$ is nearly constant around $\langle\text{cluster size}\rangle \approx 4$ as a function the layer number for the identical chip thresholds, $\langle\text{cluster size}\rangle$ for the individual chip thresholds fluctuates similar to the measured data. Therefore, the fluctuations of the average cluster size in the measured data are attributed to the different chip thresholds in EPICAL-2 which lead to a non-uniform chip response across chips.

4.2.3 Track Selection

Since the overall EPICAL-2 response results from an interplay of the 48 contributing chips, each chip should behave similar and the chip positions within the EPICAL-2 stack have to be known with high precision. Unfortunately, the chip behaviour is influenced by several operating conditions and thus not uniform across all chips as shown in the previous section. Furthermore, the chip positions are not precisely defined as a result of the mechanical construction tolerance. To achieve a similar chip behaviour and a precise chip positioning, data-driven calibrations and alignments are used in this thesis. Both the calibration to equalise the chip response and the alignment correction to align the chips within the EPICAL-2 stack are based on the analysis of track events (see Figure 39). Tracks serve as ideal candidates for both corrections as they traverse EPICAL-2 as straight line, which is used to align the chips

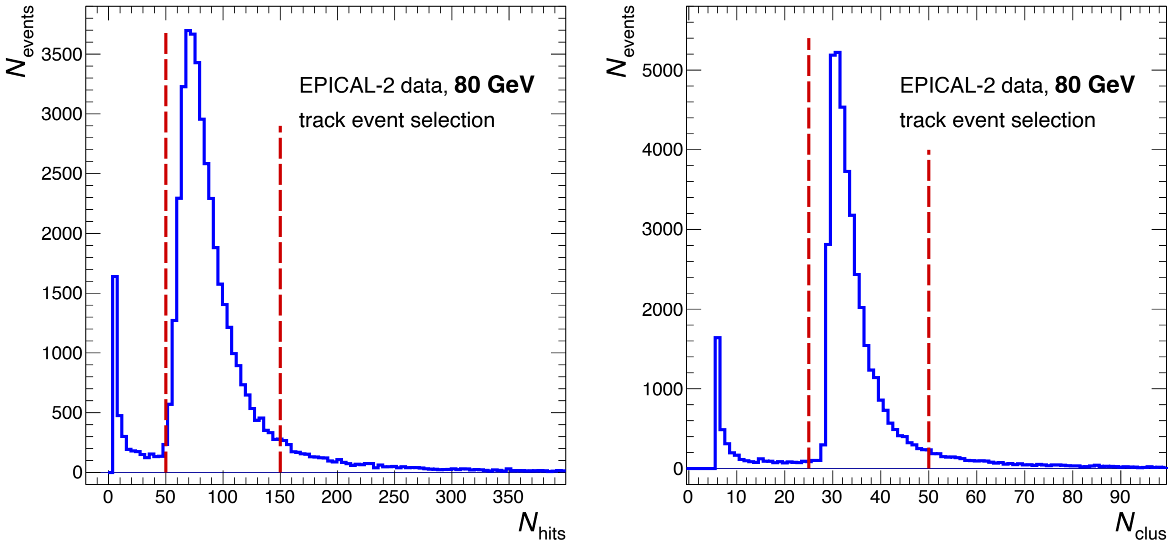

Figure 50: *Distribution of the total number of hits (left) and clusters (right) at 80 GeV. The dashed red lines visualise the track selection interval defined by Equation 22 and Equation 23.*

accordingly, and they interact similarly in every chip, which is the basis to equalise the chip responses. Before the details of the calibration and the alignment procedure are discussed, the selection of tracks as used in this thesis is presented first. The track selection procedure is adopted from [Alm+23], where the procedure is applied to cosmic muon data, whereas here the procedure is applied to the SPS data.

In general, track events are selected on the basis of the total number N_{hits} of hits and the total number N_{clus} of clusters, which satisfy the following criteria:

$$50 \leq \; N_{\text{hits}} \; \leq 150 \tag{22}$$

$$25 \leq \; N_{\text{clus}} \; \leq \; 50 \tag{23}$$

Figure 50 shows the N_{hits} - (left) and N_{clus} -distribution (right) for 80 GeV together with the corresponding track selection intervals indicated as the dashed red lines resulting from satisfying Equation 22 and Equation 23. The peaks at $N_{\text{hits}} \sim 70$ in the N_{hits} -distribution and at $N_{\text{clus}} \sim 30$ in the N_{clus} -distribution correspond to track events, both showing an asymmetric shape with a tail to the right hand side. The asymmetric shape emerges from the Landau-distribution describing the energy deposition in silicon [GZ+20], which is directly linked to the N_{hits} - and N_{clus} -response. In addition, in both distributions a narrow peak at a value of ~ 7 appears due to malfunctioning pixels which result in single-hit clusters. Both, the N_{hits} - and N_{clus} - distribution shown in Figure 50 look similar for all SPS energies and also for cosmic muons.

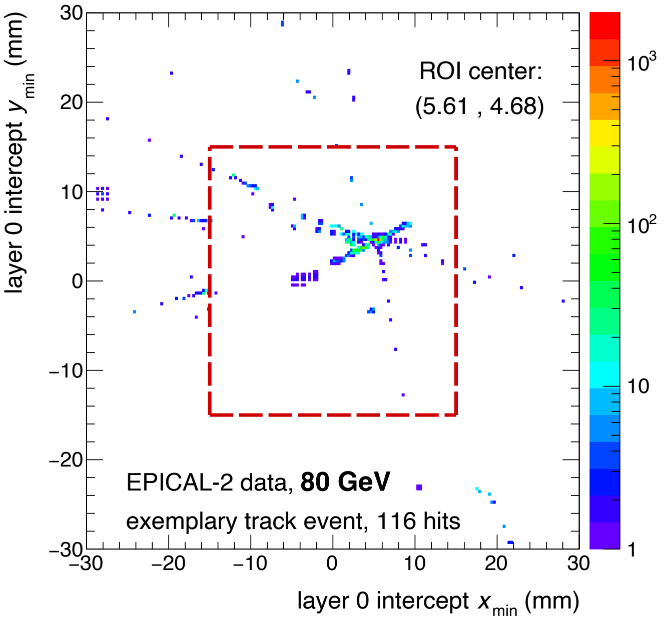

Figure 51: *Abundance distribution of layer 0 intercepts as a function of x_{min} and y_{min}. The intercepts are calculated from the track candidates and the red rectangle illustrates the active region of* EPICAL-2*.*

Since the alignment and the calibration procedure is based on distinct tracks and their parametrisation with a 3D straight line, the following procedure is applied on top of the selection based on N_{hits} and N_{clus} :

First, all possible combinations of two clusters from different layers are formed. A cluster pair is referred to as a "track candidate" because two clusters from different layers already define a straight line by demanding the line to go trough both cluster positions.

Second, the intercepts with the first layer 0 (x_{min}, y_{min}) and the last layer 23 (x_{max}, y_{max}) are calculated for each track candidate, to determine which track candidates are suitable to represent the true particle track. The result of the calculation of the intercepts with layer 0 is shown in Figure 51 for an exemplary event. The distribution for the intercept positions with layer 23 look similar. The red rectangle illustrates the active region of EPICAL-2 , i.e. $|x_{\text{min,max}}| < 15$ mm or $|y_{\text{min,max}}| < 15$ mm. All track candidates with their intercepts lying outside of this region are discarded for further analysis to ensure that only those track candidates fully contained in EPICAL-2 are taken into account. Inside of the active region, in both layer 0 and in layer 23 a so-called region of interest (ROI) is defined as the densest $0.5 \times 0.5\,\text{mm}^2$ region in the intercept parameter space. For example, the centre of the layer 0 ROI in Figure 51 is situated at $x_{\text{min}} \sim 5.61$ and $y_{\text{min}} \sim 4.68$. All track candidates with their intercepts not crossing one of the two ROIs are sorted out. For events where only a few layers contain clusters, the total number of track candidates

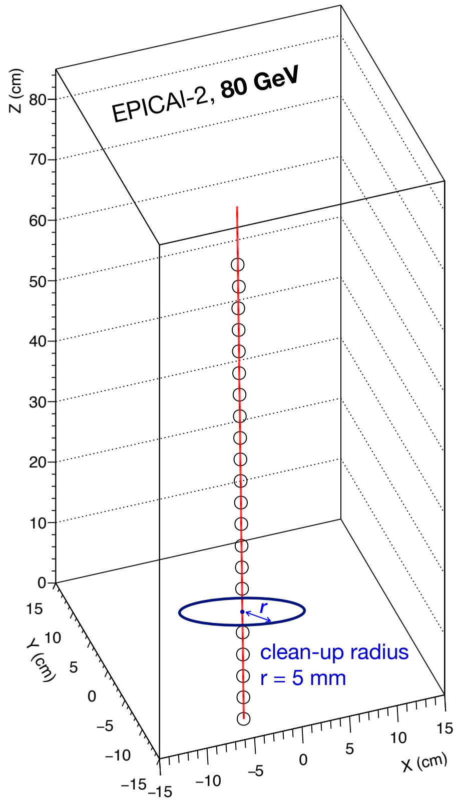

Figure 52: *3D spatial position of the clusters from a track event cleaned up by the procedure described in the text. The result of a 3D straight line parametrisation is shown in red and the clean-up radius outside clusters are excluded is illustrated.*

will be small and the track will not be well constraint. Therefore, only those events with more than 200 track candidates within the ROIs are used for further track analyses.

In a third step, a so-called seed track is determined as the most probable track candidate as follows: For each remaining track candidate the number of neighbours is calculated. Therefore, the distance $l(i,j)$ between the intercepts of two track candidates i and j is used as measure:

$$l(i,j)^2 := \left(x^i_{\text{min}} - x^j_{\text{min}}\right)^2 + \left(y^i_{\text{min}} - y^j_{\text{min}}\right)^2 + \left(x^i_{\text{max}} - x^j_{\text{max}}\right)^2 + \left(y^i_{\text{max}} - y^j_{\text{max}}\right)^2 \quad (24)$$

All track candidates within a relative distance $l_{\text{max}} = 1/\sqrt{2}\,\text{mm}$ are counted as neighbours, which define the number $N_{\text{n}}(i)$ of neighbours of a track candidate i as:

$$N_{\text{n}}(i) = \sum_{\text{j}}^{l(\text{i,j}) < l_{\text{max}}} \quad (25)$$

The sum runs over track candidates j which satisfy $l(i,j) < l_{\text{max}}$. The track candidate i with the highest value of $N_{\text{n}}(i)$ is the most probable track candidate and thus defined

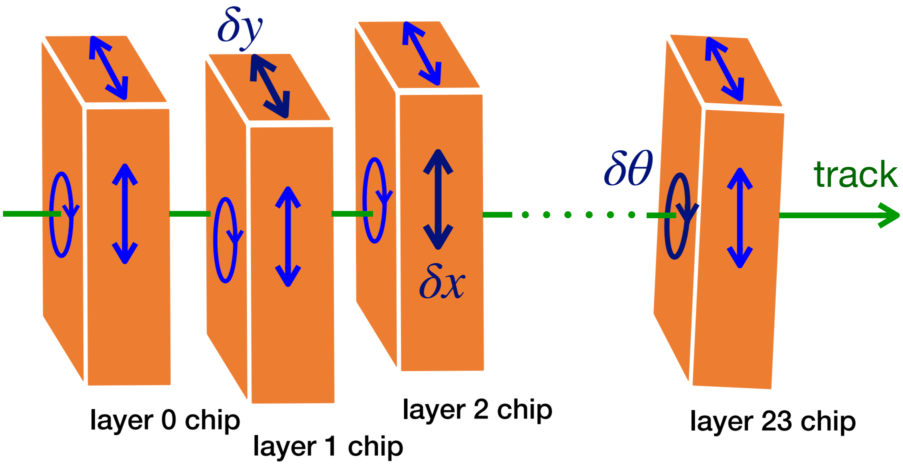

Figure 53: *Illustration of the alignment procedure, where δX ,δY and $\delta\theta$ are small corrections for each chip which are iteratively used to update the alignment parameters ΔX ,ΔY and $\Delta\theta$ of each chip.*

as track seed i_{seed}. For each track a seed score S_{seed} is defined as the proportion of neighbouring tracks to the total number N_{tot} of track candidates:

$$S_{\text{seed}} = \frac{N_{\text{n}}\left(i_{\text{seed}}\right)}{N_{\text{tot}}}. \tag{26}$$

To ensure a distinct seed track, the condition $S_{\text{seed}} > 0.95$ is required for seed tracks to be used in further analyses. Finally, the seed track is used to clean up the event from clusters which are clearly not belonging to the track. Therefore, clusters exceeding the relative distance $R = 5\,\text{mm}$ to the track seed are discarded in all chips the track traverses.

After cleaning up, the track parametrisation is performed for events with more than 17 layers containing only one cluster in one of the two chips per layer. Figure 52 shows an exemplary track event display where only chips containing single clusters are shown as they are used for the 3D track parametrisation. In addition, Figure 52 illustrates the radius, outside clusters are excluded by the seed track. Based on the seed track, the cluster positions are parametrised with a 3D straight line as shown in Figure 52 as red line. The track trajectory is defined by the parametrisation and used for the chip alignment and calibration procedure discussed next.

4.2.4 Chip Alignment

In this thesis, the chip alignment from [Alm+23] is adopted which has been obtained from cosmic muon tracks as measured at the University of Utrecht in the Netherlands. The chip alignment procedure is described in the following.

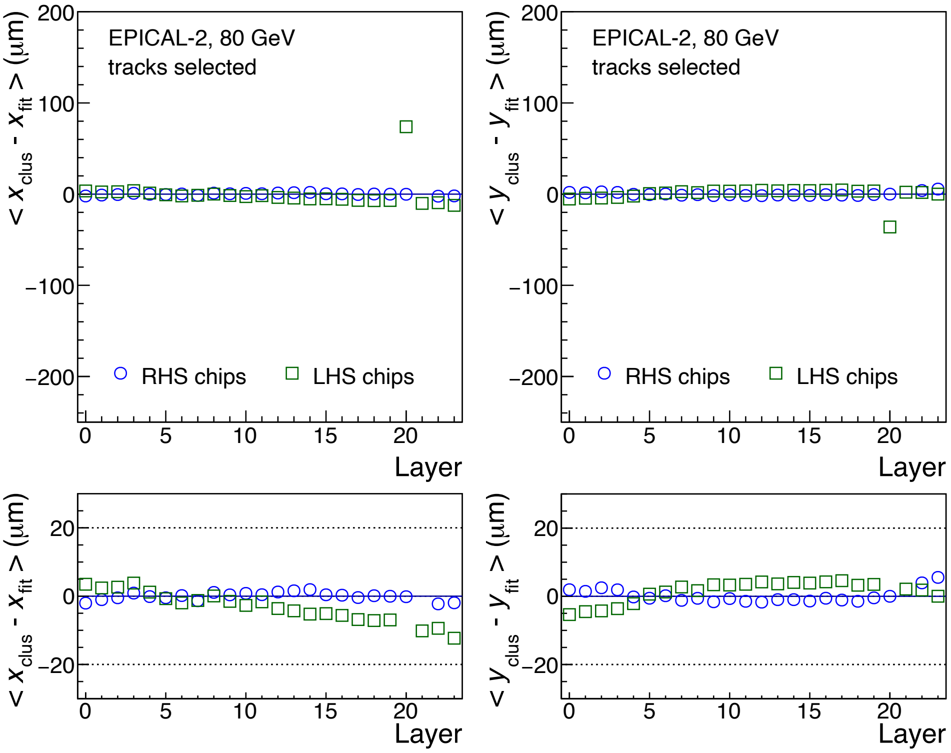

Figure 54: *Mean value of the track residual in* x*- (left) and* y*-direction (right), i.e. the mean of the distribution of the difference between expected track position and cluster position, as a function of the layer for both RHS (green) and LHS (blue) chips.*

As discussed in section 2.4, for each chip, the three free alignment parameters ΔX , ΔY and $\Delta\theta$ are used to align the chips in the EPICAL-2 stack. The determination of the alignment parameters is based on the track parametrisation described in the previous section 4.2.3. Figure 53 illustrates the general idea to determine the alignment parameters. Small changes δX , δY and $\delta\theta$ are introduced to the alignment parameters ΔX , ΔY and $\Delta\theta$ for each chip until the χ^2 of the track parametrisation is minimised and the alignment parameters converge to stable values.

In more detail, the alignment procedure is performed in three stages: First, the RHS and LHS chips are aligned separately using only those tracks going through either of the two halves. Second, the alignment for either of the halves is fixed and the other halve is aligned w.r.t. to the fixed one by using tracks crossing from one half to the other half. Third, the alignment of both RHS and LHS chips is updated at once using all track events.

For each of the three stages, the average over the track parametrisation χ^2 from all used track events defines a global χ^2_{glob}, which is minimised in the alignment procedure by iteratively varying the alignment parameters by δX , δY and $\delta\theta$ in all three stages until they converge. In [Alm+23], the described procedure leads to the improvement of the EPICAL-2 alignment precision from $\sim 100\,\mu m$ before alignment to $\sim 5\,\mu m$ and less after alignment.

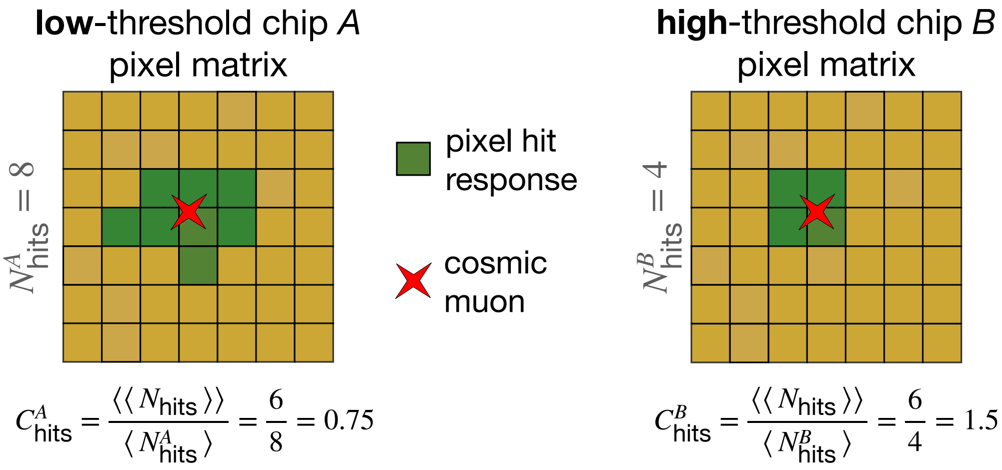

Figure 55: *Illustration of the conceptual idea of the chip calibration procedure resulting in a calibration factor C for each chip which is used to equalise the different chip responses in* EPICAL-2.

As EPICAL-2 has been transported between the University of Utrecht, DESY and SPS, here, the stability of the chip alignment is verified by studying the chip alignment using 80 GeV data from SPS. In the measured 80 GeV data, track events are selected as discussed in the previous section 2.4, but the track parametrisation is performed here 24 times excluding each layer from the parametrisation once. For each excluded layer, the track residuals, i.e. the difference between expected track position $(x_{\text{fit}}, y_{\text{fit}})$ from the track parametrisation and the cluster position $(x_{\text{clus}}, y_{\text{clus}})$, is calculated.

Figure 54 shows the mean track residuals in the x- and y-direction separately for both RHS and LHS chips. The two lower panels show the same track residuals but in a smaller range to highlight the alignment precision. The single outlier, the LHS chip in layer 20, is a result of the cosmic muon alignment procedure without this particular chip, which was malfunctioning during the cosmic muon data taking. For all the analyses presented in this thesis, the cosmic muon alignment from [Alm+23] is used.

In general, the EPICAL-2 alignment precision of $\sim 5\,\mu\text{m}$ presented in [Alm+23] is preserved. The alignment precision as verified above is sufficient within the scope of this work for a proper usage of the EPICAL-2 data.

4.2.5 Chip Calibration

The overall response of EPICAL-2 is an interplay of the contributing chips and therefore, each chip should behave similar. As discussed in section 2.1.2, the EPICAL-2 chips have different chip thresholds, which lead to chip-by-chip variations in their behaviour, particularly in the response to charged shower particles. In this thesis, a calibration procedure based on the response to cosmic muon tracks in

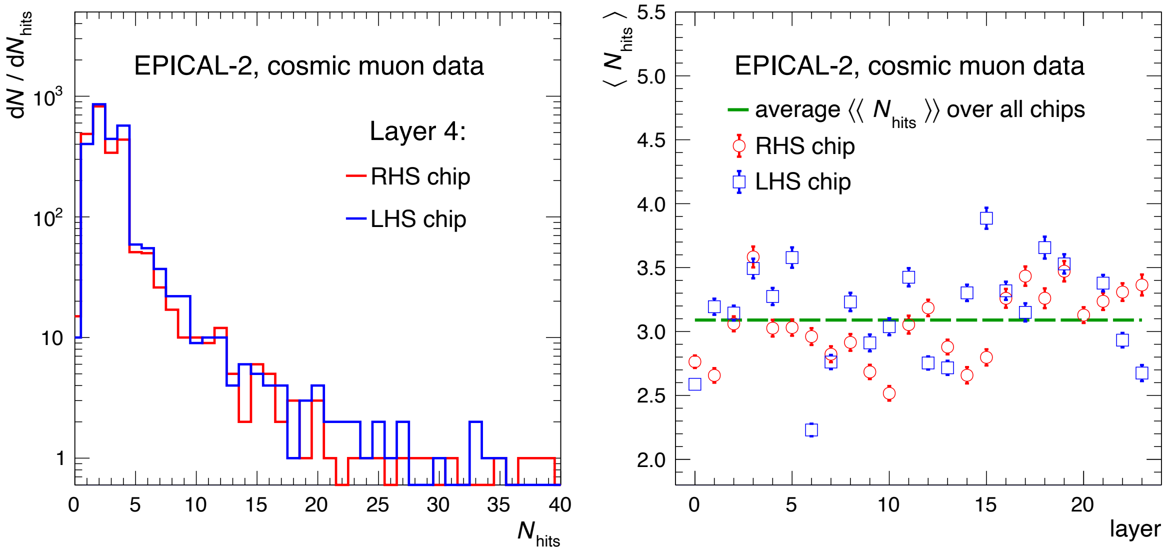

Figure 56: Left: *N_{hits} -distribution for the RHS and LHS chips of layer 4 obtained from cosmic muon track events as measured at the University of Utrecht in the Netherlands.* ***Right:*** *Mean number $\langle N_{hits} \rangle$ of the N_{hits} -distribution for each chip.*

individual chips as measured at the University of Utrecht in the Netherlands is used to equalise the chip responses [Alm+23].

Figure 55 illustrates the general idea of the chip calibration procedure: Assuming a cosmic muon crosses two chips A and B. The cosmic muon deposits the same energy in both chips and the same number of electron-hole pairs is generated in the epitaxial layers. The two chips are identical except that one chip A has a low-threshold and the other chip B has a high-threshold. Due to the different thresholds of the two chips, the same energy deposition in both chips leads to different hit responses: eight pixel hits in chip A and four pixel hits in chip B as shown in Figure 55. In reality, the in-chip pixel hit response to cosmic muons is subject to fluctuations given the Landau distribution describing the energy deposition in silicon [GZ+20]. However, the mean number $\langle N_{\text{hits}} \rangle$ of pixel hits for chip A and B over many cosmic muon events will result in a similar response difference namely that $\langle N^A_{\text{hits}} \rangle > \langle N^B_{\text{hits}} \rangle$. To equalise the chip responses, the average $\langle\langle N_{\text{hits}} \rangle\rangle$ of the mean number $\langle N_{\text{hits}} \rangle$ of pixel hits over both chips is used to derive a calibration factor C_{hits} for each chip:

$$C^A_{\text{hits}} = \frac{\langle\langle N_{\text{hits}} \rangle\rangle}{\langle N^A_{\text{hits}} \rangle} \quad \text{and} \quad C^B_{\text{hits}} = \frac{\langle\langle N_{\text{hits}} \rangle\rangle}{\langle N^B_{\text{hits}} \rangle} \tag{27}$$

Each pixel hit in chip A and B is weighted with the corresponding chip calibration factor C^A_{hits} respectively C^B_{hits}, to account for the difference in pixel hit response between the two chips A and B as illustrated in Figure 55.

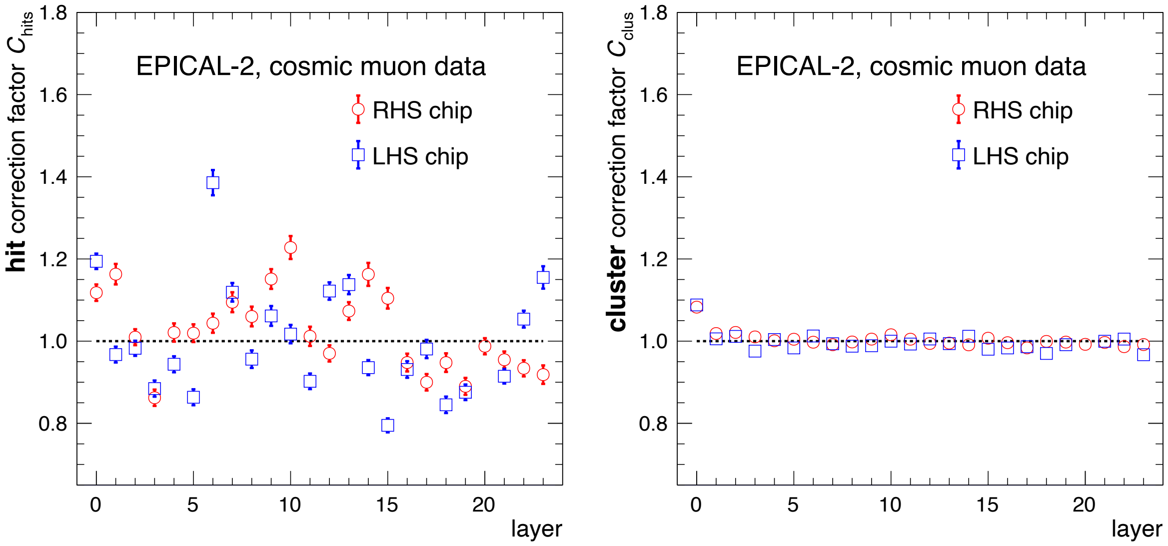

Figure 57: *Hit calibration factors C_{hits} (left) and cluster calibration factors C_{clus} (right) for each chip derived from the ratio between the average $\langle\langle N_{hits,clus}\rangle\rangle$ over all chips and $\langle N_{hits,clus}\rangle$.*

In the context of the EPICAL-2 response: Without such a calibration procedure, low-threshold chips would dominate the total response. A calibration is particular important when pixel hits of different chips are added together over many events. The details of the EPICAL-2 chip calibration procedure are described below.

The first step in the chip calibration procedure is the selection of cosmic muon tracks as presented in 4.2.3. The track parametrisation is performed 24 times excluding each layer from the parametrisation once similarly to the first step of the alignment procedure discussed in the previous section. Second, for each excluded layer, all pixel hits N_{hits} within a radius of $r = 3\,\text{mm}$ around the expected track position are considered as chip response to the track. Figure 56 (left) shows the N_{hits} -distribution exemplary for the RHS and LHS chips of layer 4. The majority of cosmic muon tracks causes a number of pixel hits which is in between $N_{hits} = 1$ to $N_{hits} = 4$, while higher N_{hits} are unlikely. For each chip, the mean number $\langle N_{hits}\rangle$ of pixel hits is calculated from the corresponding N_{hits} -distribution. For instance, $\langle N_{hits}\rangle \approx 3.25$ for the LHS chip of layer 4 and $\langle N_{hits}\rangle \approx 3$ for the RHS chip of layer 4. Figure 56 (right) shows $\langle N_{hits}\rangle$ for each chip. $\langle N_{hits}\rangle$ fluctuates between $\langle N_{hits}\rangle \approx 2.2$ for the LHS chip in layer 6 and $\langle N_{hits}\rangle \approx 3.9$ for the LHS chip in layer 15. The average $\langle\langle N_{hits}\rangle\rangle$ of $\langle N_{hits}\rangle$ over all EPICAL-2 chips is shown as a dashed green line at $\langle N_{hits}\rangle \approx 3.1$ in Figure 56 (right). Finally, the hit calibration factors C_{hits} for each chip are calculated. Figure 57 (left) shows the hit correction factors C_{hits} for each chip, which fluctuate between $C_{hits} \approx 1.4$ and $C_{hits} \approx 0.8$.

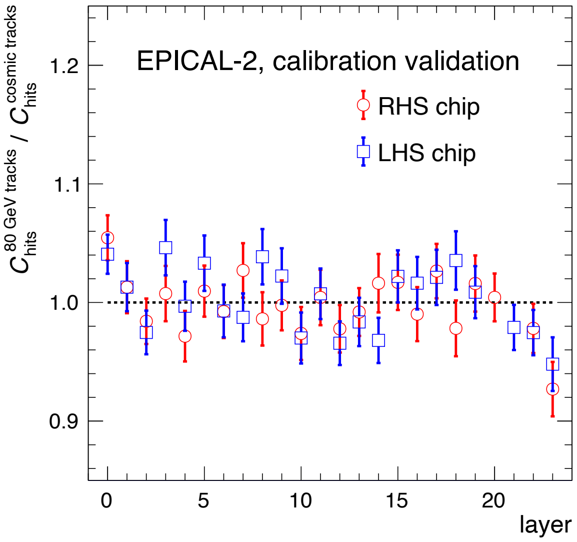

Figure 58: *Ratio of the calibration factor* $C_{hits}^{80\,GeV\ tracks}$ *obtained from track events at 80 GeV and the calibration factor* $C_{hits}^{cosmic\ tracks}$ *obtained from cosmic muon events.*

In addition to $N_{\rm hits}$ as EPICAL-2 observable also $N_{\rm clus}$ is used in this thesis. Therefore, the same calibration procedure as described above for hits is performed for clusters resulting in a cluster calibration factor for each chip. Figure 57 shows the cluster calibration factors $C_{\rm clus}$ for each chip which are fluctuating around $C_{\rm clus} \approx 1.0$ with the single exception of $C_{\rm clus} \approx 1.1$ in layer 0 where cosmic tracks traverse no detector material leading to a lower number of clusters as response to the cosmic muon track. In general, one observes that $C_{\rm clus} \ll C_{\rm hits}$ and that $C_{\rm clus}$ shows less fluctuations than $C_{\rm hits}$, because the cluster measurement absorbs the differences in the number of pixel hits as a result of different thresholds into the same single cluster.

The correction factors $C_{\rm hits}$ and $C_{\rm clus}$ for each chip are applied in any hits or clusters measurement with EPICAL-2 presented in this thesis. In particular, all observables based on $N_{\rm hits}$ ($N_{\rm clus}$) take the hit (cluster) correction factors into account by weighting each pixel hit (cluster) with the corresponding correction factor $C_{\rm hits}$ ($C_{\rm clus}$) of the chip.

Furthermore, the stability of the chip calibration factors is verified here by studying the chip calibration factors obtained from 80 GeV track events at SPS. The calibration procedure using track events at 80 GeV is performed as described above and the resulting calibration factors are compared with those obtained from the cosmic muon tracks. Figure 58 shows the ratio between the calibration factor $C_{\rm hits}^{\rm 80\,GeV\ tracks}$ obtained from track events at 80 GeV and the calibration factor $C_{\rm hits}^{\rm cosmic\ tracks}$ obtained from cosmic muon track events for each chip. As visible in Figure 58, the ratio fluctuates around one within the statistical uncertainties. Similar fluctuations are observed in the ratio of calibration factors obtained from two sub samples of the 80 GeV tracks and also in the comparison between other SPS energies.

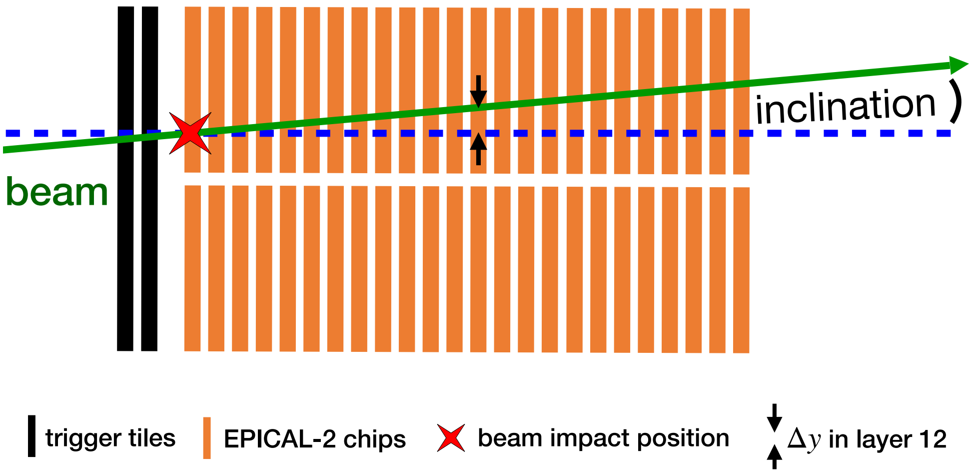

Figure 59: *Illustration of the beam inclination w.r.t. the* EPICAL-2 *setup.*

Therefore, the deviations from unity in Figure 58 are considered as statistical fluctuations and the calibration factors shown in Figure 57 can be applied to all acquired data without introducing a bias to the EPICAL-2 response obtained at the different energies. The calibration factors are considered as stable.

4.2.6 Inclination Correction

Although EPICAL-2 was carefully aligned along the test beam axis, eventually a residual inclination of the test beam with respect to the EPICAL-2 setup is left as illustrated in Figure 59. The inclination, i.e. a displacement in the transverse directions as a function of depth in EPICAL-2, is taken into account by using so-called inclination functions. In the following, the determination of the inclination functions based on track events is described exemplary for 20 GeV. Track events are selected as described in section 4.2.3.

First, for each layer, the difference between the beam impact position $(x_{\text{beam pos}}, y_{\text{beam pos}})$, considered as the cluster position in the first layer, and the position $(x_{\text{pixel hit}}, y_{\text{pixel hit}})$ of all pixel hits is calculated for both the vertical $\Delta x = x_{\text{pixel hit}} - x_{\text{beam pos}}$ and the horizontal $\Delta y = y_{\text{pixel hit}} - y_{\text{beam pos}}$ direction. Figure 60 shows the distribution for Δx (left) and Δy (right) exemplary for layer 12 at 20 GeV together with the parametrisation of the distribution with

$$f_{\text{Gaus}}(\Delta) = A + B \cdot \mathrm{e}^{-\frac{1}{2}\left(\frac{(\Delta-\mu)}{\sigma}\right)^2} \tag{28}$$

The parametrisation with $f_{\text{Gaus}}(\Delta)$ describes the peak of the distribution for both Δx and Δy. Consequently, the peak positions μ derived from the parameterisation of the Δx- and Δy-distribution reflect the average displacement in the vertical and horizontal

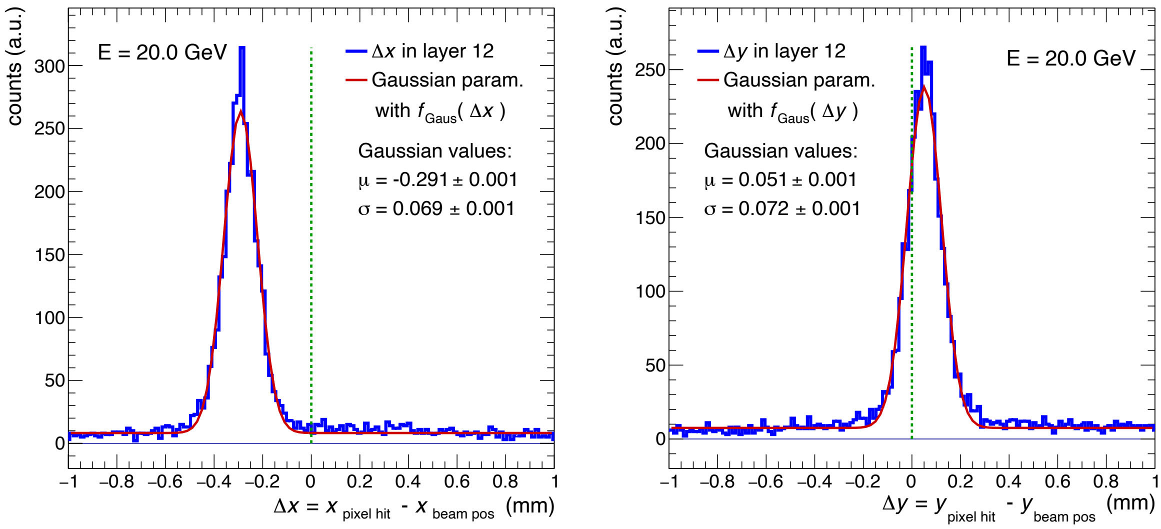

Figure 60: *For layer 12 at 20 GeV: Distribution of Δx (left) and Δy (right), the difference between pixel hits and the beam impact position.*

direction for the given layer and thus the depth z in EPICAL-2. In Figure 60, μ clearly deviates from the nominal value zero (no inclination) depicted as a dotted green line and, therefore, indicates an inclination of the beam with respect to EPICAL-2 setup.

In a second step, the peak positions μ from $f_{\mathrm{Gaus}}(\Delta)$ for all layers are extracted. Figure 61 (left) shows the peak position μ of the Δx-distribution in red and the Δy-distribution in blue as a function of z for 20 GeV. Since in the first layers the Δx- and Δy-distributions are delta-peak like, the determination of the peak positions via a parametrisation with $f_{\mathrm{Gaus}}(\Delta)$ is insignificant and thus inappropriate to utilise for further analysis steps. Furthermore, the peak positions for layer 20 and 21 are not extracted, because one chip in layer 20 was malfunctioning during the cosmic-muon data taking and one chip in layer 21 during the DESY and SPS test-beam measurements. In general, the peak position μ increases with depth z for both the vertical (Δx) and the horizontal (Δy) direction.

Finally, the peak positions are parametrised with a first order polynomial $f_{\mathrm{incl}}(z)$, here referred to as the inclination function which is used to correct for the inclination between the test beam and the EPICAL-2 setup:

$$f_{\mathrm{incl}}(z) \;=\; m \cdot (z - 0.028\,\mathrm{mm}) \tag{29}$$

Table 7 lists the slope m of the inclination functions for all SPS energies determined from the parametrisation with Equation 29 to the peak positions. The value of 0.028 mm takes the global z-position of the first sensor layer into account.

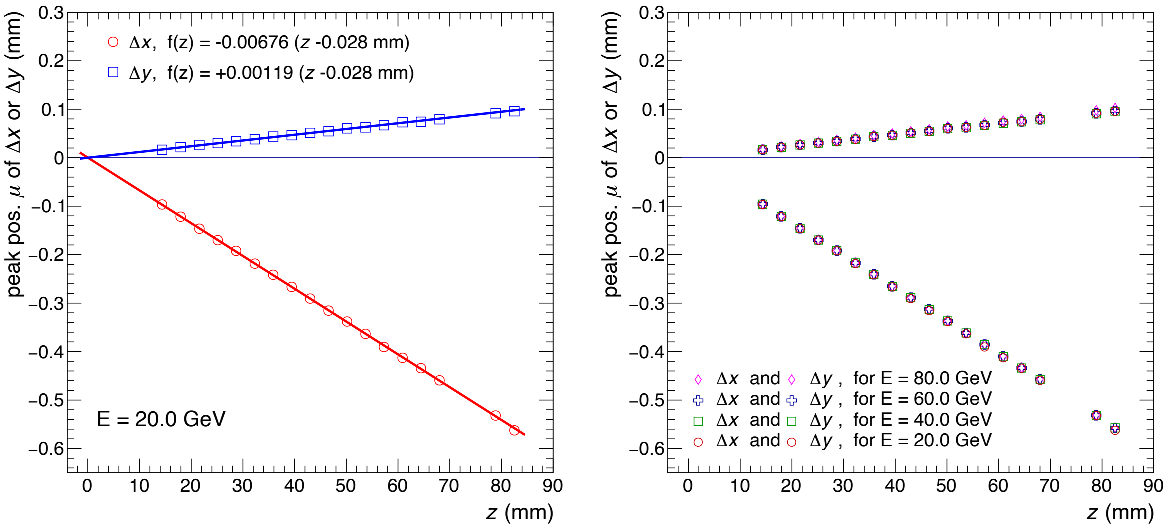

***Figure 61: Left:** Peak position of Δx and Δy as a function of depth z in* EPICAL-2 *for 20 GeV together with the corresponding inclination function (Equation 29).* ***Right:** Peak position of Δx and Δy as a function z for all* SPS *energies.*

energy (GeV)	$m \cdot 10^{-3}$	
	Δx	Δy
0 to 5.8	- 6.4427	3.3934
20.0	- 6.7649	1.1863
40.0	- 6.7349	1.1785
60.0	- 6.7286	1.1876
80.0	- 6.7199	1.2692

***Table 7:** The slope m of the inclination functions for all* SPS *energies. The slope m of the common inclination function used for the* DESY *energies ranging from 1 GeV to 5.8 GeV is shown as well.*

In addition, Table 7 includes the slope m used in a common inclination function for all DESY energies. The DESY inclination functions are adopted from [Alm+23]. In [Alm+23], a similar approach as used in this work is used, with the single exception that electromagnetic showers are used to derive a 2D Δx- and Δy-distribution and the peak positions are extracted using the 2D parametrisation with $f = (A/r) \cdot exp(B \cdot r)$, where $r = \sqrt{C + (x - \mu_x)^2 + (y - \mu_y)^2}$ and A, B, C, μ_x and μ_y are free parameters.

The precise alignment of the chips at a level of ∼5 μm as discussed in section 4.2.4 is also reflected in the comparison between the inclination functions and the data points showing fluctuations less than the order of the alignment precision. Figure 61 (right) shows the peak positions as a function of z for all SPS energies. Since the peak positions are similar at all energies, the inclination of the beam is also the same for all energies. This clearly visualises that the SPS beam is inclined in the negative vertical direction and tilted in the horizontal direction. Assuming there is no beam inclination w.r.t. the EPICAL-2 setup, the inclination functions effectively correct for an overall sheer of the EPICAL-2 stack in x and y direction, which is not taken into account using the alignment procedure as there is no global reference point and a track fit would always account for a global sheer.

The slope m converts into an inclination angle of ~ 6.8 mrad in the negative vertical direction and of ~ 1.2 mrad in the horizontal direction for all energies. Determined as quadratic sum, this results in a total inclination to the z-axis of ~ 6.9 mrad $= 0.4°$. E.g. in layer 8, which corresponds to a depth of $z \approx 28$ mm in EPICAL-2, the inclination translates into a displacement of ~ 6 pixels. In the last layer, $z \approx 85$ mm, an ~ 18 pixel offset is present. For each energy, the inclination functions presented here are taken into account in all analysis steps, e.g. when referring to a distance to the shower axis.

4.2.7 DESY Electron Event Selection

Due to the high-intensity DESY electron beam, in some cases multiple electrons entered EPICAL-2 at once. These pile-up events, already discussed in section 4.1. would not only bias the estimate of the energy response but also any observable related to single electromagnetic showers. In this thesis, single electron events are selected in the DESY data using the jet-finding algorithm from [Alm+23]. The algorithm to select single electron events is described below.

First, the EPICAL-2 surface is divided into cells with two different sizes: $0.5 \times 0.5\,\mathrm{mm}^2$ large cells are used for the central part of the detector ($|x| < 12\,\mathrm{mm}$ and $|y| < 12\,\mathrm{mm}$), and cells of size $1 \times 1\,\mathrm{mm}^2$ are used in the outer part ($|x| \geq 12\,\mathrm{mm}$ and $|y| \geq 12\,\mathrm{mm}$). Second, every cluster from all the EPICAL-2 layers is assigned to a cell in the grid of cells via its cluster position. If a cell c_i contains clusters from at least three different layers, the cell is assigned as a so-called pseudo-jet i with the following parameters:

$$\begin{aligned} N^c_{\mathrm{clus}} &\quad\rightarrow\quad p^i_{\mathrm{T}} \text{ (transverse momentum)} \\ x^c &\quad\rightarrow\quad y^i \text{ (rapidity)} \\ y^c &\quad\rightarrow\quad \phi^i \text{ (azimuth)} \end{aligned}$$

N^c_{clus} corresponds to the number of clusters in the cell with the transverse position x^c and y^c. Finally, the anti-k$_\mathrm{t}$ algorithm [CSS+08] with $R = 0.5\,\mathrm{mm}$ is applied to the pseudo-jets. Only those events where a single jet is reconstructed are selected with the exception of reconstructed jets from a single pseudo-jet as single pseudo-jets are unlikely to be the outcome of an electromagnetic shower from an electron entering EPICAL-2.

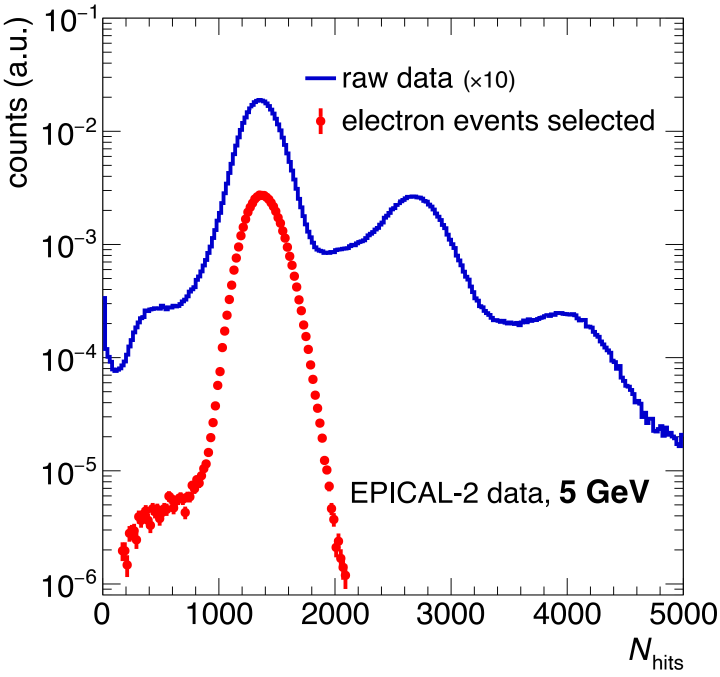

Figure 62: *N_{hits}-distributions at 5 GeV before (blue) and after (red) the electron event selection.*

To reduce contamination from overlapping showers which yield a single jet when applying the anti-k_t algorithm, single jet events are tested for the following two criteria: First, the clusters contributing to the jet in the first two layers are situated within 1 mm around the jet axis. Second, any two clusters in those two layer are less than 0.5 mm apart from each other. Events satisfying both criteria are used in further analyses.

After selecting single electron events, only those events with a beam impact position in the central part of the detector are selected. The beam impact position $(x_{\text{beam}}, y_{\text{beam}})$ is defined as the single cluster position in layer 0 and the central part is defined as follows:

$$\begin{aligned} -8\,\text{mm} &\leq x_{\text{beam}} \leq 8\,\text{mm} \\ -8\,\text{mm} &\leq y_{\text{beam}} \leq 8\,\text{mm} \end{aligned}$$

For beam impact positions close to the edge of EPICAL-2 , electromagnetic showers are leaking out of the EPICAL-2 active volume ($30 \times 30 \times 80\,\text{mm}^3$). Therefore, this beam impact position selection criterium ensures that only events with electromagnetic showers being fully contained are selected.

Figure 62 shows the N_{hits}-distribution for raw data in blue and for selected single electron events in red exemplary for 5 GeV. The raw distribution shows several Gaussian peak structures at multiples of the average single electron response of $\sim$ 1400 hits as already described in context of Figure 43. In contrast, the distribution of selected single electron events contains primarily the Gaussian peak structure at ~ 1400 hits. The low-intensity tail towards lower N_{hits} as visible in both distributions has been studied and is a result of small single electromagnetic showers, which are consistent with single low-energy electrons in the DESY beam. Most likely these electrons are produced in interactions of the beam particles with the beam collimators. From all acquired events, ~ 20 % remain after the single electron selection.

4.2.8 SPS Event Selection

For the analysis of many electron events combined, first of all, electron events need to be selected from the acquired SPS data containing electron, hadron and muon events as discussed in context of section 2.3 and 4.1.3. For the electron selection, the particle composition of the SPS data is particularly important as it can be used to estimate the contamination of other particles than electrons under the application of a selection criterium.

In this section, first, the beam composition at SPS is discussed. Second, the selection criteria for electrons as used in this work are defined on the basis of the total number N_{hits} of hits. After this, further observables which characterise an event and which are different for electrons and hadrons or muons are presented. The potential to discriminate electrons and hadrons with these observables is discussed as well.

(1) Estimate of the Beam Composition at SPS

The composition of the SPS beam is estimated using templates of the N_{hits}-distributions for positrons, pions, kaons, protons and muons, which are individually obtained from EPICAL-2 simulations. For each energy, the particle templates are used in a MC template parametrisation of the N_{hits}-distribution in the measured data. Only events with a beam impact position in the central part of the detector are selected as applied to the DESY data.

Figure 63 shows the N_{hits}-distribution in the measured data together with the result of the MC template parametrisation as red lines for the SPS energies 20, 40, 60 and 80 GeV. In addition, the particle contributions to the MC template result are shown. The general decomposition of the distributions is similar for all energies. Muons only contribute at the lower end of the distribution where the track peak is situated (compare to Figure 42 in section 4.1.3). Positrons dominate the higher end of the spectrum and dominantly contribute to the electron peak. In contrast to muons and positrons, hadrons contribute in the whole range of the distribution. Pions dominate the hadron contribution followed by protons and then kaons.

Figure 64 shows the estimate of the composition of the SPS beam obtained from the MC template parametrisation as a function of the SPS test-beam energy. With the

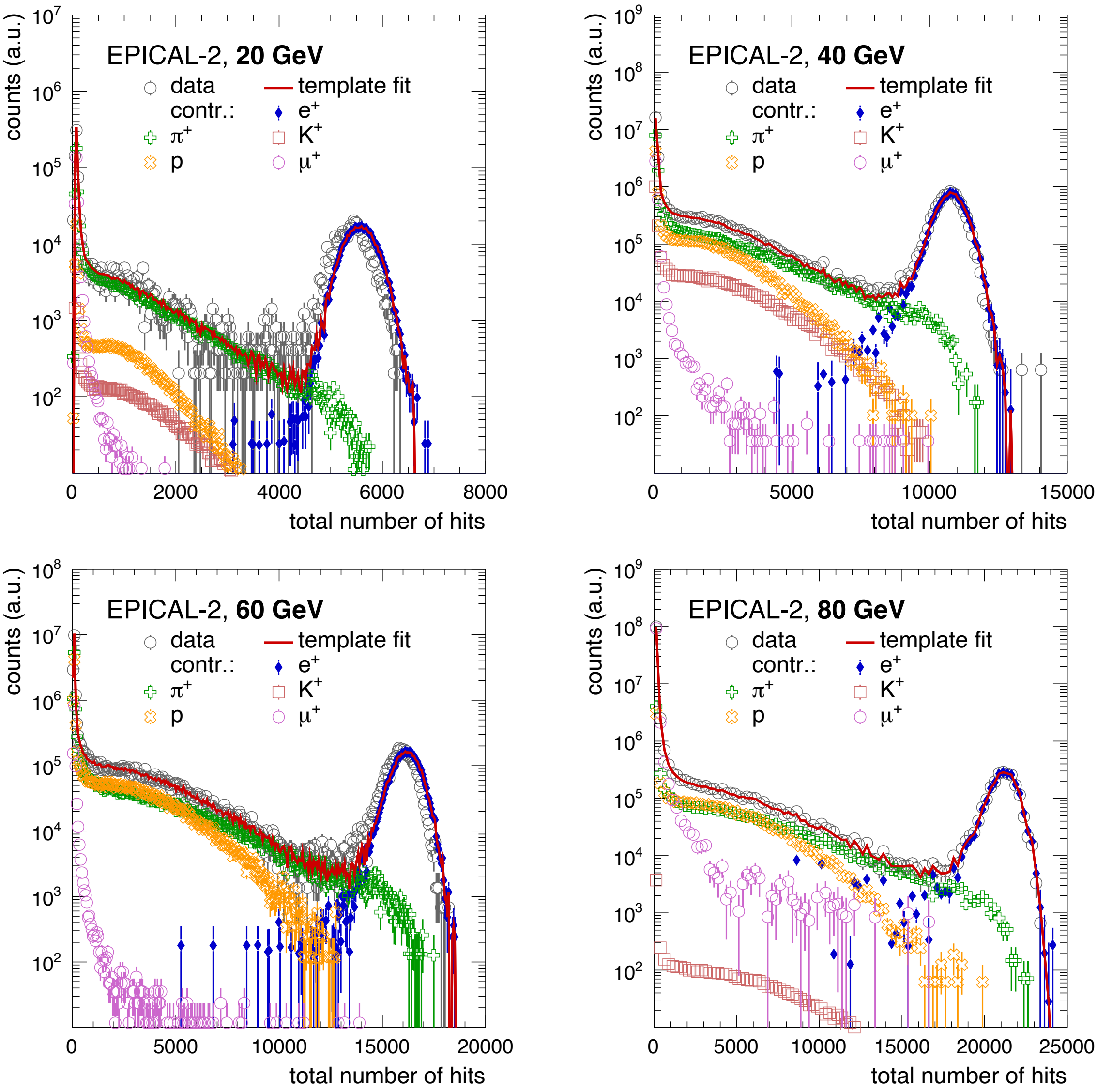

Figure 63: *Total number N_{hits} of hits distribution in data and the corresponding MC template parametrisation result including the particle decomposition of the MC template result distribution for each* SPS *energy.*

exception of 80 GeV, the general trend can be described as follows: The higher the energy the lower the electron and muon contribution and the higher the proton contribution, while the pion contribution stays constant at $\sim$ 40 % and the kaon contribution is negligible. The contributions change as follows:

contribution of:	20 GeV	60 GeV
proton	$\sim$ 5 %	$\sim$ 35 %
electron	$\sim$ 35 %	$\sim$ 15 %
muon	$\sim$ 20 %	$\sim$ 5 %

At 80 GeV, muons contribute the most with a contribution estimated at $> 85\%$. The beam collimator openings have been reduced during the test-beam measurement at

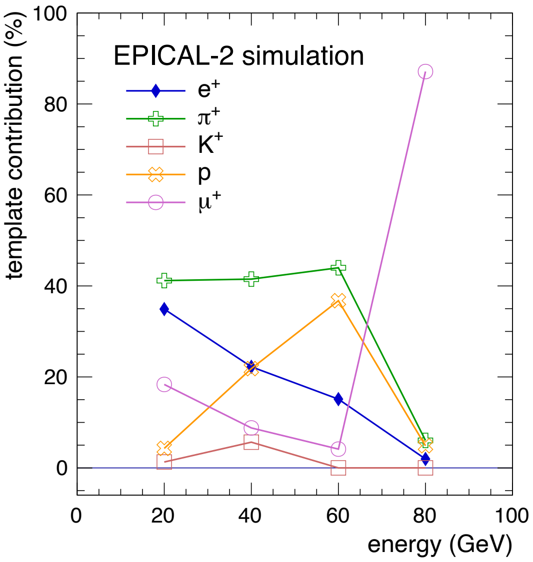

Figure 64: *Estimate of the* SPS *beam composition as a function of the energy.*

SPS to avoid excessive beam rates risking a shut down of the beam. While the amount of hadrons and positrons reaching EPICAL-2 is reduced since they do not pass the collimator because they are absorbed, muons penetrate the collimators which results in the enhanced muon contribution.

The estimated MC template contributions have been cross-checked by repeating the procedure but using the total number of clusters distribution yielding deviations less than 2 % for positrons, less than 20 % for pions, less than 15 % for muons and less than 45 % for protons neglecting the contribution of kaons. In addition, the estimated MC template contributions have been cross-checked with a measurement of the particle production in p+Be reactions [Ath+80], which is the initial reaction in the test-beam generation at SPS as discussed in section 2.3.3. In [Ath+80], a parametrisation of the production rates of pions, kaons and protons in p+Be reactions with an incident proton momentum p_0 of $p_0 = 400\,\text{GeV}$ is performed. For the comparison with the results obtained here, the parametrisation has been scaled to $p_0 = 120$ GeV, the initial proton momentum during the EPICAL-2 data taking at SPS. The contributions of the different particles derived from [Ath+80] are similar to the results obtained here.

(2) Electron Selection Based on N_{hits}

As visible in the total number N_{hits} of hits distributions in Figure 63, the electrons show a clear Gaussian peak structure and therefore can be selected using a cut on N_{hits}. To define a cut region, first, the electron peak in the N_{hits}-distribution is parametrised with a Gaussian function. The Gaussian mean μ and width σ obtained from the parametrisation are used to define the cut region for each energy. Only

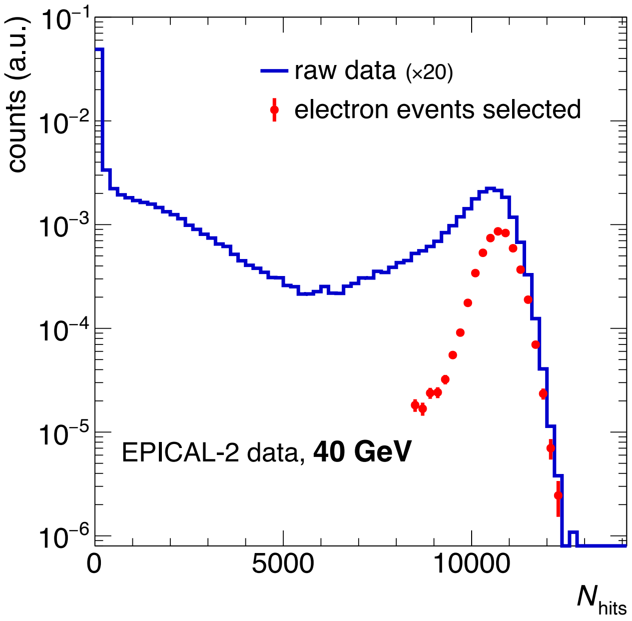

Figure 65: *N_{hits}-distributions at 40 GeV before (blue) and after (red) the selection of electron events as described in the text.*

events that satisfy the following condition are selected in this thesis and considered as electrons:

$$\mu - 5 \cdot \sigma < N_{\text{hits}} < \mu + 5 \cdot \sigma$$

The MC templates of the N_{hits}-distributions, also shown in Figure 63, are used to estimate the contamination in the electron sample. The obtained cut values on N_{hits} and the contamination in the resulting electron sample are as follows:

energy (GeV)	$\mu - 5\sigma$	$\mu + 5\sigma$	**contamination (%)**
20.0	3843	6946	1.54 ± 0.04
40.0	8398	13003	1.60 ± 0.06
60.0	12868	18971	1.89 ± 0.08
80.0	17545	24665	1.33 ± 0.07

Overall, the contamination is estimated to be less than 2 % for all energies and is therefore neglected in the analysis.

Figure 65 shows the N_{hits}-distribution for the raw data in blue and for the selected electron events at 40 GeV as example. While the raw distribution includes hot pixels, tracks, hadron showers and electromagnetic showers as discussed in section 4.1.3, the event selection clearly identifies single electromagnetic showers from the whole data set.

(3) Further Event Characterising Observables

Besides the total number of hits as observables to characterise an event, here, further event characterising observables are defined to study the behaviour of different particle types in EPICAL-2. The event characterising observables can also be used to refine the electron selection discussed before or to select hadrons which however are both beyond the scope of this work.

The event characterising observables are designed to take both the transverse and the longitudinal shower development into account. The following observables are defined:

(a) the layer l_{ss} of the shower start

(b) the forward-to-total ratio f_{l4} of the number of hits integrated up to layer 4 and total number N_{hits} of pixel hits

(c) the forward-to-total ratio f_{l8} of the number of hits integrated up to layer 8 and total number N_{hits} of pixel hits

(d) the transverse shower width σ_{hits}

(e) the fraction $R_{\mathrm{hits}}^{\mathrm{r}<2\mathrm{mm}}$ of hits in the shower core

The observables (a) to (e) are described below. Each observable is presented in terms of the distribution of the observable itself and the total number N_{hits} of hits exemplary at 40 GeV for data and simulation. Both pion and electron simulations are shown to illustrate the difference between both event types.

(a) **Layer l_{ss} of the Shower Start:**

As pointed out in context of Figure 38, a single EPICAL-2 layer corresponds to one radiation length X_0, while all 24 EPICAL-2 layers together correspond to one nuclear interaction length λ_i. Therefore, an electron shower is likely to develop within the first layers. In contrast, most hadrons traverse EPICAL-2 without showering. However, the shower is likely to develop in the later layers if they shower at all. Therefore, the layer l_{ss} of the shower start, considered as the EPICAL-2 layer where the shower evolution starts, can be used to discriminate between electron and hadron events. l_{ss} is defined as the layer, after which the number $N_{\mathrm{clus}}^{<1.5\,\mathrm{mm}}$ of clusters is greater than two within a cylinder of 1.5 mm centred to the beam impact position in three consecutive layers.

Figure 66 shows the distribution of N_{hits} and l_{ss} at 40 GeV for the measured data (left) and for both the electron and pion simulation (right). If no l_{ss} is determined up to layer 20, a determination of l_{ss} is not possible regarding the three consecutive layer condition. Therefore, those events are set to $l_{\mathrm{ss}} = 24$ and are regarded as non-showering with no shower start. In data, two striking features at $N_{\mathrm{hits}} \sim 10.5\,\mathrm{k}$

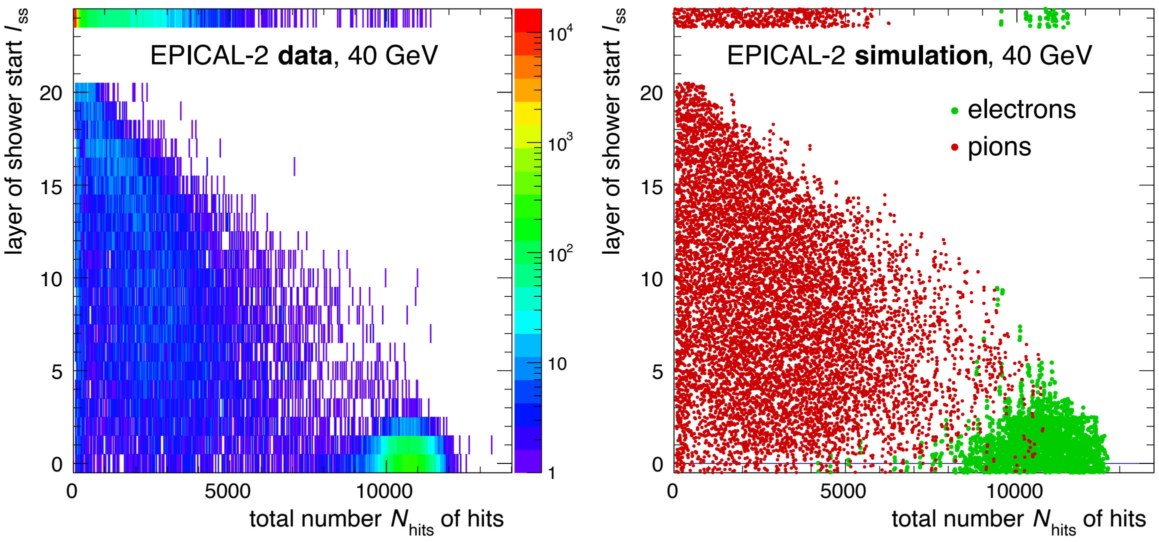

Figure 66: Distribution of the layer l_{ss} of the shower start and the total number N_{hits} of pixel hits for 40 GeV in the measured data (left) and in the simulation (right).

and $l_{ss} < 2$ and at $N_{hits} \sim 80$ and $l_{ss} = 24$ are visible in Figure 66 (left). The latter corresponds to the non-showering (track) events with no shower and a low number of hits, while the former is attributed to electron showers starting early and having a high number of hits. Figure 66 (right) shows the different population of electrons and pions in the $N_{hits} - l_{ss}$-space demonstrating their distinct behaviour in EPICAL-2. In rare cases it may be, that an electron does not interact within layer 0 but e.g. a backscattered shower particle produces a cluster in layer 0 which is considered as beam impact position. The l_{ss}-finding algorithm will not find clusters behind this beam impact position as the shower evolves elsewhere and therefore no shower start is found. A few electron events without l_{ss} are also visible in Figure 66 at $N_{hits} \sim 10.5\,\mathrm{k}$ and $l_{ss} = 24$.

(b) Forward-to-Total Ratio f_{14}:

Similar to l_{ss}, the forward-to-total ratio f_{14} quantifies the longitudinal shower development. f_{14} is defined as the ratio between the number N^{l4}_{hits} of hits integrated up to layer 4 and the total number N_{hits} of hits:

$$f_{l4} = \frac{N^{l4}_{hits}}{N_{hits}} = \frac{\sum\limits_{\text{layer } l=0}^{l\leq 4} \text{hits}}{\sum\limits_{\text{layer } l=0}^{l\leq 23} \text{hits}} \tag{30}$$

Figure 67 shows the distribution of N_{hits} and f_{14} at 40 GeV for the measured data (left) and for both the electron and pion simulation (right). A clear feature appears

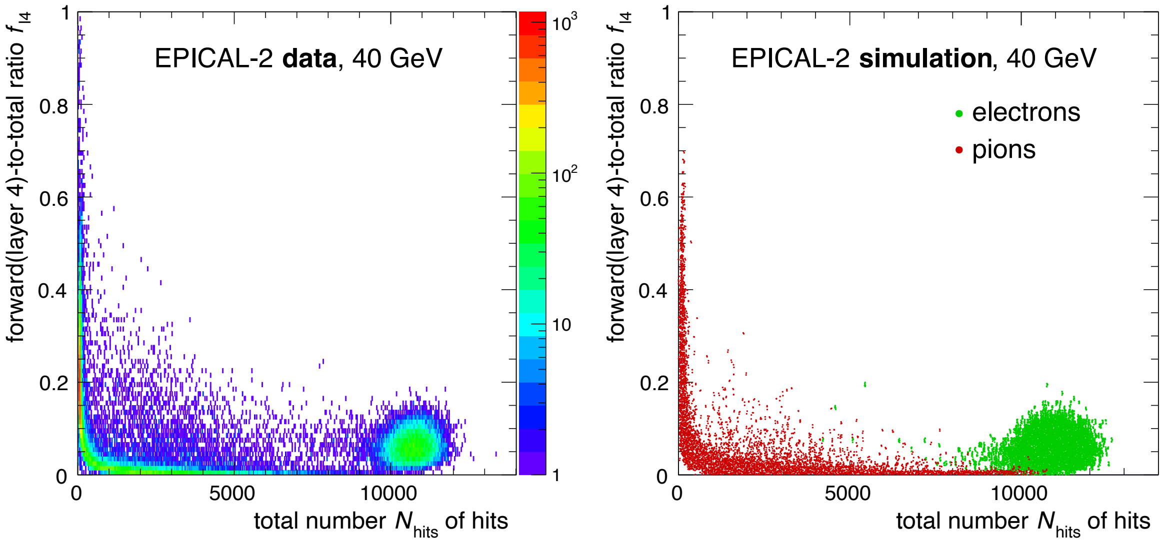

Figure 67: *Distribution of the forward-to-total ratio f_{14} and the total number N_{hits} of pixel hits for 40 GeV in data (left) and in simulation (right).*

around $f_{14} = 5/24 \approx 0.2$ and $N_{\text{hits}} \sim 80$ for track events with a similar number of hits in every layer in the data. The band structure from this feature to lower f_{14} and higher N_{hits} with a lower probability reflects the transition from non-showering hadrons to hadrons with $l_{\text{ss}} \to 0$ as also visible in the pion simulation in Figure 67 (right). In contrast, electrons populate the $N_{\text{hits}} - l_{\text{ss}}$-space at $f_{14} \sim 0.06$ and $N_{\text{hits}} \sim 10.5\,\text{k}$ because of $l_{\text{ss}} \lesssim 2$ for electrons, which is visible for both the data and the electron simulation. While a selection of showering hadrons with $f_{14} \to 0$ is barely possible, tracks with $f_{14} \gtrsim 0.15$ at $N_{\text{hits}} \approx 80$ can be identified.

(c) **Forward-to-Total Ratio f_{18}:**

f_{18} is defined analogue to f_{14} as the ratio between the number N^{18}_{hits} of hits integrated up to layer 8 and the total number N_{hits} of hits:

$$f_{18} = \frac{N^{18}_{\text{hits}}}{N_{\text{hits}}} = \frac{\sum_{\text{layer } l=0}^{l\leq 8} \text{hits}}{\sum_{\text{layer } l=0}^{l\leq 23} \text{hits}} \qquad (31)$$

Figure 68 shows the distribution of N_{hits} and f_{18} at 40 GeV for the measured data (left) and for the electron and pion simulation (right). The general features of the distributions in Figure 68 are similar to those discussed in context of Figure 67 with f_{14}: a band structure from $f_{18} \approx 0.4$ and $N_{\text{hits}} \sim 80$ to lower f_{18} and higher N_{hits} as well as a clear electron hotspot at $f_{18} \approx 0.4$ and $N_{\text{hits}} \sim 10.5\,\text{k}$ are visible. However, in contrast to f_{14}, (late) showering hadrons still appear at $f_{18} \to 0$ but are well separated

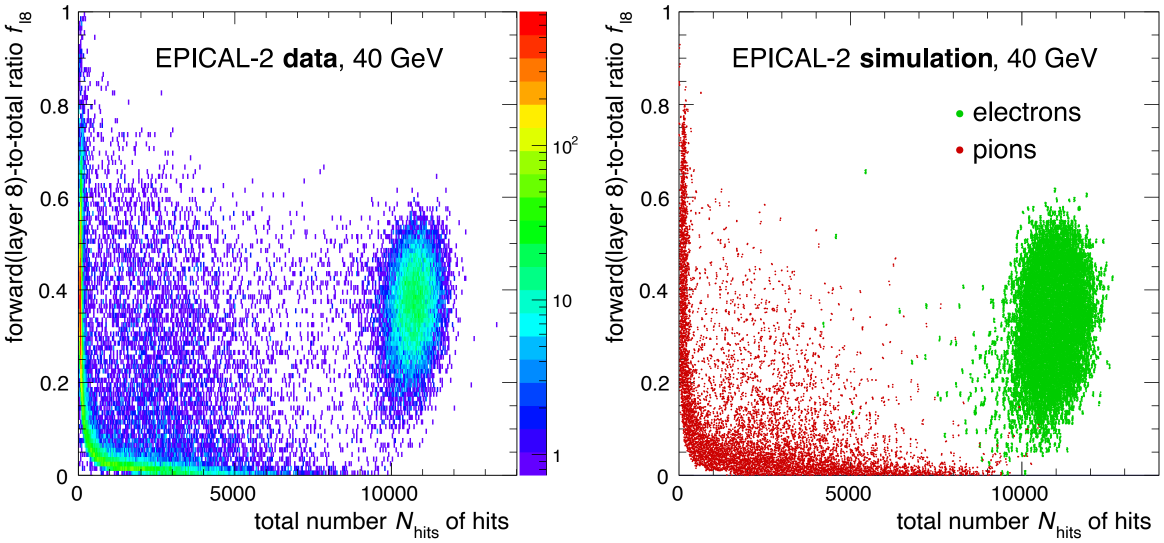

Figure 68: *Distribution of the forward-to-total ratio f_{18} and the total number N_{hits} of pixel hits for 40 GeV in data (left) and in simulation (right).*

from the electron hotspot. Therefore, f_{18} can be used for a selection of showering hadrons whereas tracks are indistinguishable from electrons as they appear at a similar f_{18}.

(d) **Transverse Shower Width σ_{hits}:**

In contrast to the previous observables l_{ss}, f_{14} and f_{18} related to the longitudinal shower evolution in EPICAL-2, the transverse shower width σ_{hits} addresses the transverse shower evolution in EPICAL-2. σ_{hits} is defined as the root of the quadratic sum of the standard deviation in x- and y-direction of all pixel hits in EPICAL-2:

$$\sigma_{\text{hits}} = \sqrt{\sigma_x^2 + \sigma_y^2} \qquad \text{with: } \sigma_x^2 = \frac{1}{N_{\text{hits}}} \sum_{\text{hits}} (x_{\text{hit}} - \langle x_{\text{hit}} \rangle)^2$$
$$\text{and } \sigma_y^2 = \frac{1}{N_{\text{hits}}} \sum_{\text{hits}} (y_{\text{hit}} - \langle y_{\text{hit}} \rangle)^2$$

Figure 69 shows the distribution of N_{hits} and σ_{hits} at 40 GeV for the data (left) and for both the electron and pion simulation (right). While track events have $\sigma_{\text{hits}} \to 0$ as visible in Figure 69 (left) around (80, 0) in the N_{hits}-σ_{hits}-space, any other activity in EPICAL-2, like a shower, results in a higher σ_{hits}.

Figure 69 (right) shows the separation between electrons and pions. While electrons are distributed between $\sigma_{\text{hits}} \sim 4$ and $\sigma_{\text{hits}} \sim 6$, pions appear to fluctuate between $\sigma_{\text{hits}} \sim 0$ and $\sigma_{\text{hits}} \sim 10$. A hadronic shower probably appears for $\sigma_{\text{hits}} \gtrsim 2$.

Figure 69 (left) shows some rare events with $\sigma_{\text{hits}} \gtrsim 6$ but with N_{hits} similar to the electron peak, which are not predicted by the simulation. These events have been

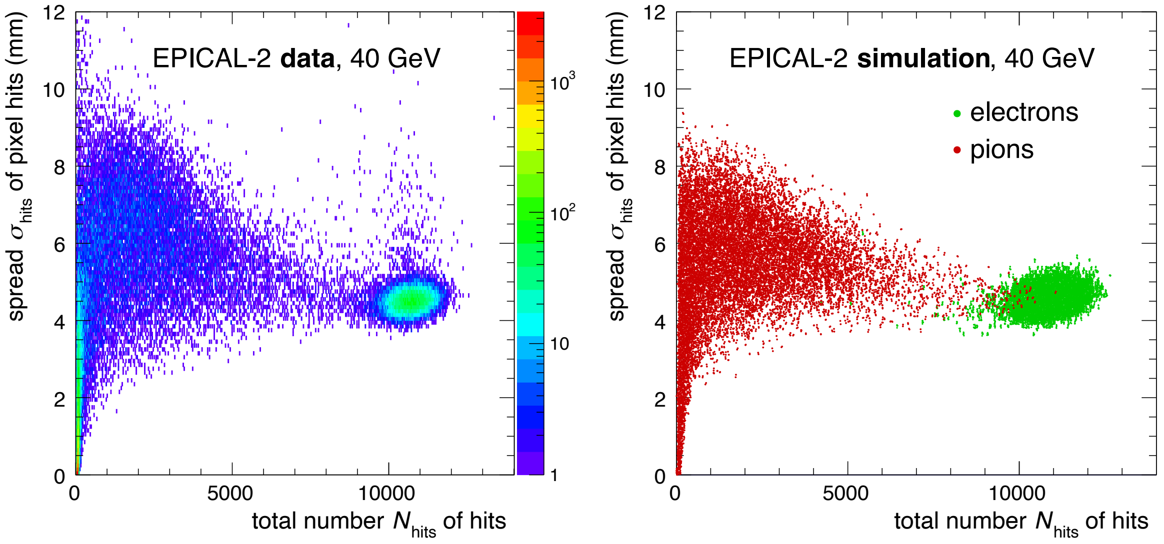

Figure 69: *Distribution of the transverse shower width σ_{hits} and the total number N_{hits} of pixel htis at 40 GeV in data (left) and in simulation (right).*

studied and are identified as rare occurring pile-up where multiple particles like an electron and a track or multiple hadrons enter EPICAL-2 at once.

σ_{hits} allows to discriminate between tracks with small spread and hadron showers with a larger spread than electrons. In addition, pile-up events in data can be identified and rejected.

(e) Fraction $R_{\text{hits}}^{\text{r}<2\text{mm}}$ of Hits in the Shower Core:

For electromagnetic showers, the shower particle density is highest around the shower axis and less affected by fluctuations compared to the transverse shower tail. Therefore, the fraction $R_{\text{hits}}^{\text{r}<2\text{mm}}$ of hits in the shower core aims at using the transverse evolution in EPICAL-2 to disentangle different event types similar to the transverse shower width σ_{hits} discussed before. $R_{\text{hits}}^{\text{r}<2\,\text{mm}}$ is defined as:

$$R_{\text{hits}}^{\text{r}<2\text{mm}} = \frac{\sum\limits_{r<2\text{mm}} N_{\text{hits}}(r)}{N_{\text{hits}}} \tag{32}$$

$N_{\text{hits}}(r)$ denotes the local number of hits at a distance r from the beam impact position as determined from the layer 0 cluster position.

Figure 70 shows the distribution of N_{hits} and $R_{\text{hits}}^{\text{r}<2\text{mm}}$ at 40 GeV for the measured data (left) and for both the electron and pion simulation (right). In Figure 70 (right), pions populate the N_{hits}-$R_{\text{hits}}^{\text{r}<2\text{mm}}$-space between the two extreme scenarios of first, the track events where all pixel hits are situated within the 2 mm radius and second, the hadron showers which have a higher N_{hits} and a strong, l_{ss}-dependent fluctuation of $R_{\text{hits}}^{\text{r}<2\text{mm}}$. In contrast, about 50 % of all hits in electromagnetic showers are situated

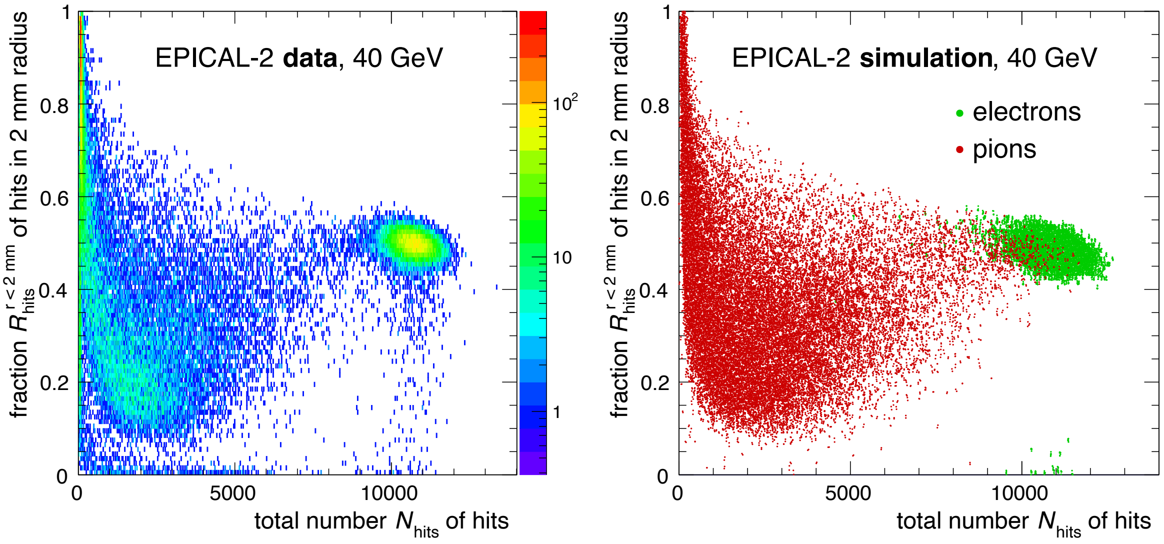

Figure 70: *Distribution of the fraction* $R_{hits}^{r<2mm}$ *of hits in the shower core and the total number* N_{hits} *of pixel hits at 40 GeV in data (left) and in simulation (right).*

within a radius r of $r \sim 2\,\mathrm{mm}$ as visible in Figure 70 for electrons. The described behaviour for electrons and pions can be found in the data in Figure 70 (left) as well. However, some events with $R_{\mathrm{hits}}^{\mathrm{r<2mm}} \lesssim 0.4$ at the electron peak at $N_{\mathrm{hits}} \sim 10.5\,\mathrm{k}$ occur. These events emerge from pile-up as discussed in context of σ_{hits} or due to misidentified beam impact positions where the particle shower actually starts elsewhere as described in context of the l_{ss} finding. Both can be identified and rejected in data.

In general, pions extend over the full $R_{\mathrm{hits}}^{\mathrm{r<2mm}}$ range compared to electromagnetic showers as visible in Figure 70. The majority of pions is well separated from electrons in the N_{hits}-$R_{\mathrm{hits}}^{\mathrm{r<2mm}}$-space. Therefore, $R_{\mathrm{hits}}^{\mathrm{r<2mm}}$ can serve as a discriminator between hadron showers and hadron tracks outside of the electron peak.

(4) Electron Efficiency and Pion Rejection

The potential of selecting either electrons or hadrons via the event characterising observables is discussed in this section using a sample of electron events and a sample of pion events from EPICAL-2 simulations. Under application of different cuts on each of the event characterising observables, the number of retained electron events (electron efficiency) and the number of rejected pion events (pion rejection) are studied in simulation.

The electron efficiency is defined as ratio of the number $N_{\mathrm{events}}^{\mathrm{selected}}$ of electron events satisfying a selection criterium and the total number $N_{\mathrm{events}}^{\mathrm{tot}}$ of electron events in the

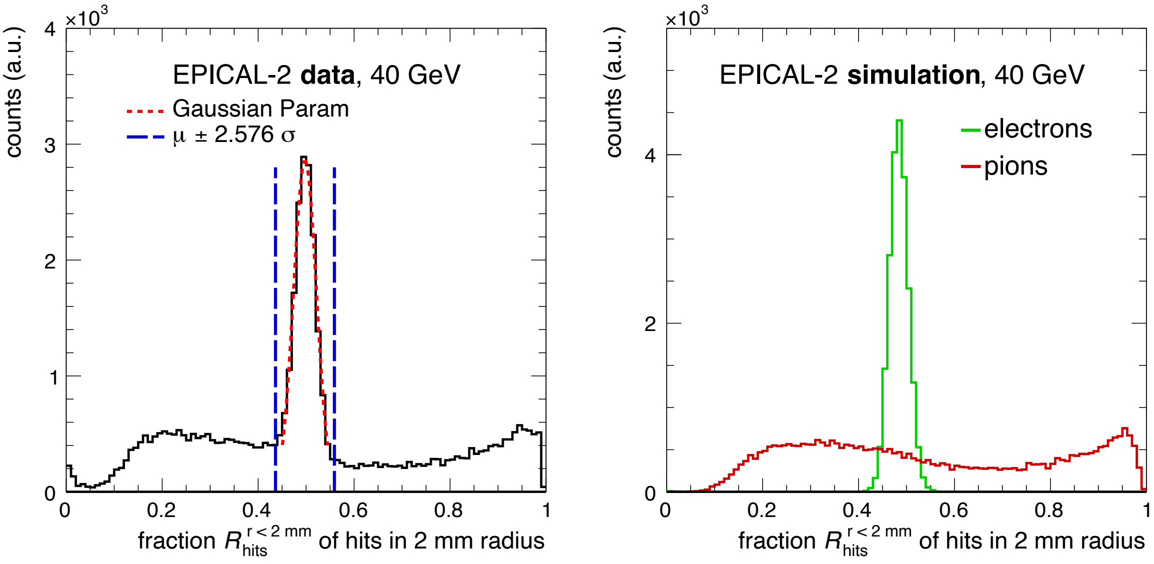

Figure 71: *Distribution of the fraction $R_{hits}^{r<2mm}$ of hits in the shower core for 40 GeV in the measured data (left) and in the simulation (right).*

sample of electron events from simulation:

$$\text{electron efficiency} = \frac{N_{\text{events}}^{\text{selected}}}{N_{\text{events}}^{\text{tot}}} \tag{33}$$

The pion rejection is defined in a similar manner but using pion events from simulation:

$$\text{pion rejection} = 1 - \frac{N_{\text{events}}^{\text{selected}}}{N_{\text{events}}^{\text{tot}}} \tag{34}$$

$N_{\text{events}}^{\text{selected}}$ refers to the number of pions events satisfying a selection criterium and $N_{\text{events}}^{\text{tot}}$ is the total number of pion events in the pion sample from simulation.

The selection criteria for each observable used for this study are defined in the measured data. To define the criterium, first, for each 2D distribution as shown in the Figures 66 to 70, the projection onto the event-characterising observable (y-axis) is performed. Figure 71 shows the projections exemplary for the last observable discussed: the fraction $R_{\text{hits}}^{\text{r}<2\text{mm}}$ of hits in the shower core for 40 GeV in the measured data (left) and in the simulation (right). In the distributions of the measured data, the electron peak is parametrised with a Gaussian function as exemplary shown in Figure 71 (left) with the exception of l_{ss} and f_{14} where the distributions exhibit a clear non-Gaussian shape. The Gaussian mean μ and width σ are obtained from each parametrisation and are used to define a selection region for each observable i using the scalar N_{i}^{σ}:

$$\mu_{\text{i}} \pm N_{\text{i}}^{\sigma} \cdot \sigma_{\text{i}}$$

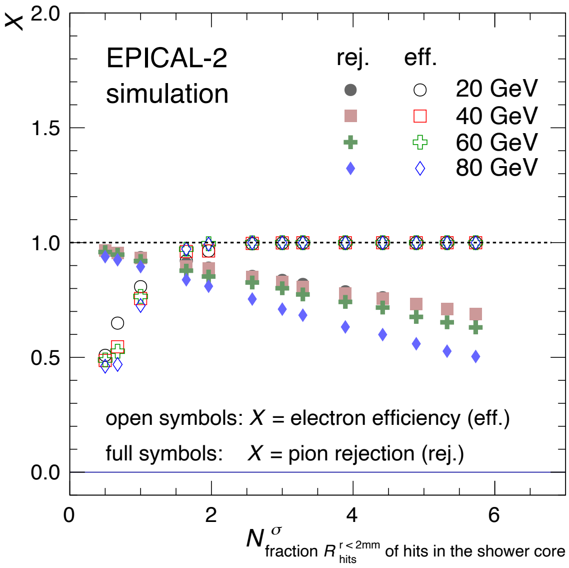

Figure 72: *Pion rejection and electron efficiency as a function of* $N^{\sigma}_{R^{r<2mm}_{hits}}$*, a selection based on the fraction* $R^{r<2mm}_{hits}$ *of hits in the shower core.*

Figure 71 (left) shows an exemplary selection region $(\mu \pm 2.576 \cdot \sigma)$ in the $R^{\mathrm{r}<2\mathrm{mm}}_{\mathrm{hits}}$-distribution, i.e. $N^{\sigma}_{R^{\mathrm{r}<2\mathrm{mm}}_{\mathrm{hits}}} = 2.576$.

To study the electron efficiency and pion rejection, the selection region derived from the measured data is applied to the electron and pion distribution from the simulations. For the observables $R^{\mathrm{r}<2\mathrm{mm}}_{\mathrm{hits}}$, σ_{hits} and f_{18}, all events within the selection interval $(\mu_{\mathrm{i}} \pm N^{\sigma}_{\mathrm{i}} \cdot \sigma_{\mathrm{i}})$ are taken into account ($N^{\mathrm{selected}}_{\mathrm{events}}$). In contrast, fixed cut values $N^{\mathrm{cut}}_{\mathrm{i}}$ are defined for l_{ss} and f_{14}, where all events up to $N^{\mathrm{cut}}_{l_{\mathrm{ss}}}$ and N^{cut}_{14} are selected. In the following, the dependence of the electron efficiency and the pion rejection on the selection region is discussed for each observable.

Figure 72 displays the pion rejection (full symbols) and the electron efficiency (open symbols) as a function of $N^{\sigma}_{R^{\mathrm{r}<2\mathrm{mm}}_{\mathrm{hits}}}$ for all SPS energies. For instance, the electron efficiency is $\sim 100\,\%$ with a pion rejection of $\sim 80\,\%$ for $N^{\sigma}_{R^{\mathrm{r}<2\mathrm{mm}}_{\mathrm{hits}}} = 2.576$.

Figure 73 (top) shows the pion rejection and the electron efficiency for both σ_{hits} (left) and l_{ss} (right). For example, for events with $l_{\mathrm{ss}} < 1$, the pion rejection is close to $100\,\%$ while the electron efficiency is $\sim 50\,\%$. The higher $N^{\sigma}_{\sigma_{\mathrm{hits}}}$ the lower the pion rejection and the higher the electron efficiency. For example, the electron efficiency is $\sim 100\,\%$ with a pion rejection of $\sim 80\,\%$ for $N^{\sigma}_{\sigma_{\mathrm{hits}}} = 2.576$.

Finally, Figure 73 (bottom) shows the pion rejection and the electron efficiency for both f_{14} (left) and f_{18} (right). While the pion rejection is similar for all SPS energies, the electron efficiency decreases (increases) the higher the energy for f_{18} (f_{14}). The efficiency increase for f_{14} is a result of the fixed $N^{\mathrm{cut}}_{f_{14}}$ value, because the mean of the f_{14}-distribution for electrons is at higher f_{14} the lower the energy as a result of an

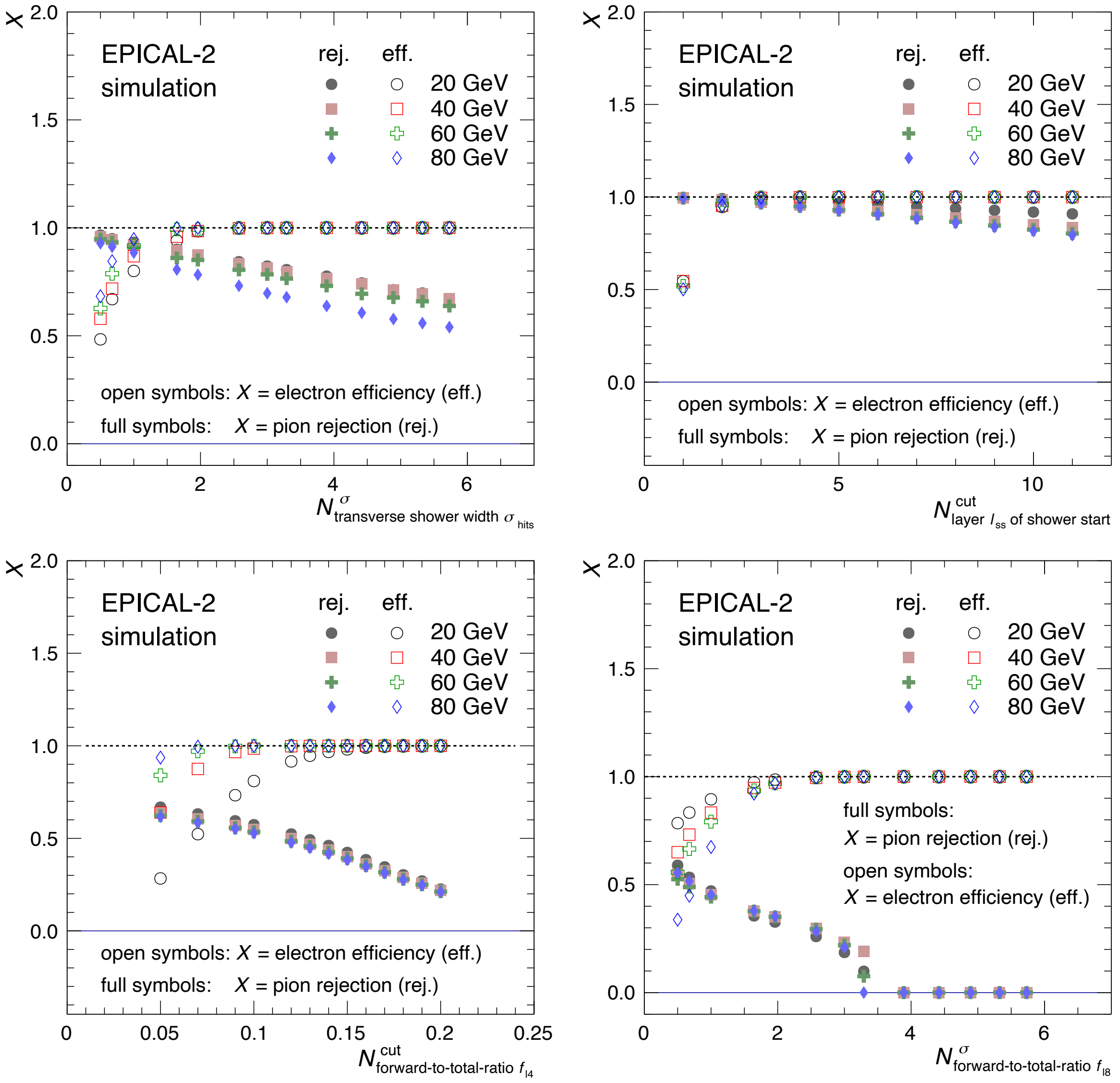

Figure 73: *Pion rejection and electron efficiency as a function of the selection on the observables σ_{hits} (top left), l_{ss} (top right), f_{14} (bottom left) and f_{18} (bottom right).*

earlier shower maximum for lower energies. Therefore, a selection up to $N^{cut}_{f_{14}}$ for all energies leads to less events satisfying the condition the lower the energy. The argument is valid for f_{18} as well with the exception, that for f_{18}, the selection is derived from the Gaussian width which differs from energy to energy: The higher the energy, the broader the f_{18}-distribution.

Depending on the scope of the analysis, either electron or hadrons can be selected using the event characterising observables as presented via the electron efficiency and pion rejection. In addition, both the purity and the contamination of a sample can be controlled by using different selection regions as they effect the electron efficiency and the pion rejection.

5 Results

5.1 Electromagnetic Shower Shape

The shape of electromagnetic showers is typically described by the longitudinal shower profile and the lateral shower profile. While the longitudinal profile corresponds to the evolution of the electromagnetic shower along its shower axis, i.e. the depth in EPICAL-2, the lateral profile reflects the transverse shower evolution, i.e. the evolution perpendicular to the shower axis.

In this chapter, the measurement of the electromagnetic shower shape in EPICAL-2 is presented. Both the longitudinal and the lateral shower profile are discussed. In addition to the profiles, the average electromagnetic shower shape is characterised in terms of the longitudinal shower maximum position and the lateral shower width.

5.1.1 Longitudinal Profile

The longitudinal shower profile is obtained as the mean detector response as a function of the layer number l. Since hits and clusters are used as a measure of the detector response, here, both the mean number $\langle N_{\text{hits}}\rangle(l)$ of pixel hits and the mean number $\langle N_{\text{clus}}\rangle(l)$ of clusters per layer are considered:

$$\begin{aligned}\langle N_{\text{hits}}\rangle\,(l) &= \frac{1}{N_{\text{events}}}\sum_{\text{events}} N^{l}_{\text{hits}}\\ \langle N_{\text{clus}}\rangle\,(l) &= \frac{1}{N_{\text{events}}}\sum_{\text{events}} N^{l}_{\text{clus}}\end{aligned}$$

The mean refers to the average over all events analysed and N^{l}_{hits} (N^{l}_{clus}) corresponds to the total number of hits (clusters) in layer l.

Figure 74 shows the longitudinal shower profiles, i.e. $\langle N_{\text{hits}}\rangle$ (left) and $\langle N_{\text{clus}}\rangle$ (right), as a function of the layer number for electron energies between 1 GeV and 5.8 GeV (top) and between 20 GeV and 80 GeV (bottom). In Figure 74, the measured data is shown as dots while the simulation is displayed as lines. Starting from layer 0, both $\langle N_{\text{hits}}\rangle$ and $\langle N_{\text{clus}}\rangle$ increase with later layers until they reach an energy dependent maximum. The layer which corresponds to the maximum is here referred to as the shower maximum position. Also the layer, i.e. the depth, at which the maximum of $\langle N_{\text{hits}}\rangle$ and $\langle N_{\text{clus}}\rangle$ is reached increases with energy. After this shower maximum position, $\langle N_{\text{hits}}\rangle$ and $\langle N_{\text{clus}}\rangle$ decrease the later the layer.

Overall, the longitudinal profiles shown in Figure 74 clearly reflect the electromagnetic shower evolution with its three typical stages: First, the start of the shower evolution yielding to more and more shower particles and thus an increase in

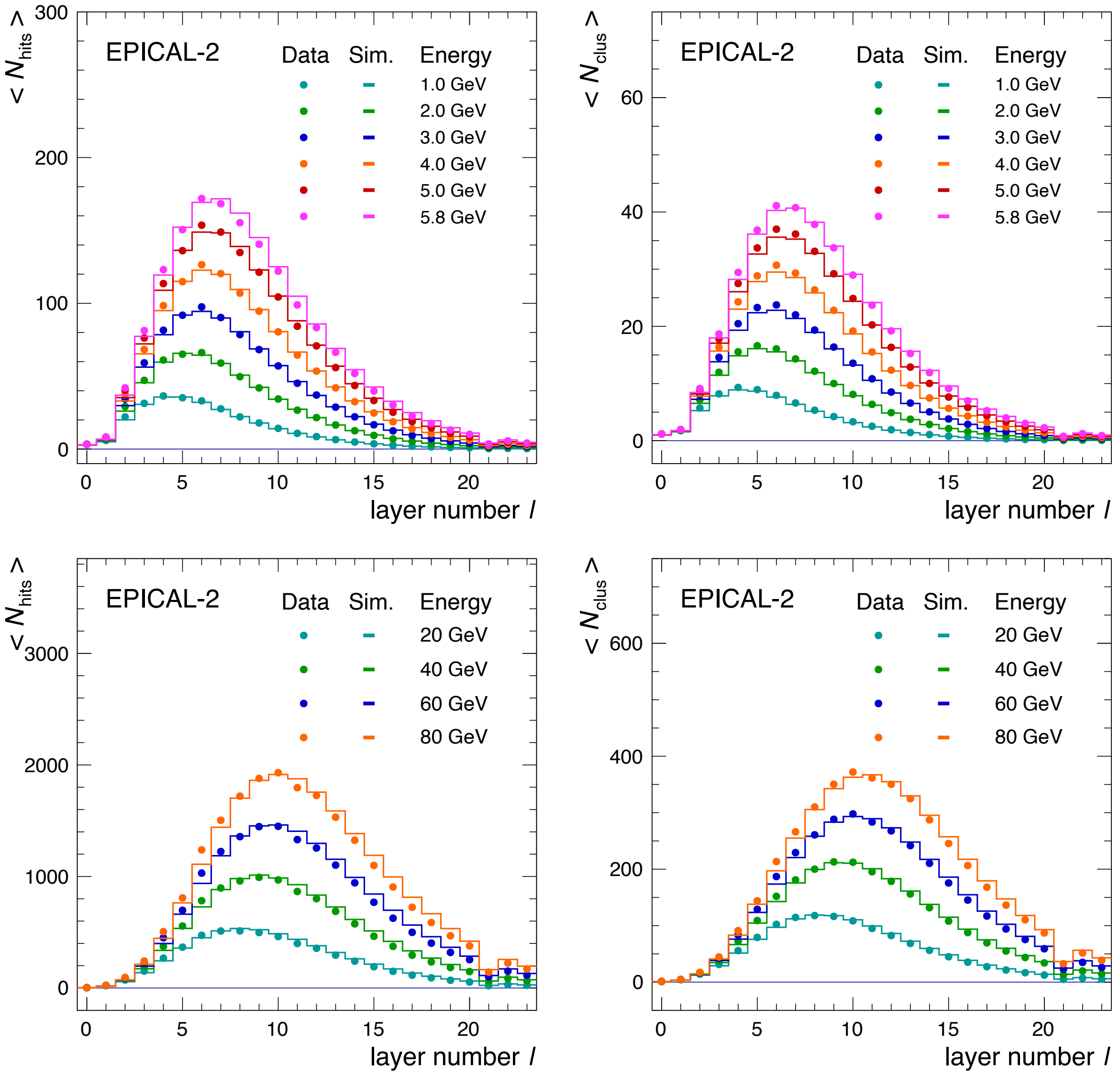

Figure 74: *Energy dependence of the longitudinal shower profile for the hits (left) and the clusters (right) measurement: The* DESY *energies from* 1 *GeV to* 5.8 *GeV are shown in the top figures and the* SPS *energies from* 20 *GeV to* 80 *GeV are shown in the bottom figures.*

$\langle N_{\text{hits}} \rangle$ and $\langle N_{\text{clus}} \rangle$ is observed in Figure 74. Second, the shower maximum where a maximum number of shower particles is reached similar to the maximum in the profiles shown in Figure 74. The higher the electron energy, the later the shower maximum position as expected given a mean energy loss per depth. And third, the tail of the shower where the number of shower particles thins out which is reflected by the decline in $\langle N_{\text{hits}} \rangle$ and $\langle N_{\text{clus}} \rangle$ shown in Figure 74.

Similar to the measured data, the profiles from the simulation show the clear longitudinal shower shape. However, minor discrepancies between the measured data and the simulation are visible: For both hits and clusters, the simulation predicts a later shower maximum position. While this feature is not clearly visible at low energies, e.g. at 1 GeV, for the higher energies, e.g. at 80 GeV, a shift towards a later shower maximum can be observed in Figure 74. Still, overall, the simulation provides a good description of the measured data. Even the reduction of $\langle N_{\mathrm{hits}} \rangle$ and $\langle N_{\mathrm{clus}} \rangle$ in layer 21 which results from the inactive chip in this layer during the data-taking campaigns is modelled by simulation.

5.1.2 Shower Maximum Position

In the previous section, it is found that the simulation predicts a later position of the shower maximum compared to data. In this section, the shower maximum position is determined for both hits and clusters in the data and in the simulation to compare their shower maximum positions and to compare hits with clusters in more detail.

To use a general description of the depth in calorimeters, the EPICAL-2 -specific layer number is expressed in terms of the radiation lengths X_0. The following relation between the layer number and the depth t in terms of X_0 is used here, taking only the tungsten absorber into account:

$$t = \mathrm{layer} \cdot \frac{t_W}{X_0(W)} = \mathrm{layer} \cdot 0.856 \tag{35}$$

The thickness of tungsten per EPICAL-2 layer corresponds to $t_W = 3$ mm and the tungsten radiation length amounts to $X_0(W) = 3.504$ mm [Gro20].

Figure 75 shows the longitudinal profiles for both hits (left) and clusters (right) as a function of the depth in terms of X_0 for selected energies separately for the measured data (top) and for the simulation (bottom).

Each longitudinal profile shown in Figure 75 is parametrised with $f(t)$, an empirical formula typically referred to as the Gamma distribution [GZ+20]:

$$f(t) = A \cdot t^{\alpha} \cdot e^{-\beta \cdot t} \tag{36}$$

t describes the depth in EPICAL-2 and A, α and β are free parameters. The parametrisations with $f(t)$ are shown in Figure 75 as solid lines for each energy. Overall, $f(t)$ describes both the data and the simulation. However, the fluctuation of the data around $f(t)$ are stronger compared to the simulation. A better description of the simulation by $f(t)$ makes sense as $f(t)$ itself is a parametrisation of simulated data [LS75]. Since $f(t)$ is used to determine the shower maximum position, instead of using all data and simulation points, the parametrisation with $f(t)$ is performed in a limited range of the depth t to achieve a better description around the shower maximum. The ranges of the depth t are given in Figure 75.

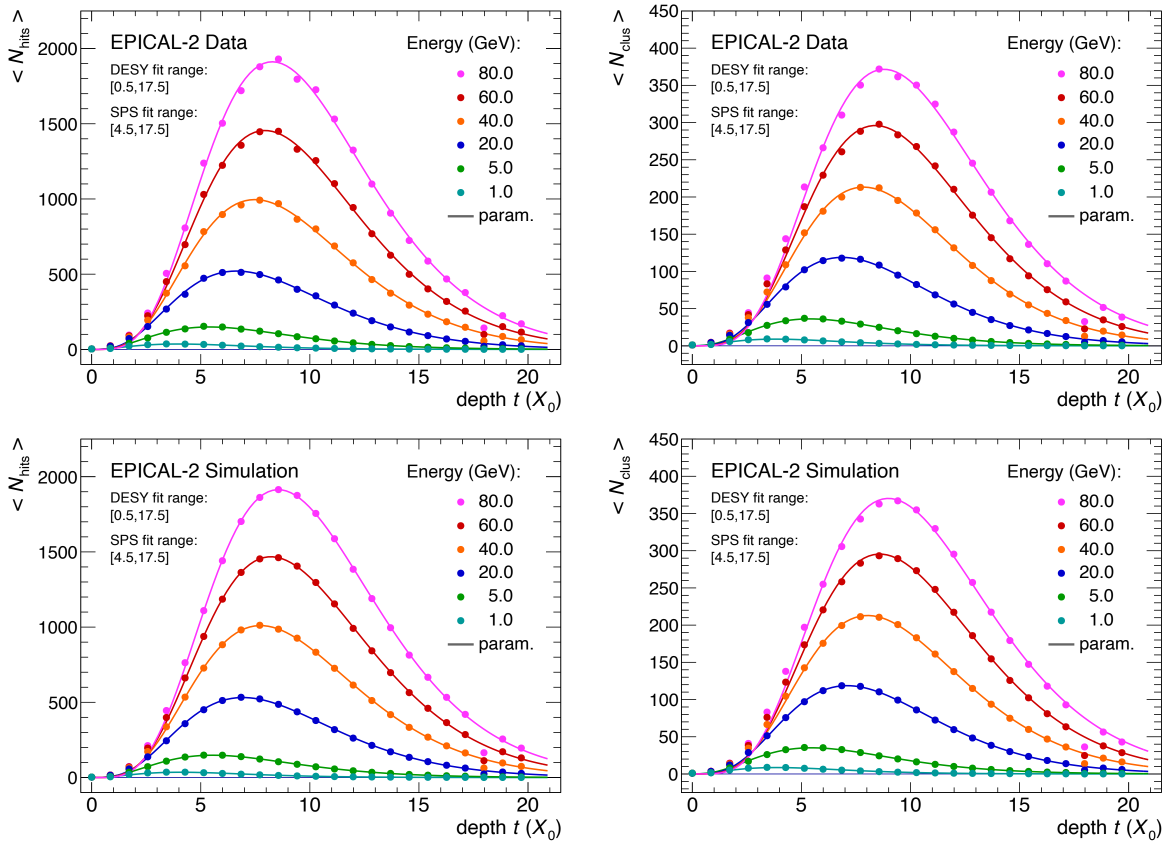

Figure 75: *Longitudinal profile and the corresponding parametrisation with Equation 36 for selected energies for the measured data (top) and the simulation (bottom) and for both hits (left) and clusters (right).*

For each energy, the shower maximum position $t_{\text{max}}^{\text{exp}}$ is calculated from the parametrisation $f(t)$ of the longitudinal profile as [GZ+20]:

$$t_{\text{max}}^{\text{exp}} = \frac{\alpha}{\beta} \tag{37}$$

As discussed in section 1.2, the energy dependence of the shower maximum $t_{\text{max}}^{\text{theo.}}$ is often described by the following empirical function using the critical energy E_C [GZ+20]:

$$t_{\text{max}}^{\text{theo}} = \ln\left(\frac{E}{E_C}\right) - 0.5 \tag{38}$$

$E_C = 7.825$ MeV is used here, which reflects the average of 7.97 MeV for electrons and 7.68 MeV for positrons taken from [Gro20].

Figure 76 shows the shower maximum position $t_{\text{max}}^{\text{exp}}$ calculated with Equation 37 as a function of energy for the measured data in blue and for the simulation in red. Hits are shown as open circles whereas clusters are shown as open squares. Overall, the simulation predicts a later shower maximum position for both hits and clusters

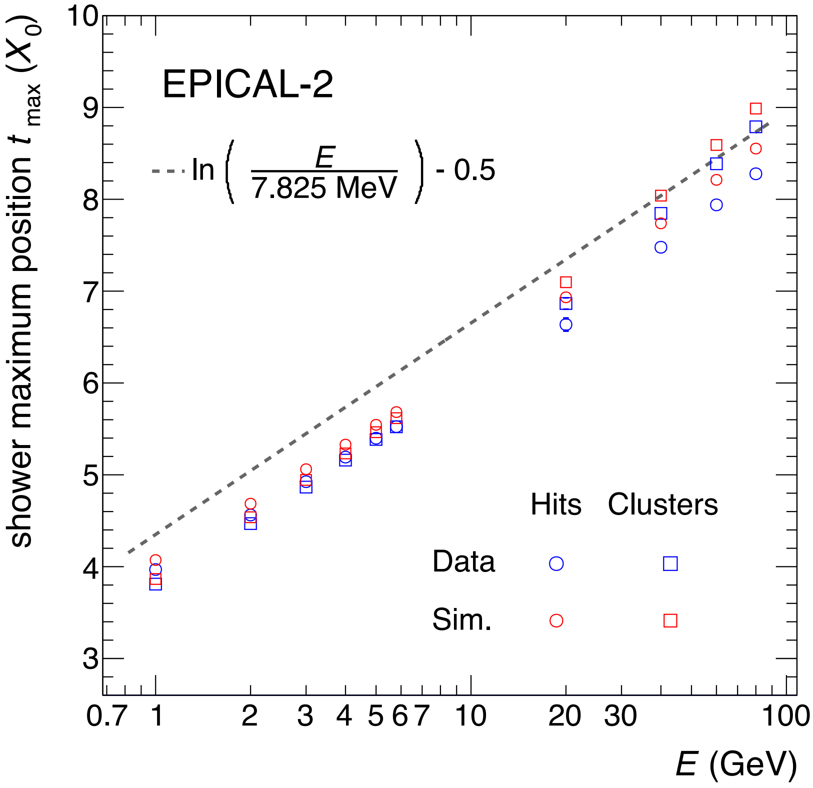

Figure 76: *Energy dependence of the shower maximum position.*

compared to the data. This is consistent with the direct comparison of the longitudinal shower profiles between the data and the simulation as discussed in context of Figure 74 in the previous section. The shower maximum positions $t_{\text{max}}^{\text{exp}}$ for hits and for clusters differ. In addition to the data and simulation, Figure 76 shows the empirical shower maximum position $t_{\text{max}}^{\text{theo}}$ as dashed grey line. $t_{\text{max}}^{\text{theo}}$ is greater than $t_{\text{max}}^{\text{exp}}$ for hits and clusters for the data and simulation at the low DESY energies. In contrast to DESY, at the higher SPS energies, the discrepancy between $t_{\text{max}}^{\text{theo}}$ and $t_{\text{max}}^{\text{exp}}$ decreases the higher the energy for hits and for clusters in the data and simulation. For instance, $t_{\text{max}}^{\text{exp}}$ for clusters is greater than $t_{\text{max}}^{\text{theo}}$ for both the data and simulation at 80 GeV.

In summary, a different shower maximum position is observed for hits and clusters, the shower maximum $t_{\text{max}}^{\text{exp}}$ obtained in the data and simulation differs from $t_{\text{max}}^{\text{theo}}$ and the simulation predicts a later shower maximum position compared to the data. To further elaborate on these three observations, in the following, each observation is discussed separately.

(1) $t_{\text{max}}^{\text{exp}}$ **difference between hits and clusters:**

While the absolute values of the shower maximum position t_{max} differ between data and simulation which is discussed later in this section, the difference of t_{max} between

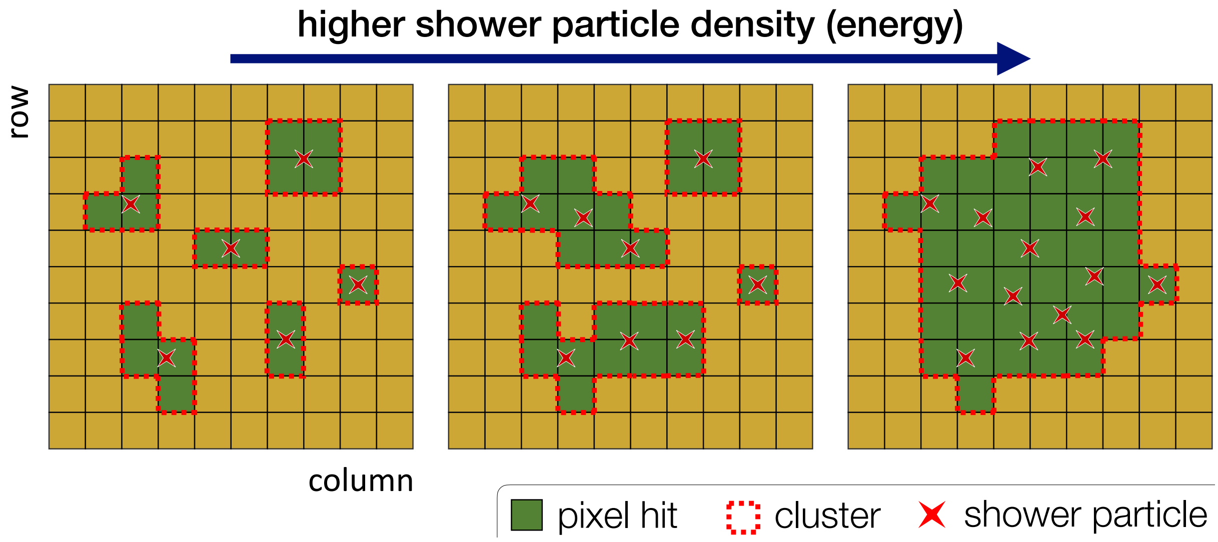

Figure 77: *Illustration of saturation.*

hits and clusters is consistent between data and simulation as can be seen in Figure 76. At the DESY energies below 5.8 GeV, t_{max} is greater for hits than for clusters. In contrast, at the SPS energies above 20 GeV, t_{max} is smaller for hits than for clusters.

Two effects which influence hits and clusters differently play an important role here and reasonably explain the observation: saturation and a chip response that depends on the angle at which a charged shower particle traverses the chip.

The former comprises the saturation of the number of hits and clusters due to high particle densities especially around the shower maximum position and close to the shower axis. When the particle density increases, first, multiple shower particles merge into the same cluster and at even higher densities also into the same hits, i.e. saturation is stronger for clusters than for hits. As the shower particle density increases also with the energy, the saturation is stronger the higher the energy. Both the hit and cluster saturation are illustrated in Figure 77.

The latter refers to the fact that the higher the angle at which a charged shower particle traverses a chip, the higher the number of pixel hits and the more hits contribute to the resulting cluster, i.e. the cluster size increases but the number of clusters remains constant. As discussed in section 3.2.3, the distribution of the angle at which charged shower particles traverse the EPICAL-2 chips shows forward-moving and backward-moving shower particles. Furthermore, forward-moving particles dominate the distribution. Figure 78 shows the median shower particle angle as a function of the layer number for forward-moving and backward-moving particles for electron events at 1 GeV and at 20 GeV in simulation. Overall, the median angle increases with the layer number. The median angle of forward-moving particles is about 0° in layer 0 and increases the later the layer, up to

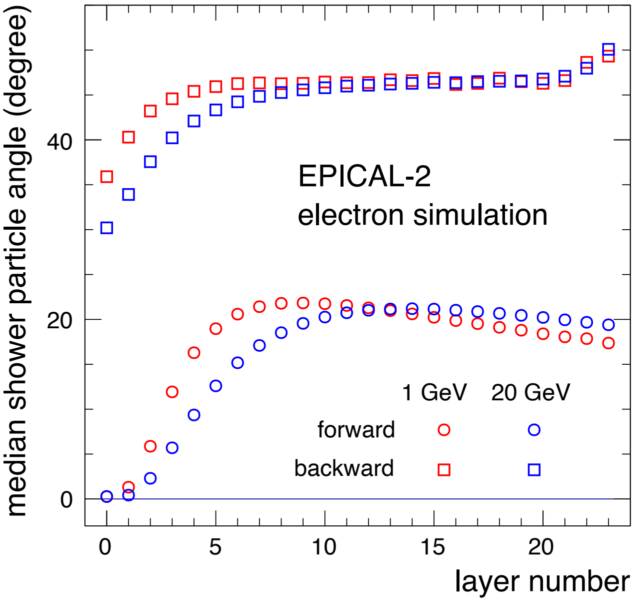

Figure 78: *Median of the distribution of the angle at which charged shower particles traverse the* EPICAL-2 *chips as a function of the layer number for 1 GeV and 20 GeV. Forward-moving and backward-moving particles are distinguished.*

an energy and layer specific maximum, after which the median angle slightly decreases. In contrast, the median angle of backward-moving particles is about 30° (35°) in layer 0 for 20 GeV (1GeV). The median angle increases to 45° and remains at 45° until layer 22, where a further increase is observed. For both 1 and 20 GeV, the maximum of the median shower particle angle is deeper in the detector compared to the calculated shower maximum position $t_{\max}^{\exp}$ as shown in Figure 76.

Considering the energy and layer dependence of both effects together, the observation of a greater $t_{\max}^{\exp}$ for hits than for clusters at low energies and the smaller $t_{\max}^{\exp}$ for hits than for clusters at high energies as shown in Figure 74 can be explained as following:

At low energies and in the absence of saturation, the larger shower particle angles in later layers shift the maximum hit response towards later layers. Since the higher number of hits due to the larger particle angles is absorbed by measuring clusters, a later shower maximum position is observed for hits compared to clusters at low energies. At high energies, saturation reduces the response especially before the actual shower maximum and thus the shower maximum position appears in later layers. Since the effect of saturation is much stronger for clusters than for hits, at high energies, the shower maximum position is higher for clusters compared to hits.

In summary, while the saturation yields to a later shower maximum position for clusters compared to hits, the increasing shower particle angles in later layers lead to a later shower maximum for hits compared to clusters. Since cluster saturation increases the higher the energy and the effect of larger shower particle angles the later the layer is present at all energies, the shower maximum position is greater for clusters compared to hits at high energies and vice versa for low energies.

(2) **Comparison between $t_{\mathrm{max}}^{\mathrm{exp}}$ and $t_{\mathrm{max}}^{\mathrm{theo}}$:**

As can be seen in Figure 76, the shower maximum position $t_{\mathrm{max}}^{\mathrm{exp}}$ for hits and for clusters deviate from $t_{\mathrm{max}}^{\mathrm{theo}}$ (Equation 38). The different trends observed for hits and for clusters as well as their energy dependence is explained by the discussed effects of saturation and hit response dependence on the shower particle angle. Especially the tendency for clusters to yield a later shower maximum the higher the energy is reasonably explained by saturation. Therefore, one can conclude that the agreement between $t_{\mathrm{max}}^{\mathrm{theo}}$ and $t_{\mathrm{max}}^{\mathrm{exp}}$ for clusters in the simulation at 40 GeV and higher, as well in the data for 80 GeV is caused by saturation. In general, $t_{\mathrm{max}}^{\mathrm{theo}}$ overestimates $t_{\mathrm{max}}^{\mathrm{exp}}$ for hits and clusters in both the data and simulation.

As discussed, both $f(t)$ (Equation 36) and the derived quantity $t_{\mathrm{max}}^{\mathrm{theo}}$ (Equation 38), are empirical functions that have been determined in a simulation [GZ+20]. In particular, they are derived from the mean longitudinal energy profile, i.e. the fractional energy deposition in an electromagnetic shower per radiation length. The characteristics of the longitudinal shower profile are highly device dependent, especially dependent on what the calorimeter measures. In [GZ+20], an EGS4 simulation [NHR85] of a 30 GeV electron shower is presented showing a later shower maximum position of the energy deposition compared to the maximum number of electrons in the electromagnetic shower. Since individual shower particles are counted with EPICAL-2 rather than measuring the fractional energy loss per radiation length, the discrepancy between $t_{\mathrm{max}}^{\mathrm{theo}}$ and $t_{\mathrm{max}}^{\mathrm{exp}}$ may be well explained by the difference in measuring shower particles rather than energy deposition.

(3) **Comparison of $t_{\mathrm{max}}^{\mathrm{exp}}$ in data and simulation**

Overall, the simulation predicts a later shower maximum position compared to the data for both hits and clusters consistent with the direct comparison of the longitudinal shower profiles between the data and simulation discussed in context of Figure 74 in the previous section. The shift of the shower maximum position between the data and simulation increases from 1 GeV to 80 GeV as follows:

shift for:	1 GeV :	80 GeV :
hits	$0.1033 \pm 0.0095\ X_0$	$0.2747 \pm 0.0568\ X_0$
clusters	$0.0557 \pm 0.0072\ X_0$	$0.1986 \pm 0.0541\ X_0$

Three major potential differences between the data and simulation are considered here to cause the observed shift of the shower maximum position in simulation compared to data: a difference in the amount of the physical material per layer, additional material in front of EPICAL-2 and a difference in the shower evolution. The three potential differences are discussed below:

Averaged over all energies, the total shift of the shower maximum position translates into a shift of $0.0265 \pm 0.0014\ X_0$ per layer for hits and $0.0169 \pm 0.0012\ X_0$ per layer for clusters. Consequently, the shower maximum position in data and simulation would agree if the amount of material per layer would be $0.0265 \pm 0.0014\ X_0$ higher in data compared to the implementation in simulation for the hits measurement and $0.0169 \pm 0.0012\ X_0$ for the clusters measurement. In relation to hits, $0.0265\ X_0$ corresponds to ~ 0.09 mm of tungsten, which is equal to ~ 3 % of the tungsten absorber thickness of 3 mm equipped in a single EPICAL-2 layer. $0.0265\ X_0$ of other materials equipped in EPICAL-2 translates to e.g. 8 m for air or 2.5 cm for silicon.

Similar to the difference in the amount of material per layer, material in front of EPICAL-2 in the beam line could cause an earlier shower maximum position. Typical for test-beam measurements, the beam approaches an exit window, air and scintillators before reaching the test device which introduces some additional material in front of the test device. In [Zha17], the additional material in the beam line is estimated conservatively as an equivalent depth of $0.12\ X_0$ for SPS, and $0.15\ X_0$ for DESY according to their specifications. Although the additional material could explain a total shift, the increase with energy cannot be explained.

An overall shift of the shower maximum position and additional material per layer were considered in the discussion before. While an overall shift cannot explain the increasing difference of the shower maximum position between data and simulation, the additional material per layer is considered unlikely as the amount of material necessary would not fit into the EPICAL-2 setup. Both together could potentially explain the observed difference between data and simulation. However, it is unlikely that the amount of material is equipped in EPICAL-2 and not known and thus not implemented in simulation.

Since the shower maximum position directly relates to the longitudinal shower profiles and thus the shower evolution itself, the discrepancy between the data and simulation could be caused by imperfections of the GEANT4 simulation while describing the shower evolution.

5.1.3 Lateral Shower Profile

The lateral shower profile refers to the density of hits or clusters, both used as a detector response measure, as a function of the radial distance to the shower axis. The distance r' between every pixel hit or cluster and the shower axis is calculated as follows:

$$r' = \sqrt{(x - x_{\mathrm{beam}})^2 + (y - y_{\mathrm{beam}})^2} \tag{39}$$

As discussed in section 4.2.7, the shower axis is defined by the layer 0 cluster position $(x_{\mathrm{beam}}, y_{\mathrm{beam}})$ and the inclination of the beam (see section 4.2.6). For each layer l, the density $\rho^l_{\mathrm{hits,clusters}}(r, \Delta r)$ is calculated in narrow rings of Δr in a distance of r to the shower axis, by summing all pixel hits or clusters $N^l_{\mathrm{hits,clusters}}$ that lie in a given ring divided by the number of active pixels $N^l_{\mathrm{act.\ pixels}}$ in this ring:

$$\begin{aligned} \rho^l_{\mathrm{hits,clusters}}(r, \Delta r) &= \frac{1}{29.24\ \mu\mathrm{m} \cdot 26.88\ \mu\mathrm{m}} \frac{N^l_{\mathrm{hits,\ clusters}}(r, \Delta r)}{N^l_{\mathrm{active\ pixels}}(r, \Delta r)} && (40) \\ &= \frac{1272.3}{\mathrm{mm}^2} \frac{N^l_{\mathrm{hits,clusters}}(r, \Delta r)}{N^l_{\mathrm{act.\ pixels}}(r, \Delta r)} && (41) \end{aligned}$$

Furthermore, the ratio $N^l_{\mathrm{hits,clusters}}/N^l_{\mathrm{act.\ pixels}}$ is normalised to the pixel size yielding to the maximum density of 1272 pixel hits per millimetre squared if all active pixels register a hit. In this thesis, the ring width is chosen as 0.1 mm for $r < 2$ mm and 0.5 mm for $r > 2$ mm. A previous analysis [Zha17] has shown that these two ring widths allow the detailed shape to be explored in both the shower centre and the tail. Figure 79 illustrates the density calculation. For instance, the blue circles with radii at $r = 0.1\,\mathrm{mm}$ and at $r = 0.2\,\mathrm{mm}$ centred at the beam impact position as shown by the red cross define a ring of width Δr. Inside of the ring, all pixel hits as shown in green are summed up (N^l_{hits}). Then, all active pixels are counted ($N^l_{\mathrm{act.\ pixels}}$), i.e. all pixels shown in green and in gold omitting the masked ones shown in gray. Finally, the ratio of both normalised to the pixel area is calculated yielding the hit density in the given ring.

The upper panel of Figure 80 shows the lateral hit (left) and cluster (right) density distribution for selected energies and exemplary for layer 7. The measured data are shown as full circles, whereas the simulations are shown as open squares. Overall, the simulation describes the measured data and a clear energy ordering is visible; an increasing density with energy which reflects the increasing shower particle density with higher energies. At 80 GeV, the hit density is highest and close to the maximum hit density of 1272 pixel hits per millimetre squared. This leads to the saturation of clusters, which can be observed in the cluster density at 80 GeV, where a decrease in the density is observed for $r \lesssim 0.4$ mm in Figure 80 (top right).

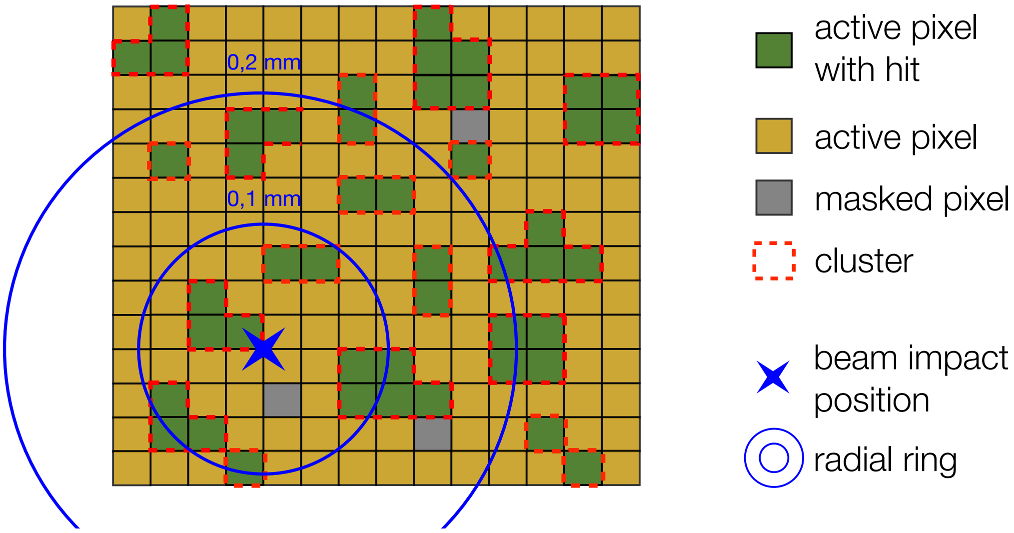

Figure 79: *Illustration of the lateral density calculation by counting pixel hits or clusters in narrow rings around the shower axis.*

The lower panel of Figure 80 shows the lateral hit (left) and cluster (right) density distribution for selected layers and exemplary for 40 GeV: the measured data as full circles and the simulations as open squares. Both clusters and hits show a clear layer ordering. However, a saturation of the density can be observed in layer 7 for clusters compared to hits due to saturation. The observed layer ordering directly relates to the different stages of the electromagnetic shower development as discussed in context of the longitudinal shower profiles in the previous section 5.1.1: From the start of the shower evolution to the maximum number of shower particles and to the thinning-out of the shower particle number in the shower tail. The layer 2 density distribution is shown in green and reflects the start of the shower evolution with a high density close to shower axis and a steep decrease of the density the larger the radius. Layer 7 corresponds to the shower maximum and is shown in blue with an overall high density and a broader distribution compared to layer 2. After the shower maximum, the shower gets broader and the number of hits and clusters thins out. Therefore, layer 12 shows a density distribution which is broader compared to layer 7 with a lower density close to the shower axis and a higher density in the lateral shower tail for larger radii. Finally, layer 18 reflects the end of the shower evolution where the density distribution is broadest and the density is generally low.

The minor discrepancies between the measured data and the simulation are directly linked to the difference in the longitudinal shower profiles between data and simulation as discussed in the previous section. The simulation predicts the shower developing deeper in EPICAL-2. Therefore, when comparing the lateral density in the measured data and in the simulations for the same layer, a shift in the longitudinal

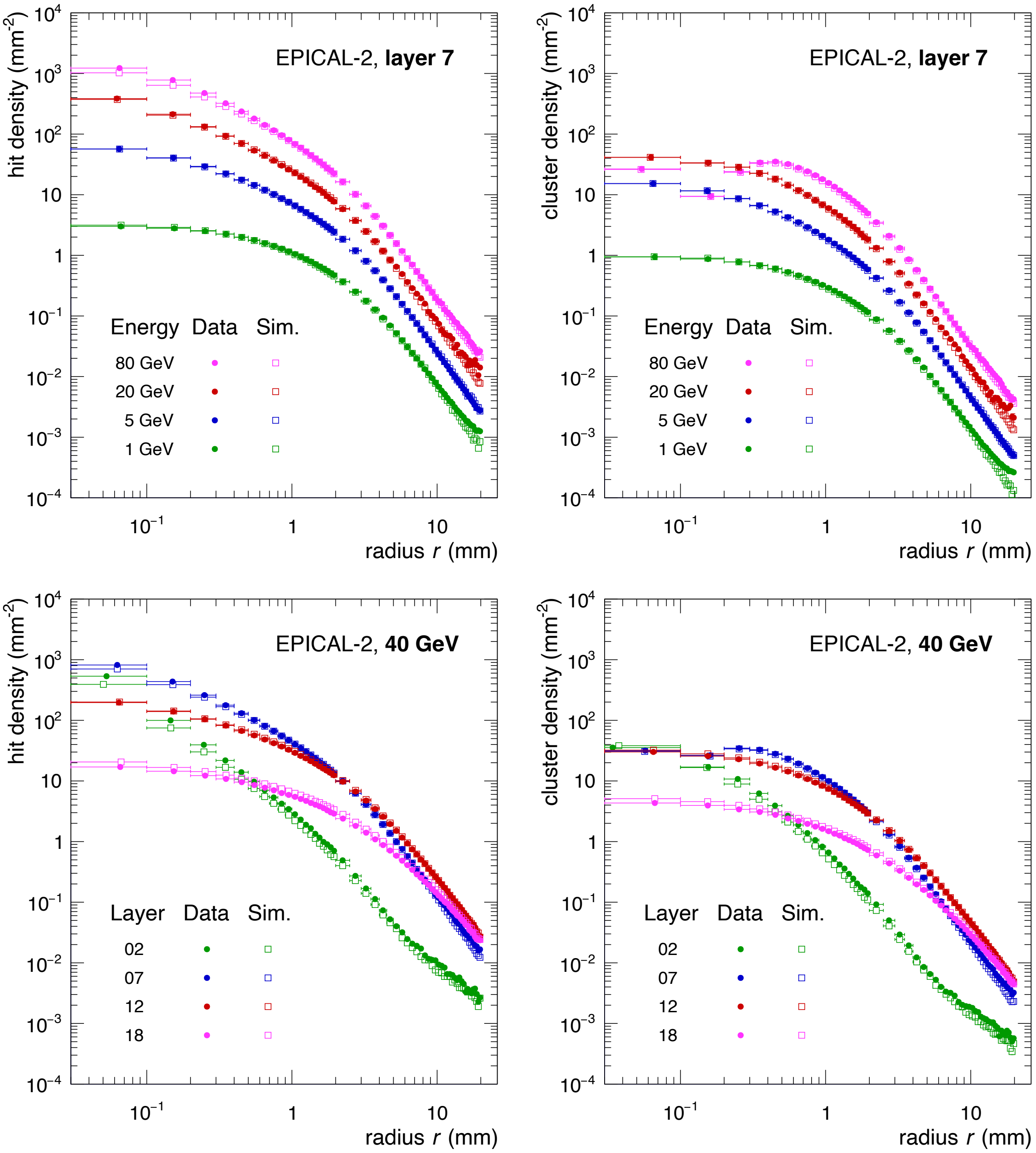

Figure 80: *Energy dependence (top) and layer dependence (bottom) of the lateral hit (left) and cluster density (right) as a function of radial distance r to the shower axis.*

profiles between data and simulation leads to a comparison of different stages of the shower evolution. For layer 2 and layer 7, the measured data is above the simulation since the shower is further developed in data. Whereas in layer 12, the measured data and the simulation are right on top of each other, in layer 18, simulation is above data since in data the shower is further thinned out than in simulation. Despite the difference in the density due to a shift of the longitudinal profiles, overall, the measured data is well described by the simulation over several orders of magnitude.

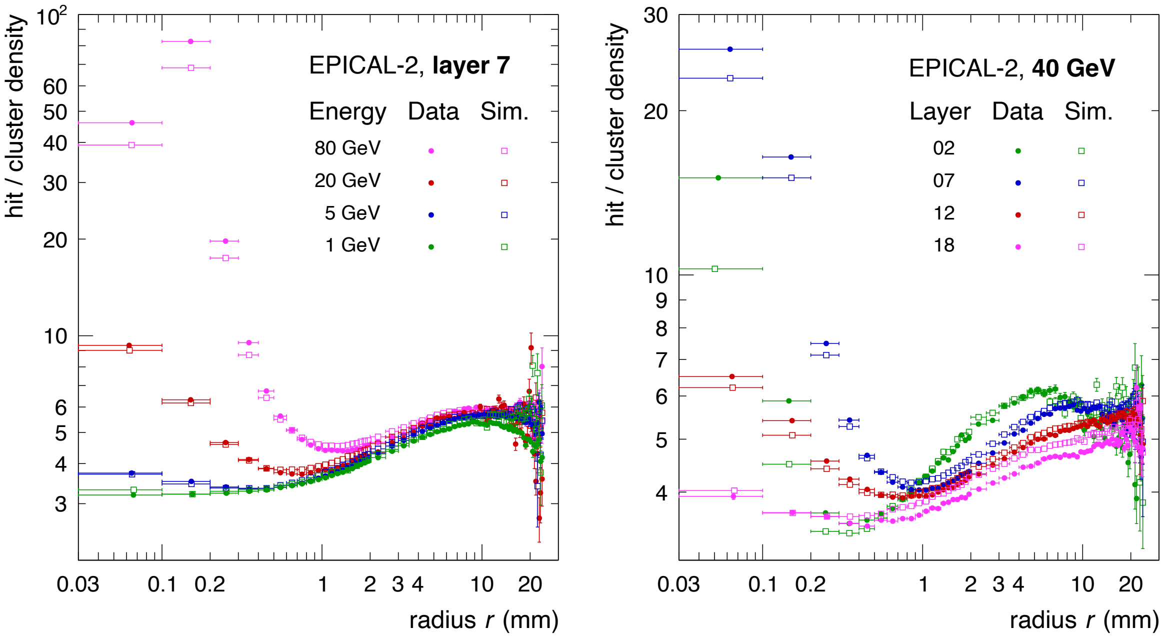

Figure 81: *Energy dependence (left) and layer dependence (right) of the ratio of hit and cluster density as a function of radial distance r to the shower axis.*

To further investigate the effect of saturation, the ratio of the hit density and the cluster density is calculated and both the energy and layer dependence is studied:

Figure 81 (left) shows the hit-to-cluster ratio for selected energies exemplary in layer 7. While at 1 GeV and 5 GeV the hit-to-cluster ratio is around 3 to 4 for $r \rightarrow 0$, the ratio increases up to 40 to 80 hits per cluster at 80 GeV for $r \rightarrow 0$. In addition, the higher the energy, the stronger the increase of the hit-to-cluster ratio for $r \rightarrow 0$. Towards the lateral shower tail, i.e. for $r \rightarrow 20\,\mathrm{mm}$, the hit-to-cluster ratios for the different energies converge to a hit-to-cluster ratio around 6. The general trend of an increasing hit-to-cluster ratio for $r \rightarrow 10\,\mathrm{mm}$ is explained by shower particles traversing the EPICAL-2 layers with a larger angle, which produces more hits and thus larger clusters. After careful investigations it is still unclear why the hit-to-cluster ratio decreases for $r \rightarrow 25\,\mathrm{mm}$ at 1 and 5 GeV in the measured data and stays constant in the simulation. In context of the energy dependence, one can conclude that the higher the energy the higher the hit-to-cluster ratio close to the shower axis. This also shows that cluster saturation increases the higher the energy and that it is strongest around the shower axis.

Figure 81 (right) shows the layer dependence of the hit-to-cluster ratio for selected layers and exemplary for 40 GeV. For $r \rightarrow 0$, the observed layer dependence of the hit-to-cluster ratio directly reflects the longitudinal shower evolution. The highest ratio is observed in layer 7 in the shower maximum where the cluster saturation is strongest due to highest shower particle densities. Before the shower maximum, during the

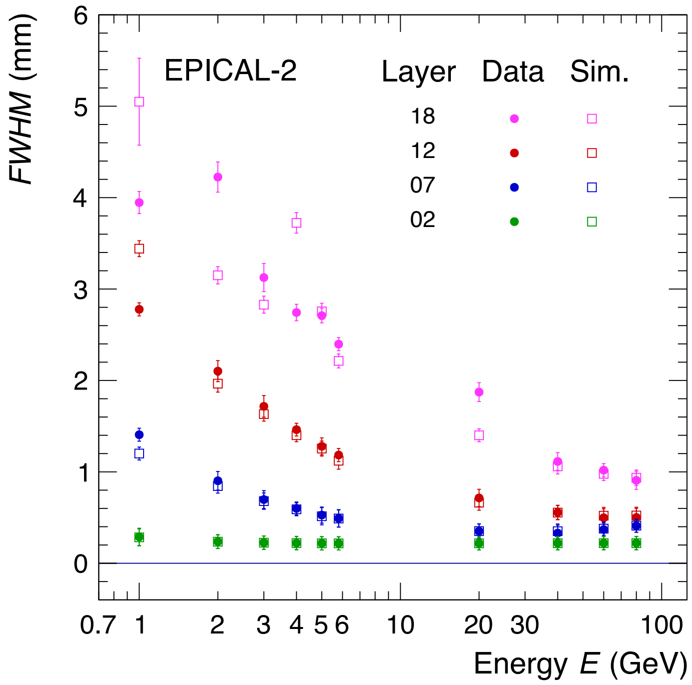

Figure 82: *Energy dependence of the average shower width for selected layers.*

shower start, a high particle density only prevails close to the shower axis. After the shower maximum, in layer 12 and layer 18, the particle density decreases leading to a lower hit-to-cluster ratio and thus a lower cluster saturation.

5.1.4 Average Shower Width

The lateral density profiles discussed in the previous section provide great detail of the lateral shower evolution as a function of the distance to the shower axis for each layer. However, it is useful to determine one value per layer which reflects the average lateral width of the electromagnetic shower in this layer. Since the cluster density suffers from saturation, here, only the hit density is considered. The average shower width is calculated as the full width half maximum (FWHM) of the lateral hit density distribution.

Figure 82 shows the average shower width as a function of the electron energy for selected layers. The measured data are shown as full circles, whereas the simulations are shown as open squares. A clear layer ordering can be observed: the later the layer, the greater the shower width. For instance, the width is $\sim 0.2\,\mathrm{mm}$ across all energies in layer 2, the shower start. In layer 7, the shower width decreases the higher the energy for $E < 20$ GeV and increases for $E \geq 20$ GeV. This increase is a result of saturation which limits the density close to the shower axis and enhances the calculated shower width. An overall energy dependence of the shower width can be observed for the

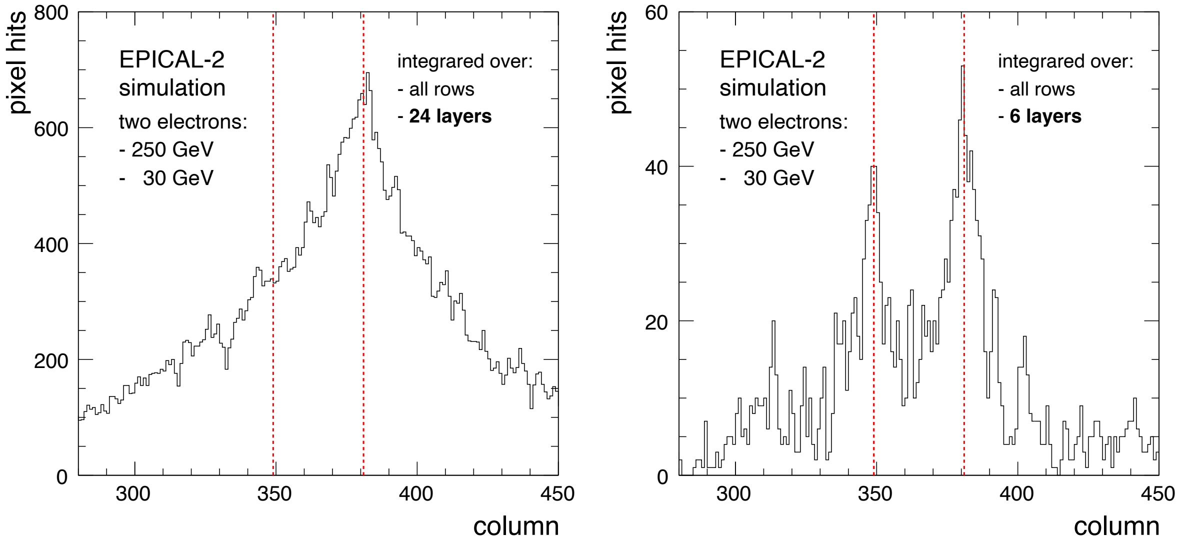

Figure 83: *Simulation of two electrons with a spatial distance of* $\sim$ 1.1 mm*: Number of pixel hits integrated over one transverse dimension and either over all 24 layers of* EPICAL-2 *(left) or integrated over the first 6 layers (right) as a function of column. The dashed red lines indicate the spatial position of incidence of the primary particles.*

layers 7, 12 and 18: the higher the energy the lower the width. Overall, the simulation describes the measured data and the observed trends.

The average shower width directly corresponds to the possibility of separating nearby showers. If one assumes two 20 GeV showers at a distance of 1 mm, then the two showers can be identified given the width of a shower at 20 GeV of $\sim$ 0.2 mm in layer 2, $\sim$ 0.4 mm in layer 7 and $\sim$ 0.7 mm in layer 12 as shown in Figure 82. One can conclude, that the power of separating nearby showers in EPICAL-2 can be applied to all calorimeter applications utilising pixel layers. Even if only one pixel layer is available, if positioned in the right depth of a calorimeter, a separation of multiple showers is possible at a distance of the average shower width as shown in Figure 82. The separation of nearby showers is further discussed in context of ALICE-FOCAL in the next section.

5.1.5 Shower Separation and the ALICE-FOCAL

With the usage of silicon sensor layers that have a high granularity of $\sim 30 \times 30\,\mu\text{m}^2$, a separation of electromagnetic showers which are more than one millimetre apart from each other should be possible, based on the analysis of the average shower width presented in the previous section. The separation of showers using high granularity sensor layers is further elaborated in this section by presenting two distinct simulation scenarios. In addition, the separation of showers is discussed in the context of the ALICE-FOCAL.

To demonstrate the separation power provided by high granularity layers, a single event containing two electrons with a spatial separation of $\approx 1.1\,\text{mm}$ is simulated: One electron with an energy of 250 GeV and a second electron with an energy of 30 GeV. For this single event in simulation, Figure 83 shows two distribution of the number of pixel hits as a function of column integrated over all 24 layers in EPICAL-2 (left) and integrated over the first 6 layers only (right). The dashed red lines indicate the spatial positions of incidence of the two primary electrons.

Integrated over all layers, only a single peak of the high-energy electron can be seen and the lower-energy electron cannot be identified. When integrating over the first 6 layers only, two peaks are visible, each at the spatial position of incidence of the primary electron. This visualises the separation of nearby electromagnetic showers with a spatial distance of a few millimetres with the EPICAL-2 prototype. In a conventional calorimeter, the two showers would be measured as a single electromagnetic shower.

The primary objective of the ALICE-FOCAL is the measurement of direct photons with high precision, which requires the capability to separate nearby electromagnetic showers, especially to identify decay photons and to reconstruct photon pairs with a spatial separation of a few millimetres. The usage of individual pixel layers in the ALICE-FOCAL will ensure the particle separation as visualised with the EPICAL-2 in Figure 83. Assuming the two electromagnetic showers shown in Figure 83 emerge from two photons from a π^0 decay, photon γ_1 and a photon γ_2. This means that γ_1 and γ_2 are separated by ≈ 35 pixels which corresponds to a distance d of $d \approx 1.1\,\text{mm}$ given a pixel size of $30 \times 30\,\mu\text{m}^2$. This distance translates to an energy of the π^0 in a certain distance to the detector surface. For a symmetric π^0 decay and the ALICE-FOCAL beeing positioned 7 m away from the interaction point of the collision, the distance of $d \approx 1.1\,\text{mm}$ translates to a π^0 energy of ≈ 1.6 TeV. That means, by using pixel layers, two photons from a pion with an energy up to ≈ 1.6 TeV can be recognised.

In addition to silicon pixel layers, the FOCAL will contain silicon pad layers with a lower granularity of $1 \times 1\,\text{cm}^2$. To visualise the difference between pixel and pad layers, here, the EPICAL-2 surface of $\approx 30 \times 30\,\text{mm}^2$ is divided into 16 regions of the size $7.5 \times 7.5\,\text{mm}^2$ and the number of pixel hits in each region is considered as a pad amplitude to emulate the response of silicon pad layers. Figure 84 shows the simultaneous measurement of an electron (red) with an energy of 20 GeV and a hadron (blue) with an energy of 30 GeV at a distance of $\approx 7.5\,\text{mm}$ in simulation. The top panels show the EPICAL-2 measurement, i.e. the measurement with a high granularity of $\approx 30 \times 30\,\mu\text{m}^2$, whereas the bottom panels shows the amplitudes of the pads as the size of the boxes calculated from the number of pixel hits in the $7.5 \times 7.5\,\text{mm}^2$ regions. The left figures show the detector response as a function of the transverse positions x and y integrated over all 24 layers and the right figures show

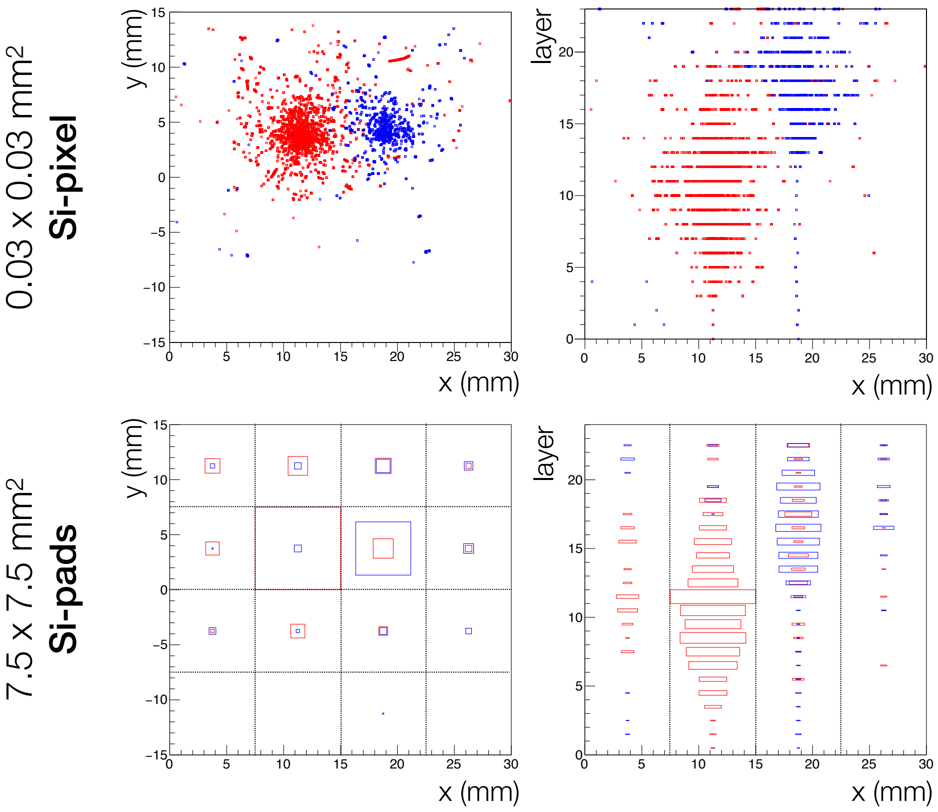

Figure 84: *Simultaneous measurement of en electron* (20 *GeV*) *and a hadron* (30 *GeV*) *at a distance of* ≈ 7.5 mm *in simulation. The electron response is shown in red whereas the pion response is shown in blue.*

the longitudinal response, i.e. layer number, as a function of x integrated over y. In the pad case (bottom), a full reconstruction of the electron and the hadron is impossible. In contrast, in the pixel case (top), the clear topology of the electron and the hadron can be seen and a full reconstruction should be possible. The shower start and the shower shape of both particle showers can be identified by eye and one can track the evolution of the particles in the detector.

The two simulation scenarios discussed in this section demonstrate the potential of a high-granularity pixel layer. The simulation scenario with two electrons shows that a discrimination of two particle showers in a distance of ≈ 1.1 mm is possible with the EPICAL-2 prototype and that by using high-granularity layers in the ALICE-FOCAL the discrimination between the two photons from a neutral pion decay is possible up to pion energies of ≈ 1.6 TeV. Furthermore, the simulation scenario with one hadron and one electron demonstrates the power of the high-granularity by comparing the EPICAL-2 measurement to an emulation of a pad measurement and the ALICE-FOCAL.

5.2 Energy Measurement Performance

One of the main objectives to utilise an electromagnetic calorimeter in high-energy physics experiments is to measure the energy of particles which produce an electromagnetic shower. To measure the energy of particles, both the energy response and the energy resolution of deployed calorimeters are important properties to be known. The energy response describes how the measured calorimeter signal relates to the actual incident particle energy and the energy resolution addresses how good the incident particle energy can be measured.

This section presents the energy measurement with EPICAL-2. Parts of the energy measurement results obtained in this thesis are published in [Alm+23]. As discussed in section 2.2, the EPICAL-2 energy measurement relies on counting individual charged shower particles. Both the total number N_{hits} of hits and the total number N_{clus} of clusters are used here as a proxy for the number of charged particles in an electromagnetic shower.

In this section, first, the signal distributions for N_{hits} and N_{clus} are presented. Second, the energy response derived from the signal distributions is discussed and finally, the energy resolution is presented. All results are compared to simulation.

5.2.1 Signal Distributions

Figure 85 shows the N_{hits}- and N_{clus}-distributions, i.e. the EPICAL-2 signal distributions obtained from using hits (top panel) as a measure for the incident particle energy and from using clusters (bottom panel), for DESY energies (left) and for SPS energies (right). Data are shown as symbols, whereas simulations are shown as lines. All distributions show a clear Gaussian peak structure with an increasing mean value the higher the incident particle energy. Overall, the distributions from data are well described by the EPICAL-2 simulations. Only small systematic shifts can be observed, which, however, do not influence the energy measurement performance obtained from simulation as pointed out in section 3.4.6.

To determine the energy measurement performance of EPICAL-2, the mean value μ and the width σ of each signal distribution is calculated numerically, i.e. in particular the standard deviation (RMS) is taken for the calculation of σ. The obtained values μ and σ for both hits and clusters at all energies for data and for simulation are summarised in appendix A.2.

To cross-check the numerically obtained results for the mean μ and the width σ of the signal distributions, each signal distribution is also parametrised with a Gaussian function and the function parameters, the Gaussian mean and width, are extracted. For the rest of this section, μ and σ are now called μ_{num} and σ_{num} for the numerical

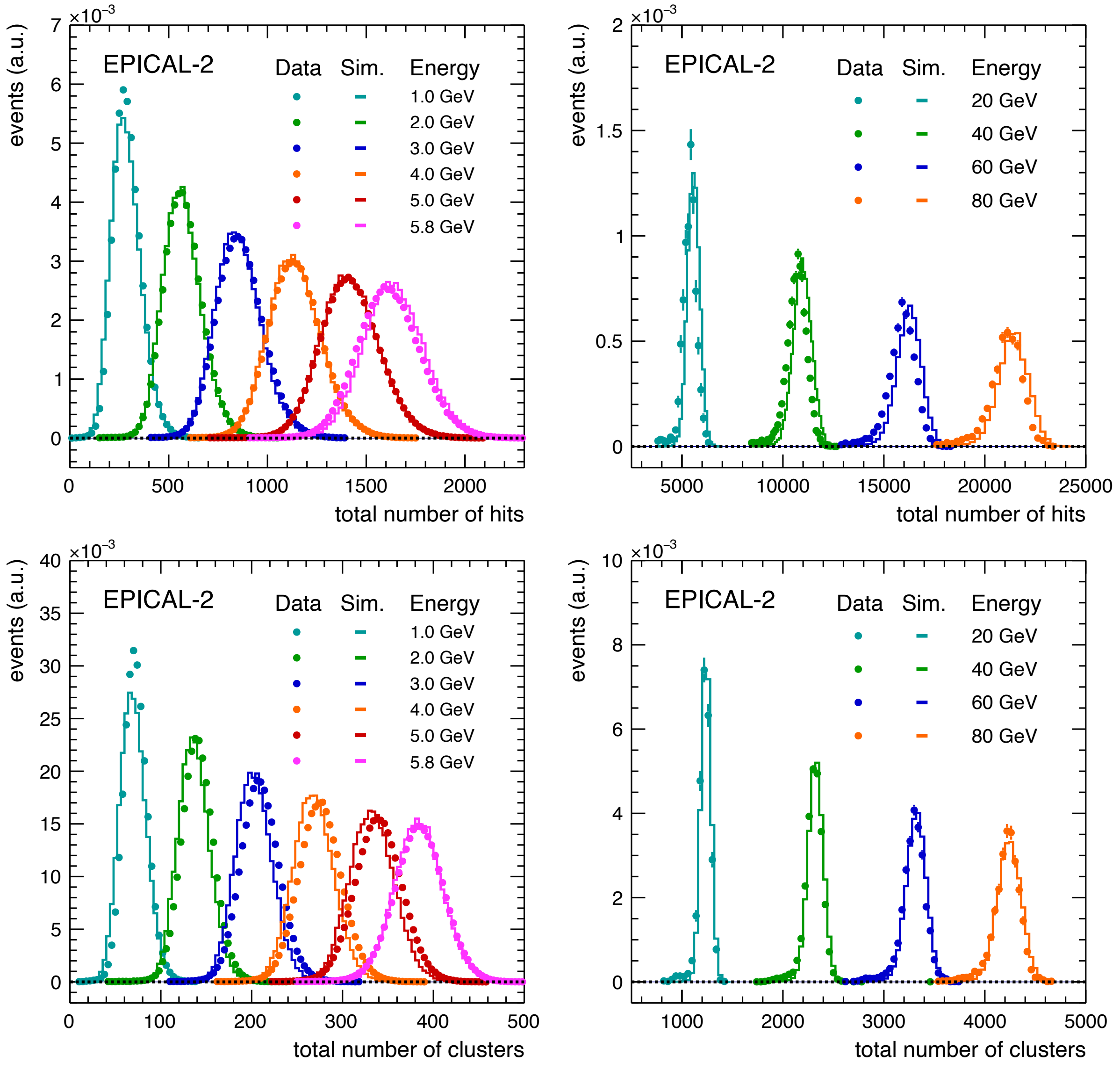

Figure 85: *Comparison between data and simulation for the* N_{hits}*- (top) and* N_{clus}*-distributions (bottom) at the* DESY *energies ranging from* 1.0 GeV *to* 5.8 GeV *(left) and at the* SPS *energies ranging from* 20 GeV *to* 80 GeV *(right).*

calculation and μ_{gaus} and σ_{gaus} is used for the values derived from the Gaussian parameterisations to distinguish both methods.

Figure 86 shows the ratios $\mu_{\text{num}}/\mu_{\text{gaus}}$ (left) and $\sigma_{\text{num}}/\sigma_{\text{gaus}}$ (right) as a function of the incident electron energy E. The mean values μ_{num} and μ_{gaus} obtained from the different methods are in agreement as visible in Figure 86 (left) with deviations mostly much smaller than 1 %. In contrast, σ_{gaus} deviates from σ_{num}; σ_{num} is systematically higher than σ_{gaus} as shown in Figure 86 (right).

The deviations between σ_{num} and σ_{gaus} are a result of the Gaussian parametrisation being insensitive to the tails of the signal distributions. Any deviations from the Gaussian form will yield higher σ_{num} compared to σ_{gaus}.

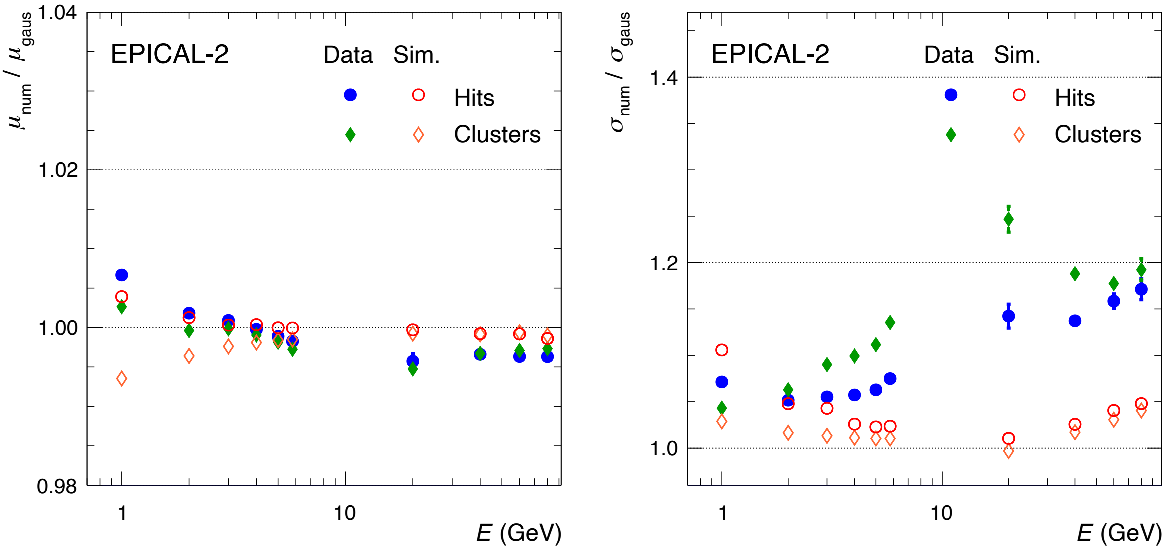

Figure 86: The ratio $\mu_{\text{num}}/\mu_{\text{gaus}}$ *(left) and the ratio* $\sigma_{\text{num}}/\sigma_{\text{gaus}}$ *(right) as a function of the energy for both the measured data and the simulation.*

Consequently, the numerical calculation is used throughout this work because the calculation is more sensitive to the actual signal distributions. Furthermore, the numerical values are preferred as a robust method without relying on any parametrisation.

5.2.2 Energy Response and Linearity

The energy response of a calorimeter refers to the signal that is generated in the calorimeter as a response to an incident particle with a certain energy.

In this section, the energy response is determined for the EPICAL-2 prototype. Furthermore, the energy response is parametrised using both a linear function and a non-linear function to evaluate the linearity of the energy response, i.e. how well the calorimeter signal scales linearly with the incident energy.

Figure 87 shows the mean values of the N_{hits} -distributions ($\mu = \langle N_{\text{hits}} \rangle$) as blue dots and the mean values of the N_{clus} -distributions ($\mu = \langle N_{\text{clus}} \rangle$) as blue squares for data as a function of the incident electron energy E.

As discussed in context of Table 3 in section 2.3.2, the set electron beam energy at DESY deviates from the true beam energy. Therefore, the difference between set and true energy is attributed as one-sided systematic uncertainty on the DESY energy in data, which is represented by the horizontal error bars on the DESY beam energies in Figure 87.

In addition to the mean values obtained from data, the results from simulation are shown in the figure as open red circles for hits and as open red squares for clusters. Over the full energy range, the results from data and the simulation prediction are in

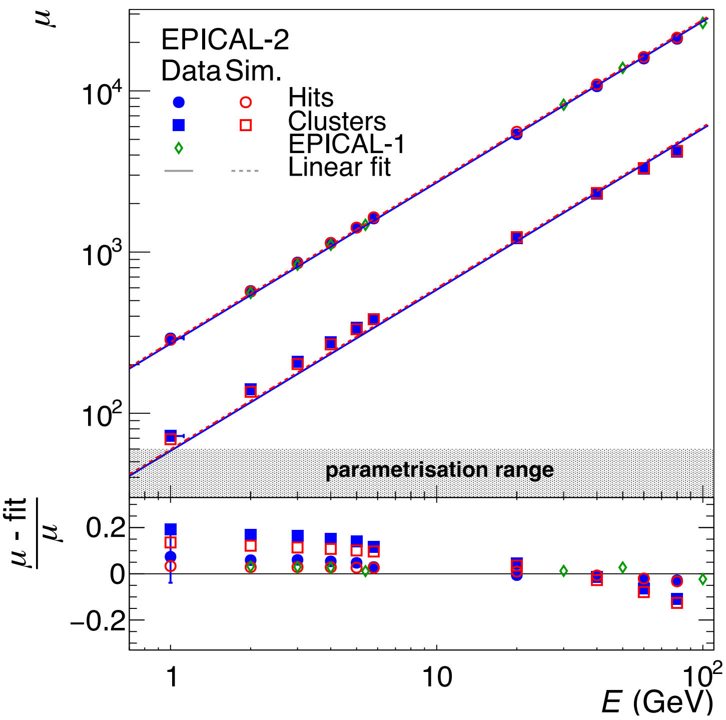

Figure 87: *EPICAL-2 energy response using the observables hits and clusters as a function of beam energy for both data and simulation (values are given in appendix A.2). The energy response is parametrised with the linear fit $f_R^{\text{lin.}}(E)$ (Equation 42) taking the full energy range into account.*

good agreement. To test the linearity of the energy response of EPICAL-2, both a linear parameterisation and a non-linear parameterisation of the energy response are discussed in the following.

(1) **Linear Parametrisation of the Energy Response:**

The energy response is parametrised with a first order polynomial response function $f_R^{\text{lin.}}(E)$ separately for hits and clusters:

$$f_R^{\text{lin.}}(E) = C_{\text{hits, clus}} \cdot E + b_{\text{hits, clus}} \tag{42}$$

C_{hits} (C_{clus}) converts the beam energy into hits (clusters) and b_{hits} (b_{clus}) corresponds to the y-axis intercept. The top panel of the plot in Figure 87 shows the parametrisation of the hit and cluster energy response for both data and simulation each separately with $f_R^{\text{lin.}}(E)$, which is referred to as linear fit in the legend of the figure. The parametrisation range is shown as a gray shaded region in Figure 87, which is the full energy range including all data points from $E = 0$ to $E = 80$ GeV. At $E = 0$ a data point obtained from pedestal measurements is used in the parametrisation of the data with $f_R^{\text{lin.}}(E)$, which, however, cannot be displayed on a

energy param. range (GeV)	C_{hits} (GeV^{-1})		C_{clus} (GeV^{-1})	
	data	simulation	data	simulation
[0, 85]	270.16 ± 0.07	275.99 ± 0.04	58.36 ± 0.01	59.67 ± 0.01

Table 8: *Parameters of $f_R^{\text{lin.}}(E)$ obtained from the parametrisation of the energy response in data and simulation for both hits and clusters.*

logarithmic scale. The pedestal measurements are performed without beam, yielding the response at zero energy, i.e. the noise level, with both N_{hits} and N_{clus} at $(2.900 \pm 0.009) \cdot 10^{-3}$ after pixel masking. For simulation, the intercept is fixed to zero ($b_{\text{hits, clus}} := 0$) as no hits and thus clusters are observed. The parametrisation of $f_{\text{R}}^{\text{lin.}}(E)$ to the data effectively leads to $b_{\text{hits, clus}} \approx 0$ as expected from the constraint at $E = 0$ given the pedestal measurement. Table 8 lists C_{hits} and C_{clus} as obtained from the parameterisations for both data and simulation.

The lower panel of Figure 87 shows the relative difference r between data or simulation and the corresponding parametrisation with $f_{\text{R}}^{\text{lin.}}(E)$:

$$r = \frac{\mu - f_{\text{R}}^{\text{lin.}}(E)}{\mu} = 1 - \frac{f_{\text{R}}^{\text{lin.}}(E)}{\mu} \tag{43}$$

The DESY beam energy uncertainty displayed as horizontal error bars in the top panel of Figure 87 translates into an uncertainty on the ratio points shown as one-sided vertical error bar in the bottom panel.

Overall, the energy response of EPICAL-2 deviates from linearity up to $\sim 5\,\%$ for hits and up to $\sim 18\,\%$ for clusters in the measured data. The deviation from linearity is largest for both hits and clusters at 1 GeV, where the uncertainty of the DESY beam energy is largest. For the SPS energies, the deviation from linearity increases the higher the energy. In simulation, the general trend is similar to the data, but deviations from linearity are less than $\sim 3\,\%$ for hits and less than $\sim 10\,\%$ for clusters.

Although the deviation from linearity differs between data and simulation on an absolute scale, the difference between the deviation from linearity for hits and clusters is similar for both data and simulation. Therefore, the cluster measurement introduces a non-linear behaviour due to saturation as discussed in section 5.1.3. Saturation is stronger for clusters than for hits and the stronger the higher the energy. Furthermore, the higher the energy the stronger the influence of lateral and longitudinal leakage which also leads to a larger deviations from linearity at high energies.

While deviations from linearity are stronger in the data than in the simulation for the DESY energies, at the SPS energies, the deviations from linearity are similar for both the data and simulation. This means that the stronger deviation from linearity in the data compared to the simulation at DESY can be attributed to the uncertainty of the beam energy at DESY.

energy param. range (GeV)	C		β	
	data	simulation	data	simulation
hits				
[0, 85]	296.20 ± 0.24	290.91 ± 0.10	0.9719 ± 0.0002	0.9826 ± 0.0001
clusters				
[0, 85]	78.18 ± 0.06	73.54 ± 0.02	0.9144 ± 0.0002	0.9319 ± 0.0001

Table 9: *Parameters of $f_{\mathrm{R}}^{\mathrm{pow.}}(E)$ obtained from the parametrisation of the energy response for both hits and clusters for simulation and data.*

Moreover, Figure 87 includes the energy response of the EPICAL-1 prototype using the total number hits [Haa+18]. Even on an absolute scale, the EPICAL-1 data agree with those from EPICAL-2, which is likely a result of a similar number of pixels with a similar pixel size. The similar energy response behaviour of the prototypes supports the conclusion that the deviations from linearity in the measured data at the DESY energies with EPICAL-2 is mainly a result of the DESY beam energy uncertainty.

(2) **Non-Linear Parametrisation of the Energy Response:**

After the discussion of the linear parametrisation of the energy response, a non-linear energy response description is discussed next to investigate the non-linearity and if a non-linear function can better describe the energy response. Therefore, the energy response is parametrised with a power-law function $f_{\mathrm{R}}^{\mathrm{pow.}}(E)$:

$$f_{\mathrm{R}}^{\mathrm{pow.}}(E) \;=\; C_{\mathrm{hits,\,clus}} \cdot (E/\mathrm{GeV})^{\beta_{\mathrm{hits,\,clus}}} \tag{44}$$

Here, C_{hits} (C_{clus}) converts the power β_{hits} (β_{clus}) of the beam energy E into the total number of hits (clusters). As for zero energy, $0^{\beta_{\mathrm{hits,\,clus}}}$ always yields zero, the y-axis intercept is effectively fixed to zero. The top panel of Figure 88 shows the parametrisation of both data and simulation each with $f_{\mathrm{R}}^{\mathrm{pow.}}(E)$ referred to as power law fit in the legend. The lower panel of Figure 88 displays the relative difference between data or simulation and the corresponding parametrisation with $f_{\mathrm{R}}^{\mathrm{pow.}}(E)$. The parameters obtained from the parametrisation with $f_{\mathrm{R}}^{\mathrm{pow.}}(E)$ to data and simulation are shown in Table 9 for both hits and clusters.

Over the full energy range, the power law function describes the hit measurement very well with deviations below 2 % for both data and simulation. The cluster measurement shows deviation from $f_{\mathrm{R}}^{\mathrm{pow.}}(E)$ up to ~ 8 % for data and up to ~ 5 % for simulation both at the lowest energy point at 1 GeV. A power $\beta = 1$ in $f_{\mathrm{R}}^{\mathrm{pow.}}(E)$ would correspond to a linear behaviour and the lower the β ($\beta \to 0$) the stronger the non-linearity. The hit measurement in data shows a lower non-linearity compared to the cluster measurement in data as visible by the power β which is $\beta_{\mathrm{hits}} \sim 0.97$ for hits and $\beta_{\mathrm{clus}} \sim 0.91$ for clusters. In contrast, the energy response in simulation appears to

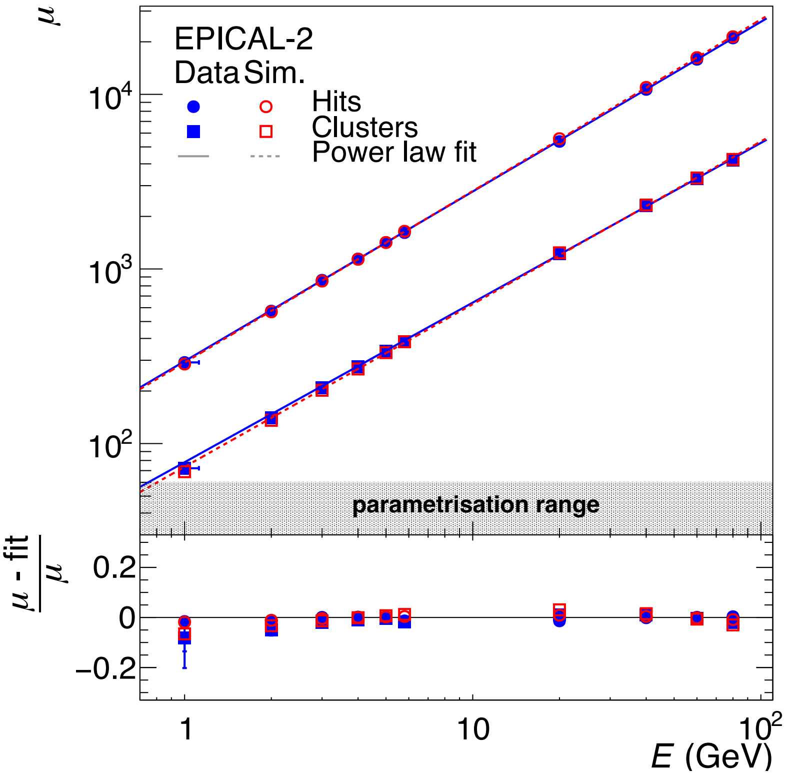

Figure 88: *E*PICAL*-2 energy response using the observables hits and clusters as a function of beam energy for both data and simulation (values are given in appendix A.2). The energy response is parametrised with the power law fit* $f_R^{pow.}(E)$ *(Equation 44) taking the full energy range into account.*

behave more linear with the beam energy given the power $\beta_{\text{hits}} \sim 0.98$ for hits and $\beta_{\text{clus}} \sim 0.93$ for clusters.

The deviations r between data or simulation and the corresponding parameterisations presented in Figure 87 and Figure 88 show that a non-linear function of the mean energy response offers a better description of the EPICAL-2 energy response over the full energy range for both hits and clusters. The deviations from linearity are higher for the cluster measurement than for the hit measurement consistent in simulation and data. A portion of the non-linearity in data is, however, embedded in the DESY beam energy uncertainty as discussed in context of the linear parameterisation approach.

Taking both parameterisation approaches together, one can conclude that the EPICAL-2 energy response shows a non-linear behaviour using the total number of hits or the total number of clusters as a proxy for the energy measurement with the EPICAL-2 prototype. The causes of the apparent non-linearity are summarised below: Saturation for both clusters and hits leads to a non-linear energy response. The effect of saturation is stronger for clusters than for hits. In addition, the limited detector

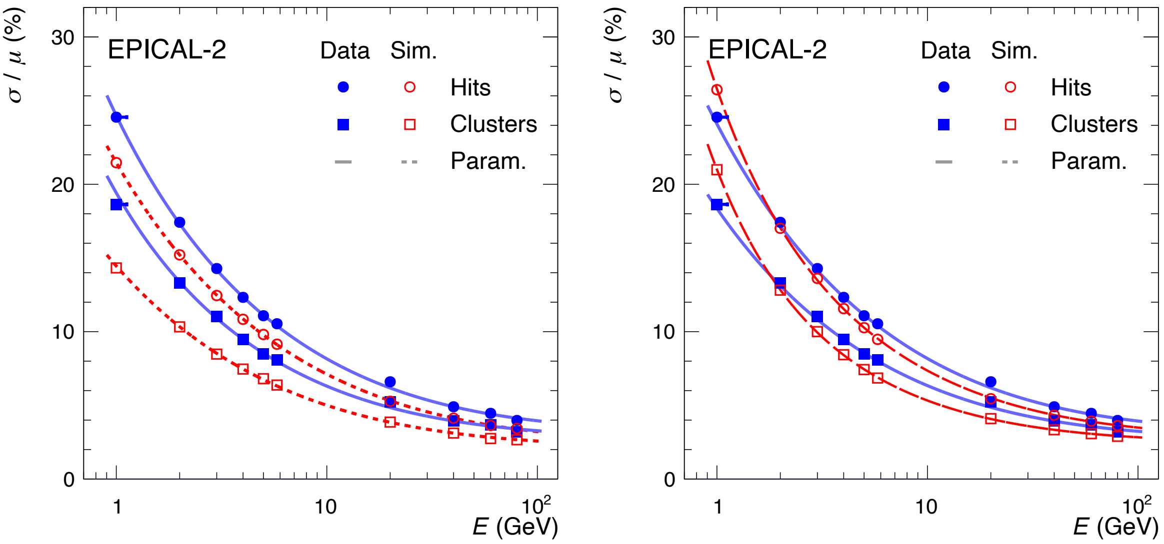

Figure 89: Energy resolution σ/μ as a function of the beam energy E. The results obtained from the measured data are compared to those obtained from simulation using two different simulation scenarios: On the left, the simulation uses a constant beam energy. On the right, the simulation includes the energy spread of the beams at DESY *[Die+19] and at* SPS *[GF22].*

volume of EPICAL-2 leads to a non-linear response because of longitudinal and lateral leakage. Both effects, leakage and saturation, increase with energy. Furthermore, part of the non-linearity is a result of the uncertainty of the beam energy at DESY and residual contamination in the data sample.

5.2.3 Energy Resolution

The EPICAL-2 energy resolution σ_E/E is calculated for both hits and clusters using the numerical values for the mean μ and the width σ obtained from the signal distributions discussed in section 5.2.1:

$$\frac{\sigma_E}{E} = \frac{\sigma_{\text{hits, clus}}}{\mu_{\text{hits, clus}}}$$

Figure 89 shows the energy resolution σ/μ of EPICAL-2 as a function of the incident particle energy E obtained from the test-beam measurements at DESY and SPS. The results obtained from the EPICAL-2 data are shown in blue as filled circles for hits and as filled squares for clusters and the results from simulation are shown as the corresponding open red symbols. Two simulation scenarios are considered: Figure 89 (left) shows the "ideal" simulation scenario without the spread of the beam energies at DESY and SPS (see section 2.3). In contrast, Figure 89 (right) displays the comparison between data and the simulation scenario, where the beam energy spread is taken into account as quoted by the test-beam facilities DESY and SPS [Die+19; GF22].

hits	a (%)	b (%)	c (%)
data	23.90 ± 0.03	3.13 ± 0.03	-
sim ($E_{\text{spread}} = 0$)	21.22 ± 0.03	2.40 ± 0.03	-
sim with E_{spread}	20.91 ± 0.07	2.74 ± 0.02	15.99 ± 0.19

clusters	a (%)	b (%)	c (%)
data	18.16 ± 0.02	2.68 ± 0.03	-
sim ($E_{\text{spread}} = 0$)	14.30 ± 0.02	2.15 ± 0.02	-
sim with E_{spread}	14.15 ± 0.06	2.45 ± 0.01	15.32 ± 0.12

Table 10: *Parameters a, b and c derived from the parameterisation of the energy resolution with Equation 45 for hits and clusters and for both data and simulation. c is fixed to zero for data and the simulation scenario without beam-energy spread.*

As expected for a typical calorimeter, the energy resolution increases, the lower the energy. Over the full energy range, the energy response obtained from N_{clus} is better compared to the one obtained from N_{hits} which is consistently observed in the measured data and in the simulation.

Comparing the two simulation scenarios, the inclusion of a beam energy spread leads to a worsening of the energy resolution as expected. The difference between the two simulation scenarios visualises the influence of a beam energy spread. Moreover, it visualises a maximum of the component in the EPICAL-2 energy resolution obtained in the measured data that is inherited from the beam-energy spread of the test beams. Therefore, the energy resolution obtained in the measured data can be considered as an upper limit for the energy resolution of EPICAL-2 given the intrinsic energy resolution from the test beams.

Surprisingly, at the lowest energy of 1 GeV, the resolution in the measured data is worse compared to the simulation scenario without the beam energy spread and better than the scenario with beam energy spread. For all other energies, the resolution obtained in simulation increases with the inclusion of the beam energy spread but stays consistently below the measured data. From this it seams, that not only the beam energy is uncertain at DESY but also the beam energy spread quoted by DESY [Die+19] may deviate from the true beam energy spread.

The energy resolution σ_E/E of a calorimeter is typically described as:

$$\frac{\sigma_E}{E} = \frac{a}{\sqrt{E/\text{GeV}}} \oplus b \oplus \frac{c}{E/\text{GeV}} \tag{45}$$

As discussed in detail in section 1.2, $a/\sqrt{E}$ refers to the stochastic term, the parameter b to the constant term and the c/E term corresponds to the noise term.

The EPICAL-2 energy resolution for hits and clusters in both the measured data and the simulation as shown in Figure 89 is parametrised with Equation 45. Each

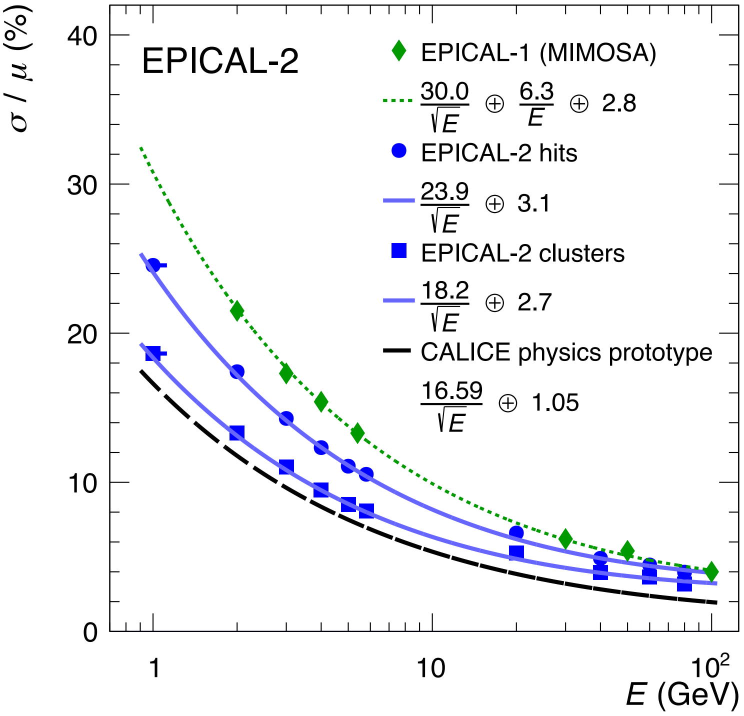

Figure 90: *Energy resolution σ/μ as a function of the beam energy E. The* EPICAL-2 *results are shown and compared to those obtained with* EPICAL-1 *[Haa+18] and the* CALICE *physics prototype [Adl+09].*

parametrisation is included in Figure 89 referred to as Param. in the legend of the figure. For the measured data, the parametrisation is performed without the noise term given the low noise level of $(2.900 \pm 0.009) \cdot 10^{-3}$. A parametrisation of the measured data including the noise term has been performed as cross-check which leads to the parameter c effectively being zero. The simulation scenario without beam energy spread can also be described without the noise term. However, the parametrisation without noise term fails to describe the simulation scenario with beam energy spread. Therefore, in the latter case the noise term is included in the parametrisation of the simulation. The obtained parameters are given in Table 10 for the measured data and for the two simulation scenarios.

After the discussion of the comparison between the measured data and the simulation in context of Figure 89, in the following, the EPICAL-2 energy resolution is compared to two other prototypes: the older EPICAL-1 prototype [Haa+18] using pixel sensors and the so-called CALICE physics prototype [Adl+09], an analog silicon-tungsten calorimeter constructed by the CALICE collaboration. Both were described in section 1.3.

Figure 89 compares the EPICAL-2 energy resolution to the energy resolution of EPICAL-1 and the CALICE physics prototype. The green filled diamonds show the energy resolution measured with EPICAL-1 [Haa+18] where N_{hits} are used as the energy response observable. The energy resolution obtained with EPICAL-2 is better than the one measured with EPICAL-1 mainly as a result of the large fraction of malfunctioning or dead sensor areas in EPICAL-1 [Haa+18] leading to a worsening of the performance. The parametrisation of the energy resolution obtained with the CALICE physics prototype, where the intrinsic beam energy spread is subtracted, is shown as dashed black line in Figure 89. The energy resolution of the digital EPICAL-2 prototype is close to the one of the analog CALICE physics prototype. This is interesting in a sense, that the EPICAL-2 prototypes is competitive regarding energy resolution although the two prototypes are using different sensor technologies.

The energy resolution of EPICAL-2 for cluster is better compared to the resolution for hits. The energy response of EPICAL-2 is non-linear, while hits show smaller deviations from a linear energy response compared to clusters. The observed non-linearity is mainly due to saturation, energy leakage out of EPICAL-2 and the beam energy uncertainty at DESY. Overall, the simulation agrees with the energy response and energy resolution obtained in the measured data. In detail, lower deviations from linearity and a better energy resolution are found in the simulation compared to the measured data. Especially the energy resolution in the simulation degrades when comparing a simulation scenario with no beam-energy spread to a simulation with beam-energy spread. This demonstrates that the EPICAL-2 resolution obtained in the measured data can be considered as an upper limit of the intrinsic energy resolution of EPICAL-2. Furthermore, the energy resolution may be affected by the energy leakage out of EPICAL-2, the beam energy uncertainty and residual contamination in the test data. Parts of the results of this thesis presented in this section are published in [Alm+23].

Part Two:

Soft-Photon Background Studies in ALICE 3

6 Soft Photons

Part two of this thesis encompasses the simulation studies of the background in a soft-photon measurement in ALICE 3, which is the proposed next-generation heavy-ion collision experiment starting in 2035 [ALI+22].

Just like part one of the thesis, part two is in context of upgrade programs of the ALICE experiment. However, the two parts are related to two different programs. While part one belongs to the second stage of a typical upgrade program of the ALICE experiment, i.e. prototype developments and test measurements along with finalising the detector design, part two of the thesis relates to the first stage of an ALICE upgrade, i.e. fundamental simulation studies for the feasibility of a measurement that refines a physics signal or allows to measure it for the first time.

To study the different sources of background in a soft-photon measurement in the second part of this thesis, first, soft photons are introduced and naming conventions are defined. Both the experimental situation and theoretical description of soft-photons are discussed to evaluate the studies of this thesis. Furthermore, detector requirements for a new soft-photon measurement in ALICE 3 are described focussing on the so-called Forward Conversion Tracker (FCT) as proposed soft-photon detector in ALICE 3. Finally, the study of the background in such a measurement with a future collider experiment is presented. For this background study, the ALICE 3 detector geometry is used as a baseline.

6.1 Terminology

Photons are extensively produced in high-energy particle collisions and are put into different categories and are named according to various aspects like their production mechanism or kinematics. To be clear about the conventions used throughout this thesis, important photon categories and terminologies are introduced in the following.

In general, one can distinguish between direct photons and decay photons. While direct photons are typically considered as signal, decay photons are referred to as the background in a direct photon measurement. Most of the decay photons emerge from π^0 and η decays. Direct photons are emitted in inelastic parton-parton reactions such as quark-gluon Compton scattering or quark-anti-quark annihilation. Furthermore, direct photons are produced via Bremsstrahlung in the fragmentation process. Decay and direct photons can have both a high or low p_{T} depending on their production.

Just as direct photons that can be produced via Bremsstrahlung in the collisions itself, photons are also produced via Bremsstrahlung due to charged particle interactions with any material. In this thesis, photons produced by charged particles in material interactions are referred to as "photons from external Bremsstrahlung" and those produced in the collisions itself are called "photons from internal

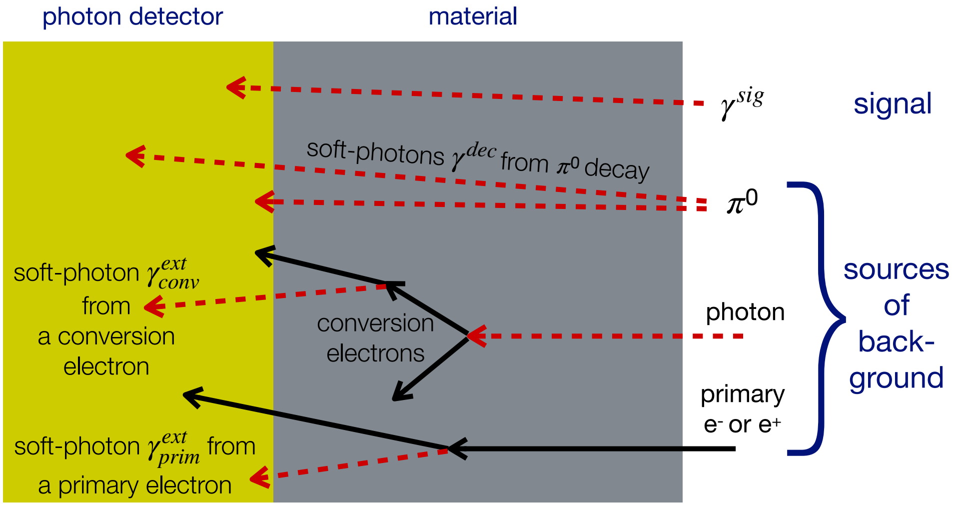

Figure 91: *Illustration of soft photons from different sources.*

Bremsstrahlung". Photons from internal Bremsstrahlung are considered as the physics signal to be measured experimentally and other photons are background in the experimental measurement.

All photons with very low p_T of a few MeV to several tens of MeV are referred to as "soft photons" in the following. To further distinguish soft photons depending on their different production mechanisms, soft photons from different different sources are called as follows:

signal:	$\gamma^{\rm sig}$	soft-photon signal (from internal Bremsstrahlung)
background:	$\gamma^{\rm dec}$	soft photons from decays
	$\gamma^{\rm ext}$	soft photons from external Bremsstrahlung
	$\gamma^{\rm ext}_{\rm prim}$	$\gamma^{\rm ext}$ from primary electrons
	$\gamma^{\rm ext}_{\rm conv}$	$\gamma^{\rm ext}$ from conversion electrons

Figure 91 illustrates a general photon detector with material in front of the detector and the soft-photons from different sources as discussed above. Those soft-photons have been considered in previous measurements and will be discussed in more detail in the next sections.

For a $\gamma^{\rm sig}$ -measurement in an experiment, the background, i.e. both $\gamma^{\rm dec}$ and $\gamma^{\rm ext}$, needs to be subtracted from all measured soft-photons. However, it is not directly possible to determine the source of a measured photon on an event-by-event basis experimentally. To disentangle different photon sources, the photon yield in data is compared with the expectation from MC simulation. Since typical existing MC generators include the simulation of $\gamma^{\rm dec}$ and $\gamma^{\rm ext}$ but not $\gamma^{\rm sig}$, the general

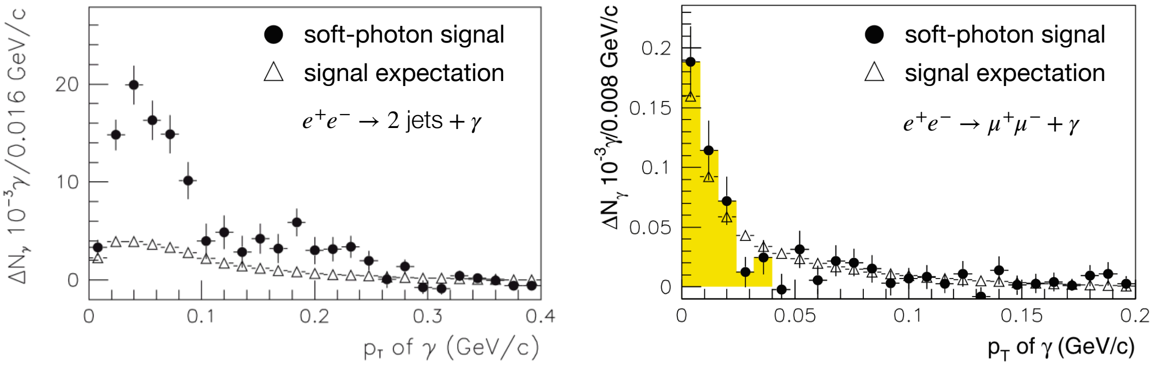

Figure 92: *Soft-photon signal and expectation as a function of p_T for $e^+e^- \to 2\,\text{jets} + \gamma$ reactions (left) and for $e^+e^- \to \mu^+\mu^- + \gamma$ reactions (right) [DEL06; DEL08]. The yellow region in the right figure corresponds to the integration region $p_T < 40\,\text{MeV}$ used for the quantification of the soft-photon excess.*

γ^{sig} measurement strategy in experiments is based on calculating the difference between the total soft-photon yield in data and the total soft-photon yield from MC simulation [Bel+02; DEL06; DEL08].

6.2 Experimental Situation

Several experimental investigations of the soft-photon production have been carried out using different setups and measurement techniques. The latest soft-photon measurements at the time of this thesis were presented by the DELPHI collaboration in 2006 and 2008 [DEL06; DEL08].

Figure 92 shows the soft-photon yield as a function of p_T in $e^+e^- \to 2\,\text{jets} + \gamma$ reactions (left) and in $e^+e^- \to \mu^+\mu^- + \gamma$ reactions (right) as full circles measured by the DELPHI collaboration. In these measurements, p_T is defined relative to the closest jet axis and muon axis respectively. Moreover, photons were measured in the photon energy range of $0.2\,\text{GeV} < E_\gamma \leq 1\,\text{GeV}$. Similar to the discussion in the previous section, in Figure 92, γ^{sig} is measured by calculating the difference between the photon yield in data and the photon yield in MC simulation, where the main background sources are identified as both γ^{dec} and γ^{ext}. In addition to the γ^{sig}-measurement, Figure 92 shows the theoretical γ^{sig}-expectation of photons produced via inner Bremsstrahlung as open triangles. The theoretical expectation for both inner and external Bremsstrahlung are discussed in the next section.

In Figure 92, a clear discrepancy between the γ^{sig}-measurement and the theoretical expectation can be observed in hadronic $e^+e^- \to 2\,\text{jets} + \gamma$ reactions but not in purely electromagnetic $e^+e^- \to \mu^+\mu^- + \gamma$ reactions. This hints towards a mechanism of QCD and not QED enhancing the soft-photon production at low p_T in hadronic reactions.

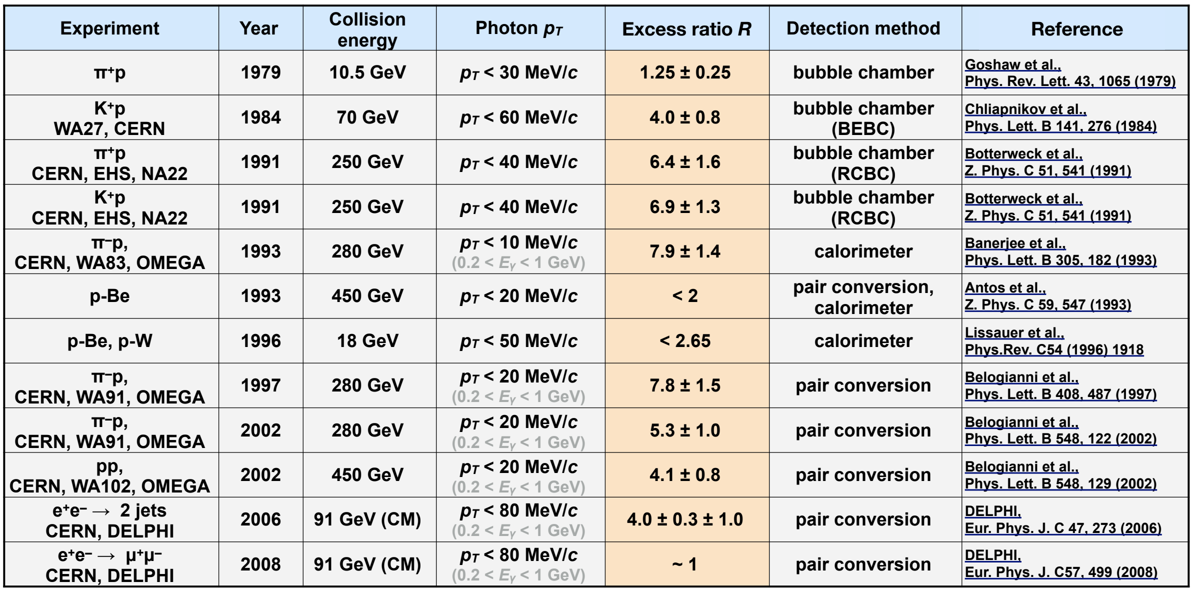

Experiment	Year	Collision energy	Photon p_T	Excess ratio R	Detection method	Reference
π^+p	1979	10.5 GeV	$p_T < 30$ MeV/c	1.25 ± 0.25	bubble chamber	Goshaw et al., Phys. Rev. Lett. 43, 1065 (1979)
K^+p WA27, CERN	1984	70 GeV	$p_T < 60$ MeV/c	4.0 ± 0.8	bubble chamber (BEBC)	Chliapnikov et al., Phys. Lett. B 141, 276 (1984)
π^+p CERN, EHS, NA22	1991	250 GeV	$p_T < 40$ MeV/c	6.4 ± 1.6	bubble chamber (RCBC)	Botterweck et al., Z. Phys. C 51, 541 (1991)
K^+p CERN, EHS, NA22	1991	250 GeV	$p_T < 40$ MeV/c	6.9 ± 1.3	bubble chamber (RCBC)	Botterweck et al., Z. Phys. C 51, 541 (1991)
π^-p, CERN, WA83, OMEGA	1993	280 GeV	$p_T < 10$ MeV/c $(0.2 < E_\gamma < 1$ GeV)	7.9 ± 1.4	calorimeter	Banerjee et al., Phys. Lett. B 305, 182 (1993)
p-Be	1993	450 GeV	$p_T < 20$ MeV/c	< 2	pair conversion, calorimeter	Antos et al., Z. Phys. C 59, 547 (1993)
p-Be, p-W	1996	18 GeV	$p_T < 50$ MeV/c	< 2.65	calorimeter	Lissauer et al., Phys.Rev. C54 (1996) 1918
π^-p, CERN, WA91, OMEGA	1997	280 GeV	$p_T < 20$ MeV/c $(0.2 < E_\gamma < 1$ GeV)	7.8 ± 1.5	pair conversion	Belogianni et al., Phys. Lett. B 408, 487 (1997)
π^-p, CERN, WA91, OMEGA	2002	280 GeV	$p_T < 20$ MeV/c $(0.2 < E_\gamma < 1$ GeV)	5.3 ± 1.0	pair conversion	Belogianni et al., Phys. Lett. B 548, 122 (2002)
pp, CERN, WA102, OMEGA	2002	450 GeV	$p_T < 20$ MeV/c $(0.2 < E_\gamma < 1$ GeV)	4.1 ± 0.8	pair conversion	Belogianni et al., Phys. Lett. B 548, 129 (2002)
$e^+e^- \rightarrow$ 2 jets CERN, DELPHI	2006	91 GeV (CM)	$p_T < 80$ MeV/c $(0.2 < E_\gamma < 1$ GeV)	4.0 ± 0.3 ± 1.0	pair conversion	DELPHI, Eur. Phys. J. C 47, 273 (2006)
$e^+e^- \rightarrow \mu^+\mu^-$ CERN, DELPHI	2008	91 GeV (CM)	$p_T < 80$ MeV/c $(0.2 < E_\gamma < 1$ GeV)	~ 1	pair conversion	DELPHI, Eur. Phys. J. C57, 499 (2008)

Table 11: *Summary of soft-photon measurements by various experiments [Rey+21; Won14].*

In [DEL06; DEL08], the discrepancy between the γ^{sig} -measurement and theoretical expectation is quantified by the so called excess ratio R:

$$R = \frac{\int_{p_T} \text{signal measurement}}{\int_{p_T} \text{signal expectation}} \tag{46}$$

The integration is performed for $p_T < 80\,\text{MeV}$ for the measurement in hadronic reactions and for $p_T < 40\,\text{MeV}$ in electromagnetic reactions leading to an excess ratio of $R = 4.0 \pm 0.3 \pm 1.0$ and $R = 1.06 \pm 0.12 \pm 0.07$.

The excess ratio of $R = 4.0 \pm 0.3 \pm 1.0$ in hadronic reactions obtained by the DELPHI collaboration is in general agreement with previous measurements as shown in Table 11, which summarises several soft-photon measurements including the latest DELPHI measurements. As can be seen in Table 11, all measurements involving hadronic processes show an excess ratio between $R \approx 2$ and $R \approx 8$, except the first measurement in hadronic $\pi + p \rightarrow \gamma + X$ reactions at 10.5 GeV in 1979 and the DELPHI measurement in purely electromagnetic reactions discussed above.

In [DEL06; DEL08] and the previous papers referenced in Table 11, the observed excess photons at low p_T were called "anomalous" which leaded to the introduction of the term "anomalous soft-photon production". More recently, this long standing discrepancy between measurement and expectation is referred to as the "soft-photon puzzle" [Rey+21].

Several theoretical models (see references in [ALI+22] or [DEL06]) exist, trying to explain the effect of anomalous soft-photon production by introducing new mechanisms for soft-photon production. However, in general, there is no agreement on the description of the observed low-p_T excess in data; the puzzle remains unsolved.

A new soft-photon measurement at LHC energies would allow to investigate, if the soft-photon excess appears also at LHC energies. In addition, a new measurement could confirm or disagree with previous measurements, characterise the soft-photon excess and make useful contributions in solving the puzzle.

In chapter 7, a background study for a soft-photon measurement in pp collisions at a new LHC collider experiment is presented. The study of this thesis has been performed in context of the endeavour of the ALICE collaboration to design ALICE 3, the heavy-ion collision experiment proposed for Run 5 and 6 at the LHC starting in 2035 [ALI+22]. To determine the key requirements of the new experiment for a successful soft-photon measurement, it is important to understand the different sources producing soft-photons. Therefore, before key aspects of ALICE 3 relevant to this study are presented, the theoretical expectation for photons from internal and external Bremsstrahlung are discussed next.

6.3 Theoretical Description

The theoretical expectations for photons from internal Bremsstrahlung is taken from [Völ22], where the signal is estimated using a PYTHIA simulation and Low's theorem, both discussed in this section.

The theoretical expectations for photons from external Bremsstrahlung is estimated in this section based on [Rey+21] by using the production function of photons from external Bremsstrahlung per electron [GZ+20].

6.3.1 Internal Bremsstrahlung: Signal Expectation

Low's theorem [Low58], very fundamentally relating soft-photon production via inner Bremsstrahlung and the spectrum of charged hadrons, is used by various experiments to calculate the soft-photon signal expectation (see references in Table 11). For instance in Figure 92 in the previous section, the soft-photon signal expectation is shown for $e^+e^- \to 2\,\text{jets} + \gamma$ and $e^+e^- \to \mu^+\mu^- + \gamma$ reactions calculated on the basis of Low's theorem by the DELPHI collaboration [DEL06].

Figure 93 (a) illustrates a process with two particles with momenta p_1 and p_2 in the initial state and two particles with momenta p_3 and p_4 in the final state. One can now imagine the same process to occur including the production of an additional soft photon with momentum k. This can be either an external photon emission, i.e. an additional photon along an incoming particle (Figure 93 b) or beside an outgoing particle (Figure 93 c), or an internal photon emission (Figure 93 d).

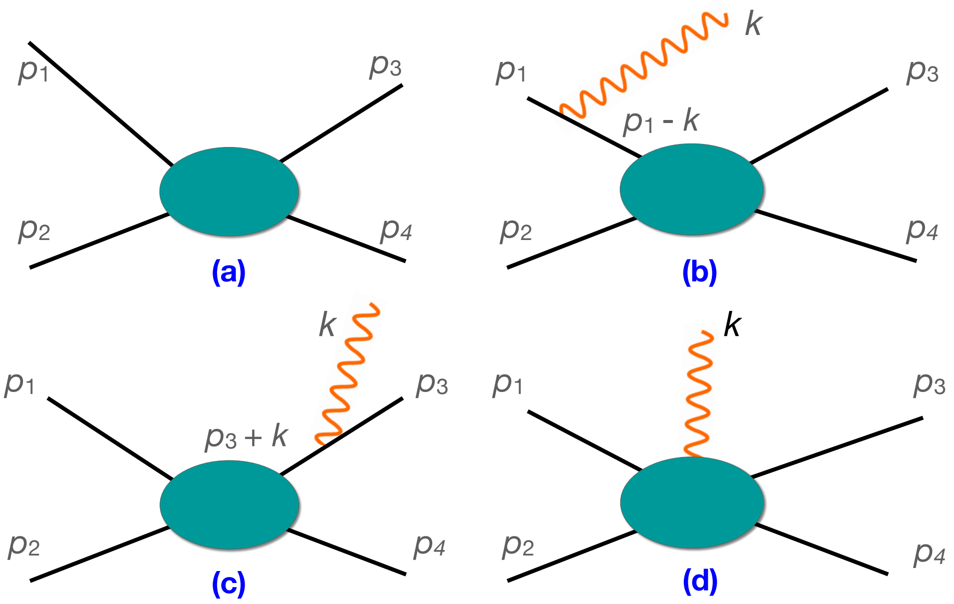

Figure 93: *Illustration for the process $p_1 + p_2 \to p_3 + p_4$ with and without emission of an additional photon with momentum k, to visualise the conceptual idea of Low's theorem relating the "raw" process $p_1 + p_2 \to p_3 + p_4$ without photon emission (a) to the ones with additional outgoing photon (b,c,d).*

The conceptual idea of Low's theorem is the relation between the process without an additional photon as shown in Figure 93 (a), and the processes with an additional photon as shown in Figure 93 (b,c,d). Low's theorem states that the cross section of the process without the additional photon is proportional to the cross section of the process including the soft-photon emission, if all incoming and outgoing particles are known [Low58]. Therefore, if for a certain reaction as e.g. shown in Figure 93 (a), the momenta p_i of all incoming and outgoing charged particles are known, the soft-photon spectrum can be computed [Won14].

The formula commonly used by experiments to calculate the soft-photon spectrum $\mathrm{d}N_\gamma/\mathrm{d}^3\vec{k}$ derived from Low's theorem reads as [DEL06; DEL08; Völ22; Won14]:

$$\frac{\mathrm{d}N_\gamma}{\mathrm{d}^3\vec{k}} = \frac{\alpha}{(2\pi)^2}\frac{-1}{E_\gamma}\int \mathrm{d}^3\vec{p}_1 \ldots \mathrm{d}^3\vec{p}_\mathrm{N} \left(\sum_i \frac{s_\mathrm{i}\, e_\mathrm{i}\, P_\mathrm{i}}{P_\mathrm{i}\, K}\right)^2 \frac{\mathrm{d}N_\mathrm{hadrons}}{\mathrm{d}^3\vec{p}_1 \ldots \mathrm{d}^3\vec{p}_\mathrm{N}} \tag{47}$$

K and $\vec{k}$ denote the photon four- and three momentum vector; $E_\gamma = |\vec{k}|$. In contrast, P_i and $\vec{p}_i$ are the four and the three momentum vector of a particle i. The electric charge e_i of a particle i is taken into account as $e_i = 1$ for positive charged and $e_i = -1$ for negative charged particles. The particle state s is $s_i = 1$ for outgoing particles and $s_i = -1$ for incoming particles. For instance, for pp collisions, the summation over $N + 2$ particles is computed since there are always the two incoming protons and N outgoing particles.

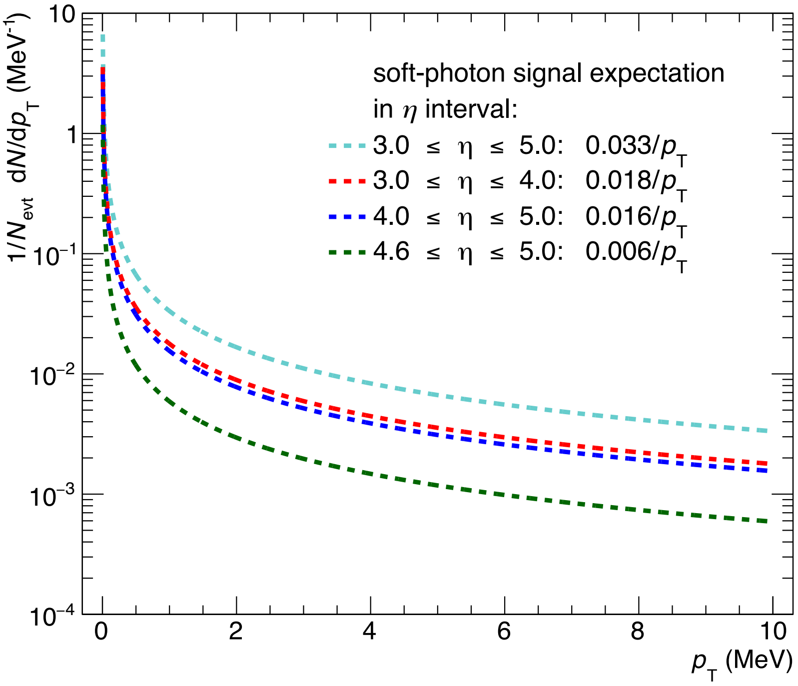

Figure 94: *Soft-photon signal expectation derived from Low's theorem for different pseudorapidity η intervals using pp collisions at $\sqrt{s} = 13$ TeV from* PYTHIA .

In [Völ22], Equation 47 is evaluated for pp collisions at $\sqrt{s} = 13\,\text{TeV}$ using PYTHIA events, resulting in the soft-photon signal expectation S_γ, which is used in chapter 7 for the study of the soft-photon background. S_γ is determined to [Völ22]:

$$S_\gamma = \frac{\lambda^{\text{signal}}(\eta)}{p_\text{T}} \quad ; \; \lambda^{\text{signal}}(\eta) = \begin{cases} 0.033\,, \text{ for } 3.0 < \eta < 5.0 \\ 0.018\,, \text{ for } 3.0 < \eta < 4.0 \\ 0.016\,, \text{ for } 4.0 < \eta < 5.0 \\ 0.006\,, \text{ for } 4.6 < \eta < 5.0 \end{cases} \tag{48}$$

Figure 94 shows the soft-photon signal expectation S_γ for several η intervals as example. One can observe the $1/p_\text{T}$ shape as well as a divergence of the soft-photon production for $p_\text{T} \to 0$.

6.3.2 External Bremsstrahlung

As known from previous experiments (see references in Table 11), the main background in the γ^{sig}-measurement is γ^{ext}. Here, an estimate of the γ^{ext}-yield based on [Rey+21] is presented.

The spectrum $\mathrm{d}N_{\gamma}^{\text{bck. per}\,e}/\mathrm{d}p$ of photons with momentum p emitted per electron with energy E_e via Bremsstrahlung can be expressed as [GZ+20]:

$$\begin{aligned}
\frac{\mathrm{d}N_{\gamma}^{\text{bck. per}\,e}}{\mathrm{d}p} &= \frac{4}{3}\frac{d}{X_0}\left(\frac{1}{p}-\frac{1}{E_e}+\frac{3}{4}\frac{k}{E_e^2}\right) && (49)\\
&\approx \frac{4}{3}\frac{d}{X_0}\frac{1}{p} \quad \text{for } p \ll E_e \qquad \Big|\; p = p_{\mathrm{T}}\cosh\eta && (50)\\
\Rightarrow \quad \frac{\mathrm{d}N_{\gamma}^{\text{bck. per}\,e}}{\mathrm{d}p_{\mathrm{T}}} &\approx \frac{4}{3}\frac{d}{X_0}\frac{1}{p_{\mathrm{T}}} && (51)
\end{aligned}$$

In the following, the approximation for $p \ll E_e$ is used, which assumes that the photon spectrum is independent of E_e.

An estimate of the total background γ^{ext}-yield in a certain pseudorapidity range can be achieved by multiplying Equation 51 with the corresponding electron pseudorapidity density.

As discussed in context of Figure 91, one can distinguish two sources producing photons via external Bremsstrahlung:

1. Primary electrons from the pp collision vertex and
2. conversion electrons from a photon conversion in material.

In the following, both contributing electron sources are treated separately.

(1) Primary electrons:

Primary electrons originate mostly from π^0 Dalitz decays with a branching ratio of $\mathrm{BR}(\pi^0 \rightarrow \gamma e^+ e^-) = (1.174 \pm 0.035)\%$ [GZ+20]. Therefore, the primary electron pseudorapidity density $\mathrm{d}N_e^{\text{primary}}/\mathrm{d}\eta$ can be approximated as [Rey+21]:

$$\begin{aligned}
\frac{\mathrm{d}N_e^{\text{primary}}}{\mathrm{d}\eta} &\approx \frac{\mathrm{d}N_{\pi^0}}{\mathrm{d}\eta}\,\mathrm{BR}\left(\pi^0 \rightarrow \gamma\, e^+ e^-\right)\cdot 2 && (52)\\
&\approx \frac{1}{2}\frac{\mathrm{d}N_{\pi^\pm}}{\mathrm{d}\eta}\,\mathrm{BR}\left(\pi^0 \rightarrow \gamma e^+ e^-\right)\cdot 2 && (53)\\
&\approx \frac{\mathrm{d}N_{ch}}{\mathrm{d}\eta}\,1.174\% && (54)\\
&\approx 0.07 && (55)
\end{aligned}$$

$\mathrm{d}N_{\pi^0}/\mathrm{d}\eta$ represents the π^0 pseudorapidity density and the factor of two takes the electron and positron produced in a π^0 Dalitz decay into account. $\mathrm{d}N_{\pi^0}/\mathrm{d}\eta$ is approximated by half the pseudorapidity density $\mathrm{d}N_{\pi^\pm}/\mathrm{d}\eta$ of charged pions (π^+ and π^-), since in relation to isospin symmetry all pion flavours are produced in equal amounts. In addition, $\mathrm{d}N_{\pi^\pm}/\mathrm{d}\eta$ can be approximated by the pseudorapidity density

$\mathrm{d}N_{ch}/\mathrm{d}\eta$ of charged particles, because charged pions are produced most abundant of all charged particles produced in particle collisions [ALI+18].

To approximate $\mathrm{d}N_e^{\text{primary}}/\mathrm{d}\eta$ for pp collisions at $\sqrt{s} = 13\,\text{TeV}$ similar to the γ^{sig}-expectation discussed in the previous section, here, $\mathrm{d}N_{ch}/\mathrm{d}\eta \approx 6$ is used exemplary for $4.0 < \eta < 5.0$, which is based on the ALICE measurement of $\mathrm{d}N_{ch}/\mathrm{d}\eta$ for $|\eta| < 0.5$ in pp collisions at $\sqrt{s} = 13\,\text{TeV}$ [ALI+16]. As the typical $\mathrm{d}N_{ch}/\mathrm{d}\eta$ distribution decreases for higher η, using an average value for $\mathrm{d}N_{ch}/\mathrm{d}\eta$ over $|\eta| < 0.5$ yields an upper limit for $\mathrm{d}N_e^{\text{primary}}/\mathrm{d}\eta$ at forward rapidities and thus also for the photon background from primary electrons.

Combining Equation 51 and Equation 55 gives the yield $B_\gamma^{\text{prim. }e}$ of photons produced by primary electrons via external Bremsstrahlung:

$$B_\gamma^{\text{prim. }e} = \frac{\mathrm{d}N_\gamma^{\text{prim. }e\text{ bckg.}}}{\mathrm{d}p_\mathrm{T}\mathrm{d}\eta} = \frac{\mathrm{d}N_e^{\text{primary}}}{\mathrm{d}\eta} \cdot \frac{\mathrm{d}N_\gamma^{\text{bckg. per }e}}{\mathrm{d}p_\mathrm{T}} \tag{56}$$

$$= 0.07 \cdot \frac{4}{3}\frac{d}{X_0}\frac{1}{p_\mathrm{T}} \tag{57}$$

(2) Conversion electrons:

In contrast to the number of primary electrons, the number of photon conversion electrons clearly depends on the probability $P_{\text{conv.}}(d)$ for pair production of a photon after travelling a distance d. In general, the higher the distance d, i.e. the more material a particle traverses, the higher the chance of a conversion. $P_{\text{conv.}}(d)$ is defined as [Kle92]:

$$P_{\text{conv.}}(d) = 1 - e^{-\frac{7}{9}\frac{d}{X_0}} \tag{58}$$

$$\overset{\substack{\text{first-order}\\ \text{Taylor polynomial}}}{\approx} \frac{7}{9}\frac{d}{X_0} \tag{59}$$

Utilising Equation 59 and the fact that most photons originate from π^0's ($\pi^0 \to \gamma\gamma$), the pseudorapidity density $\mathrm{d}N_e^{\text{conv.}}/\mathrm{d}\eta$ of conversion electrons can be expressed as:

$$\frac{\mathrm{d}N_e^{\text{conv.}}}{\mathrm{d}\eta} \approx 2 \cdot P_{\text{conv.}}(d) \cdot \frac{\mathrm{d}N_\gamma}{\mathrm{d}\eta} \approx 2 \cdot P_{\text{conv.}}(d) \cdot 2\frac{\mathrm{d}N_{\pi^0}}{\mathrm{d}\eta} \tag{60}$$

$$\approx 2 \cdot \left(\frac{7}{9}\frac{d}{X_0}\right) \cdot \frac{\mathrm{d}N_{ch}}{\mathrm{d}\eta} \tag{61}$$

Where $2 \cdot \mathrm{d}N_{\pi^0}/\mathrm{d}\eta$ is substituted by $\mathrm{d}N_{ch}/\mathrm{d}\eta$ as already discussed in context of Equation 53.

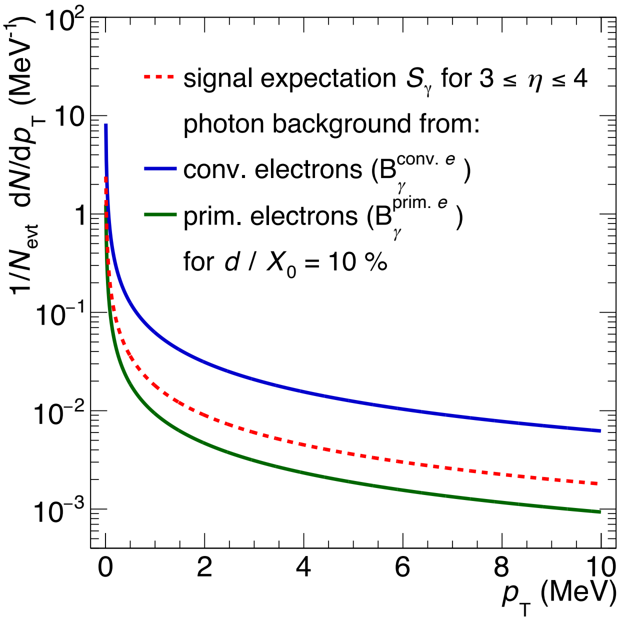

Figure 95: *$B_\gamma^{\text{conv. } e}$ (blue) and $B_\gamma^{\text{prim. } e}$ (green) exemplary for a material budget of $d/X_0 = 10\,\%$. The soft-photon signal S_γ (red) is shown for $3 \leq \eta \leq 4$.*

Combining Equation 51 and Equation 61 results in the yield $B_\gamma^{\text{conv. } e}$ of photons produced by conversion electrons via external Bremsstrahlung:

$$B_\gamma^{\text{conv. } e} = \frac{dN_\gamma^{\text{conv. } e \text{ bckg.}}}{dp_T d\eta} = \frac{1}{2} \cdot \frac{dN_e^{\text{conv.}}}{d\eta} \cdot \frac{dN_\gamma^{\text{bckg. per } e}}{dp_T} \tag{62}$$

$$= \frac{7}{9}\frac{d}{X_0}\frac{dN_{ch}}{d\eta} \cdot \frac{4}{3}\frac{d}{X_0}\frac{1}{p_T} \tag{63}$$

$$= \frac{28}{27}\frac{dN_{ch}}{d\eta}\left(\frac{d}{X_0}\right)^2 \frac{1}{p_T} \tag{64}$$

$$= \frac{56}{9}\left(\frac{d}{X_0}\right)^2 \frac{1}{p_T} \tag{65}$$

Some conversion electrons are produced very early in the ALICE 3 setup, while others are produced late. Depending on the conversion position, a different amount of material is traversed by the electrons, which would lead to a different number of background photons. Therefore, in Equation 62 the factor 1/2 is used, assuming that produced electrons and positrons approximately traverse through half of the detector material [Rey+21]. Similar to Equation 53, in Equation 64, $dN_{ch}/d\eta \approx 6$ is used.

Figure 95 shows $B_\gamma^{\text{conv. } e}$ as blue line and $B_\gamma^{\text{prim. } e}$ as green line exemplary for a material budget of $d/X_0 = 10\,\%$. In addition to the background from external Bremsstrahlung, Figure 95 shows the soft-photon signal S_γ for $3 \leq \eta \leq 4$ as a red line. In this example, $B_\gamma^{\text{prim. } e}$ is a factor ~ 2 below S_γ while $B_\gamma^{\text{conv. } e}$ is a factor ~ 4 above S_γ.

$B_{\gamma}^{\text{conv. } e}$ clearly dominates the background from external Bremsstrahlung for $d/X_0 = 10\,\%$.

Both signal and background as shown in Figure 95 are similar in their $1/p_{\mathrm{T}}$ shape and therefore, photons from external Bremsstrahlung could mimic the soft-photon signal. Since the soft-photon signal is extracted relying on the MC simulation to accurately describe the yield of photons produced via external Bremsstrahlung, an underestimate of the material in the simulation would increase the excess observed by various experiments as discussed in section 6.2.

An observed excess ratio of $R = 4$ as result of an underestimate of the material translates into four times $B_{\gamma}^{\text{conv. } e}$. As the material enters quadratic in the calculation of $B_{\gamma}^{\text{conv. } e}$ (see Equation 65) this corresponds to a doubling of the material. It seems unlikely, that all experiments listed in Table 11 have underestimated their material by a factor of two or even more. However, assuming $d/X_0 = 10\,\%$ a factor of two would be achieved by e.g. circa 0.56 mm of lead, 1.75 mm of iron or 8.8 mm of aluminium [Gro20].

6.4 A new Measurement at a Future LHC Collider Experiment

As discussed in section 6.2, several experiments observed a soft-photon excess for $p_{\mathrm{T}} < 80\,\mathrm{MeV}$. A new soft-photon measurement at the LHC would allow for testing Low's theorem and to help to resolve the long standing "soft-photon puzzle".

In the following, the photon-measurement method and the measurement position for a new detector at the LHC to measure soft photons are discussed. Two methods are commonly used in high energy physics to measure photons: the photon conversion method and the calorimeter method. The energy resolution of a calorimeter typically degrades with lower photon energies E_{γ}. In addition, the photon conversion probability decreases the lower E_{γ}, which leads to a worsening of the photon conversion reconstruction efficiency. For instance, the probability that the interaction of a 10 MeV photon results in a photon conversion and not in Compton scattering is $\approx 70\,\%$ in lead and $\approx 50\,\%$ in iron [Gro20; GZ+20].

Because of the low energy resolution and conversion probability as discussed above, a measurement of photons with energies of a few MeV is challenging. However, the goal with the future LHC experiment would be to measure the soft-photon yield as a function of p_{T} to compare the results with the previous experiments discussed in context of Table 11.

For the positioning and the choice of a photon detector to measure soft photons it is useful to recall the relation between the photon energy E_{γ}, transverse momentum p_{T} and pseudorapidity η [SSS10]:

$$E_{\gamma} = p_{\mathrm{T}} \cdot \cosh \eta \tag{66}$$

η	0	1	2	3	4	5
E_γ (MeV)	3.0	4.6	11.3	30.2	81.9	222.6

Table 12: *Relation between η and E_γ calculated for $p_T = 3$ MeV with Equation 66.*

Both methods discussed above are not suited for a low-p_T photon measurement at mid-rapidity $\eta \approx 0$ where $E_\gamma \approx p_\mathrm{T}$. In contrast to mid-rapidity, at forward direction $\eta > 3$ the situation is completely different: For instance, a photon with $p_\mathrm{T} = 10$ MeV at $\eta = 4.5$ has an energy of $E_\gamma = 450$ MeV. Even a very low-p_T photon at $\eta = 4.5$ with e.g. $p_\mathrm{T} = 3$ MeV still has an energy of $E_\gamma \approx 82$ MeV. Table 12 shows the photon energy E_γ at several pseudorapidities η for a fixed transverse momentum of $p_\mathrm{T} = 3$ MeV to illustrate the relation in Equation 66. In general, the higher the η the higher E_γ at an equal p_T. This means, that the low-p_T region of interest can be accessed by a forward photon measurement.

In a forward photon measurement, both methods to measure forward photons are possible. However, a calorimeter would suffer from hadronic background and the difficulty to distinguish between electrons and photons. Both influence the conversion method less than a calorimeter. Moreover, the conversion method would allow for a precise determination of the photon conversion point, which would provide a clean photon identification.

6.5 ALICE 3 and the FCT

In this section, both ALICE 3 and the FCT are presented, since the ALICE 3 setup is used in this work as a baseline for the background study to measure soft photons at forward rapidity in pp collisions at $\sqrt{s} = 13\,\mathrm{TeV}$, which is presented in the next chapter 7. The ALICE collaboration has proposed ALICE 3, a heavy-ion collision experiment for Run 5 and 6 of the LHC starting in 2035 [ALI+22]. In this proposal, a Forward Conversion Tracker (FCT) is foreseen to measure soft photons in forward direction using the photon conversion method discussed in the previous section.

ALICE 3 is designed to address several fundamental questions covering a wide range of topics such as (multi-)heavy-flavour hadrons, di-electrons, beyond standard model physics and soft photons [ALI+22]. The ALICE 3 physics goals leaded to the main requirements for the ALICE 3 detector concept:

ALICE 3 is conceptualised as a low material budget experiment, basically a compact all-silicon tracker, which covers a wide range in acceptance, $|\eta| < 4$, and allows for measuring over a large p_T range: from $p_\mathrm{T} \approx 0.05$ to $3\,\mathrm{GeV}$ for electrons, to very low $p_\mathrm{T} \to 0$ for (heavy-flavour) hadrons and nuclei and from $p_\mathrm{T} \approx 0.1$ to $50\,\mathrm{GeV}$ for photons [ALI+22]. A key focus is a high efficiency and resolution in the measurements

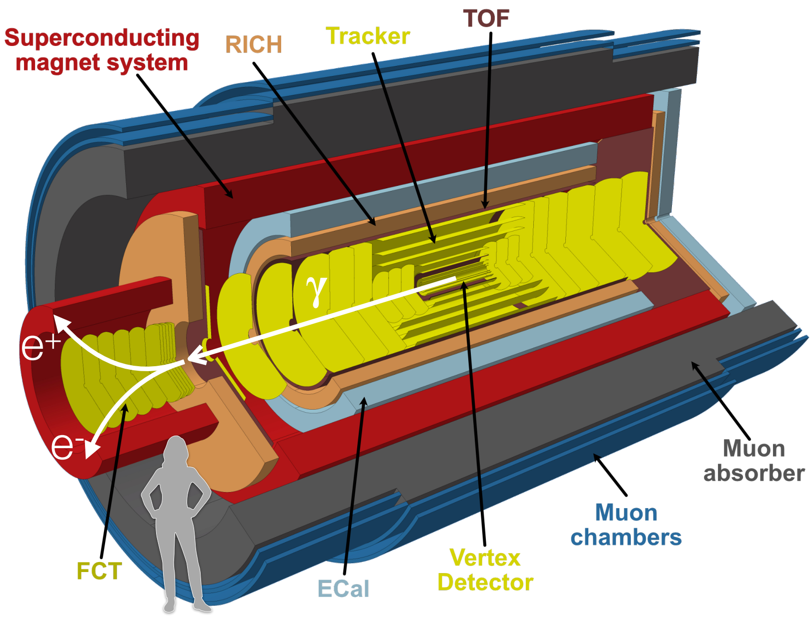

Figure 96: *Conceptual design of the* ALICE 3 *setup [ALI+22]. The Forward Conversion Tracker FCT for soft-photon measurements is located at forward rapidities.*

as well as strong particle identification capabilities for the background suppression [ALI+22].

Figure 96 illustrates the proposed ALICE 3 detector design. Both the Vertex Detector and the Tracker are shown in yellow and build the heart of ALICE 3's tracking system by measuring the trajectory of charged particles. High resolution tracking and vertexing are achieved by the use of MAPS sensors which allow for high spatial resolution and precise timing.

The Vertex Detector consists of 3 layers of bent MAPS and is positioned inside of the LHC beam pipe in a secondary vacuum as a retractable device with two settings: opened and closed. Therefore, the Vertex Detector is also referred to as "iris" since it can open and close like an optics diaphragm [ALI+22]. At injection energy, the LHC beam is spatially spread out and thus the iris is opened with a distance of $r = 15$ mm to the interaction point. When the beam is focussed, the iris is shut to be as close as possible to the interaction point in a distance of $r = 5$ mm, which allows for vertex determination with a position resolution of $\sigma_{\text{pos}} = 2.5$ μm. Each of the three layers of the detector are foreseen with a thickness of 0.1% X_0 and with a pixel size of 10 μm.

The Tracker can be subdivided into barrel tracking layers and forward tracking disks with a thickness of 1% X_0 each. A spatial resolution of ~ 10 μm with 50 μm pixel size and a timing resolution of 100 ns is foreseen.

The barrel tracking system is surrounded by the Time Of Flight (TOF), which is displayed in Figure 96 in brown: Two barrel TOF's, one inner layer at $r = 19$ cm, one outer layer at $r = 85$ cm and one forward TOF at $z = 405$ cm. A precise timing with a

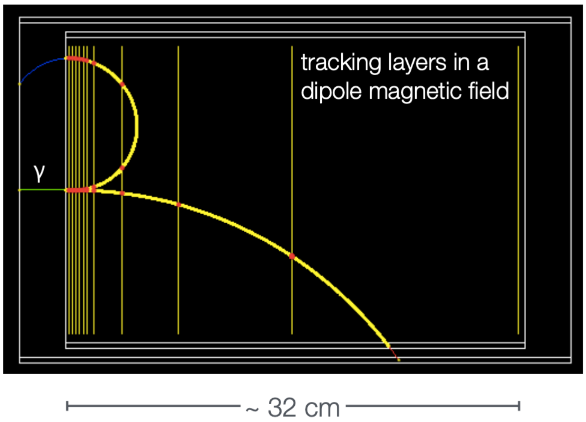

Figure 97: Simple GEANT4 *setup of the proposed Forward Conversion Tracker layout [Rey+21] using silicon sensor layers shown in orange and a converter plate in front, where a photon converts into an electron-positron pair.*

resolution of $\sim$ 20 ps is foreseen to be achieved by the proposed use of silicon timing sensors. To extend the PID reach of the outer TOF layer to higher transverse momenta a Ring-imaging Cherenkov (RICH) detector is proposed as shown in Figure 96 in pale orange. In light blue in Figure 96, the large acceptance Electromagnetic Calorimter (ECal) is shown, proposed as a sampling calorimeter. Outermost, a superconducting magnet system in red and a muon measurement system in dark gray and ozean blue are displayed in Figure 96.

At forward rapidities on the left side of ALICE 3 in Figure 96, the Forward Conversion Tracker (FCT) is shown in dark yellow. The FCT as proposed detector to measure soft photons is described in more detail in the following:

In [ALI+22], the FCT is proposed as a dedicated device to measure soft-photons by utilising silicon sensor layers similar to the other barrel and forward tracking layers in ALICE to reconstruct the electron-positron pair of converted soft photons. The general idea of how to measure soft-photons through conversion with the FCT is depicted in Figure 96, where a photon converts in front of the FCT and the electron-positron pair traverses the tracking layers of the FCT.

Figure 97 displays a simple GEANT4 setup of the proposed FCT, which is composed of silicon sensor layers shown as orange vertical lines. In this simple GEANT4 setup, a converter plate is positioned in front of the first silicon sensor layer. In Figure 97, a 100 MeV photon converts in front of the FCT in an electron-positron pair. The electron and positron trajectories can be tracked via their space points in the silicon sensor layers shown as red dots. The space points in the silicon layers can be used to reconstruct the original photon. To reconstruct electrons with high resolution at low p_{T}, a dipole magnetic field perpendicular to the photon line of flight is used to bend the electron trajectories. The distance between the first FCT silicon layers is foreseen to amount some centimetres, while for the later layers a larger spacing is required for the measurement of electrons with higher momenta.

The importance of a forward photon measurement as discussed in the previous section leads to the FCT coverage of $3 < \eta < 5$ and to measure both high-p_{T} and low-p_{T} electrons the FCT layout is foreseen as depicted in Figure 97, which is proposed in [ALI+22].

7 Investigation of the Background

As consistently noted by the previous experiments discussed in section 6.2, a deep understanding of the background in a soft photon measurement is key for a successful measurement. To study and assess the background, typically, simulations of the experimental measurement are used.

In this chapter, first, the simulation setup for the investigation of the background in a forward soft-photon measurement at the future LHC experiment is presented. Second, the production vertex of all soft photons in the simulation setup is discussed to identify the spacial origin of soft photons in the simulation setup. Third, the background, i.e. γ^{dec}-yield and γ^{ext}-yield, in the simulation setup is discussed and the comparison between both, γ^{dec}-yield and γ^{ext}-yield, and the γ^{sig}-expectation (see section 6.3.1) is presented. In addition, the dependence of γ^{ext}-yield on the material budget in the simulation setup is discussed. After this, background-suppression capabilities are elaborated. Finally, implications for a successful soft-photon measurement with ALICE 3 at the LHC are discussed based on the results of the background study.

This background study has contributed to the ALICE 3 Letter of intent and part of this work is published in [ALI+22].

7.1 Simulation Setup

Monte Carlo simulations of parts of the proposed ALICE 3 detector geometry, relevant to the soft-photon background, are performed with G4ME [Pre22]. G4ME is based on PYTHIA for the event generation and GEANT4 for the geometry implementation. In the following, the GEANT4 simulation setup of parts of the proposed ALICE 3 detector geometry, used in this thesis for the background studies, is referred to as ALICE 3*.

The components of the ALICE 3 setup [ALI+22] extending into the proposed FCT η region of $3 < \eta < 5$ have been implemented in ALICE 3*, namely the beam pipe, the barrel tracking layers, and the forward disks. ALICE 3 detector components outside of this η region are neglected since they will not contribute to the soft-photon background. Figure 98 shows a GEANT4 visualisation of ALICE 3* as implemented in G4ME containing the beam pipe, the barrel tracking layers, the forward disks and a counting volume referred to as the "photon detector" in Figure 98. The coloured trajectories represent particles produced either in a primary pp collision at $\sqrt{s} = 13\,\text{TeV}$ or via detector material interactions. In the following, the position, size and material of all ALICE 3* components as shown in Figure 98 are specified[2]:

---

[2] The geometry here is given in cylindrical coordinates: While the beam axis, similar to the beam pipe, is referred to as the z-axis, the radius R represents the distance to the z-axis. l describes the length along

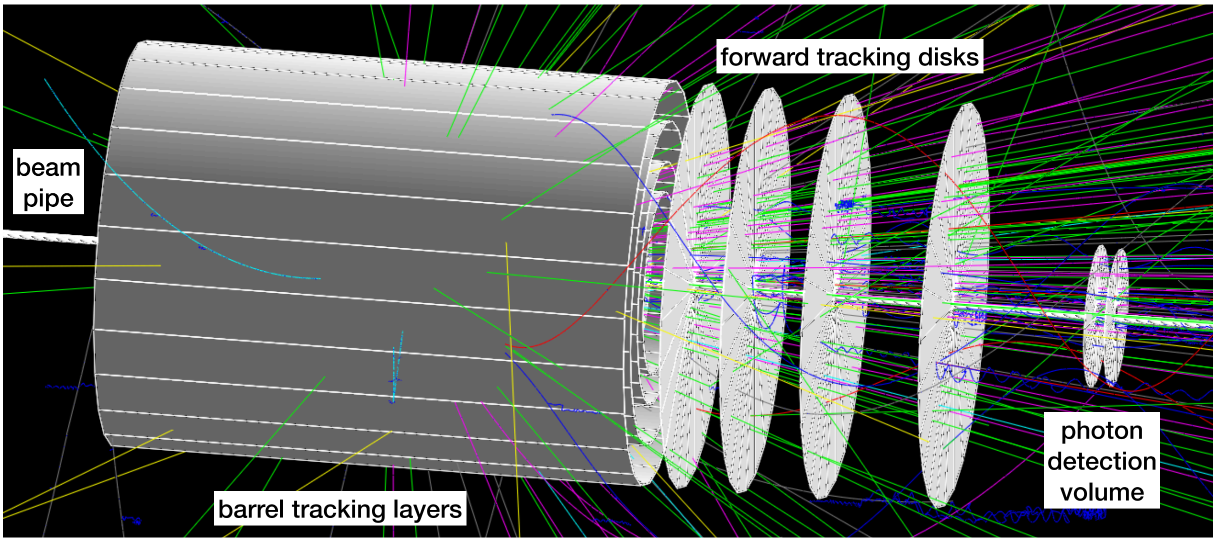

Figure 98: *Visualisation of* ALICE 3* *including the beam pipe, the barrel tracking layers, and the forward disks. The coloured lines represent the trajectories of different particle species produced via* PYTHIA *in a pp collision at* $\sqrt{s} = 13$ *TeV.*

The beam pipe is constructed as a cylindrical shell made up of beryllium with a thickness of 500 µm, a radius of 4.0 cm and a total length of 8 m.

12 barrel tracking layers are implemented as cylindrical shells with constant radius R, wall thickness d and length l. Table 13 lists the dimensions of the barrel tracking layers. The barrel tracking layers are made up of silicon. In general, the tracking layers can be subdivided into inner, middle and outer layers. All 100 µm thick inner layers are placed inside the beam pipe and have a total length of 30 cm. While the innermost layer of the middle layers is 100 µm thick and also placed within the beam pipe, all the other middle and outer layers are 1000 µm thick and positioned outside of the beam pipe. With a total length of 2.64 m, the outer layers are even longer compared to the middle layers with a length of 1.24 m. The length of the barrel layers increases as their radius increases, so that all layers cover a similar η region.

10 forward tracking disks are implemented with a radius coverage R of the disks that is larger, the farther away they are positioned (z) from the interaction point. The radius coverage R of the forward tracking disks increases, the farther away they are positioned (z) from the interaction point. Table 14 lists the dimensions of the 10 proposed forward tracking disks. The three innermost disks extend to $R = 3$ cm, disks with number 3, 4 and 5 extend to $R = 35$ cm and the outer disks extend even further to $R = 100$ cm. While the innermost three disks are foreseen with a Si wall of thickness $d = 100$ µm, all the others are 1000 µm thick.

---

the z-axis and the thickness d refers to the thickness of the detector component, either along the z-axis for the forward disks or along the R-axis for the beam pipe and the barrel layers.

layer number	**radius R (m)**	**length l (m)**	**Si thickness d (µm)**
inner barrel tracker layers			
0	0.0050	2 x 0.15	100
1	0.0120	2 x 0.15	100
2	0.0250	2 x 0.15	100
middle barrel tracker layers			
3	0.0375	2 x 0.62	100
4	0.0700	2 x 0.62	1000
5	0.1200	2 x 0.62	1000
6	0.2000	2 x 0.62	1000
7	0.3000	2 x 0.62	1000
outer barrel tracker layers			
8	0.4500	2 x 1.32	1000
9	0.6000	2 x 1.32	1000
10	0.8000	2 x 1.32	1000
11	1.0000	2 x 1.32	1000

Table 13: *Specification of the barrel tracking layers in* ALICE *3*. Each layers is constructed as cylinder shell with radius R, length l and wall thickness d of the material silicon (Si).*

disk number	**position z (m)**	**radius coverage R (m)**	**Si thickness d (µm)**
0	0.26	0.005 – 0.03	100
1	0.30	0.005 – 0.03	100
2	0.34	0.005 – 0.03	100
3	0.77	0.05 – 0.35	1000
4	1.00	0.05 – 0.35	1000
5	1.22	0.05 – 0.35	1000
6	1.50	0.05 – 1.00	1000
7	1.80	0.05 – 1.00	1000
8	2.20	0.05 – 1.00	1000
9	2.79	0.05 – 1.00	1000

Table 14: *Specification of the forward tracking disks in* ALICE *3*. Each disk is constructed at the position z with given radius coverage R and wall thickness d of the material silicon (Si).*

Finally, the simulation setup involves a particle counting volume used as "photon detector" at $z = 3.5$ m covering $3 < \eta < 5$, the η region of the proposed FCT.

In addition to omitting parts of the ALICE 3 detector geometry not reaching into $3 < \eta < 5$, the following simplifications are introduced in ALICE 3*: The implementation of the FCT geometry which involves several silicon sensor layers as proposed in [ALI+22] is neglected. To study the background in a soft-photon measurement and to qualitatively determine the strength of different contributions in simulation, the true GEANT4 particle information of all particles entering the particle counting volume is used. This simplification, i.e. using the true particle information,

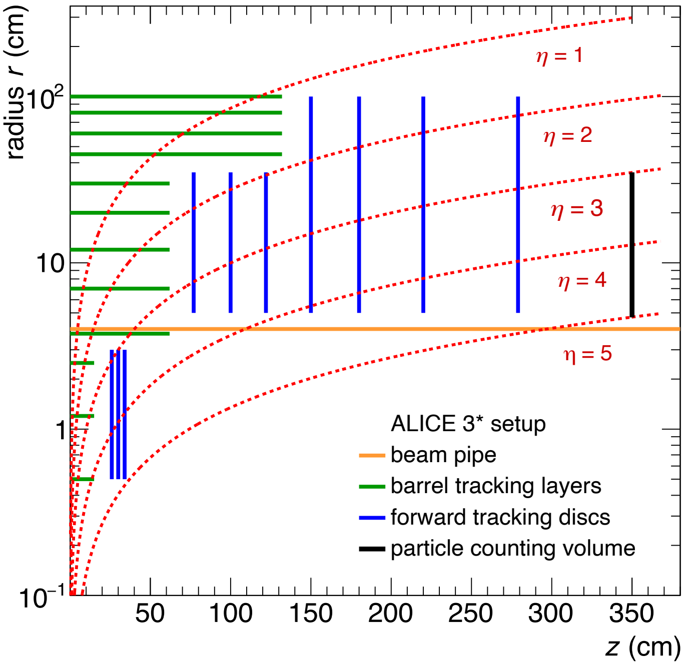

Figure 99: *A*LICE *3* detector map as function of radius r and beam axis z with the geometry description as implemented in* G4ME *used in this work. The beam pipe, barrel tracking layers, forward discs of* ALICE *3* and the particle counting volume are shown.*

omits any measurement process with the FCT silicon layers and therefore electron tracking or detector effects like resolution. In contrast to the beam pipe with a constant radius as used in the background study here, in [ALI+22], the beam pipe is foreseen with two different radii, one radius to provide the secondary vacuum and space for the discussed iris tracker (see section 6.5) and one slightly smaller radius for larger z. Modification of the beam pipe are discussed in section 7.5.1 in more detail.

To summarise the ALICE 3* simulation setup and the details of the geometry implementation of ALICE 3* in GEANT4, Figure 99 displays all the detector components as a function of the radius r and distance z to the collision vertex which are implemented in the simulation setup and used for the background studies in this thesis. Forward tracking disks are shown in blue, barrel tracking layers in green and the beam pipe in orange. In addition, r-z coordinates of constant pseudorapidity η are shown as red dotted lines, which illustrate the detector components a particle with distinct η traverses. For instance, at $\eta = 1$ the material budget a particle encounters involves the beam pipe and all barrel tracking layers. However, for specific η regions, a certain combination of the beam pipe, barrel tracking layers and forward tracking disks contribute to the material budget. The material budget and the η dependence of the material budget are discussed in more detail in section 7.4.1.

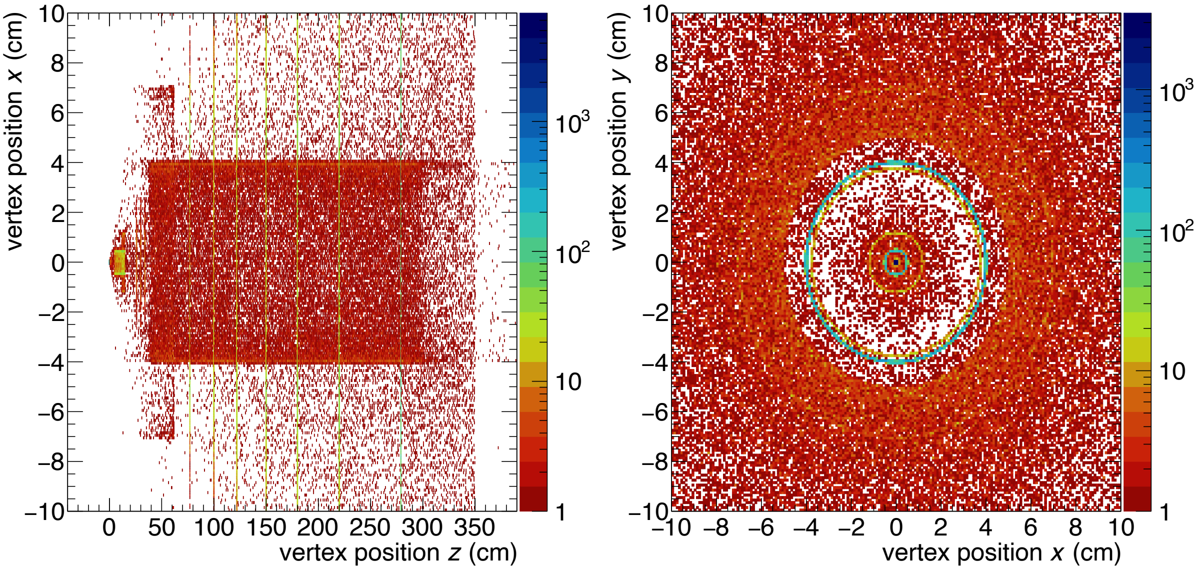

Figure 100: *Distribution of the photon production vertex in pp collision at* $\sqrt{s} = 13$ *TeV in* $3 < \eta < 5$. ***Left:*** *Side view of the vertex distribution, i.e. vertices as a function the position* x *and position* z. ***Right:*** *In-beam view of the vertex distribution, i.e. photon vertices as a function of position* y *and position* x.

7.2 Photon Production Vertex

To identify the spacial origin of soft photons in the simulation setup, the production vertex of soft photons in the setup is analysed and discussed in this section.

The two sources of γ^{ext} and γ^{dec} discussed in context of Figure 91 can be distinguished by studying the photon vertex position. The decay length $c\tau$ of unstable particles produced in particle collisions is short enough to assume that γ^{dec} are directly produced at the collision vertex neglecting rare-occurring late decays. For example, the decay length of the π^0 is $c\tau = 25.5\,\text{nm}$ [GZ+20].

In contrast to γ^{dec}, γ^{ext} most likely have their origin in detector material as the emission probability increases with the amount of material as discussed in section 6.3.2. Therefore, one can expect that most γ^{ext} are produced in the beam pipe, barrel layers and forward discs.

Figure 100 shows the distribution of photon vertices produced in pp collision at $\sqrt{s} = 13\,\text{TeV}$ for $3 < \eta < 5$ in side view (left) and in-beam view (right) for ALICE 3*. Figure 100 shows a considerably high number of photon vertices at the origin (0,0), which are all photons produced in the primary pp collision. In contrast, all photons with a vertex different from (0,0) are produced in the detector material.

By studying the photon production vertex distribution, the different components in the ALICE 3* simulation setup described in the previous section can be identified as they appear as γ^{ext}-origin: Clearly, a substantial amount of photons is produced in the forward disks visible in Figure 100 (left) as vertical lines at the z-positions of the

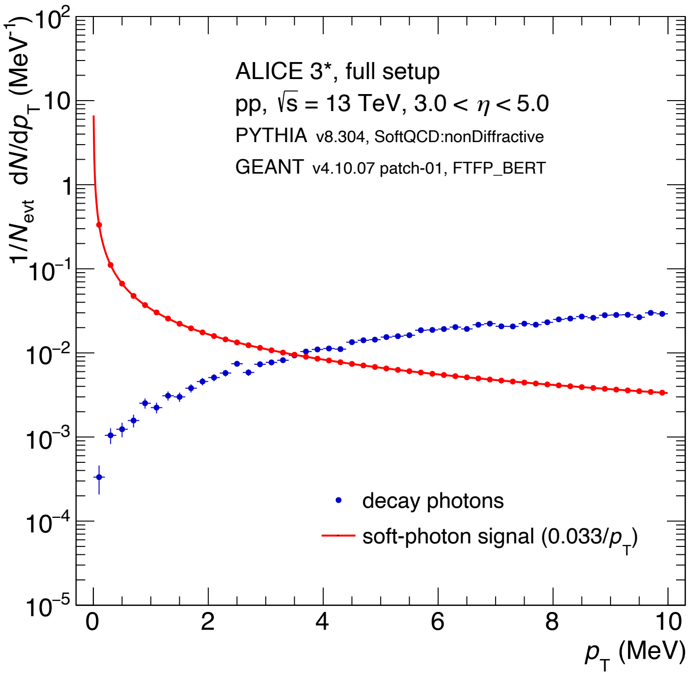

Figure 101: *Decay-photon yield in* ALICE 3* *and the soft-photon signal expectation from [Völ22] in pp collisions at* $\sqrt{s} = 13\,\text{TeV}$ *for* $3 < \eta < 5$*. For details about the expectation see section 6.3.1.*

forward disks (see Table 14). However, in the beam pipe with radius $r = 4\,\text{cm}$ even more γ^{ext} are produced as shown in Figure 100 (right) by the green circle at radius $r = 4\,\text{cm}$ and in Figure 100 (left) by the horizontal band at the vertex position $x = \pm 4$. In addition, the inner barrel tracking layers can be identified as strong γ^{ext}-origin, visible in Figure 100 (right) by the circles with radii of the inner barrel tracking layers (see Table 13).

7.3 Decay Photon Background

The true particle information from simulation is used to study the background. Here, all γ^{dec} entering the particle counting volume at $3 < \eta < 5$ in ALICE 3* are considered. Figure 101 shows the γ^{dec}-yield in blue and the γ^{sig}-expectation [Völ22] in red as a function of p_{T} for $3 < \eta < 5$.

One can observe the $1/p_{\text{T}}$ shape for the γ^{sig}-yield as well as the strong increase of the γ^{sig}-yield for $p_{\text{T}} \to 0$, as discussed in section 6.3. In contrast, the γ^{dec}-yield decreases for $p_{\text{T}} \lesssim 10\,\text{MeV}$ and becomes smaller than the γ^{sig}-expectation below $p_{\text{T}} \approx 3 - 4\,\text{MeV}$. While for $p_{\text{T}} \approx 10\,\text{MeV}$ the γ^{dec}-yield is a factor ~ 10 above the γ^{sig}-expectation, for $p_{\text{T}} \approx 1\,\text{MeV}$ the expectation is a factor ~ 10 above the γ^{dec}-yield.

Considering only γ^{dec}, γ^{sig} should be accessible for $p_{\text{T}} \lesssim 3 - 4\,\text{MeV}$ where the γ^{dec}-yield, i.e. the background, is small. Moreover, at forward rapidities, E_γ is

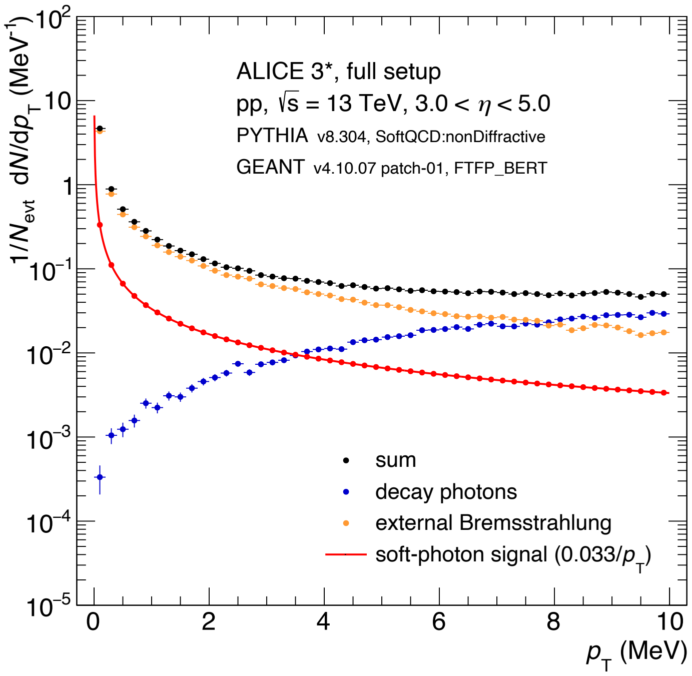

Figure 102: *Yield of decay photons, photons produced via external Bremsstrahlung in* ALICE 3* *and the soft-photon signal expectation from [Völ22] in pp collisions at* $\sqrt{s} = 13$ *TeV for* $3 < \eta < 5$. *For details about the expectation see section 6.3.1.*

significantly larger than p_T, e.g. $E_\gamma \approx 82$ MeV for $p_\mathrm{T} = 3$ MeV at $\eta = 4.5$, which should allow to measure the signal as discussed in section 6.4.

7.4 Background from Photons Produced via External Bremsstrahlung

Similar to the decay photons as discussed in the previous section, here, all photons produced via external Bremsstrahlung in the detector material of ALICE 3* which enter the counting volume at $3 < \eta < 5$ in ALICE 3* are considered via the true particle information in simulation.

Figure 102 shows the γ^dec-yield, γ^ext-yield and the γ^sig-expectation as a function of p_T for $3 < \eta < 5$. The γ^sig-expectation is approximately five to ten times smaller than the γ^ext-yield. For p_T less than $p_\mathrm{T} \approx 8\,\mathrm{MeV}$ the γ^ext-yield becomes greater than the γ^dec-yield. In contrast to the γ^dec-yield which drops for $p_\mathrm{T} \to 0$, the γ^ext-yield shows a similar $1/p_\mathrm{T}$ shape as the γ^sig-expectation and increases for smaller p_T.

The similarity between the γ^sig-expectation and the γ^ext-yield w.r.t. their p_T shape is already discussed in section 6.3.2, where both distributions are compared for an exemplary material budget of $d/X_0 = 10\,\%$.

In the next section, the comparison between the γ^sig-expectation and the γ^ext-yield in ALICE 3* is discussed with an emphasis on the material budget dependence.

7.4.1 Material Budget Dependence

To study the influence of the material budget on the background photons produced via external Bremsstrahlung, first, the ALICE 3* material budget is investigated using so-called geantinos in GEANT4. Furthermore, based on the estimate of the photon background $B_\gamma^{\text{prim. } e}$ from primary electrons and the photon background $B_\gamma^{\text{conv. } e}$ from conversion electrons discussed in section 6.3.2, both background sources are put in context of the ALICE 3* material budget in this section.

Geantinos are special, virtual particles in GEANT4 without any interaction. That means, they are transported through the whole ALICE 3* detector, but they do not interact with any material at all. Here, geantinos are used to probe the ALICE 3* setup to build a so called geantino map, i.e. a map of the ALICE 3* material budget as a function of η. For this purpose, technically, neutral geantinos are propagated through the ALICE 3* setup in GEANT4 in steps of $\Delta\eta = 0.05$ between $\eta = 0$ and $\eta = 5.5$. By histogramming the integrated material in terms of radiation length X_0 that the geantinos have passed through the detector material, the geantino map is obtained[3]. The integrated material M is computed as:

$$M(\eta) = \sum_{\substack{\text{material } i \\ \text{at } \eta}} \frac{l_{\text{step,i}}}{X_{0,\text{i}}} \tag{67}$$

Where $l_{\text{step,i}}$ represents the length of a whole step traversed by the geantino within the material i. $X_{0,\text{i}}$ refers to the radiation length of the corresponding material i.

Figure 103 shows the integrated material M as a function of the pseudorapidity η obtained by probing the ALICE 3* setup with geantinos. The contribution from the forward tracking discs is shown in blue, which increases until $\eta \approx 3.3$, where all particles traverse the 10 discs and approximately the integrated material of $8\,\% X_0$. For $\eta \geq 3.3$ the discs successively stop contributing to the material budget in steps of $\Delta\eta \approx 0.2$. In contrast to the vertically oriented forward discs, the barrel tracking layers are positioned horizontally. The larger η, i.e. the shallower the angle at which particles cross the material, the higher the integrated material traversed by the particle. The contribution from barrel tracking discs is shown in green and the shallow angle particle crossing explains the peak structure in the material budget contribution.

In the acceptance of the photon detecting volume ($3 < \eta < 5$) in ALICE 3*, only the inner barrel tracking layers contribute to the material budget with approximately 3 to 4 % X_0 and only for $\eta < 4$. The contribution from the beam pipe is shown in gray.

---

[3] Contributions from air surrounding the detector components and the secondary vacuum within the beam pipe are neglected.

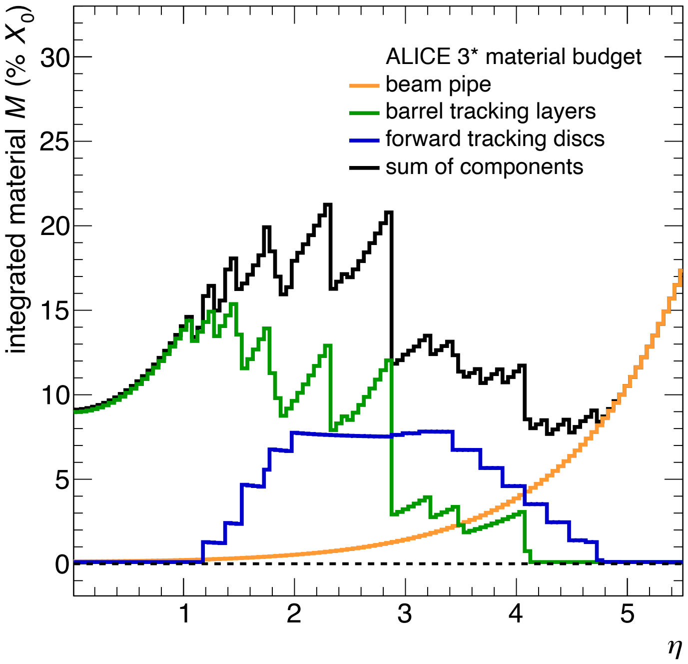

Figure 103: *Geantino map, i.e. the effective material budget as function of η separately for the* ALICE 3* *detector components as well as for their sum obtained by probing the* ALICE 3* *setup with geantinos in* GEANT4*. The components have the same colour code as used for the* ALICE 3* *detector map shown in Figure 99.)*

Similar to the barrel tracking layers, the beam pipe contribution increases for higher η. The contribution rises as $\cosh\eta$ from circa 2% X_0 at $\eta = 3$ up to 11% X_0 at $\eta = 5$.

To summarise, the total material budget of ALICE 3* fluctuates between approximately 8% X_0 to 22% X_0. The highest contribution to the integrated material arises from the barrel tracking layers contribute for $\eta \lesssim 3$, from the forward tracking discs for $3 \lesssim \eta \lesssim 4$ and the beam pipe contributes the most for $\eta \gtrsim 4$.

For the background study of this work, the integrated material in the acceptance of the photon detector $(3 < \eta < 5)$ is particularly relevant which fluctuates between circa 8% X_0 and 13% X_0. Focussing on this material, in the following, the soft-photon signal S_γ is compared to the estimated background photons from both conversion electrons $B_\gamma^{\text{conv.}\,e}$ and primary electrons $B_\gamma^{\text{prim.}\,e}$.

Figure 104 shows the signal-to-background ratio S_γ/B_γ^X in pp collision at $\sqrt{s} = 13\,\text{TeV}$ as a function of the integrated material for three scenarios with different background considered: Only $B_\gamma^{\text{conv.}\,e}$ in blue, only $B_\gamma^{\text{prim.}\,e}$ in green and their sum $(B_\gamma^{\text{conv.}\,e} + B_\gamma^{\text{prim.}\,e})$ in red. The signal equals the total background for the integrated material of $\approx 5\,\%$ as visible by the crossing of the red and the dotted line at unity in Figure 104.

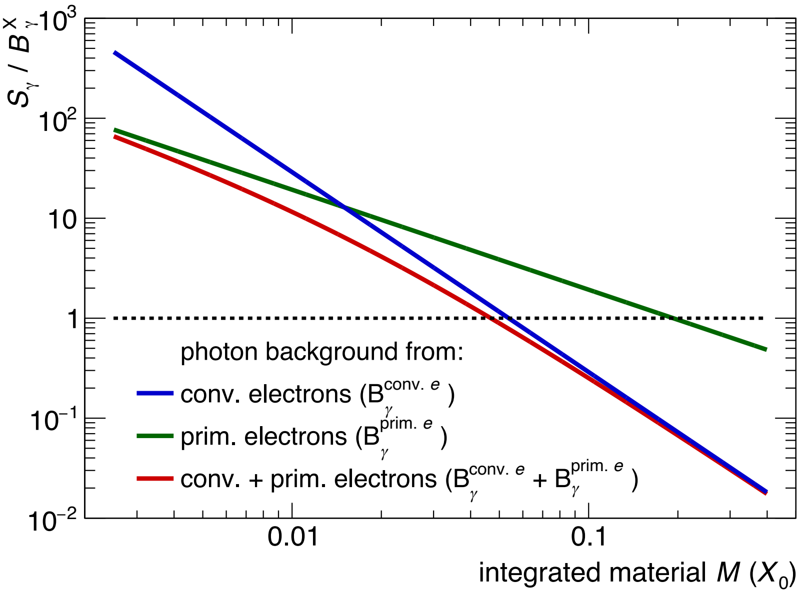

Figure 104: *Signal [Völ22] over background as a function of the material budget in pp collision at* $\sqrt{s} = 13$ *TeV for* $3 < \eta < 4$.

Considering only background photons from primary electrons, the signal over background $S_\gamma / B_\gamma^{\text{prim. } e}$ would be unity for an integrated material of $20\,\%X_0$, which is higher than the integrated material of $\sim 8\%\,X_0$ to $\sim 13\%\,X_0$ in the acceptance of the photon detector in ALICE 3*. Surprisingly, the background from conversion electrons equals the background from primary electrons $(B_\gamma^{\text{conv. } e} \overset{!}{=} B_\gamma^{\text{prim. } e})$ for an integrated material of $1.5\,\%X_0$, which is visible through the crossing of the green and blue line in Figure 104. For an integrated material greater than $1.5\,\%X_0$, the background from conversion electrons dominates the total background. Therefore, the dominant background source in ALICE 3* is the background from conversion electrons as the integrated material in ALICE 3* always greater $8\,\%$ in $3 < \eta < 4$.

In summary, two sources producing photons via external Bremsstrahlung are considered here, primary electrons from the collision vertex and electrons from photon conversion. The photon background from conversion electrons dominates the total photon background in ALICE 3*. In addition, both signal and background photons produced via external Bremsstrahlung have a similar $1/p_{\mathrm{T}}$ dependence and are already equal for an integrated material of $\approx 5\,\%X_0$, which is approximately only half of the ALICE 3* material budget in the acceptance of the photon detector. Overall, the yield of background photons produced via external Bremsstrahlung is approximately five to ten times greater than the signal expectation for $3 < \eta < 5$ and dominates the total photon background below $p_{\mathrm{T}} \approx 8\,\mathrm{MeV}$ where the decay-photon yield decreases as shown in Figure 102.

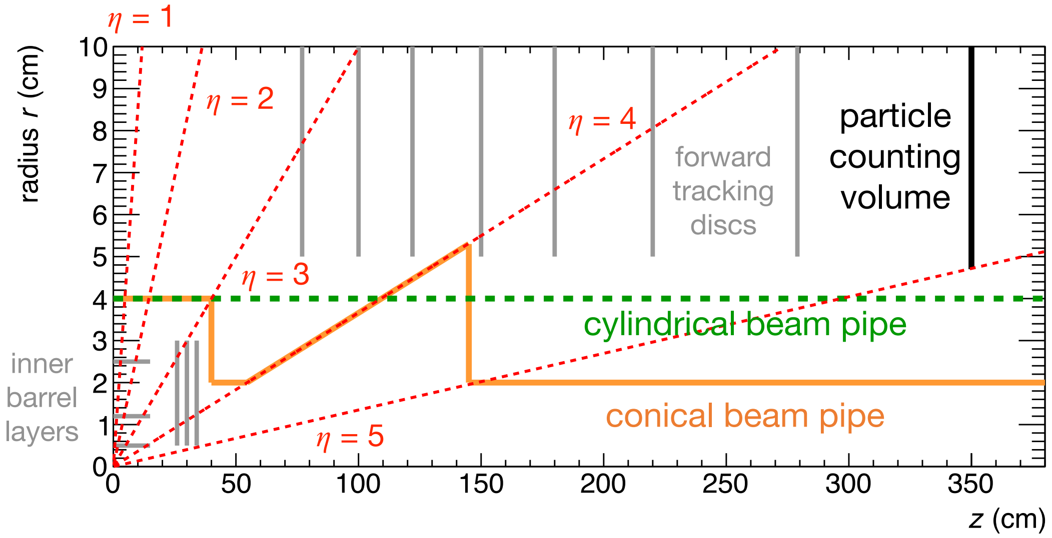

Figure 105: *Part of the* ALICE 3* *setup illustrating the conical beam pipe in orange and the cylindrical beam pipe in green. Note the different axis scales.*

7.5 Background Rejection Considerations

As shown in the previous sections, the dominant background in the soft-photon measurement are photons produced via external Bremsstrahlung. A reduction of the γ^{ext}-background could be achieved by lowering the material budget in front of the photon detector. Another way could be to control the background with dedicated analysis techniques such as an electron veto. The two possibilities to reduce the γ^{ext}-background are discussed in this section.

7.5.1 Material Reduction via Optimised Beam-Pipe Shape

As discussed in context of Figure 103, especially for $\eta > 3$ the beam pipe strongly contributes to the total material budget: the higher the η, the shallower the angle at which the particles cross the beam pipe. Similar to the relation between photon energy and p_{T} via $\cosh(\eta)$ as discussed in section 6.4, the effective distance $d_{\text{eff.}}$ at which a particle penetrates the beam pipe depends on the beam pipe wall thickness t and η as follows:

$$d_{\text{eff.}} = t \cdot \cosh(\eta) \tag{68}$$

Here, the factor $\cosh(\eta)$ leads to an increase of $d_{\text{eff.}}$ for higher η, which corresponds to the particles crossing the beam pipe at shallow angles and leads to an increase of the γ^{ext}-background given a higher material budget.

For instance, at $\eta = 5$, particles traverse approximately 75 times the wall thickness of the beam pipe. Therefore, a beam pipe with an opening window in the η-range of the particle counting volume would reduce the background drastically. Obviously, to

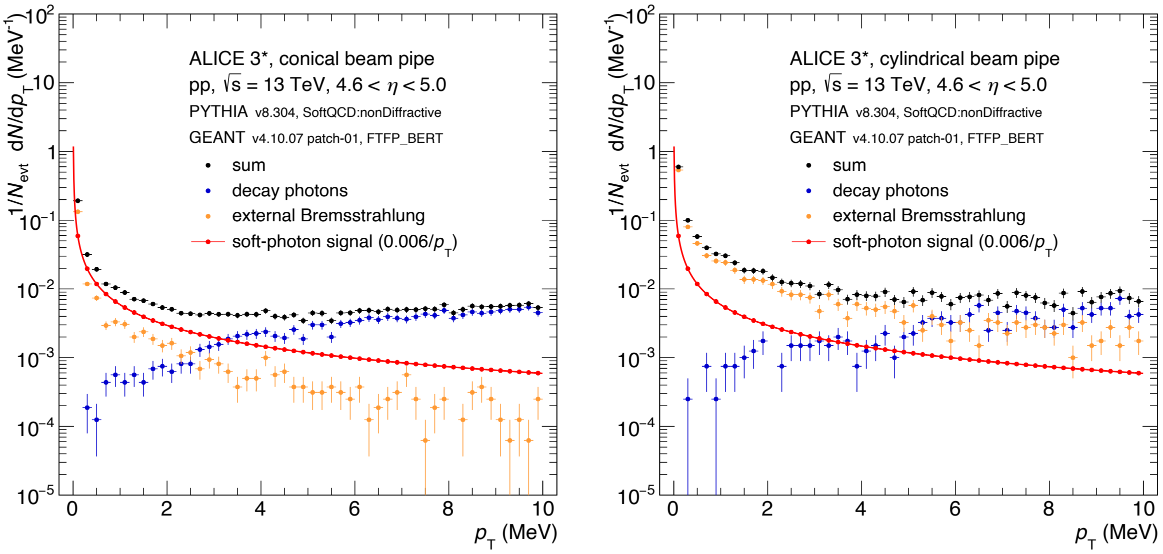

Figure 106: *Photon yields for decay photons in blue, external Bremsstrahlung in orange, the soft-photon signal in red and their sum in black for* $4.6 < p_T < 5.0$ *in pp collisions at* $\sqrt{s} = 13$ *TeV generated via* PYTHIA. *Here the* GEANT4 *setups used involve only a beam pipe, which is the standard cylindrical beam pipe (right) and the optimised conical beam pipe (left).*

guarantee a clean vacuum within the beam pipe, an opening window in the beam pipe is impossible. However, the same result would be obtained by an optimised beam pipe shape, so that shallow angle crossings are avoided in a certain η-range. Here, the investigation of the gain in performance of such an optimised beam-pipe shape is presented.

The photon background in two different GEANT4 simulation setup scenarios is compared in this thesis: one with the optimised beam-pipe shape and one with a "standard" cylindrical beam pipe. Therefore, in the following, ALICE 3* is reduced to only include a beam pipe and the particle counting volume. Figure 105 shows the two scenarios: First, the cylindrical beam pipe as a dashed green line and second, a conically shaped beam pipe as an orange line which offers the opening window in the particle counting volume acceptance. In Figure 105, the detector components of ALICE 3* not used in the beam-pipe simulation scenarios are also shown in grey to visualise the placement of the conical beam pipe in the original ALICE 3* setup.

Figure 106 show the yield of photons of different origins as a function of p_T exemplary for $4.6 < \eta < 5$. The γ^{dec}-yield is shown in blue, the γ^{ext}-yield in orange, the γ^{sig}-expectation in red and the sum of all three in black. While Figure 106 (left) shows the photon yields for the conical beam pipe scenario, the photon yields for the cylindrical beam pipe scenario are shown in Figure 106 (right). Already at this stage, by comparing the two scenarios, obviously a soft-photon measurement would benefit from a conical beam pipe. In the cylindrical beam pipe scenario, the γ^{ext}-background

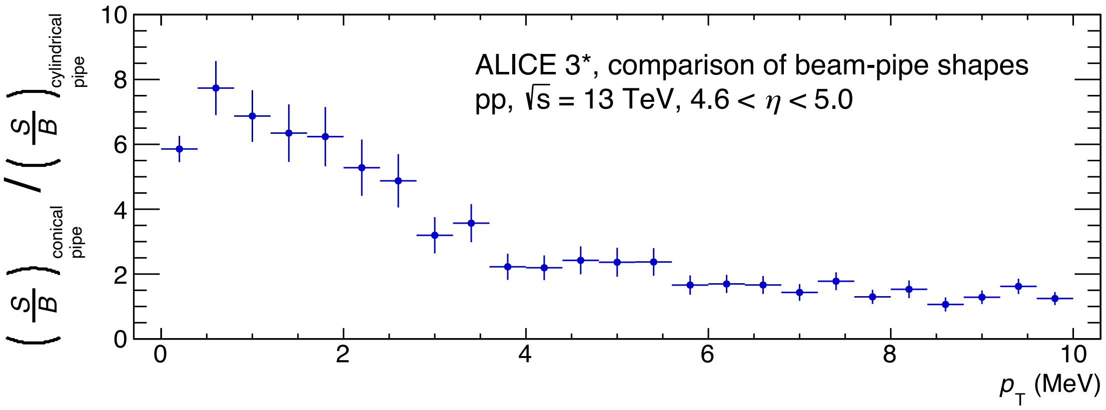

Figure 107: *Comparison of the signal-to-background ratio derived from the two* GEANT4 *setup scenarios involving the conical beam pipe (see Figure 106 on the left) and the cylindrical beam pipe (see Figure 106 on the right).*

is above the γ^{sig}-expectation. In contrast, the γ^{sig}-expectation is above the γ^{ext}-background for the conical beam pipe case.

The gain G in performance is extracted in terms of comparing the signal-to-background ratio S/B for both scenarios:

$$G = \frac{\left(\frac{S}{B}\right)_{\text{conical pipe}}}{\left(\frac{S}{B}\right)_{\text{cylindrical pipe}}} \tag{69}$$

The background B equals the sum of the contributions from external Bremsstrahlung and decay photons and the signal S reflects the soft-photon signal expectation.

Figure 107 shows the gain achieved by instrumenting a conical beam pipe instead of the standard, cylindrical beam pipe for $4.6 < \eta < 5$. In the low-p_T region of interest, by operation of a conical beam pipe, the signal-to-background ratio can be improved by a factor of ~ 6 at $p_T \approx 1$ MeV. In contrast, with a factor of ~ 2, the improvement is less strong at high p_T above $p_T \approx 4$ MeV, since there, decay photons dominate the background which remain unaffected by the beam-pipe shape.

To summarise, the findings presented in this section clearly speak in favour of a conical beam pipe shape. The advantage of a conical beam pipe compared to a cylindrical beam pipe is the reduction of the integrated material budget in front of the photon detector. By using a conical beam pipe, the beam-pipe crossing of particles under shallow angles is avoided. In general, the γ^{ext}-background can be reduced by lowering the material budged.

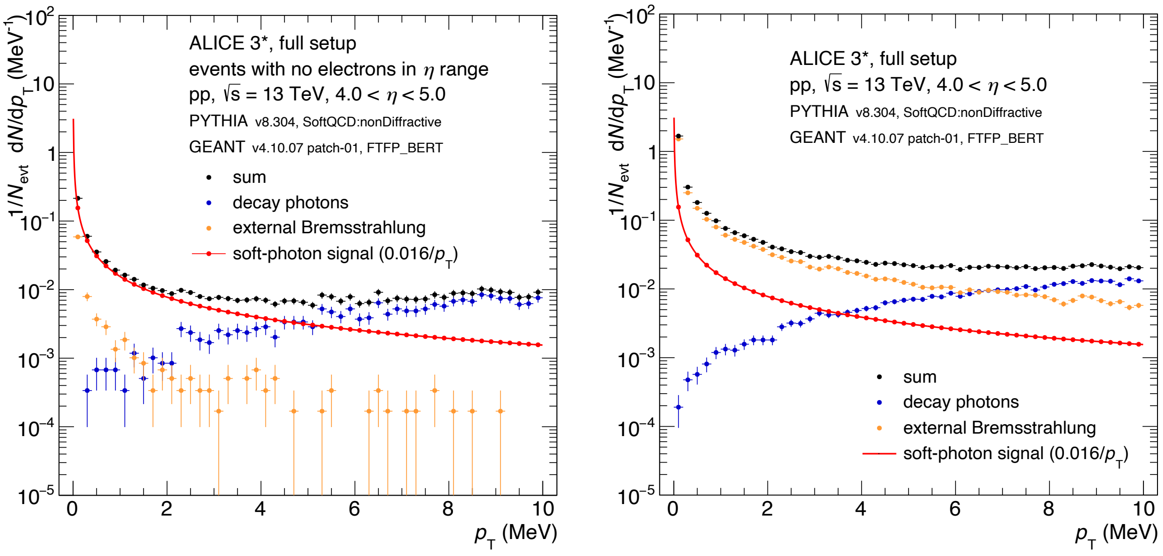

Figure 108: *Photon yields for decay photons, photons from external Bremsstrahlung, the soft-photon signal and their sum for* $4 < p_T < 5$ *in pp collisions at* $\sqrt{s} = 13$ *TeV. Both, all events (right) and events without an electron or positron in* $4 < p_T < 5$ *(left) are shown.*

7.5.2 Ideal Electron Veto Event Rejection

In contrast to the approach to reduce the photon background discussed in the previous section, which basically reduces the probability for the generation of external Bremsstrahlung, the second approach discussed below aims at identifying the emitter of external Bremsstrahlung, i.e. the electrons.

An idealised version of the electron veto approach has been studied in simulation in this thesis by the rejection of whole events with an electron in the acceptance of the particle counting volume in ALICE 3*. The fraction of events retained with an electron veto in different η-ranges is e.g. $\sim 28\,\%$ for $4 < \eta < 5$ and $\sim 4\,\%$ for $3 < \eta < 5$.

Figure 108 shows the yield of photons of different origin as a function of p_T for $4 < \eta < 5$ in pp collisions at $\sqrt{s} = 13\,\text{TeV}$. The γ^{dec}-yield is shown in blue, the γ^{ext}-yield produced in ALICE 3* in orange, the γ^{sig}-expectation in red and the sum of all three in black. Figure 108 (left) shows the background photon yields under application of the ideal electron veto discussed above, while the full γ^{sig}-expectation is assumed[4]. In contrast, Figure 108 (right) shows the signal and background without any event rejection. The application of the ideal electron veto strongly reduces the γ^{ext}-background while affecting the γ^{dec}-background only little.

Figure 109 shows the gain achieved by applying the ideal electron veto event rejection instead of analysing all events for $4 < \eta < 5$. The application of the electron

---

[4] Potentially, also the signal could be affected by the application of an electron veto event rejection. Therefore, this should be subject to further simulation studies (see section 7.6)

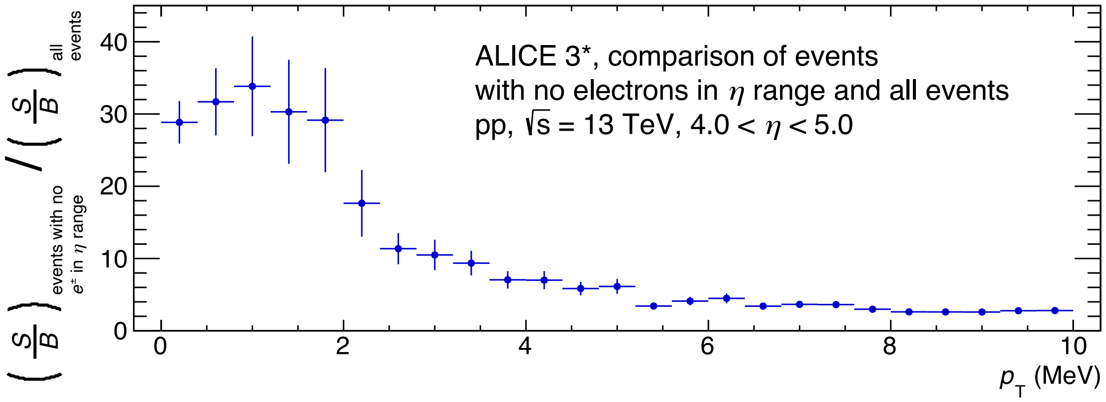

Figure 109: *Comparison of the signal-to-background ratio derived from both scenarios considering all events (top right) and only those without an electron or positron in the η range (top left).*

veto improves the signal-to-background ratio by a factor of ~ 30 below $p_\mathrm{T} \approx 2$ MeV. For higher p_T the improvement falls from ~ 10 at $p_\mathrm{T} \approx 3$ MeV to ~ 3 at $p_\mathrm{T} \approx 10$ MeV.

In summary, despite some idealisations in the electron veto approach, the presented performance gain clearly demonstrates the potential of the application of an electron veto. As electrons are identified as the main source of the γ^{ext}-background, the application of an electron veto leads to the rejection of the electrons as source. This leads to a reduction of the strength of the γ^{ext}-background.

7.6 Implications for a Soft-Photon Measurement in ALICE 3

A forward soft-photon measurement at very low p_T with the FCT in ALICE 3 is challenging and requires an effective handling of the background from external Bremsstrahlung as the decay-photon background appears to be low in the p_T-region of interest. In this region, the background exceeds the soft-photon signal by approximately an order of magnitude and will therefore overshadow the signal. The discussed background rejection scenarios are promising and show that a soft-photon measurement profits from lowering the material budget in front of the photon detector and profits from a rejection of electrons producing the photons. This applies directly to the overall design consideration of the ALICE 3 setup. The material in front of the FCT should be held as low as possible and analysis strategies to reject the background should be established.

The background studies presented in this work are based on a fast Monte Carlo simulation approach including a simplistic setup containing only the active elements and the beam pipe. The studies have been carried out in context of the ALICE 3 Letter of Intent and need to be extended for the upcoming ALICE 3 Technical Design Report as the next step of this ALICE upgrade program.

In particular, a full Monte Carlo simulation of the ALICE 3 setup e.g. in the so-called "ALICE 02 framework" is indispensable for a more realistic background study. Moreover, within a full Monte Carlo simulation the performance of the soft-photon measurement in ALICE 3 can be estimated, i.e. for example the signal-to-background ratio and the significance of the measurement.

In this full Monte Carlo simulation, a realistic implementation of the FCT setup including the silicon sensor layers would be necessary as well as an implementation of electron tracking for the photon reconstruction in the FCT layers via conversion electrons. Such a realistic simulation setup would allow to emulate the experimental soft-photon measurement and to perform a thorough estimate of the performance.

To refine the FCT implementation, the optimal positions of the FCT layers could be studied in a systematic way to find the configuration that gives the best performance in terms of reconstruction, efficiency and resolution. This study could be extended to find a magnet configuration that is optimal for the photon measurement.

Furthermore, analysis cuts could be established and e.g. the performance of the electron veto could be assessed. Besides the rejection of full events, one could consider the rejection of photons within a given radius around a charged particle track. Therefore, the identification of electrons, positrons or in general charged particles would need to be studied.

In the studies presented in this work, the full signal expectation is compared to the background. For a more realistic study, the injection of a pseudo soft-photon signal within a pp collision simulated via PYTHIA should be considered, to determine how much signal actually reaches the FCT and how much signal can be reconstructed. In addition, the influence of cuts on the signal could be studied in detail.

The different studies discussed above are beyond the scope of this work, but could be considered in further studies like in context of the ALICE 3 Technical Design Report.

8 Summary

The overall topic of this thesis is the measurement of photons with particle detectors based on silicon digital pixel sensors. Two different steps in upgrade programs of the ALICE experiment, one of the four big experiments in the field of high-energy physics at the CERN-LHC, are discussed in this thesis.

The ALICE experiment frequently develops new detectors in context of upgrade programs for their usage in the experiment to refine or expand the measurement program of the experiment. An upgrade project in ALICE typically involves the following steps: The motivation to measure a physics signal for the first time or with higher precision is followed by basic simulation studies of the detectability of the signal and the design of the detector. Afterwards, prototypes are developed and test measurements are performed until at the end of the construction and development process a new detector can be integrated into the ALICE experiment.

In this thesis, two different steps from two different upgrade programs of the ALICE experiment are combined: In context of the ALICE-FOCAL upgrade [ALI+20] planned for 2027, in this thesis, the detector response of the Electromagnetic Pixel Calorimeter Prototype EPICAL-2 and the shape of electromagnetic showers in EPICAL-2 are studied using measurements in a test beam and simulations (Part 1). In context of the ALICE 3-upgrade [ALI+22], the next-generation heavy-ion collision experiment for 2035, simulation studies of the background in a soft-photon measurement with a Forward Conversion Tracker FCT based on silicon sensors are discussed (Part 2). In the following, both parts of the thesis are summarised:

Part 1: Performance of the Electromagnetic Pixel Calorimeter EPICAL-2

EPICAL-2 has been designed and constructed within the endeavour to develop a novel electromagnetic calorimeter based on a SiW sampling design using silicon pixel sensors with binary readout. It utilises ALPIDE sensors developed for the ALICE-ITS upgrade and is refining the first prototype EPICAL-1 with MIMOSA sensors. EPICAL-2 consists of 24 identical layers. Each layer is 3.5 mm thick and consists of a tungsten absorber plate and two ALPIDE chips. EPICAL-2 has a total thickness of approximately 20 radiation lengths, an active area of 30 mm × 30 mm, and about 25 million pixels each of size of $26.88 \times 29.24\,\mu\text{m}^2$.

Test measurements with EPICAL-2 have been performed at the University of Utrecht in the Netherlands using cosmic muons in 2020. Furthermore, test-beam measurements have been performed at DESY in 2020 and as part of this work at CERN-SPS in 2021. While the DESY test beam contains only electrons, the test beam at SPS is a mixed beam containing muons, hadrons and electrons. At DESY, electron events were recorded at 1, 2, 3, 4, 5 and 5.8 GeV. At SPS, electron, muon and hadron events were recorded at 20, 40, 60 and 80 GeV.

In this thesis, the EPICAL-2 prototype is implemented in the Allpix^2 framework to compare and validate the test-beam measurements with a Monte Carlo simulation and to understand and assess the behaviour of the detector response in simulation. This EPICAL-2 simulation is the first implementation of a fully digital calorimeter in the Allpix^2 framework.

Every property of EPICAL-2 is carefully implemented in the simulation. The detailed EPICAL-2 geometry with every single detector component is implemented with high precision. In collaboration with [Has21b], the exact pixel electric field of ALPIDE is implemented using a TCAD simulation with a total reverse bias voltage of $V_{\mathrm{RB}} = 1.4\,V$ and the exact doping concentrations of each ALPIDE component. The pixel threshold (82 e) and the pixel noise (20 e) as average of the chips in EPICAL-2 are implemented.

Besides the EPICAL-2 properties, the characteristics of the test-beams are implemented in the simulation. To particularly model the test-beam measurements, the charge propagation time is determined to 25.1 ns based on testing the agreement of the number of hits distribution between the measured data and the simulation at an electron energy of 5 GeV using a χ^2 test, a Kolmogorov test and the mean value of the distributions.

Using only the simulation, in this thesis, a systematic simulation study of the EPICAL-2 behaviour under variation of the EPICAL-2 implementation has been performed. For example, the pixel threshold strongly influences the behaviour: The higher the threshold, the lower the number of pixel hits and the smaller the cluster size. Overall, this study validates the implementation of EPICAL-2 in the simulation.

To measure the shape of single electromagnetic showers and to determine the energy measurement with EPICAL-2, the following data preparation steps are performed in this thesis:

- Malfunctioning pixel masking
- Clustering pixel hits
- Chip alignment
- Chip calibration
- Inclination correction
- Electron event selection

In particular: Less than 1 % of all pixels are malfunctioning. The cluster size distribution shows a high probability ($\sim 72\,\%$) for clusters with a size smaller than four pixels. It is particularly noteworthy, that the simulation can model the distribution over several orders of magnitude in probability; also very large clusters and their track-like shape are correctly modelled. The specific chip response of the EPICAL-2 chips is due to the different chip thresholds. The chip calibration and alignment correction are stable between using cosmic muon and SPS track events. The inclination of the test-beam is very similar for all DESY and SPS energies. The hadron contamination in the SPS data is less than 2 %.

In this work, the longitudinal and lateral shower profiles of electromagnetic showers in EPICAL-2 are determined. The longitudinal profiles show a later shower maximum position for hits than for clusters at DESY and the opposite trend at SPS. The general profile features agree between the measured data and the simulation. However, the simulation predicts a later shower maximum position compared to data. This can be caused by additional material in the measurement or by imperfections of the GEANT4 simulation while describing the shower evolution.

The lateral profiles increase with higher energy and a clear layer ordering is found that corresponds to the different stages in the shower development. The lateral hit and cluster densities are compared showing cluster saturation especially at high energies, around the shower maximum and close to the shower axis.

The distance at which nearby showers can be separated is assessed using the average shower width. A clear layer ordering is observed: the later the layer, the broader the shower. It is particularly noteworthy, that the average shower width is determined to approximately 0.2 mm for all energies early in the shower development demonstrating the possibility to separate nearby showers at this distance.

The separation of nearby showers is further studied in a simulation of two electrons (30 and 250 GeV, 1.1 mm distance). Both showers can be identified with EPICAL-2. It is impressive that in context of ALICE-FOCAL, this corresponds to a separation of two photons from a decay of a pion with an energy of about 1.6 TeV.

In this thesis, the energy response of EPICAL-2 is determined and parametrised with a linear function and a power-law function to test the linearity of the response in the measured data and the simulation. The response is non-linear with greater deviations from linearity for clusters (up to $\sim 18\,\%$) than for hits (up to $\sim 5\,\%$). In simulation, the trend is the same but deviations from linearity are less than $\sim 10\,\%$ for clusters and less than $\sim 3\,\%$ for hits. The observed non-linearity is mainly due to saturation, energy leakage out of EPICAL-2 and the beam energy uncertainty at DESY.

The energy resolution of EPICAL-2 is obtained, showing a better resolution for clusters than for hits. The EPICAL-2 resolution using hits is superior to the EPICAL-1 resolution [Haa+18]. Using clusters, the energy resolution of EPICAL-2 is obtained to

$$\frac{\sigma_E}{E} = \frac{18.16\ \%}{\sqrt{E/\mathrm{GeV}}} \oplus 2.68\ \%$$

which is very close to the energy resolution of the analog CALICE physics prototype [Adl+09]. This makes the digital pixel technology competitive with an analog energy measure. Overall, the energy resolution in the simulation degrades when comparing a simulation with no beam-energy spread to a simulation with beam-energy spread. This demonstrates that the EPICAL-2 resolution obtained in the measured data can be considered as an upper limit of the intrinsic energy resolution of EPICAL-2. Furthermore, the energy resolution is affected by the beam energy uncertainty and residual contamination in the test-beam data.

Parts of the results obtained from the simulation and the test-beam measurements with EPICAL-2 in this thesis are published in [Alm+23]. The results show the overall good performance of EPICAL-2 in terms of the energy measurement and the accessibility of the details of the electromagnetic shower shape based on the ultra high-granularity. In context of FOCAL as an upgrade of the ALICE experiment, the shower shape studies support the application of high-granular pixel layers in FOCAL. Overall, the EPICAL-2 performance demonstrates the potential of the digital calorimeter technology also for future applications in the field of high-energy physics.

Part 2: Soft-Photon Background Studies in ALICE 3

In ALICE 3 a Forward Conversion Tracker FCT ($3 < \eta < 5$) is foreseen to measure soft-photons at forward rapidities. A new soft-photon measurement could resolve the striking discrepancies between the theoretical expectation and various experimental measurements, with all measurements yielding an excess of typically two to eight. In this thesis, the background in a soft-photon measurement is studied in a simulation. Parts of the background studies are published in [ALI+22].

The proposed ALICE 3 detector geometry is implemented in a GEANT4 setup using the G4ME framework [Pre22]. In particular, the beam pipe, barrel tracking layers, end caps and a photon detection volume at the FCT position are implemented. To study the background, particles are generated via PYTHIA in pp collisions at $\sqrt{s} = 13$ TeV and propagated through the GEANT4 setup.

In this thesis, the study of the background shows that the dominant background sources are decay photons and external Bremsstrahlung from detector-material interaction. While the decay photon yield decreases for $p_{\mathrm{T}} < 10\,\mathrm{MeV}$, the yield of external Bremsstrahlung diverges as $1/p_{\mathrm{T}}$ for $p_{\mathrm{T}} \to 0$ similar to the soft-photon signal itself. In the acceptance-region of the FCT the background exceeds the signal expectation by a factor of 5 to 10 for $p_{\mathrm{T}} < 4\,\mathrm{MeV}$. It is key to reduce the background from external Bremsstrahlung produced in the ALICE 3 detector material, which is estimated to 8% X_0 and 14% X_0 using geantinos in GEANT4 .

Possibilities to reduce the background are investigated in this thesis. Major improvements can be achieved by an electron veto (signal-to-background improves by a factor of ~ 30) and by reducing the material in optimising the shape of the beam pipe to avoid particles to cross the beam pipe at shallow angles (signal-to-background improves by a factor of ~ 7).

A Appendix

A.1 Pixel Mask for all Chips

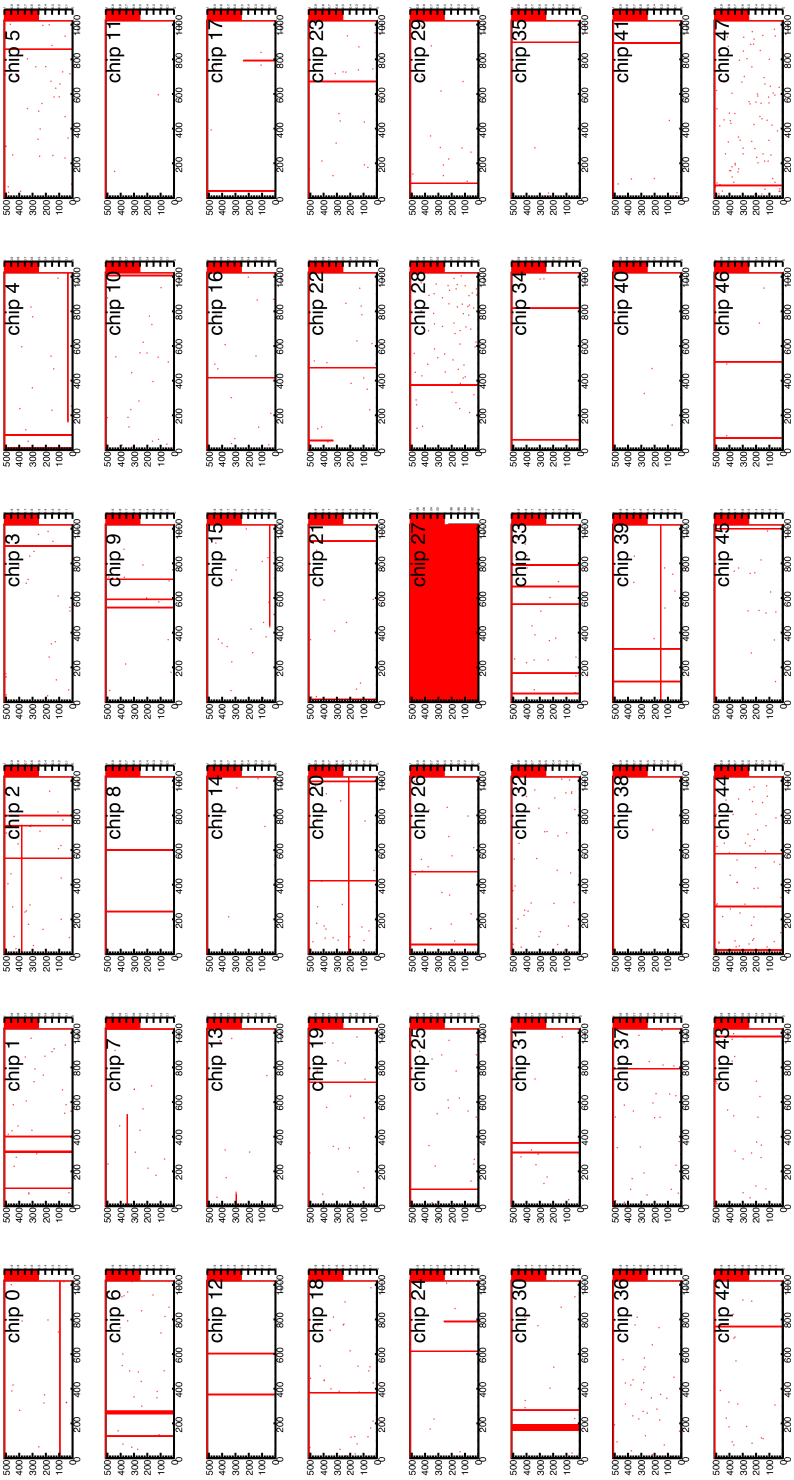

Figure 110: *Pixels masks for each* EPICAL-2 *chip. Red areas correspond to masked pixels.*

A.2 Mean and Width of Signal Distributions

data	**hits**		**clusters**	
E (GeV)	μ	σ	μ	σ
1.0	291.63 ± 0.13	71.65 ± 0.09	72.20 ± 0.02	13.47 ± 0.02
2.0	574.17 ± 0.22	100.05 ± 0.16	140.47 ± 0.04	18.72 ± 0.03
3.0	862.39 ± 0.26	123.20 ± 0.19	209.33 ± 0.05	23.07 ± 0.04
4.0	1141.96 ± 0.25	140.80 ± 0.18	275.20 ± 0.05	26.10 ± 0.03
5.0	1417.88 ± 0.20	157.14 ± 0.14	339.04 ± 0.04	28.84 ± 0.03
5.8	1613.99 ± 0.29	170.08 ± 0.20	383.36 ± 0.05	30.99 ± 0.04
20.0	5370.58 ± 7.69	355.55 ± 5.44	1221.93 ± 1.41	65.37 ± 1.00
40.0	10665.15 ± 4.34	523.84 ± 3.10	2304.56 ± 0.77	91.88 ± 0.54
60.0	15861.19 ± 8.92	709.37 ± 6.31	3292.95 ± 1.52	121.19 ± 1.08
80.0	21026.25 ± 14.86	841.31 ± 10.51	4214.68 ± 2.37	134.37 ± 1.68

Table 15: *Mean μ and standard deviation σ of the N_{hits} - and N_{clus} - distributions shown in Figure 85 for data (see section 5.2.1).*

simulation	**hits**		**clusters**	
E (GeV)	μ	σ	μ	σ
1.0	286.02 ± 0.32	75.48 ± 0.22	69.52 ± 0.06	14.50 ± 0.04
2.0	568.80 ± 0.42	96.71 ± 0.30	136.34 ± 0.08	17.42 ± 0.05
3.0	853.13 ± 0.50	116.11 ± 0.35	202.50 ± 0.09	20.21 ± 0.06
4.0	1136.74 ± 0.57	131.42 ± 0.40	267.93 ± 0.10	22.57 ± 0.07
5.0	1418.08 ± 0.64	145.58 ± 0.45	332.33 ± 0.11	24.66 ± 0.08
5.8	1643.47 ± 0.69	155.71 ± 0.48	383.50 ± 0.12	26.26 ± 0.08
20.0	5573.92 ± 2.30	304.46 ± 1.63	1237.65 ± 0.39	51.86 ± 0.28
40.0	10959.55 ± 3.68	475.61 ± 2.60	2324.03 ± 0.61	78.52 ± 0.43
60.0	16225.39 ± 4.10	639.54 ± 2.90	3318.07 ± 0.66	102.77 ± 0.47
80.0	21381.53 ± 8.83	780.13 ± 6.24	4239.51 ± 1.40	123.37 ± 0.99

Table 16: *Mean μ and standard deviation σ of the N_{hits} - and N_{clus} - distributions shown in Figure 85 for simulation (see section 5.2.1).*

Bibliography

[Aar+07] G. Aarons et al.
"ILC Reference Design Report Volume 4 - Detectors."
In: *FERMILAB-DESIGN-2007-02, FERMILAB-PUB-07-793-E* (Dec. 2007).
arXiv: `0712.2356 [physics.ins-det]`.

[Adl+09] C. Adloff et al.
"Response of the CALICE Si-W electromagnetic calorimeter physics prototype to electrons."
In: *Nuclear Instruments and Methods in Physics Research Section A: Accelerators, Spectrometers, Detectors and Associated Equipment* 608.3 (2009), pp. 372–383.
DOI: `https://doi.org/10.1016/j.nima.2009.07.026`.

[Agl+21] G. Aglieri Rinella et al.
"Charge collection properties of TowerJazz 180nm CMOS Pixel Sensors in dependence of pixel geometries and bias parameters, studied using a dedicated test-vehicle: The Investigator chip."
In: *Nuclear Instruments and Methods in Physics Research Section A: Accelerators, Spectrometers, Detectors and Associated Equipment* 988 (2021), p. 164859.
DOI: `https://doi.org/10.1016/j.nima.2020.164859`.

[Agl17] G. Aglieri Rinella.
"The ALPIDE pixel sensor chip for the upgrade of the ALICE Inner Tracking System."
In: *Nucl. Instrum. Meth. A* 845 (2017), pp. 583–587.
DOI: `10.1016/j.nima.2016.05.016`.

[Ago+03] S. Agostinelli et al.
"Geant4 — a simulation toolkit."
In: *Nuclear Instruments and Methods in Physics Research Section A: Accelerators, Spectrometers, Detectors and Associated Equipment* 506.3 (2003), pp. 250–303.
DOI: `https://doi.org/10.1016/S0168-9002(03)01368-8`.

[ALI+08a] CERN ALICE Collaboration et al.
"The ALICE experiment at the CERN LHC."
In: *Journal of Instrumentation* 3.08 (Aug. 2008), S08002–S08002.
DOI: `10.1088/1748-0221/3/08/s08002`.

[ALI+08b] CERN ALICE Collaboration et al.
"ALICE Electromagnetic Calorimeter Technical Design Report."

In: *CERN-LHCC-2008-014, ALICE-TDR-14* (2008).
URL: https://cds.cern.ch/record/1121574.

[ALI+12] CERN ALICE Collaboration et al.
"Upgrade of the ALICE Experiment: Letter of Intent."
In: *CERN-LHCC-2012-012, LHCC-I-022, ALICE-UG-002* (Aug. 2012).
DOI: 10.1088/0954-3899/41/8/087001.

[ALI+14] CERN ALICE Collaboration et al.
"Technical Design Report for the Upgrade of the ALICE Inner Tracking System."
In: *Journal of Physics G: Nucl. Part. Phys.* 41.8 (July 2014), p. 087002.
DOI: 10.1088/0954-3899/41/8/087002.

[ALI+16] CERN ALICE Collaboration et al.
"Pseudorapidity and transverse-momentum distributions of charged particles in proton–proton collisions at s=13 TeV."
In: *Physics Letters B* 753 (2016), pp. 319–329.
DOI: https://doi.org/10.1016/j.physletb.2015.12.030.

[ALI+18] CERN ALICE Collaboration et al.
"Transverse momentum spectra and nuclear modification factors of charged particles in pp, p-Pb and Pb-Pb collisions at the LHC."
In: *CERN-EP-2018-025* 11 (Nov. 2018), 013. 27 p.
DOI: 10.1007/JHEP11(2018)013.

[ALI+20] CERN ALICE Collaboration et al.
"Letter of Intent: A Forward Calorimeter (FoCal) in the ALICE experiment."
In: *CERN-LHCC-2020-009, LHCC-I-036* (June 2020).
URL: https://cds.cern.ch/record/2719928.

[ALI+21a] CERN ALICE Collaboration et al.
"A Large Ion Collider Experiment: The heavy ion experiment at the LHC."
Webpage, last access in 2021.
URL: https://alice.cern/#experiment.

[ALI+21b] CERN ALICE Collaboration et al.
"ALICE tracks new territory."
In: *Cerncourier - Reporting on international high-energy physics* (Webpage, last access in 2021).
URL: https://cerncourier.com/a/alice-tracks-new-territory/.

[ALI+22] CERN ALICE Collaboration et al.

"Letter of intent for ALICE 3: A next generation heavy-ion experiment at the LHC."
In: *CERN-LHCC-2022-009, LHCC-I-038* (Mar. 2022).
URL: `https://cds.cern.ch/record/2803563`.

[ALI+23] CERN ALICE Collaboration et al.
"ALICE upgrades during the LHC Long Shutdown 2."
In: *CERN-EP-2023-009* (2023).
URL: `https://cds.cern.ch/record/2847599`.

[ALI+95] CERN ALICE Collaboration et al.
"ALICE: Technical proposal for a Large Ion collider Experiment at the CERN LHC."
In: *LHC technical proposal, CERN-LHCC-95-71; LHCC-P-3* (1995).
URL: `https://cds.cern.ch/record/293391`.

[ALI+99] CERN ALICE Collaboration et al.
"ALICE Photon Spectrometer (PHOS): Technical Design Report."
In: *Technical design report. ALICE* (1999).
URL: `https://cds.cern.ch/record/381432`.

[ALI20] CERN ALICE-ITS.
Private Database.
2020.

[All+16] J. Allison et al.
"Recent developments in Geant4."
In: *Nuclear Instruments and Methods in Physics Research Section A: Accelerators, Spectrometers, Detectors and Associated Equipment* 835 (2016), pp. 186–225.
DOI: `https://doi.org/10.1016/j.nima.2016.06.125`.

[All21] Authors of Allpix Squared.
Allpix Squared - Generic Pixel Detector Simulation Framework.
Webpage, last access in 2021.
URL: `https://project-allpix-squared.web.cern.ch/project-allpix-squared/`.

[Alm+23] J. Alme et al.
"Performance of the electromagnetic pixel calorimeter prototype Epical – 2."
In: *Journal of Instrumentation* 18.01 (Jan. 2023), P01038.
DOI: `10.1088/1748-0221/18/01/P01038`.

[Ama+00] S. Amato et al.

“LHCb calorimeters: Technical Design Report.”
In: *Technical design report. LHCb - CERN-LHCC-2000-036; LHCb-TDR-2* (2000).
URL: `https://cds.cern.ch/record/494264`.

[Ath+80] H. W. Atherton et al.
“Precise measurements of particle production by 400 GeV/c protons on beryllium targets.”
In: *CERN Yellow Reports: Monographs - CERN-80-07* (1980).
DOI: `10.5170/CERN-1980-007`.

[Bar09] J. Bartke.
“Introduction to Relativistic Heavy Ion Physics.”
In: *World Scientific Publishing Co. Pte. Ltd.* (2009).

[Bel+02] A Belogianni et al.
“Observation of a soft photon signal in excess of QED expectations in pp interactions.”
In: *Physics Letters B* 548.3 (2002), pp. 129–139.
DOI: `https://doi.org/10.1016/S0370-2693(02)02837-X`.

[Bil+15] B. Bilki et al.
“Testing hadronic interaction models using a highly granular silicon–tungsten calorimeter.”
In: *Nuclear Instruments and Methods in Physics Research Section A: Accelerators, Spectrometers, Detectors and Associated Equipment* 794 (2015), pp. 240–254.
DOI: `https://doi.org/10.1016/j.nima.2015.05.009`.

[BR97] R. Brun et al.
“ROOT: An object oriented data analysis framework.”
In: *Nucl. Instrum. Meth. A* 389 (1997). Ed. by M. Werlen et al., pp. 81–86.
DOI: `10.1016/S0168-9002(97)00048-X`.

[CMS97] CERN CMS Collaboration.
“The CMS electromagnetic calorimeter project: Technical Design Report.”
In: *Technical design report. CMS* (1997).
URL: `https://cds.cern.ch/record/349375`.

[CSS+08] M. Cacciari et al.
“The anti-k_t jet clustering algorithm.”
In: *JHEP* 04 (2008), p. 063.
DOI: `10.1088/1126-6708/2008/04/063`.

[DEL06] Collaboration DELPHI.

"Evidence for an excess of soft photons in hadronic decays of Z0."
In: *The European Physical Journal C - Particles and Fields* 47 (2006), pp. 273–294.
DOI: https://doi.org/10.1140/epjc/s2006-02568-8.

[DEL08] Collaboration DELPHI.
"Observation of the muon inner bremsstrahlung at LEP1."
In: *The European Physical Journal C - Particles and Fields* 57 (2008), pp. 499–514.
DOI: https://doi.org/10.1140/epjc/s10052-008-0779-z.

[Die+19] R. Diener et al.
"The DESY II test beam facility."
In: *Nuclear Instruments and Methods in Physics Research Section A: Accelerators, Spectrometers, Detectors and Associated Equipment* 922 (Apr. 2019), pp. 265–286.
DOI: 10.1016/j.nima.2018.11.133.

[Eft03] I. Efthymiopoulos.
"T4 Wobbling and P41 beam."
In: *Secondary Beams and Areas (SBA) CERN webpage* (Webpage, last access in 2003).
URL: https://sba.web.cern.ch/sba/Documentations/Target/T4/T4Wobbling3.pdf.

[Est+96] M Ester et al.
"A density-based algorithm for discovering clusters in large spatial databases with noise."
In: *CONF-960830 - TRN: 96:005928-0038* (Dec. 1996).
URL: https://www.osti.gov/biblio/421283.

[Gea22] Collaboration Geant4.
"Physics List Guide."
Aug. 2022.
URL: https://geant4-userdoc.web.cern.ch/UsersGuides/AllGuides/html/PhysicsListGuide/physicslistguide.html.

[GF22] A. Gerbershagen et al.
"The H6 Secondary Beam Line of EHN1/SPS."
In: *Secondary Beams and Areas (SBA) CERN webpage* (July 2022).
URL: https://sba.web.cern.ch/sba/BeamsAndAreas/H6/H6_presentation.html.

[Goo21] Google LLC - Google Maps.

"CERN's North Area: CERN Prevessin."
2021.
URL: https://www.google.com/maps/place/CERN+Prevessin/@46.2544915,6.0505239,2983m/data=!3m1!1e3!4m9!1m2!2m1!1sCERN+prevessin!3m5!1s0x478c637b966a068f:0x44130099e2c910d4!8m2!3d46.2551762!4d6.0585774!15sCg5DRVJOIHByZXZlc3NpbiIDiAEBkgEQY29ycG9yYXRlX29mZmljZQ.

[Gro20] D. Groom for the Particle Data Group.
"Atomic and Nuclear Properties of Materials for more than 350 materials."
Webpage, last access in 2020.
URL: https://pdg.lbl.gov/2020/AtomicNuclearProperties/.

[GZ+20] Particle Data Group et al.
"Review of Particle Physics."
In: *Progress of Theoretical and Experimental Physics* 2020.8 (2020), p. 083C01.
DOI: 10.1093/ptep/ptaa104.

[Haa+18] A.P. de Haas et al.
"The FoCal prototype—an extremely fine-grained electromagnetic calorimeter using CMOS pixel sensors."
In: *JINST* 13.01 (2018), P01014.
DOI: 10.1088/1748-0221/13/01/P01014.

[Has21a] J. A. Hasenbichler.
"Development of Novel Pixel CMOS Sensors Optimised for Time Resolution."
2021.
URL: https://cds.cern.ch/record/2806261.

[Has21b] J. A. Hasenbichler.
Private communication.
2021.

[Hoo15] J. W. van Hoorn.
"Study and Development of a novel Silicon Pixel Detector for the Upgrade of the ALICE Inner Tracking System."
2015.
URL: https://cds.cern.ch/record/2119197.

[Kle92] Konrad Kleinknecht.
Detektoren für Teilchenstrahlung, 3. Auflage.
Teubner Studienbücher.
Stuttgart: B.G. Teubner, 1992.

[KW16] Hermann Kolanoski et al.
Teilchendetektoren: Grundlagen und Anwendungen.
Life Science and Basic Disciplines (German Language).
Springer Verlag Berlin Heidelberg 2016, 2016.
DOI: 10.1007/978-3-662-45350-6.

[Low58] F. E. Low.
"Bremsstrahlung of Very Low-Energy Quanta in Elementary Particle Collisions."
In: *Phys. Rev.* 110 (4 May 1958), pp. 974–977.
DOI: 10.1103/PhysRev.110.974.

[LS75] E. Longo et al.
"Monte Carlo calculation of photon-initiated electromagnetic showers in lead glass."
In: *Nuclear Instruments and Methods* 128.2 (1975), pp. 283–307.
DOI: https://doi.org/10.1016/0029-554X(75)90679-5.

[NHR85] W. R. Nelson et al.
"The Egs4 Code System."
In: *SLAC-0265, SLAC-265, SLAC-R-0265, SLAC-R-265* (Dec. 1985).

[Nuc21] European Organization for Nuclear Research: Engineering Department.
"How to Control the North Area Beam Lines."
Webpage, last access in 2021.
URL: http://sba.web.cern.ch/sba/documentations/how2controlnabeams.htm.

[Pli22] F. Pliquett.
Private communication.
2022.

[Pre22] R. Preghenella.
"A Next Generation Experiment Lightweight Application."
Webpage, last access in 2022.
URL: https://github.com/preghenella/g4me.

[Rey+21] K. Reygers et al.
"Soft photons with ALICE 3 - EMMI Rapid Reaction Task Force (RRTF)."
Webpage, last access in 2021.
URL: https://indico.gsi.de/event/12990/contributions/55294/attachments/36960/49406/2021-09-14-fct-emmi-workshop-v2.pdf.

[Sch23] J. Schoengarth.

"Simulation der Detektorantwort von MAPS auf einzelne Schauerteilchen."
2023.
URL: http://www.ikf.physik.uni-frankfurt.de/~buschin/thesis/Bachelorarbeit_Jan_Schoengarth.pdf.

[Sem+23] Tower Semiconductor Ltd. et al.
"CMOS IMAGE SENSORS - Tower Semiconductor."
Webpage, last access in 2023.
URL: https://towersemi.com/technology/cmos_image_sensor/.

[Sno14] W. Snoeys.
"CMOS monolithic active pixel sensors for high energy physics."
In: *Nuclear Instruments and Methods in Physics Research Section A: Accelerators, Spectrometers, Detectors and Associated Equipment* 765 (2014), pp. 167–171.
DOI: https://doi.org/10.1016/j.nima.2014.07.017.

[Sol20] E. H. Solheim.
"Characterisation of a Digital Sampling Calorimeter Prototype for Proton Computed Tomography With Electron Beams."
UNIVERSITY OF BERGEN, Department of Physics and Technology, Nov. 2020.
URL: https://bora.uib.no/bora-xmlui/handle/11250/2720436.

[Spa+18] S. Spannagel et al.
"Allpix2: A modular simulation framework for silicon detectors."
In: *Nuclear Instruments and Methods in Physics Research Section A: Accelerators, Spectrometers, Detectors and Associated Equipment* 901 (2018), pp. 164–172.
DOI: https://doi.org/10.1016/j.nima.2018.06.020.

[SSS10] S. Sarkar et al.
The Physics of the Quark-Gluon Plasma.
Springer, Lecture Notes in Physics, 2010.

[Sul18] M. Suljic.
"Study of Monolithic Active Pixel Sensors for the Upgrade of the ALICE Inner Tracking System."
2018.
URL: https://cds.cern.ch/record/2303618.

[Völ22] M. Völkl.
"Calculations for Soft Photon Measurements (ALICE3 – Dileptons and photons meeting)."

Webpage, last access in 2022.
URL: `https://indico.cern.ch/event/964235/contributions/4058215/attachments/2119906/3567607/2020-Oct-09Voelkl.pdf`.

[Won14] C.-Y. Wong.
"An Overview of the Anomalous Soft Photons in Hadron Production."
2014.
DOI: `10.48550/ARXIV.1404.0040`.

[Yok21] H. Yokoyama.
Private communication.
2021.

[Zha17] C. Zhang.
"Measurements with a High-Granularity Digital Electromagnetic Calorimeter."
Utrecht University Repository, 2017.